TECHNISCHE UNIVERSITÄT MÜNCHEN
Lehrstuhl für Flugantriebe

Investigation on Heat Transfer in Small Hydrocarbon Rocket Combustion Chambers

Christoph Ulrich Kirchberger

Vollständiger Abdruck der von der Fakultät für Maschinenwesen der Technischen Universität München zur Erlangung des akademischen Grades eines

Doktor-Ingenieurs

genehmigten Dissertation.

Vorsitzender:		Univ.-Prof. Dr.-Ing. Thomas Sattelmayer
Prüfer der Dissertation:	1.	Univ.-Prof. Dr.-Ing. Oskar J. Haidn
	2.	Univ.-Prof. Dr.-Ing. Stefan Schlechtriem, Universität Stuttgart

Die Dissertation wurde am 24.06.2014 bei der Technischen Universität München eingereicht und durch die Fakultät für Maschinenwesen am 08.10.2014 angenommen.

Acknowledgment

This thesis originates from my employment as member of the research staff at the space propulsion group of the Institute for Flight Propulsion, Technische Universität München. It covers work performed within the public funded projects *Förderprogramm Antriebe Bayern* (FAB, Bavarian Propulsion Development Program), *Aerodynamic and Thermal Load Interactions with Lightweight Advanced Materials for High Speed Flight* (ATLLAS) and *SFB Transregio 40* on “Technological foundations for the design of thermally and mechanically highly loaded components of future space transportation systems”.

First, I would like to thank Prof. Hans-Peter Kau who gave me the chance to work on the space propulsion subject, but who lost his fight against the cancer a short time before. I am much obliged for the trust he showed to me. I cordially thank Prof. Oskar J. Haidn for accepting the mentoring of my work and Prof. Stefan Schlechtriem for taking over the second survey as well as Prof. Thomas Sattelmayer for acting as chairman of the examination board.

I appreciate the open minded and fruitful cooperation with the colleagues of the ATLLAS project and Airbus Defence and Space (formerly EADS Astrium Space Transportation). Here, I would like to distinguish Johan Steelant, Marc Bouchez, Sebastian Soller, Markus Kuhn, Philip Martin, Christoph Höglauer, Jan Alting and Oliver Knab.

Also, I express my gratitude to the staff and the students of the Institute for Flight Propulsion. Exemplary, I like to highlight the assistance of Andreas Hupfer, Angelika Heininger and Wolfgang Erhard as well as Robert Wagner, who coded a numerousness of tools used for preparation, conducting and analysis of the tests, and Gregor Schlieben, who operated the test facility and performed the experiments.

Finally, I have to thank my parents and siblings, who always supported me and provided me a safe harbor regardless of the ups and downs of my life.

Zusammenfassung/ Abstract

Während in Russland und in den USA verschiedene Raketentriebwerke auf Basis von Kohlenwasserstoffen entwickelt und geflogen wurden, lag der Fokus der europäischen Forschung in den vergangenen drei Dekaden auf den Treibstoffkombinationen Wasserstoff mit Sauerstoff, sowie Hydrazin und seine Derivate mit Stickstoffoxiden. Im Zuge des Zwangs der Kostenreduzierung einerseits und dem Ersatz gefährlicher Stoffe andererseits sind zuletzt aber der Einsatz von Brennstoffen wie Kerosin und Methan wieder verstärkt diskutiert worden. Der Lehrstuhl für Flugantriebe der Technischen Universität München betreibt daher einen Kerosin/Sauerstoff-Raketenbrennkammerprüfstand, der Grundlagenforschung unter realitätsnahen Randbedingungen ermöglicht. Im Rahmen des Programmes ATLLAS, gefördert durch die EU im 6. Forschungsrahmenprogramm, wurden hier u.a. Untersuchungen zu Wärmeübergang, Filmkühlung, sowie transpirativ und konvektiv gekühlten faserverstärkten Keramiken durchgeführt, deren Ergebnisse – Ausbrand, Wärmestrom- und Temperaturmessungen – ein wesentlicher Gegenstand dieser Arbeit sind. Die experimentellen Daten dienen im Weiteren zur Aufstellung und Validierung ingenieursmäßiger Ansätze und Korrelation, die erste Abschätzungen bezüglich Wärmeübergang und Kühlungsbedarf im Rahmen der Vorentwicklung von Raketentriebwerken auf Basis von Kohlenwasserstoffen ermöglichen.

Whereas in Russia and the USA several rocket engines basing on hydrocarbon fuels have been developed and operated, European research focused on hydrogen with oxygen as well as hydrazine and its variants with nitrous oxides as rocket fuels in the last decades. In the course of constrained budgets and substitution of harmful substances the application of fuels like kerosene and methane has been reconsidered lately. The Institute for Flight Propulsion of Technische Universität München (Technical University of Munich) operates a kerosene/oxygen rocket combustion chamber test facility enabling fundamental research at application-oriented conditions. Within the framework of the EU-funded research project ATLLAS it served as testbed for investigations on heat transfer, film cooling, transpiration cooled fiber-reinforced ceramics and convectively cooled fiber-reinforced ceramics, whose results – combustion efficiencies, heat fluxes and temperature measurements – are an important part of this thesis. The experimental data serves as the base for design and validation of simple-to-use methods and correlations, which allow estimates of heat flux and cooling needs for the preliminary design of hydrocarbon fuel rocket engines.

Contents

List of Figures

List of Tables

Nomenclature

Acronyms

Abbreviation	**Denotation**
ATLLAS	*A*erodynamic and *T*hermal *L*oad Interactions with *L*ightweight *A*dvanced Materials for High *S*peed Flight
C/C	CMC, a Carbon Fiber/Carbon Matrix Composite
CC	Combustion Chamber
CEA	Computer Program for Calculation of Complex Chemical Equilibrium Compositions and Applications
CMC	Ceramic Matrix Composite
CFD	Computational Fluid Dynamics
CNG	Compressed Natural Gas
DAQ	Data Acquisition
DLR	Deutsches Zentrum für Luft- und Raumfahrt (German Aerospace Center)
FRSC	Fuel Rich Staged Combustion
GOX	Gaseous Oxygen
GG	Gas Generator
H/C	Hydrocarbon Fuel (for example kerosene)
HAP	Hydroxyl Ammonium Perchlorate
HF	High Frequency
HT	Heat Transfer
LF	Low Frequency
LFA	Lehrstuhl für Flugantriebe, Institute for Flight Propulsion
LH2	Liquid Hydrogen
LNG	Liquefied Natural Gas
LOX	Liquid Oxygen
MMH	Monomethylhydrazine
MON	Mixed Oxides of Nitrogen
MR	Combustion chamber mixture ratio (also called O/F)
Mu	see μ
NE	Nozzle Extension
NTO	Dinitrogen Tetroxide
NZZL	Nozzle
ORSC	Oxidizer Rich Staged Combustion
OXIPOL	CMC, SiOC matrix with alumina silicate fibers
PCC	Pressure in Combustion Chamber

Abbreviation	Denotation
PF	Pressure Fed
PSR	PTAH-SOCAR rocket duct
PTAH	Paroi Tissée Application Hypersonique
SC	Staged Combustion
SOCAR	Simple Operational Composite for Advanced Ramjet
SSTO	Single-Stage-To-Orbit
TBC	Thermal Barrier Coating
TC	Thrust Chamber
TC	Thermocouple
THW	Temperature of Hot Wall
TSTO	Two-Stage-To-Orbit
TUM	Technische Universität München
UDMH	Unsymmetrical Dimethylhydrazine
WHIPOX	CMC, alumina oxide matrix with alumina oxide fibers

Roman Symbols

Symbol	Denotation	Dimension
A	area	$[m^2]$
B_h	heat-transfer blowing parameter (Kays et al.)	$[-]$
C	optimization parameter	$[-]$
C_f	skin friction coefficient	$[-]$
c^*	characteristic velocity	$[m/s]$
c_D	discharge coefficient	$[-]$
c_e	effective exhaust velocity	$[m/s]$
c_F	thrust coefficient	$[-]$
c_p	specific heat capacity at constant pressure	$[\frac{J}{kg\,K}]$
d	diameter	$[m,\, mm]$
F	thrust	$[N]$
F	blowing ratio	$[-]$
h	specific enthalpy	$[J/kg]$
I	momentum ratio	$[-]$
I_{sp}	specific impulse	$[s]$
K	“coolant Reynolds number like term” (Grissom)	$[-]$
K_M	correction factor for molecular weight (Grissom)	$[-]$
K_t	correction factor for turbulence (Grissom)	$[-]$
k	correction factor	$[-]$
L	radiation path	$[m,\, mm]$
l	length, running length	$[m,\, mm]$
L^*	characteristic combustion chamber length	$[m]$
M	molar mass	$[kg/mol]$
m	mass	$[kg]$
$\dot{m}$	mass flow rate	$[kg/s]$
Ma	Mach number	$[-]$
n	shape factor (boundary layer)	$[-]$

Symbol	Denotation	Dimension
$\vec{n}$	normal vector	$[-]$
Nu	Nusselt number	$[-]$
O/F	mixture ratio	$[-]$
P	partial pressure	$[bar,\, MPa]$
p	pressure	$[bar,\, MPa]$
Pr	Prandtl number	$[-]$
$\dot{q}$	heat flux	$[W/m^2]$
r	coordinate, radial	$[m]$
r	curvature	$[m,\, mm]$
r	recovery factor	$[-]$
Re	Reynolds number	$[-]$
R_s	specific gas constant	$\frac{J}{kg \cdot K}$
S	surface	$[m^2]$
St	Stanton number	$[-]$
s	position from face plate	$[m]$
T	temperature	$[K]$
Tu	turbulence	$[-]$
t	thickness	$[m,\, mm]$
t	time	$[s]$
u	coordinate, circumferential	$[m]$
V	volume	$[m^3]$
v	velocity	$[m/s]$
X	none-dimensional run length	$[-]$
x	run length	$[m]$
z	coordinate, engine axis	$[m]$
z_2	modified coordinate (Stratford and Beavers)	$[m]$

Greek Symbols

Symbol	Denotation	Dimension
α	coefficient of heat transfer	$[\frac{W}{m^2\, K}]$
Δ_2	enthalpy thickness of thermal boundary layer	$[m]$
ε	area ratio, expansion ratio	$[-]$
ε_c	contraction ratio	$[-]$
ϵ	emissivity (radiation)	$[-]$
η	efficiency	$[-]$
κ	isentropic coefficient	$[-]$
λ	thermal conductivity	$[\frac{W}{m\, K}]$
μ	dynamic viscosity	$[Pa \cdot s]$
μ	film mass flow ratio	$[-]$
Θ	film cooling effectiveness	$[-]$
ρ	density	$[kg/m^3]$
Ψ	ratio of actual skin friction coefficient to skin friction coefficient for an impermeable flat plate with same momentum thickness Reynolds number (Kutateladze)	$[-]$

Superscripts and Subscripts

Symbol	Denotation
∞	static value of free stream
0	initial, at start, without blowing
$1 \ldots 4$	regarding corresponding chamber segment
a	ambient
avg	average
aw	adiabatic wall
B	final, at end
c	regarding the combustion chamber
$calc$	calculated value
cc	regarding cooling channel, bulk (water)
cf	cooling fluid (water)
cg	cold gas (ambient)
$cool$	cooling fluid (film or transpiration mass flow)
$correl$	regarding an empiric correlation
cyl	cylindrical
e	exit, at exit plane
exp	experimental
F	film related
Fu	fuel related
G	gas (general)
h	hydraulic
hg	hot gas
i	species index
in	inflow
inj	regarding injector, with respect to injector
L	liquid (general)
l	regarding length
$mean$	mean value
$nzzl$	nozzle
Ox	oxidizer related
out	outflow
P	propulsive
R	rocket
s	at a certain position from face plate
t, tot	total
tc	throat converging, convergent part of the nozzle
th	regarding nozzle throat, with respect to throat
$theo$	theoretical
w, $w1$	hot wall, inner wall
$w2$	cold wall, outer wall
x	regarding run length
z	along engine axis

Constants

Symbol	**Denotation**	**Value**
R	ideal gas constant	$8.3145\,\frac{\mathrm{J}}{\mathrm{K\cdot mol}}$
g_0	standard gravity	$9.81\,\mathrm{m/s^2}$
σ_S	Stefan-Boltzmann constant	$5.6704 \cdot 10^{-8}\,\frac{\mathrm{W}}{\mathrm{m^2\,K^4}}$

1. Introduction

When over 50 years ago, on 12th April 1961, Soviet cosmonaut Yuri Gagarin started with his space-capsule “Vostok 1” from cosmodrome Baikonur, he became the first human in space and the first man to orbit the Earth. The associated launch vehicle, which based on the R-7 intercontinental ballistic missile, was propelled by liquid oxygen (LOX) and kerosene featuring a thrust of approximately 3900 kN and a gross mass of over 280 t. This launch system is used with minor modifications as “Soyuz” in the nowadays Russian Aerospace industry up to date. Albeit in the United States the F1 rocket engine of the Saturn V launch vehicle powering the Apollo spaceships to the Moon used Kerosene and LOX as propellants, the research and development in Western civilizations focused on the more efficient rocket engines basing on liquid hydrogen (LH2) and liquid oxygen thereafter. With the demand of more cost-efficient operation of space flights, more environmentally friendly propulsion and commercial space transport evolving, the interest in hydrocarbons i.e. kerosene-based or methane-based rocket engines steadily grew within the last few years. In this context, the high pressure combustion facility of the Institute for Flight Propulsion (Lehrstuhl für Flugantriebe, LFA), Technische Universität München (TUM), has been built up as testbed for investigations on injector systems, cooling techniques and material compatibility tests with hydrocarbon fuels. The facility featured a single element subscale rocket engines operated with kerosene and gaseous oxygen (GOX) at pressure levels up to 10 MPa and hot gas temperatures exceeding 3500 K in the past. An upgrade of the testbed to provide gaseous methane is currently under construction.

The institute has participated in several national and international research programs. In the project ’Aerodynamic and Thermal Load Interactions with Lightweight Advanced Materials for High Speed Flight’, short ATLLAS, dealing with several aspects of high speed flight, detailed investigations on cooling techniques as well as thermal, mechanical and chemical compatibility of both metal-based and ceramic materials have been conducted. Thereby, film and transpiration cooling have been experimentally investigated alongside with combustion chamber segments made of ceramic matrix composites (CMC).

Although advanced materials and sophisticated cooling techniques have always been in the focus of aerospace, the high temperature and high pressure environment in the combustion chamber is still a great challenge for design engineers. The understanding of the mechanisms of heat transfer and cooling techniques is the key for mastering the designing of reliable and efficient combustion chambers. Therefore, worldwide much work is invested both in experiments as well as in tools capable to predict and analyze the heat transfer phenomena in a rocket engines. For the numerical simulation of the heat transfer within a rocket combustion chamber two different approaches can be used [1]: Either the hot gas side is simulated using a highly sophisticated computational fluid dynamics tool (CFD) or the heat transfer is modeled using semi-empiric correlations, which is the common way in engineering tools.

CFD bases on the fact, that flows and similar phenomena can be described by partial differential equations, which can usually not be solved analytically but approximated within small domains of space and/or time. The quality of the numerical solution is dependent on the quality of the approximations and the discretization used [2]. In addition to the equations for conservation of impulse, mass and energy (Navier-Stokes equations) as well as turbulence modeling in reacting flows such as in a rocket combustion chamber at least the interaction of the species (combustion) and the multi-phase nature of the flow (spray injection) must be described adequately [3]. In order to determine heat flux and wall temperature the hot gas flow simulation must be coupled with thermal calculations of the solid structure and simulations for the heat transfer to the cooling channel (“conjugate heat transfer”). In combination with the high Reynolds numbers presupposing high spatial resolutions of the meshes, CFD simulations of rocket combustion chambers cause high efforts in time and computational resources as well as skilled personnel interpreting and validating the results. Although a good agreement between CFD and experimental results is achievable (compare e.g. to [4–6] for LFA CC), for day-to-day use in test facility operations CFD is immoderate and inappropriate, but engineering tools are essentially required. Engineering tools are used for preparation of experiments in order to define e.g. the setup and adequate test conditions. Since the definition and optimization of the intended load point is often dependent of several parameters, several dozens or even some hundred calculations may have to be performed, which necessitates a robust and rapid simulation tool [7]. The correlation must have been validated against a comprehensive experimental database and calibrated using test facility specific corrections. Since the latter ones are regarded as “company know-how” few information on these enhancements has been published.

Also within ATLLAS, the test preparation and analysis at the TUM test facility has been performed with semi-empirical correlations. For this purpose, different models and correlations have been considered and evaluated by the partners involved in the testing activities and a model was defined. In this thesis this so-called “Common Approach” is presented and its application for the prediction of the heat transfer in different small rocket chamber configurations. First, a general overview of rocket engine specific terms and definitions, some useful classifications and an introduction into heat transfer and heat transfer modeling in rocket engines is given. The experimental setup as well as test data are presented next. Thereafter, the heat transfer modeling and the results of a model assessment and parameter optimization are shown as well as possibilities and limitations of the semi-empirical approach are discussed. Furthermore, applications to film and transpirations cooling as well as a convectively cooled CMC are presented. Finally, the findings will be summarized in a short conclusion.

2. Fundamentals of Rocket Propulsion

2.1 Definitions and Basic Principles

In this section basic principles which actually apply on most chemical rocket engines are presented. The relevant terms and correlations used to characterize rocket propulsion will be defined and explained.

2.1.1 Function Principle of Rocket Engines

Similar to air breathing propulsion, liquid rocket engines are reaction engines, but the inflow momentum is assumed negligible. In accordance with Newton's third law of motion ("action equals reaction"), propulsion is provided by expelling mass with high velocities, whereas the sum of momentum is conserved. A schematic overview of a rocket engine is given in Fig. 2.1.

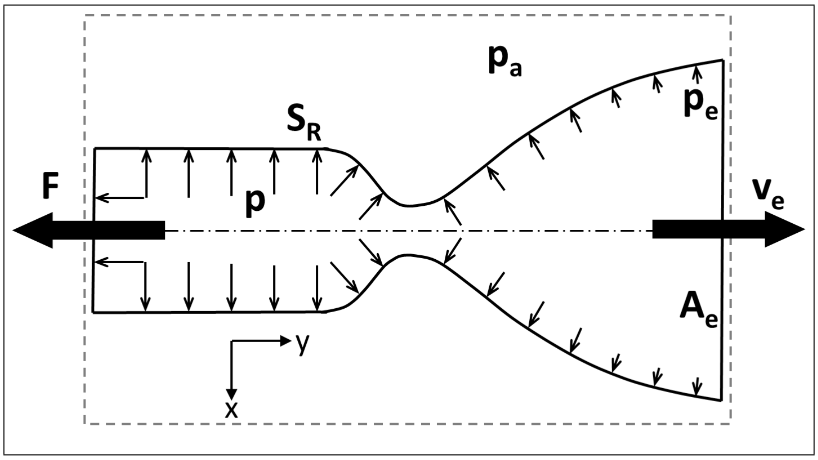

Fig. 2.1: Function Principle of a Reaction Engine

Assuming a control surface S consisting of the solid wall S_R and the nozzle exit area A_e, the resulting force in y direction from convective flows through the surface and pressure p on the surface has to be zero:

$$\iint\limits_{S} (\rho \vec{q} \vec{n})\, v \, dS + \iint\limits_{S} p \vec{n} \vec{j} \, dS = 0$$

Thereby, ρ denotes the density, $\vec{q}$ the velocity vector, v the y component of $\vec{q}$, $\vec{n}$ the normal vector on the surface dS and $\vec{j}$ the unit vector in y direction.

Since convective flow on the solid wall S_R is zero

$$\iint\limits_{S_R} (\rho \vec{q} \vec{n})\, v\, dS \equiv 0$$

the thrust F is the negative sum of the forces on the nozzle exit area A_e

$$\underbrace{\iint\limits_{A_e} (\rho \vec{q} \vec{n})\, v\, dS + \iint\limits_{A_e} p \vec{n} \vec{j}\, dS}_{F} + \underbrace{\iint\limits_{S_R} p \vec{n} \vec{j}\, dS}_{-F} = 0$$

$$F = \iint\limits_{A_e} (\rho \vec{q} \vec{n})\, v\, dS + \iint\limits_{A_e} p \vec{n} \vec{j}\, dS \tag{2.1}$$

Introducing p_a for the ambient pressure as well as average values over the nozzle exit area for pressure p_e and exit velocity v_e, the thrust F becomes with $\dot{m} = \rho\, v_e\, A_e$

$$F = \dot{m} v_e + (p_e - p_a) A_e = \dot{m} c_e \tag{2.2}$$

The effective exhaust velocity c_e represents the ideal case that exit pressure matches ambient pressure.

2.1.2 Tsiolkovsky Rocket Equation

The Tsiolkovsky rocket equation relates the change of velocity Δv of a spacecraft with the effective exhaust velocity c_e and the initial and final mass of the spacecraft, m_0 and m_B, respectively. The derivation uses the principle of the conservation of momentum neglecting any external forces like gravity or aerodynamic losses.

The sum of all changes of momentum has to be zero. At a time t a rocket may have a distinct mass m_R and velocity v_R. At the time $t + dt$ a mass $\dot{m}\, dt$ has left the rocket with velocity c_e. At the same time the mass of the rocket has been reduced by the expelled mass and the velocity of the rocket has been increased by dv_R. Details are shown in Fig. 2.2. For the momentum at t and at $t + dt$ applies

$$\begin{aligned}
\dot{\vec{I}} &= \vec{F} = 0 \\
I_R|_t &= m_R \cdot v_R \\
I_R|_{t+dt} &= (m_R - \dot{m}\, dt)\, (v_R + dv_R) \\
I_G|_{t+dt} &= (\dot{m}\, dt)\, (v_R + dv_R - c_e) \\
I|_t &= I|_{t+dt}
\end{aligned}$$

which can be expanded to

$$\begin{aligned}
m_R\, v_R &= m_R\, v_R + m_R\, dv_R - \dot{m}\, dt\, v_R \ldots \\
&\quad \ldots - \dot{m}\, dt\, dv_R + \dot{m}\, dt\, v_R + \dot{m}\, dt\, dv_R - \dot{m}\, dt\, c_e \\
m_R\, dv_R &= \dot{m}\, dt\, c_e
\end{aligned}$$

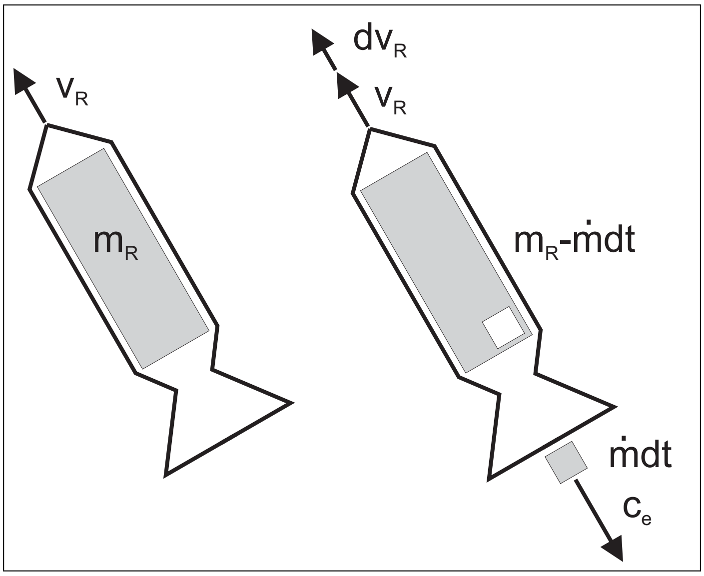

Fig. 2.2: Derivation of Tsiolkovsky Equation

Using the substitution

$$\begin{aligned} m_R(t+dt) &= m_R(t) - \dot{m}\,dt \\ \dot{m} &= -\frac{dm_R}{m_R} \end{aligned}$$

by integrating over the limits of initial v_0 and final v_B velocity of the rocket as well as over the limits of initial m_0 and final m_B mass of the rocket it can be shown

$$\begin{aligned} dv_R &= -\frac{dm_R}{m_R} c_e \\ \int_{v_0}^{v_B} dv_R &= -c_e \int_{m_0}^{m_B} \frac{1}{m_R}\, dm_R \\ \Delta v &= c_e \cdot ln\left(\frac{m_0}{m_B}\right) \end{aligned} \tag{2.3}$$

The Tsiolkovsky rocket equation is the most fundamental correlation for space transportation. It clarifies the demand for high performance propulsion, which is represented by c_e, since exhaust velocity and final velocity of the rocket are proportional. Also the necessity of lightweight structures is obvious, since structure and payload compete against each other in the final mass of the rocket m_B. Finally, the requirement for high initial masses m_0 thus high propellant masses in order to achieve high velocities, which are required for e.g. missions to the moon, is visible.

2.1.3 Specific Impulse

The specific impulse I_{sp} has been defined as ratio of thrust F and the mass flow rate of propellants $\dot{m}$, which has been normalized by the standard gravity $g_0 = 9.81\frac{\mathrm{m}}{\mathrm{s}^2}$. To avoid conversion issues between metric and imperial units, the specific impulse has the odd unit of a time[1].

$$I_{sp}[\mathrm{s}] = \frac{F}{\dot{m} \cdot g_0} = \frac{c_e}{g_0} \tag{2.4}$$

The specific impulse is a measurement for the energy content of the propellants as well as efficiency of the conversion of the energy into thrust in the rocket engine. The energy conversion should generate the highest exhaust velocity possible in order to minimize fuel consumption for a given thrust level.

2.1.4 Characteristic Velocity

The characteristic velocity c^* is given by the relation of the total pressure in the throat p_c multiplied by the throat area A_{th} divided by the propellant mass flow rate $\dot{m}$.

$$c^* = \frac{p_c \cdot A_{th}}{\dot{m}} \tag{2.5}$$

For chemical rocket propulsion the characteristic velocity is used to rate the combustion and to characterize the quality of the propellant injection process.

2.1.5 Thrust Coefficient

The thrust coefficient c_F is defined by the ratio of the total thrust F of the engine and the virtual thrust in the throat defined by the total pressure in the throat p_c multiplied by the throat area A_{th}.

$$c_F = \frac{F}{p_c \cdot A_{th}} = \frac{\dot{m}\, v_e}{p_c \cdot A_{th}} + \frac{A_e}{A_{th}} \left(\frac{p_e - p_a}{p_c} \right) \tag{2.6}$$

The thrust coefficient indicates how much the virtual thrust in the throat is increased by the nozzle. It is a measure for the quality of energy conversion in the nozzle.

2.1.6 Mixture Ratio

For rocket applications, the mixture ratio O/F marks the percentage of oxidizer mass flow and fuel mass flow.

$$\frac{O}{F} = \frac{\dot{m}_{Ox}}{\dot{m}_{Fu}} \tag{2.7}$$

In rocket applications the mixture ratio usually is always smaller than the stoichiometric O/F, since the highest specific impulses are achieved for fuel rich conditions.

---

[1] Occasionally, the specific impulse is defined without g_0 leading to the expression $I_{sp}[\mathrm{m/s}] = \frac{F}{\dot{m}} \equiv c_e$.

2.1.7 Ideal Rocket

The expansion of hot gases and thus the exhaust velocity of a chemical rocket engine can be calculated from the gas kinetics. For analysis and pre-design phases usually the following simplifications are introduced [8, 9]:

- The gas flow is assumed adiabatic, one-dimensional, steady-state and frictionless.
- The fluid is homogeneous. If any condensed species exist, they are in a thermal and kinetic equilibrium with the exhaust gas and their mass is negligible.
- Chemical equilibrium is established in the combustion chamber and the composition is frozen in the nozzle. The fluid can be considered as a perfect gas meaning that specific heat capacity and isentropic exponent are constant.
- There are no shock waves or any other discontinuities in the nozzle.

With these assumptions, the so-called ideal rocket might be calculated from several thermodynamic relations.
For an adiabatic system the total enthalpy h_{tot} is constant meaning that enthalpy $h = c_p\,T$ of within the combustion chamber is converted to kinetic energy $\frac{v^2}{2}$ in the nozzle. Since the gas is assumed to be a perfect gas, the heat capacity c_p is constant leading to a similar expression for the total temperature T_{tot}:

$$\begin{aligned} h_{tot} &= const. = \frac{v_c^2}{2} + c_p\,T_c = \frac{v^2}{2} + c_p\,T = \frac{v_e^2}{2} + c_p\,T_e \\ T_{tot} &= const. = \frac{v_c^2}{2\,c_p} + T_c = \frac{v^2}{2\,c_p} + T = \frac{v_e^2}{2\,c_p} + T_e \end{aligned}$$

Since the velocity in the combustion chamber v_c is usually small and therefore negligible ($v_c \approx 0$), the velocity can be calculated as

$$v = \sqrt{2\,c_p\;(T_c - T)} \tag{2.8}$$

Using the equation of state for adiabatic processes

$$\begin{aligned} \frac{p}{\rho^\kappa} &= const. \\ \frac{T_1}{T_2} &= \left(\frac{p_1}{p_2}\right)^{\frac{\kappa-1}{\kappa}} = \left(\frac{\rho_1}{\rho_2}\right)^{\kappa-1} \end{aligned}$$

as well as the definition for the specific heat c_p

$$c_p = \frac{\kappa}{\kappa-1}\cdot R_s = \frac{\kappa}{\kappa-1}\cdot\frac{R}{M}$$

the velocity might be rewritten as

$$\begin{aligned} v &= \sqrt{2\,c_p\,T_c}\,\sqrt{1-\left(\frac{p}{p_c}\right)^{\frac{\kappa-1}{\kappa}}} = v_{max}\,\sqrt{1-\left(\frac{p}{p_c}\right)^{\frac{\kappa-1}{\kappa}}} \\ v &= \sqrt{2\,\frac{\kappa}{\kappa-1}\cdot\frac{R}{M}\,T_c}\,\sqrt{1-\left(\frac{p}{p_c}\right)^{\frac{\kappa-1}{\kappa}}} \end{aligned} \tag{2.9}$$

This new correlation can be used for the equation of continuity in order to define the mass flow density:

$$\begin{aligned} \dot{m} &= \rho\cdot v\cdot A \\ \frac{\dot{m}}{A} &= \rho\cdot v = \frac{M}{R}\,\frac{p}{T}\cdot v = p_c\,\frac{M}{R\,T_c}\left(\frac{p}{p_c}\right)^{\frac{1}{\kappa}}\cdot v \\ &= p_c\,\frac{M}{R\,T_c}\left(\frac{p}{p_c}\right)^{\frac{1}{\kappa}}\cdot\sqrt{2\,\frac{\kappa}{\kappa-1}\cdot\frac{R}{M}\,T_c}\,\sqrt{1-\left(\frac{p}{p_c}\right)^{\frac{\kappa-1}{\kappa}}} \\ \frac{\dot{m}}{A} &= p_c\cdot\sqrt{\frac{2\,\kappa}{\kappa-1}\,\frac{M}{R\,T_c}\left[\left(\frac{p}{p_c}\right)^{\frac{2}{\kappa}}-\left(\frac{p}{p_c}\right)^{\frac{\kappa+1}{\kappa}}\right]} \end{aligned} \tag{2.10}$$

The mass flow density becomes zero (or alternatively A becomes infinite) in the case $p = 0$ or $p = p_c$. The derivation of the mass flow density with respect of p allows the determination of the maximum mass flow density and similar of the so-called critical pressure ratio in the throat:

$$\begin{aligned} \frac{d\left(\frac{\dot{m}}{A}\right)}{dp} &\equiv 0 \\ \frac{p_{th}}{p_c} &= \left(\frac{2}{\kappa+1}\right)^{\frac{\kappa}{\kappa-1}} \end{aligned} \tag{2.11}$$

Hence, the mass flow density in the throat is determinable.

$$\frac{\dot{m}}{A_{th}} = p_c\cdot\sqrt{\frac{M}{R\,T_c}\,\kappa\left(\frac{2}{\kappa+1}\right)^{\frac{\kappa+1}{\kappa-1}}} \tag{2.12}$$

The nozzle expansion ratio ε is the ratio of nozzle exit area A_e and throat area A_{th}:

$$\varepsilon = \frac{A_e}{A_{th}} = \left(\frac{p_c}{p_e}\right)^{\frac{1}{\kappa}}\cdot\frac{\sqrt{\frac{\kappa-1}{2}\left(\frac{2}{\kappa+1}\right)^{\frac{\kappa+1}{\kappa-1}}}}{\sqrt{1-\left(\frac{p_e}{p_c}\right)^{\frac{\kappa-1}{\kappa}}}} \tag{2.13}$$

As long as in the nozzle no flow separation occurs, the pressure ratio $\frac{p_e}{p_c}$ is defined by the expansion ratio $\frac{A_e}{A_{th}}$ and vice versa.
The characteristic velocity can be described as

$$c^* = \frac{p_c\,A_{th}}{\dot{m}} = \sqrt{\frac{R\,T_c}{M\,\kappa}\left(\frac{2}{\kappa+1}\right)^{\frac{\kappa+1}{\kappa-1}}} \tag{2.14}$$

This derivation shows, that the characteristic velocity is highly dependent from the characteristics of the propellants (κ, M, T_c), but is almost independent of the combustion pressure p_c (p_c might have a minor effect on dissociation of the gases thus T_c in high pressure applications).
With these correlations, the specific impulse I_{sp} can be expressed as

$$I_{sp} = \frac{c_e}{g_0} = \frac{1}{g_0} \left\{ \sqrt{\frac{2\,\kappa}{\kappa - 1} \frac{R T_c}{M} \left[1 - \left(\frac{p_e}{p_c} \right)^{\frac{\kappa-1}{\kappa}} \right]} + \frac{p_e - p_a}{p_c} \cdot c^* \cdot \varepsilon \right\} \tag{2.15}$$

A high specific impulse can be achieved with high-energy propellants (high $\frac{T_c}{M}$), a high expansion ratio ε (high $\frac{A_e}{A_{th}}$ thus high $\frac{p_c}{p_e}$ and when operating at non-negligible backpressures (sea level) a high combustion pressure.

2.1.8 Efficiency of Rocket Engines

The conversion of the chemical energy of the propellants into kinetic energy and thrust is not lossless. First of all, the burning in the combustion is uncompleted due to improper mixing and evaporation of the propellants. These losses should be minimized by proper injection systems and sufficient residence time thus combustion chamber length. Depending on the cooling technique, energy is also lost over the combustion chamber and nozzle walls. This leads to the efforts undertaken to minimize cooling requirements. Finally, the expelled gases have a residual thermal and kinetic energy, which is lost for propulsion of the spacecraft.
For rocket engines, the definitions of the nozzle efficiency η_{c_F} and the combustion efficiency η_{c^*} are of importance:

$$\eta_{c_F} = \frac{c_F}{c_{F,theo}} \tag{2.16}$$

$$\eta_{c^*} = \frac{c^*}{c^*_{theo}} \tag{2.17}$$

The resulting impulse efficiency $\eta_{I_{sp}}$ gives a description of the overall performance of the rocket engine:

$$\eta_{I_{sp}} = \frac{I_{sp}}{I_{sp,theo}} = \eta_{c^*} \cdot \eta_{c_F} \tag{2.18}$$

Since the determination of η_{c^*} and η_{c_F} requires the knowledge of the total pressure in the nozzle throat as well as the effective throat area, which measuring is non-trivial, the use of $\eta_{I_{sp}}$ is the most common performance characteristic in rocket engine development.

2.2 Classification of Liquid Rocket Propulsion

In this section an overview on liquid rocket propulsion is given. First, the different kinds of space propulsion are presented in order to characterize liquid propulsion in comparison to other chemical as well as non-chemical propulsion systems. Afterwards, components and power cycles for typical liquid rocket engines depicted. Different liquid propellants are introduced and special attention will be turned on hydrocarbon fuels. Finally, examples for hydrocarbon based liquid rocket engines are given.

2.2.1 Characterization

Space propulsion may be divided by the source of energy in either chemical propulsion or non-chemical propulsion. The chemical propulsion systems comprise of air-breathing, solid propellant and liquid propellant as well as hybrid rocket engines. Apart exotic propulsion systems like space tethers or solar sails, the group of non-chemical propulsion is mainly formed by nuclear rocket engines and electric space propulsion. An overview of space propulsion systems classified by the source of energy is given in Fig. 2.3.

Chemical Propulsion			Non-Chemical Propulsion		
Air Breathing	Liquid Rocket Engines	Solid Rocket Engines	Electric Propulsion	Nuclear Rocket Engines	„Exotic“ Propulsion
	(Hybrid Rocket Engines)				
Ramjet **Scramjet**			**Electrothermic** **Electrostatic** **Electromagnetic**		**Space Tethers** **Solar Sails**
In development	**Common use for main and upper stages, satellites**	**Common use for boosters, and military**	**Common use for satellites**	**No further developments**	**Concepts**

Fig. 2.3: Classification of Space Propulsion

Nuclear rocket engines take use of the heat release of a nuclear fission or fusion to heat up a fluid, typically hydrogen. The fluid is afterwards expanded over a convergent-divergent nozzle. Although nuclear propulsion features moderate thrust and a higher performance than conventional rocket engines, development and testing of prototypes has been cut down and finally almost cut off due to safety and legal concerns.

Electric propulsion utilizes electric power provided by, for example, a solar array or battery. In the case of an electro thermal engine the electric power is used to heat up a gas, which is expanded in a convergent-divergent nozzle. Otherwise the power might be used to accelerate ions in an electric field (electrostatic engines) or a plasma in combined electric and magnetic fields (electromagnetic engines). Electric propulsion features moderate to high performance but at very low thrust levels. It is therefore regularly applied in satellites for station keeping purposes or in deep space probes.

Air-breathing engines for space propulsion may be regarded as a special type of chemical propulsion where one propellant (oxidizer) is not stored aboard but taken from ambient.

Several concepts have especially been discussed for Single-Stage-To-Orbit (SSTO) and Two-Stage-To-Orbit (TSTO) space transport systems in order to improve the payload to gross weight ratio. Although still in focus of research, air-breathing engines play actually no role in space transport.

A solid rocket engine is characterized by the propellants, both fuel and oxidizer, being stored in solid state in the same volume, which also serves as the combustion chamber. The chemical reaction takes place on the surface of the propellant block. The hot products are expanded in a convergent-divergent nozzle. Solid rocket engines are commonly used as for instance boosters, apogee motors, sounding rockets and missiles.

Hybrid rocket engines combine one liquid propellant, which is usually the oxidizer, with a solid propellant block, forming the combustion chamber like in solid rocket engine.

In liquid rocket engines one or more gaseous or liquid propellants are stored in separate tanks. They are transported by pumps or by pressure gradient from the tank in the combustion chamber, where they are mixed-up, burnt and the hot exhaust gases are expanded over a convergent-divergent “de Laval” nozzle. Liquid rocket engines are the most common and variable type of space propulsion used in almost each space-related application worldwide.

2.2.2 Components and Cycles of Liquid Rocket Engines

As shown in Fig. 2.4 a liquid rocket propulsion system may be broken down in several parts and components. The propellant system consists of the tanks, feed lines and auxiliary valves as well as the pressure system. In case of pressure-fed rocket engines, the latter provides the pressure gradient to feed the injector and combustion chamber. In pump-fed engines the pressure system ensures a minimum suction head at pump inlet in order to prevent e.g. cavitation.

The rocket engine comprises the thrust chamber assembly (short TC or TCA), the main valves and, if applicable, the turbo pumps with associated drive (together also named “power pack”). The thrust chamber consists of the injector assembly, the combustion chamber (CC) with the nozzle throat section and the nozzle extension (NE). The breakdown in combustion chamber with nozzle throat and nozzle extension rather than cylindrical part and nozzle is practical, since in real applications the nozzle extension and the combustion chamber are usually separate components manufactured with different technologies.

Depending on the method the propellant is fed to the injector and combustion chamber, a liquid rocket engine can be classified to one of the cycles depicted in Fig. 2.5(a) to Fig. 2.5(f). The already mentioned pressure-fed engine is the simplest liquid rocket engine cycle due to the absence of any turbo components (see Fig. 2.5(a) for schematic). The propellant tanks are pressurized either during filling (blow-down) or by an external pressure gas reservoir and the propellants flow due to the pressure gradient into the engine. For pressure-fed cycles achievable mass flow rates, thrust and combustion pressure are limited, since the burst strength thus mass of the propellant tanks is crucial. Therefore, pressure-fed systems are commonly used in satellites and upper stage applications where combustion pressure and thrust rather than simplicity and reliability are of minor importance.

Gas generator cycle engines as shown in Fig. 2.5(b) are in common use for main stage and upper stage applications. The propellants are fed to the injector by turbo pumps which are driven by two turbines or alternatively one turbine with or without a gear box. The energy for the turbines is provided by a separate combustion chamber called gas generator where a

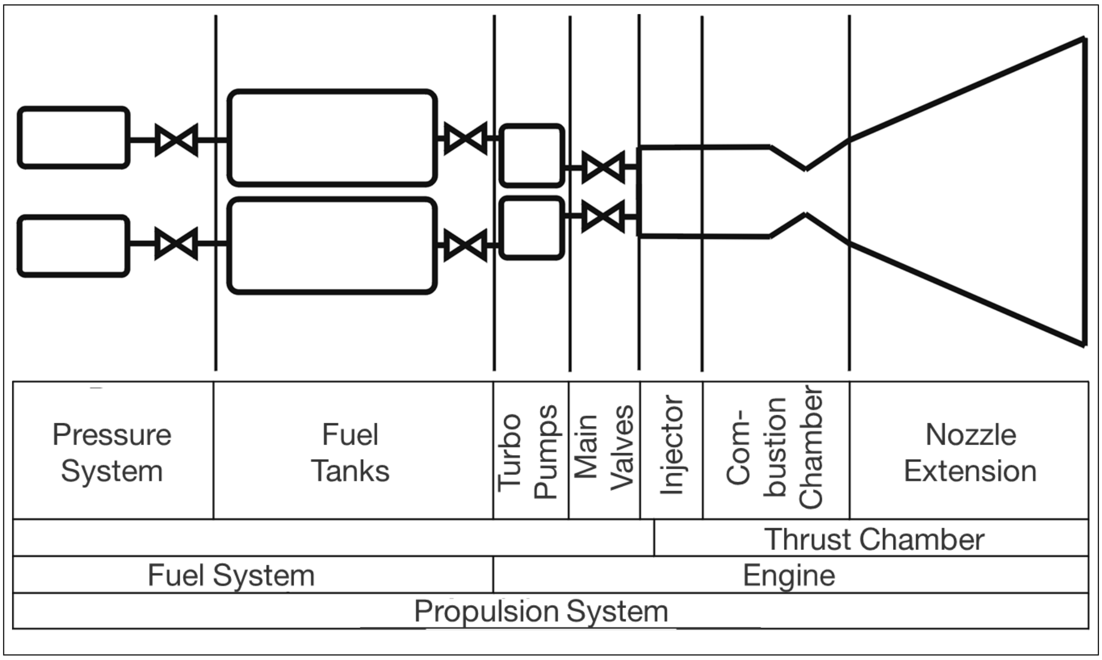

Fig. 2.4: Components of a Liquid Rocket Propulsion System

small amount of propellant is burnt at moderate pressure and temperatures. The exhaust gases of the gas generator are expanded over the turbine with a high pressure ratio and bled off downstream, being vented overboard or injected in the nozzle extension without going through the main combustion chamber (open cycle). By the tapping and burning of part of the propellants at lower efficiency in the gas generator the overall specific impulse is constrained and the achievable combustion pressure in the main chamber is limited to approximately 15 MPa depending on e.g. efficiency of turbo components. Advantages of the gas generate cycle base on the lower requirements for the turbo components and the quite strict separation of power pack and main chamber operation.

The less common variant of an expander bleed cycle as depicted in Fig. 2.5(c) uses a small part of the heated propellant which is extracted from the cooling system, expanded over turbines at a high pressure ratio for the drive of the turbo pumps and bled off afterwards. Like the gas generator cycle, the expander bleed cycle is an open cycle, but simpler with respect of component count and startup. It may be used if a high thrust by propellant mass flow rate is a more important design requirement than a high specific impulse thus overall engine efficiency.

The so-called expander cycle is shown in Fig. 2.5(d). It is the simplest closed cycle meaning all propellant is going through the main combustion chamber. For the expander cycle, a high mass flow of heated propellant from the cooling is expanded over turbines at a low pressure ratio to power the turbo pumps and then burnt in the main combustion chamber. Albeit a high specific impulse is possible, restrictions in the propellant heat up (overheating of structures, potential decomposition) and turbine expansion ratio (required pumping head) limit achievable combustion pressure to about 10 MPa. Therefore the favored application of expander cycle engines is in high performance upper stages, where high specific impulse is crucial but combustion pressure is no performance driver.

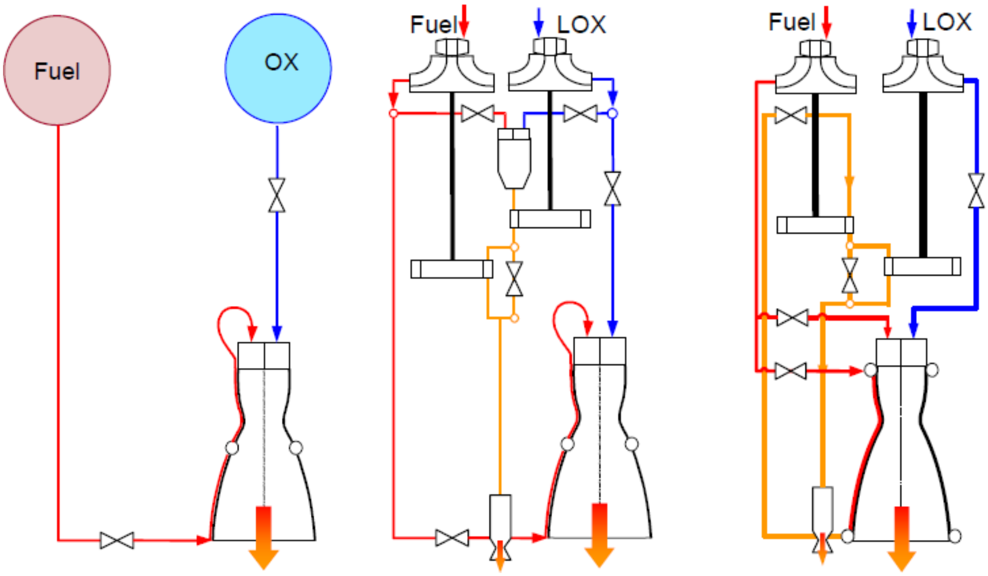

(a) Pressure Fed (b) Gas Generator (c) Expander Bleed

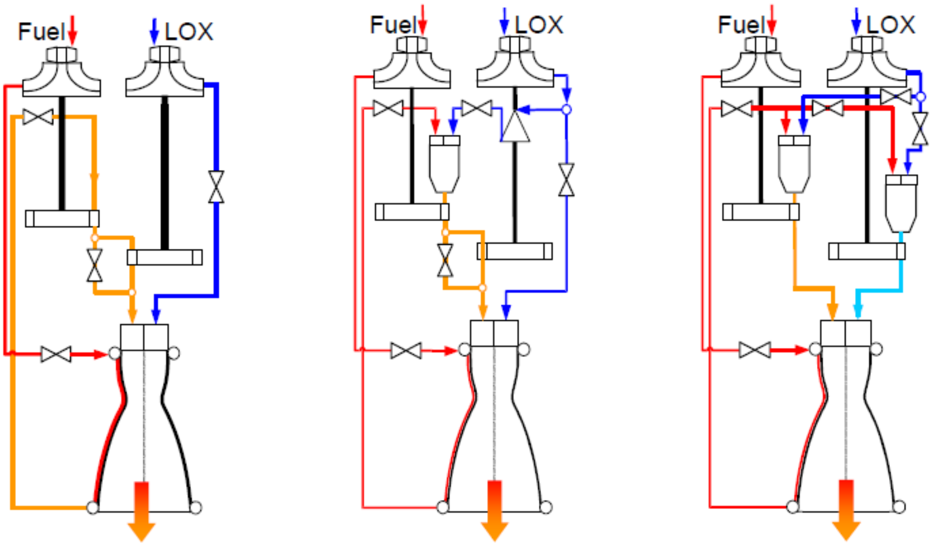

(d) Expander (e) Staged Combustion (f) Full Flow Staged Combustion

Fig. 2.5: Cycles in Liquid Rocket Engines [8]

In staged combustion cycle engines (see Fig. 2.5(e) for schematic) all or the major part of one propellant component is preburned with a small amount of the other propellant component at high pressure and moderate temperatures. The exhaust gases of the preburner are used to power the turbines for the turbo pumps and are burnt with the remaining propellant in the main combustion chamber afterwards. The staged combustion cycle allows high performance and high combustion pressures up to approximately 25 MPa but are challenging with respect to complex interaction of main combustion chamber and preburner as well as mastering stable operation of the fuel or oxidizer rich preburner. The most powerful liquid rocket engines in use nowadays are of the staged combustion type.

The full flow staged combustion cycle as depicted in Fig. 2.5(f) is a variation of the staged combustion cycle where all of the fuel and also all of the oxidizer flow through the turbines. The fuel is precombusted with a small amount of oxidizer as well as the oxidizer is precombusted with a small amount of fuel in order to provide the power for the turbo pumps. Although the design provides higher combustion pressure and efficiency than e.g. staged combustion, this concept has been realized on demonstrator level only so far.

2.2.3 Liquid Propellants

Liquid rocket propellants may be classified by the number of reactants involved. Monopropellants, which are also called monergols, are substances or homogeneous mixtures which decompose in an exothermic reaction due to the presence of a catalyst or due to heating. Examples of thermal decomposable substances are isopropyl nitrate, ethylene oxide and hydroxyl ammonium perchlorate (HAP), which, however, are rarely used. More important are catalytic decomposable substances like hydrogen peroxide and most notably hydrazine.

Bipropellants are any combinations of an oxidizer and a fuel which are stored separately and then mixed in the combustion chamber. Bipropellants are divided into combinations of fuel and oxidizer which ignite on contact (hypergolic combination) and such which require an external ignition energy. Typically hypergolic combinations consists of hydrazine or any of its derivatives monomethylhydrazine (MMH) and unsymmetrical dimethylhydrazine (UDMH) or a mixture thereof as fuel and dinitrogene tetroxide or nitric acid or a mixture thereof (called MON, Mixed Oxides of Nitrogen) as oxidizer. Although combinations of hydrogen or hydrocarbons with fluorine are also hypergolic, such combinations have not been widely used due to the high toxicity and corrosive characteristics of the fluorine. The combination of kerosene and hydrogen peroxide is improperly called a hypergolic combination since the self-ignition of this combination bases on the pre-decomposition of the hydrogen peroxide (kerosene + cold hydrogen peroxide is not hypergolic). Typical non-hypergolic combinations are liquid hydrogen and liquid oxygen or any hydrocarbons like methane, ethanol or kerosene and liquid oxygen.

Finally tripropellants[2] are bipropellants, which are combined with one of the addition agents lithium, beryllium, aluminum or boron, and may therefore be regarded as special variant of bipropellant. Albeit they feature higher performance as the associated bipropellant, tripropellants are rarely used due to complexity, costs and environmental considerations and are therefore neglected here.

---

[2] The use of the denomination *tripropellant* is inconsistent in literature. As "tripropellant rocket" a spacecraft is defined carrying two different fuels for start and final acceleration to take advantage of reduced structural mass.

For convenience, the classification of liquid rocket propellants regarding number of reactants is summarized in Fig. 2.6.

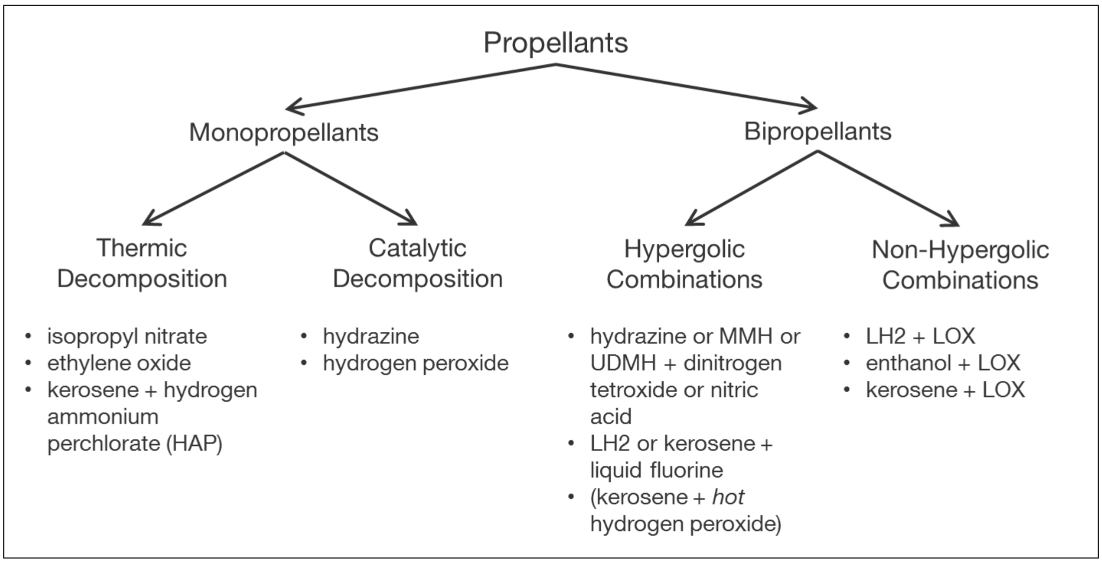

Fig. 2.6: Liquid Propellants [10]

Another classification of liquid rocket propellants is based on the suitability for storage. Storable propellants, short storables, are substances which are liquid at ambient temperature and ambient to moderate pressure. Storable fuels are e.g. hydrazine, MMH and UDMH as well as alcohols (methanol and ethanol) and kerosene. Storable oxidizers are dinitrogene tetroxide and hydrogen peroxide.

Cryogenics are substances which are liquid at temperatures well below 100 K only which requires extensive insulation and continuous cooling, making handling costly. Also for in-flight applications the reasonable storage time is limited to a few days. The most important cryogenics are liquid hydrogen and liquid oxygen.

Space storables or soft cryogenics are substances which are liquid at temperatures of approximately 120 K. These temperature level may be maintained at in-orbit applications for longer times. Also less insulation than for cryogenic substances is required reducing handling costs and tank mass. Typical space storable fuels are liquid methane and liquid propane. Although oxygen difluoride has been discussed as potential space storable oxidizer, no practical implementation can be found.

2.2.4 Use of Hydrocarbons in Rocket Engines

Hydrocarbons are organic substances consisting entirely of hydrogen and carbon and represent an important group of rocket fuels. Hydrocarbons may be divided in saturated hydrocarbons (known as alkanes or paraffins), unsaturated hydrocarbons with one or more double bonds (named alkenes or olefines), unsaturated hydrocarbons with one or more triple bonds (alkynes like acetylenes and homologous), cycloalkanes (also called naphthenes) and aromatic hydrocarbons (arenes) [10]. Since unsaturated hydrocarbons have a limited suitability for storage because of resinification due to the double or triple bonds and since cycloalkanes and aromatic hydrocarbons feature a lower hydrogen content thus performance as a result of higher molecular weight of the exhaust gases, only the alkanes are relevant as rocket fuels. Methane and kerosene are the most important hydrocarbons for rocket applications. Although they are not as powerful as hydrogen, they replaced the alcohols (usually ethanol) used in early rocket engines due to a better performance (cf. Fig. 2.7).

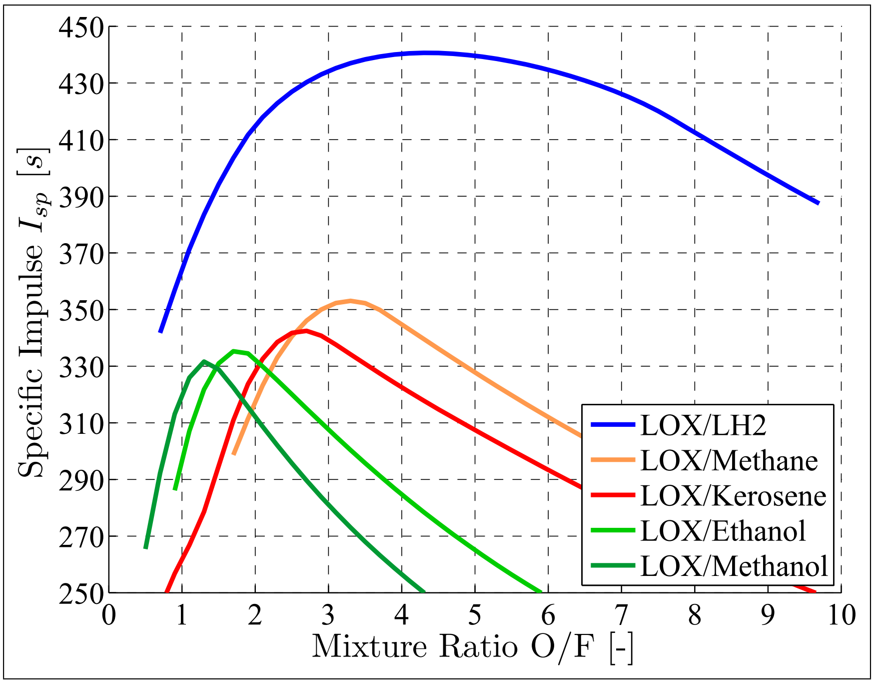

Fig. 2.7: Performance of Different Rocket Propellants ($p_c = 10$ MPa, $p_c/p_e = 100$)

Methane is a chemical substance with the chemical formula CH_4. It is the simplest of all alkanes and at ambient condition a colorless and odorless gas. Important chemical and physical properties of chemical pure methane are summarized in Tab. 2.1. Using oxygen as oxidizer the burning of methane at the stoichiometric mixture ratio $O/F = 4.0$ produces carbon dioxide and water:

$$CH_4 + 2O_2 \rightarrow CO_2 + 2H_2O$$

Property	Value
Formula	CH_4
Molar mass	16.043 kg/kmol
Freezing point	90.7 K
Boiling point	111.6 K
Critical temperature	190.6 K
Critical pressure	4.60 MPa
Critical density	162.7 kg/m^3

Tab. 2.1: Properties of Pure Methane [11]

For rocket relevant conditions with respect to pressure and nozzle expansion ratio the highest specific impulse is achieved for mixture ratios of about 3.5. However, potential soot deposition and decomposition of methane in the cooling channel has to be taken into account. Methane is the most important component of natural gas with a volume fraction of 80 % up to 99 %. Therefore, compressed natural gas (CNG) or liquified natural gas (LNG) might be used instead of pure methane although residues of e.g. sulphur or phosphor may have a negative impact on material compatibility. Requirements for different grades of technically pure methane defined by MIL-PRF-32207 standard are given in Tab. 2.2.

Property	Grade		
	A	B	C
Purity (CH_4), % Vol, min	98.7	99.9	99.97
Water, ppmV, max	1	0.5	0.5
Oxygen, ppmV, max	1	1	1
Nitrogen, ppmV, max	5000	100	100
Carbon dioxide, ppmV, max	125	50	50
Other gaseous impurities, ppmV, max (i.e. Ar, H_2, He, Ne)	5000	125	125
Ethane (C_2H_6). ppmV. max	5000	500	100
Propane (C_3H_8), ppmV, max	3000	500	100
Other volatile hydrocarbons, ppmV, max	1	1	1
Total volatile sulphur, ppmV, max	1	0.1	0.1
Non-volatile residue (NVR) & particulates	10	1	1

Tab. 2.2: Requirements for Methane According to MIL-PRF-32207 [12]

Kerosene is a substance created by fractional distillation of crude oil in a boiling range of 423 K to 623 K. Since kerosene is a mixture of different hydrocarbons, the chemical composition thus physical properties like viscosity, heat capacity, conductivity and density may vary. Applicable specifications like RP-1, Jet A-1 or JP-8 do not define certain compositions but ensure minimum requirements and standards regarding burning point, ignition point and contaminations the fuel has to comply with. An overview of the most important specifications of kerosene is given in Tab. 2.3.

Specification	Reference	Remark
Jet A-1	ASTM[3] D1655 Annex 2	Most common commercial kerosene for jet propulsion outside of the USA; similar to Jet A, Avtur and JP-8.
Jet A	ASTM D1655	Common commercial kerosene for jet propulsion in the USA; freezing point −40°C rather than −47°C for Jet A-1.
Avtur	DERD 2494	British military specification, max. freezing point −48°C and a higher fraction of aromatic hydrocarbons allowed than for Jet A-1; also known as NATO F-35.

---

[3] ASTM: American Society for Testing and Materials

Specification	Reference	Remark
JP-8	MIL-DTL-83133	US military specification, complies with Jet A-1 but defines some special additives; also known as NATO F-34.
JP-5	MIL-DTL-5624	US military specification, high flash point kerosene (minimum 60°C instead of 38°C as for Jet A-1 and JP-8), used for naval applications, higher density, lower vapor pressure and lower heat capacity than Jet A-1; similar to Avcat defined by British DERD 2498; also known as NATO F-44.
RP-1	MIL-DTL-25576	“Rocket Propellant 1”, obtained from crude oil with a high napthene content with further treatment (acid washing, sulphur dioxide extraction) [14]
T-1	GOST 10227-86	Special Russian kerosene, made from oil with low contents of sulphur [15]

Tab. 2.3: Specifications for Kerosene [13]

In this work the relevant kerosene grades are Jet A-1, which has been used in experiments, and RP-1, due to its importance for liquid rocket propulsion. Selected requirements for RP-1 are given in Tab. 2.4. Thereby, US units have been converted where reasonable. Similarly, properties of Jet A-1 are summarized in Tab. 2.5.

Property	Unit	Value
Aromatics	$[\%Vol]$ max	5.0
Olefins	$[\%Vol]$ max	2.0
Sulphur	$[\%mass]$ max	0.003
Flash Point	[°C] min	60
Density at 15°C	$[kg/m^3]$	$798\ldots814$
Freezing point	[°C] max	-51
Net heat of combustion	$[MJ/kg]$ min	43.0

Tab. 2.4: Requirements for RP-1 by MIL-DTL-25576 [16]

Rachner [13] gives the molecular formula for kerosene as $C_{12}H_{23}$. Using oxygen as oxidizer the burning of kerosene at the stoichiometric mixture ratio $O/F = 3.4$ would produce carbon dioxide and water:

$$4C_{12}H_{23} + 71O_2 \rightarrow 48CO_2 + 46H_2O$$

Optimum mixture ratios for rocket engine applications using the propellants kerosene and oxygen lie around 2.6 [14].

Albeit potential oxidizers for hydrocarbons include H_2O_2, OF_2 and F_2, where especially combinations with fluorine feature highest performance, oxygen O_2 is the only oxidizer with

Property	Unit	Value
Aromatics	$[\%Vol]$ max	22
Olefins	$[\%Vol]$ max	?
Sulphur	$[\%mass]$ max	0.3
Flash Point	[°C] min	38
Density at 15°C	[kg/m^3]	775 . . . 840
Freezing point	[°C] max	−47
Net heat of combustion	[MJ/kg] min	42.8

Tab. 2.5: Requirements for Jet-A1 by ASTM D1655 Annex 2 [17]

Property	Value
Formula	O_2
Molar mass	31.999 kg/kmol
Freezing point	54.4 K
Boiling point	90.6 K
Critical temperature	154.8 K
Critical pressure	5.08 MPa
Critical density	426.7 kg/m^3

Tab. 2.6: Properties of Oxygen [11]

practical relevance in liquid rocket propulsion. Important chemical and physical properties of oxygen are summarized in Tab. 2.6.

2.2.5 Examples for Hydrocarbon Liquid Rocket Engines

An overview on different hydrocarbon based liquid rocket engines is given in Tab. 2.7. Actually, most relevant applications use the propellant combination kerosene (RP-1) and liquid oxygen.

Engine (Spacecraft)	Origin	Propellant	Cycle	F_{vac} [kN]	$I_{sp,vac}$ [s]	In Use	First Flight
RD-107 (Sputnik)	Russia	Kerosene/ LOX	GG	971	306	N	1957
R17 (Scud B/D)	Russia	Kerosene/ Nitric Acid	GG	93.1	251	Y	1961
H-1 (Saturn I/IB)	USA	RP-1/ LOX	GG	948	289	N	1961
F-1 (Saturn IC[4])	USA	RP-1/ LOX	GG	7741	304	N	1967

---

[4] Saturn IC is the 1st Stage of Saturn V.

Engine (Spacecraft)	Origin	Propellant	Cycle	F_{vac} [kN]	$I_{sp,vac}$ [s]	In Use	First Flight
Gamma 8 (Black Arrow)	UK	Kerosene/ H2O2	SC[5]	235	265	N	1969
RD-171 (Zenit 1)	Russia	Kerosene/ LOX	ORSC	7550	337	Y	1985
RD-170 (Energia)	Russia	Kerosene/ LOX	ORSC	7906	337	N	1987
RD-180[6] (Atlas III)	Russia (USA)	Kerosene/ LOX	ORSC	4152	338	Y	2000
RD-117[7] (Soyuz ST)	Russia	Kerosene/ LOX	GG	1021	310	Y	2001
Kestrel (Falcon 1)	SpaceX USA	RP-1/ LOX	PF	31	320	N	2006
RD-0124 (Soyuz 2.1b)	Russia	Kerosene/ LOX	ORSC	294	359	Y	2006
Merlin 1C (Falcon 9 V1.0)	SpaceX USA	RP-1/ LOX	GG	615	304	N	2008
NK-33 (Taurus II)	Russia (OSC[8] USA)	Kerosene/ LOX	ORSC	1638	331	Y	2012
Merlin 1D (Falcon 9 V1.1)	SpaceX USA	RP-1/ LOX	GG	716	310	Y	2013

Tab. 2.7: Relevant Hydrocarbon Rocket Engines (in chronological order of first flight) [14, 18–21]

2.3 Heat Transfer Phenomena in Rocket Engines

Liquid rocket engines are characterized by thermo chemical processes. Within the combustion chamber, temperatures of the gases of more than 3500 K are reached. Since no technical available material can withstand such temperatures, cooling systems are obligatory.

The modeling of the heat transfer within the cooled structure of a combustion chamber may be subdivided into the following subproblems [22]:

- Determination of the resulting temperature, pressure, fluid properties, gas composition, etc. of the combustion and the hot gas in the combustion chamber.

- Evaluation of the heat transfer, i.e. the heat transfer coefficient at the hot inner chamber wall. This may include fractions driven by radiation as well as convection.

---

[5] Decomposition of H2O2

[6] RD-180 is a two thrust chamber derivative of the four-chamber RD-170/RD-171.

[7] RD-117 is an enhanced RD-107, which has been in use since 1957 in different variants.

[8] Orbital Science Corporation (OSC) uses Russian engines mothballed in the 1970s.

Aspects like film and transpiration cooling or soot deposition might be represented within the calculation of the hot gas side heat transfer coefficient.

- Calculation of the conduction of heat in the chamber wall. Effects caused by curvature of walls, fins, holes and cavities, different chamber materials and local heat soak have to be considered.
- Evaluation of the heat transfer into the coolant. The knowledge of fluid properties especially in the case of unstable and decomposing coolants might be of great importance.
- Evaluation of the heat transfer from the outer chamber wall to ambiance. While this might be neglected if the outer wall temperature is low, the heat transfer has to be modeled i.e. for radiative cooled ceramics and nozzles.

In the following sections the necessity for the high combustion temperatures as well as the functional principles, computational approaches and models for the different heat transfer phenomena and cooling techniques are presented.

2.3.1 Heat and Performance

The whole purpose of a rocket engine is to change the rockets velocity in order to fulfill the intended mission. As explained in section 2.1.2 the change of the rocket's velocity is directly proportional to the effective exhaust velocity c_e, whereas for a given mission Δv the required propellant mass $m_0 - m_B$ is determined by c_e:

$$\Delta v = c_e \, ln \frac{m_0}{m_B}$$

In assumption of adiabatic system the effective exhaust velocity is linked to the total enthalpy $h_{tot} \approx h_c$ of the system and for an ideal rocket as defined in section 2.1.7 to the combustion chamber temperature T_c.

$$\begin{aligned} c_e &= I_{sp} \cdot g_0 = \frac{F}{\dot{m}} = v_e \, \frac{p_e - p_a}{\dot{m}} \, A_e \\ v_e &= \underbrace{\sqrt{2 \cdot (h_c - h_e)}}_{\text{ideal rocket:}} \\ v_e &= \sqrt{2 \, c_p \cdot (T_c - T_e)} \\ v_e &= \sqrt{2 \, \frac{\kappa}{\kappa - 1} \cdot \frac{R}{M} \, T_c \, \left[1 - \left(\frac{p_e}{p_c} \right)^{\frac{\kappa-1}{\kappa}} \right]} \end{aligned} \tag{2.19}$$

The total enthalpy is dependent of the enthalpy change for the chemical reaction taking place during combustion.

$$h_c \propto \Delta H^0_{reaction} \tag{2.20}$$

As stated by Hess's law the enthalpy change for a reaction is independent of the reaction process but defined by the enthalpy of formation of the reactants and products.

$$\Delta H^0_{reaction} = \sum \Delta H^0_{products} - \sum \Delta H^0_{reactants} \tag{2.21}$$

This leads to the conclusion that high total enthalpies thus temperatures are required in the combustion chamber in order to provide a high-performance rocket engine. High reaction enthalpies are achieved if very reactive propellants with high enthalpy of formation are burnt to products with very low enthalpy of formation.

2.3.2 Adiabatic Wall

The model of an adiabatic wall assumes that no heat is transferred from or to the wall ($\dot{q} = 0$). A schematic is given in Fig. 2.8. In the thrust chamber hot gases flow with the velocity v_∞ and the temperature T_∞. The total temperature is T_c. In the boundary layer (dotted line) the velocity decreases down to zero (no-slip wall) and the static temperature increases up to the adiabatic wall temperature T_{aw}.

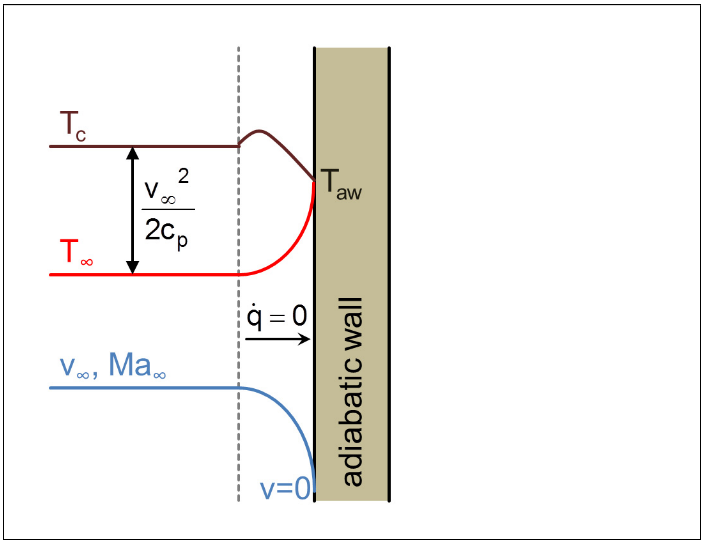

Fig. 2.8: Schematic of Adiabatic Wall

Unlike ideal and isentropic flows the total temperature is not fully recovered at the wall. Due to radiative heat transfer within the boundary layer the resulting adiabatic wall temperature is always slightly below T_c. The remaining difference between total temperature and adiabatic wall temperature is characterized by the recovery factor r.
The boundary layer theory determines r as a function of the Prandtl number Pr depending

on the intensity of turbulence.

$$r = \frac{T_{aw} - T_\infty}{T_c - T_\infty} \tag{2.22}$$

laminary:

$$r = \sqrt{Pr} \tag{2.23}$$

turbulent:

$$r = \sqrt[3]{Pr} \tag{2.24}$$

The dimensionless Prandtl number describes here the ratio of the kinematic viscosity to the thermal diffusity. Introducing recovery factor r the adiabatic wall temperature T_{aw} can be calculated as

$$T_{aw} = T_\infty \left[1 + r \cdot \underbrace{\left(\frac{T_c}{T_\infty} - 1 \right)}_{\frac{\kappa - 1}{2} \cdot Ma_\infty^2} \right] \tag{2.25}$$

The model of an adiabatic wall applies to uncooled structures in steady-state condition. Although this concept has no practical significance in rocket engines since material limits would be exceeded by far, the adiabatic wall temperature is relevant as reference case for heat transfer and used in e.g. film cooling models. Therefore, the adiabatic wall temperature T_{aw} is also sometimes referred as the recovery temperature of the hot gases near the wall.

2.3.3 Convective Heat Transfer

Convective heat transfer is linked to the transport of masses. Particles e.g. molecules or colloids move due to advection and to a minor degree due to diffusion carrying thermal energy. Free or natural convection is caused by temperature differences resulting in different densities which under influence of gravitational forces result in mass transport. In the so-called forced convection the fluid movement is induced by other external forces e.g. due to a pressure gradient. In rocket engines, forced convection is the main driver for heat transfer from the hot gases to the combustion chamber walls.

Since the materials used for rocket thrust chambers cannot withstand the high recovery temperatures, active cooling is applied. With the hot gas side wall temperature $T_{w1} \neq T_{aw}$, the resulting temperature gradient between hot gas and cooled wall causes a heat flux where the proportionality constant is the heat transfer coefficient α_{hg}.

$$\dot{q} = \alpha_{hg} \cdot (T_{aw} - T_{w1}) \tag{2.26}$$

The heat transfer coefficient is dependent of fluid properties (viscosity μ, heat conductivity λ, specific heat capacity c_p, density ρ, etc.) as well as flow characteristics (e.g. velocity v, run length s, hydraulic channel diameter d_h). For this reason, the convective heat transfer is influenced by several thermochemical and design characteristics of the combustion chamber such as geometry, contour and surface quality of the chamber wall, design of injector and combustion chamber liner, combustion pressure, perturbances, turbulence and the kind of propellants as well as reaction kinetics.

The heat transfer is usually described by four dimensionless characteristics. The Nusselt number Nu is the ratio of convective heat transfer and diffusive heat transfer, the Prandtl number Pr is the quotient of impulse propagation to heat propagation and the Reynolds Re is the ratio of inertial forces to frictional forces. The Stanton number St is the ratio of the heat transferred to the thermal capacity of a fluid. The latter one is used to describe e.g. the intensity of cooling.

$$Nu = \frac{\alpha \cdot d_h}{\lambda} \tag{2.27}$$

$$Pr = \frac{\mu \cdot c_p}{\lambda} \tag{2.28}$$

$$Re = \frac{\rho \cdot v \cdot d_h}{\mu} \tag{2.29}$$

$$St = \frac{Nu}{Re \cdot Pr} = \frac{\alpha}{\rho \cdot v \cdot c_p} \tag{2.30}$$

A common form of correlations for the heat transfer in rocket engines was proposed by *Bartz* [23], where the different correlations mainly differ in the values for the coefficients a, b and C, potential corrections for e.g. curvature or wall roughness and the reference conditions for determination of the fluid properties.

$$Nu = \frac{\alpha_{hg} \cdot d_h}{\lambda_{hg}} = C \cdot Re^a \cdot Pr^b \cdot corrections \tag{2.31}$$

The standard correlations available in open literature are often suitable for a first rough estimation only. Rocket engine operators use additional semi-empirical corrections, which are not published but regarded as “company know-how”. To model the hot gas side heat transfer the thermodynamic and transport properties of the combustions gases have to be determined with respect to a reference pressure p_{ref} and reference temperature T_{ref}. The reference temperature may be set on base of the free-stream or the recovery temperature, hot wall temperature or with respect to a mean value of recovery and hot wall temperature, where the latter approach of the so-called film-based correlations are regarded advantageous. Different approaches may also be used regarding the gas composition and chemical reactions [1,3,6,22].

For *frozen flows* the chemical reaction rate is regarded much lower than the residence time of the gases leading to a fixed gas composition depending on combustion pressure p_c and combustion temperature T_c only. This approach is often applied to the nozzle throat area and the nozzle extension due to the high Mach number thus high flow velocities there. For *equilibrium flow* it is assumed that the local gas composition is a function of the local thermodynamic conditions. In theory, this requires that the residence time of the gases or the chemical reaction rate is infinite. Practically, this assumption is more or less true within the combustion chamber for all non-complex rocket fuels. A tool to calculate equilibrium flow is the well known CEA by *Gordon and McBride* [24]. *Non-equilibrium* conditions exist, if the residence time is similar to the chemical reaction time. Thereby the specific reaction rate of each partial reaction has to be taken into account. Tools which are capable

to calculate non-equilibrium flow are e.g. TDK [25], CHEMKIN [26] or Cantera [27], but they are commercial, subject to export restrictions or poorly documented.
A well-known correlation to calculate the heat transfer coefficient in a rocket engine was presented by *Bartz* [23] in 1957:

$$Nu = 0.026 \cdot \left(\frac{\rho \cdot v_\infty \cdot d_h}{\mu}\right)^{0.8} \cdot Pr^{0.4} \cdot \left(\frac{d_{th}}{r_{tc}}\right)^{0.1} \tag{2.32}$$

As reference temperature for calculation of the hot gas properties a film temperature basing on the mean of free-flow static and hot wall temperature $T_{ref} = \frac{T_\infty + T_w}{2}$ has been used.
A modified or enhanced variant of Eq. 2.32 from 1968 by Bartz himself has been cited by *Schmidt* [1, 28, 29]. It applies correcting factors for the influence of the Mach number and the temperature gradient in the boundary layer. Also the reference temperature has been given on base of the adiabatic wall temperature T_{aw} rather than on the free-flow static temperature $T_{ref} = \frac{T_{aw} + T_w}{2}$.

$$\begin{aligned} Nu &= 0.026 \cdot \left(\frac{\rho \cdot v_\infty \cdot d_h}{\mu}\right)^{0.8} \cdot Pr^{0.4} \cdot \left(\frac{d_{th}}{r_{tc}}\right)^{0.1} \cdot \sigma \\ \sigma &= \left[\frac{1}{2} \cdot \frac{T_w}{T_{aw}} \left(1 + \frac{\kappa - 1}{2} Ma^2\right) + \frac{1}{2}\right]^{-0.68} \left[1 + \frac{\kappa - 1}{2} Ma^2\right]^{-0.12} \end{aligned} \tag{2.33}$$

Schacht [30] investigated the axial and circumferential heat transfer variations of two fuel-rich H_2/O_2 rocket combustion chambers in a pressure regime of 1.0 to 6.8 MPa. He found the best agreement between model and experimental results for a correlation using axial run length x rather than d_h.

$$Nu = 0.0215 \cdot \left(\frac{\rho \cdot v_\infty \cdot x}{\mu}\right)^{0.8} \cdot Pr^{0.3} \tag{2.34}$$

The transport properties of the gas has been determined as function of a reference enthalpy h_{ref}, which has been proposed by *Eckert* [31].

$$\begin{aligned} T_{ref} &= T\left(h_{ref}, p_\infty\right) \\ h_{ref} &= \frac{1}{2} \cdot \left(h_w + h_\infty\right) + 0.22 \cdot \left(h_c - h_\infty\right) \cdot \sqrt[3]{Pr\left(h_{ref}, p_\infty\right)} \end{aligned} \tag{2.35}$$

Polifke [32] cites a general correlation for pipe flows by *Gnielinski* [33] for $0.5 < Pr < 500$, $2300 < Re < 10^6$ and $10 < \frac{l}{d_h} < \infty$:

$$Nu_{cf} = \frac{\frac{\xi}{8} \cdot (Re - 1000) \cdot Pr}{1 + 12.7 \cdot \sqrt{\frac{\xi}{8}} \cdot \left(Pr^{\frac{2}{3}} - 1\right)} \cdot k_x \cdot k_{Pr} \tag{2.36}$$

$$\xi = \left(1.82 \cdot \lg Re - 1.64\right)^{-2} \tag{2.37}$$

The factor k_x is a correction for the start-up and k_{Pr} for the temperature-dependent properties:

$$k_x = 1 + \left(\frac{d_h}{l}\right)^{\frac{2}{3}} \tag{2.38}$$

$$k_{Pr} = \left(\frac{Pr|_{T=T_{cc}}}{Pr_w|_{T=T_w}}\right)^{0.11} \tag{2.39}$$

Sinyarev [34] has presented a correlation noting that it has been derived from pipe flow calculations by *Gukhman* [35] and proven by experience.

$$Nu = 0.0162 \cdot \left(\frac{\rho \cdot v_\infty \cdot d_h}{\mu} \cdot Pr\right)^{0.82} \left(\frac{T_{aw}}{T_w}\right)^{0.35} \tag{2.40}$$

Sinyarev uses the wall temperature as reference temperature $T_{ref} = T_w$ for the determination of the transport properties.

2.3.4 Radiative Heat Transfer

Generally speaking, radiation is the energy transfer by electromagnetic waves. In particular, thermal radiation is the energy transfer by electromagnetic waves with a wavelength of 700 *nm* up to approximately 1 *mm* due to the intrinsic temperature of the matter. In a rocket engine, radiative heat transfer takes place in different forms like e.g. from the chamber wall to the ambient (through nozzle throat), from the gas to the face plate or most important from the gas to the chamber wall. The significance of the radiative heat transfer on the total heat transfer depends on the composition of the exhaust gases thus the propellants used, load point as well as geometry and material of the chamber wall. *Schmidt* [1] shows for two different examples that the heat transfer by radiation at least one order of magnitude smaller than the heat transferred by convection. The main reaction products of hydrocarbon combustion, which are water vapor and carbon dioxide, are both known to be strong gas radiation emitters. Additional products like methane and carbon monoxide are usually disregarded [1, 11, 38]. While the partial pressure of methane in the combustion gases is usually low, the partial pressure of carbon monoxide can be at least twice as high as carbon dioxide under typical rocket conditions. However, an estimation based on figures by *Ostrander* [36] indicated that the radiosity of carbon monoxide will be still one order of magnitude lower than the one of carbon dioxide. Therefore, radiation must not be neglected, but consideration of water vapor and carbon dioxide will be sufficient in most cases.

Supposing that two isothermal diffuse surfaces with emissivities independent of frequency (gray body radiators) forming an enclosure feature uniform radiosity and irradiation, some special cases and simplified correlation may be applied in calculation [37]. The heat flux transferred by thermal radiation from the hot gas to the chamber wall may then be characterized by a heat transfer coefficient for radiation $\alpha_{hg,rad}$ as well as recovery and wall temperature (cf. Eq. 2.41) [32].

$$\dot{q} = \alpha_{hg,rad} \cdot (T_{aw} - T_w) \tag{2.41}$$

The heat transfer coefficient for radiation can be defined in the following way:

$$\alpha_{hg,rad} = \sigma_{12}\left(T_1 + T_2\right)\left(T_1^2 + T_2^2\right) \tag{2.42}$$

Hereby the variable σ_{12} represents the relation of the areas which interchange radiation. For rocket engines, a hot gas cylinder enclosed by a cylindrical wall may be supposed. For two coaxial cylinders σ_{12} is given as

$$\sigma_{12} = \frac{\sigma_S}{\frac{1}{\epsilon_1} + \frac{A_1}{A_2}\left(\frac{1}{\epsilon_2} - 1\right)} \tag{2.43}$$

whereas $\sigma_S = 5.67 \cdot 10^{-8}\frac{\mathrm{W}}{\mathrm{m^2\ K^4}}$ is the Stefan-Boltzmann-Constant for radiation [32, 38]. The symbols ϵ_1 and ϵ_1 represent the total emissivity of each radiating surface. Assuming that the effective outer diameter of the imaginary cylinder filled up with hot gas is virtually equal to the inner chamber diameter equation 2.42 can be written as

$$\alpha_{hg,rad} = \frac{\sigma_S}{\frac{1}{\epsilon_w} + \frac{1}{\epsilon_{aw}} - 1}\left(T_w + T_{aw}\right)\left(T_w^2 + T_{aw}^2\right) \tag{2.44}$$

The evaluation of the total emissivity is nontrivial both for ϵ_w and ϵ_{hg}. The total emissivity for the chamber wall can usually be only derived within a certain range resulting in the need to use average or worst case values. For the determination of emissivity of the hot gas composition usually complex analysis on the radiation spectrum of each gas component and the interaction of overlapping radiation spectrums gas has to be made. A convenient approach is the use of empirical formulation for the most important sources of gas radiation, water vapor and carbon dioxide, what should provide sufficiently exact values on one hand, but is still easily applicable.

Schmidt [1] gives an empiric correlation by *Barrère and Jaumotte* [39] both for water and carbon dioxide:

$$\dot{q}_{rad,H_2O}\left[\frac{\mathrm{W}}{\mathrm{m^2}}\right] = 4.07 \cdot \left(P_{H_2O}\right)^{0.8} \cdot \left(L_{eff}\right)^{0.6} \cdot \left(\left[\frac{T_{aw}}{100}\right]^3 - \left[\frac{T_w}{100}\right]^3\right) \tag{2.45}$$

$$\dot{q}_{rad,CO_2}\left[\frac{\mathrm{W}}{\mathrm{m^2}}\right] = 4.07 \cdot \left(P_{CO_2} \cdot L_{eff}\right)^{0.33} \cdot \left(\left[\frac{T_{aw}}{100}\right]^{3.5} - \left[\frac{T_w}{100}\right]^{3.5}\right) \tag{2.46}$$

Here, the terms P_{H_2O} and P_{CO_2} represent the partial pressure of water vapor and carbon dioxide (in [bar]), respectively, and L_{eff} the effective radiation path (in [m]), which is $\approx 0.6 \cdot l_{cyl}$ for cylindrical combustion chambers.

Schack [38] has published the following correlations:

$$\begin{aligned}\dot{q}_{rad,H_2O}\left[\frac{\mathrm{W}}{\mathrm{m^2}}\right] &= \left(46.5 - 84.9 \cdot P_{H_2O} \cdot L_{eff}\right)\left(P_{H_2O} \cdot L_{eff}\right)^{0.6} \ldots \\ &\quad \ldots \cdot \left[\frac{T_{hg}}{100}\right]^{2.32 + 1.37\sqrt[3]{P_{H_2O} \cdot L_{eff}}}\end{aligned} \tag{2.47}$$

$$\dot{q}_{rad,CO_2}\left[\frac{\mathrm{W}}{\mathrm{m^2}}\right] = 10.35 \cdot \left(P_{CO_2} \cdot L_{eff}\right)^{0.4} \cdot \left[\frac{T_{hg}}{100}\right]^{3.2} \tag{2.48}$$

Eq. 2.48 has been found valid for a product of partial pressure and radiation path of $0.004\ \text{m} \cdot \text{bar} \leq P_{H_2O} \cdot L_{eff} \leq 0.3\ \text{m} \cdot \text{bar}$. Schack states that Eq. 2.48 describes the heat flux by radiation of CO_2 with a deviation to experimental data of less than 20 % for almost all radiation paths and partial pressures in a temperature regime of 750 °C to 1800 °C (1023 K to 2073 K). Carbon dioxide has a high emissivity, which is strongly dependant of the temperature, but only slightly dependent of the radiation path. For water vapor, the temperature has a low influence, but the influence of the partial pressure is significant.

Kirchberger et al. [22] give for the thermal heat flux by radiation of water and carbon dioxide the following correlations, which have been attributed to *Schack* by *Marty* [40], but have been calibrated against other semi-empirical investigations and dedicated gas radiation computations:

$$\dot{q}_{rad,H_2O}\left[\frac{\text{W}}{\text{m}^2}\right] = 5.74 \cdot (P_{H_2O} \cdot r_c)^{0.3} \cdot \left(\frac{T_{hg}}{100}\right)^{3.5} \tag{2.49}$$

$$\dot{q}_{rad,CO_2}\left[\frac{\text{W}}{\text{m}^2}\right] = 4 \cdot (P_{CO_2} \cdot r_c)^{0.3} \cdot \left(\frac{T_{hg}}{100}\right)^{3.5} \tag{2.50}$$

The formulas presented can be used to get a first step for the modeling of the hot gas radiation in the chamber. The driving parameter of most of the radiation estimating is the product of the radiating path L and the molar partial pressure P.

2.3.5 Heat Conduction

Heat conduction is the transfer of thermal energy due to a temperature gradient. In contrast to convection, conduction is not linked to mass flow, but to energy transfer caused by the vibrations of the molecules and free electrons. In rocket engines, heat conduction is most important for the heat transfer within the combustion chamber walls, although conduction also takes place in the hot gas.

The heat conductance can be described by Fourier's law. Assuming a constant thermal conductivity λ the differential form of Fourier's law is

$$\dot{\vec{q}} = -\lambda \cdot \nabla T \tag{2.51}$$

which simplifies in the one-dimensional case over the combustion chamber wall to

$$\dot{q} = \frac{\lambda}{t_{hg}} \left(T_{w1} - T_{w2}\right) \tag{2.52}$$

where t_{hg} is the wall thickness as depicted in Fig. 2.9, T_{w1} is the (hot) inner wall and T_{w2} is the (cold) outer wall.

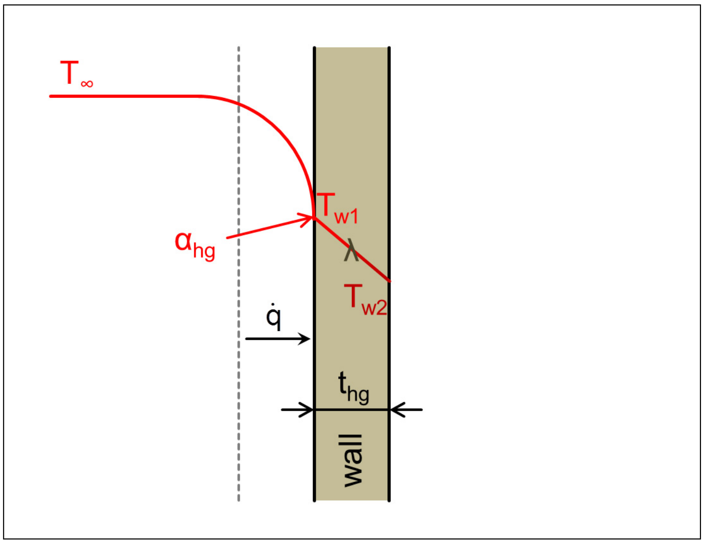

Fig. 2.9: Heat Conduction in a Combustion Chamber Wall

2.3.6 Thermal Barrier Coatings

A thermal barrier coating (TBC) is a protective layer with a lower thermal conductivity but a higher operational temperature limit than the regular combustion chamber liner material. Fig. 2.10 presents the functional principle.

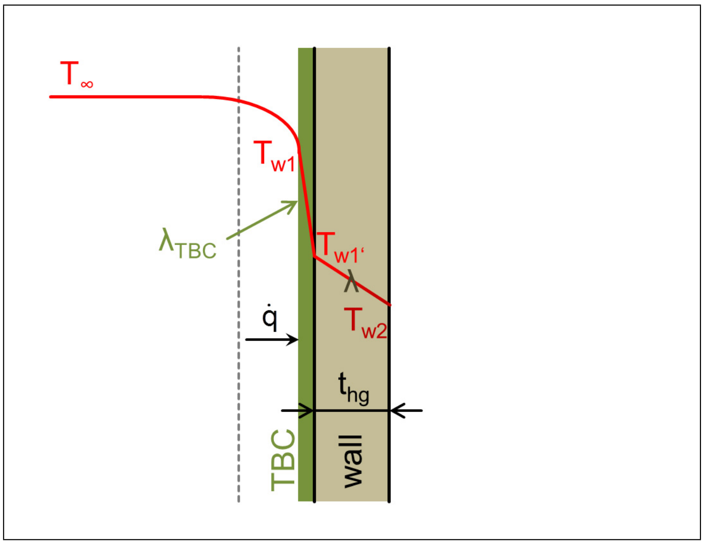

Fig. 2.10: Function Principle of Thermal Barrier Coating

The inner hot wall temperature of the liner material shall be $T_{w1'}$ and the outer wall temperature T_{w2}. The inner wall temperature of the TBC featuring a thickness t_{TBC} with thermal conductivity λ_{TBC} is T_{w1}. The heat flux $\dot{q} \propto (T_\infty - T_{w1})$ as well as the maximum liner temperature $T_{w1'}$ will them be reduced.

$$\dot{q} = \frac{\lambda_{TBC}}{t_{TBC}} \left(T_{w1} - T_{w1'}\right) = \frac{\lambda}{t_{hg}} \left(T_{w1'} - T_{w2}\right) \tag{2.53}$$

$$\dot{q} = \frac{T_{w1} - T_{w2}}{\frac{\lambda_{TBC}}{t_{TBC}} + \frac{\lambda}{t_{hg}}} \tag{2.54}$$

The application as well as safeguarding of the reliability of thermal barrier coatings is challenging. They are therefore usually used in high loaded areas only. Otherwise, in hydrocarbon based rocket engines the deposition of soot on the chamber wall might be as well regarded as a kind of TBC.

2.3.7 Radiation Cooling

Radiation cooling bases on the heat transfer from the outer rocket chamber surface to the ambient by thermal radiation. A schematic is given in Fig. 2.11. For an unimpeded radiation into a half-space, the dissipated heat flux can be described by the formula

$$\dot{q} = \epsilon \cdot \sigma \left(T_{w2}^4 - T_a^4\right) \tag{2.55}$$

where ϵ is the emissivity of the chamber wall, σ the Stefan-Boltzmann constant and T_a the ambient temperature.

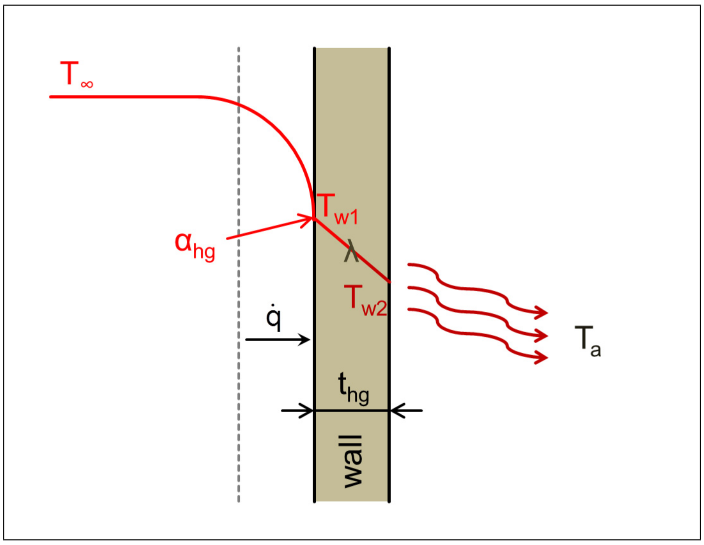

Fig. 2.11: Schematic of Radiation Cooled Wall

Due to obstruction of the radiation path and limits in the acceptable material temperatures the transmittable heat flux is limited. Therefore, radiation cooling is applied in nozzle extensions, upper stages and thrusters where combustion pressures thus heat fluxes are lower.

2.3.8 Regenerative Cooling

To maintain an acceptable wall temperature even in high performance rocket engines, regenerative cooling is deployed. Here, one fluid, typically the fuel, flows through cooling channels in the combustion chamber or nozzle wall absorbing the heat. In the case of a closed regenerative cooling the heated fuel is afterwards injected into the combustion chamber allowing practically a lossless cooling and for cryogenic or hardly vaporizable a preheating of the propellants which improves combustion stability and efficiency. For the design of a regenerative cooling several aspects like heat capacity of the available propellants, material compatibility as well as possible decomposition of the cooling fluid have to be taken into account.

The schematic of a regeneratively cooled wall is depicted in Fig. 2.12. Heat is transferred from the hot gas to the wall by convection. The heat flux increases, if the heat transfer coefficient α_{hg} increases (cf. Eq. 2.31) or the temperature difference of recovery temperature $T_{aw} = f\,(T_\infty)$ (see section 2.3.2 for definition) and wall temperature T_{w1} becomes higher. The heat conduction within the wall is determined by the wall thickness t_{hg} and the thermal conductivity λ of the chamber wall material. On the cooling channel side the heat is transferred to the coolant. The heat transfer to the coolant is dependent of the heat transfer coefficient α_{cf} and the coolant temperature T_{cc}.

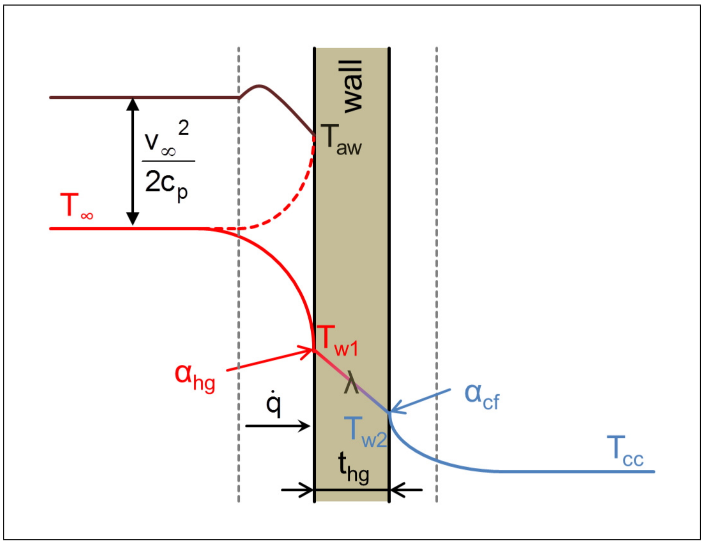

Fig. 2.12: Schematic of Regenerative Cooled Wall

For steady-state, heat transfer on the hot gas side, thermal conduction in the wall and convection on the cooling channel are in equilibrium. This leads for the one-dimensional case to a simple correlation for the heat flux $\dot{q}$.

$$\dot{q} = \alpha_{hg}\,(T_{aw} - T_{w1}) = \frac{\lambda}{t_{hg}}\,(T_{w1} - T_{w2}) = \alpha_{cf}\,(T_{w2} - T_{cc}) \tag{2.56}$$

$$\dot{q} = \frac{T_{aw} - T_{cc}}{\frac{1}{\alpha_{hg}} + \frac{t_{hg}}{\lambda} + \frac{1}{\alpha_{cf}}} \tag{2.57}$$

For the determination of the heat transfer coefficient α_{cf} on the cooling channel side different Nusselt correlations derived from models for pipe flows but extended by rocket specific corrections have been proposed. The correction comprise adaption for e.g. running-in, wall roughness, curvature, stratification and the non-symmetrical heating of the cooling channel. Similar to the hot gas side, the Nusselt correlations differ in the used reference temperature. In this connection, models using bulk temperature $T_{ref} = T_{cc}$ for reference tend to overpredict while models using a film temperature $T_{ref} = f\,(T_{cc}, T_{w2})$ often underpredict the heat transfer into the cooling channel.

In order to calculate the heat transfer from the chamber wall into the cooling channel one of many available formulations for the flow in pipes can be used. *Kraussold* [1, 41] gives the following correlation for the heat transfer to the cooling channel:

$$Nu_{cf} = \frac{\alpha_{cf} \cdot d_h}{\lambda} = 0.024 \cdot Re^{0.8} Pr^{0.37} \cdot k_x\, k_{cr} \tag{2.58}$$

$$\alpha_{cf} = 0.024\, \frac{c_p^{0.37} \cdot \lambda^{0.63}}{\eta^{0.43} \cdot d_h^{0.2}} \left[\frac{\dot{m}_{cf}}{\frac{\pi}{4} \cdot d_h^2}\right]^{0.8} \left(1 + \frac{d_h}{l}\right)\left(1 + 1.75\,\frac{d_h}{r_{cc}}\right) \tag{2.59}$$

Thereby, k_x is a correction factor for the start-up of the flow and k_{cr} is a correction for the curvature of the cooling channel. The transport properties are calculated at the bulk temperature T_{cc} of the coolant.

Sutton proposes a model by *McAdams* [9, 42], which is indeed quite comparable to Kraussold, but misses the correction factors:

$$\alpha_{cf} = 0.023\, \frac{c_p^{0.333} \cdot \lambda^{0.667}}{\eta^{0.467} \cdot d_h^{0.2}} \left[\frac{\dot{m}_{cf}}{\frac{\pi}{4} \cdot d_h^2}\right]^{0.8} \tag{2.60}$$

Similarly, the general correlation by *Gnielinski* [33] as presented in Eq. 2.36 may be used as well.

While aforementioned correlations are for general purposes, heat transfer characteristics and coking of hydrocarbon fuels has been investigated e.g. by NASA in detail [43–45]. *Liang et al.* [46] reviewed the literature and provide correlations for different hydrocarbon fuels as given in Tab. 2.8.

Fluid	Correlation	
Methane	$Nu = 0.023 \cdot Re^{0.8} \cdot Pr^{0.4}$	
Propane	$Nu = 0.005 \cdot Re^{0.95} \cdot Pr^{0.4}$	
Kerosene	$Nu = 0.005 \cdot Re^{0.95} \cdot Pr^{0.4}$	at $Re < 2 \cdot 10^4$
	$Nu = 0.023 \cdot Re^{0.8} \cdot Pr^{0.4}$	at $Re > 2 \cdot 10^4$

Tab. 2.8: Forced Convection Heat Transfer Correlations for Hydrocarbons

In the one-dimensional correlation the existence of three-dimensional structures and the “fins” has been neglected so far. A schematic of a cooling channel cross section is presented in Fig. 2.13. Here, h is the height and w the width of the cooling channel as well as t_f the web thickness. For wall materials with high thermal conductivity the heat transfer to

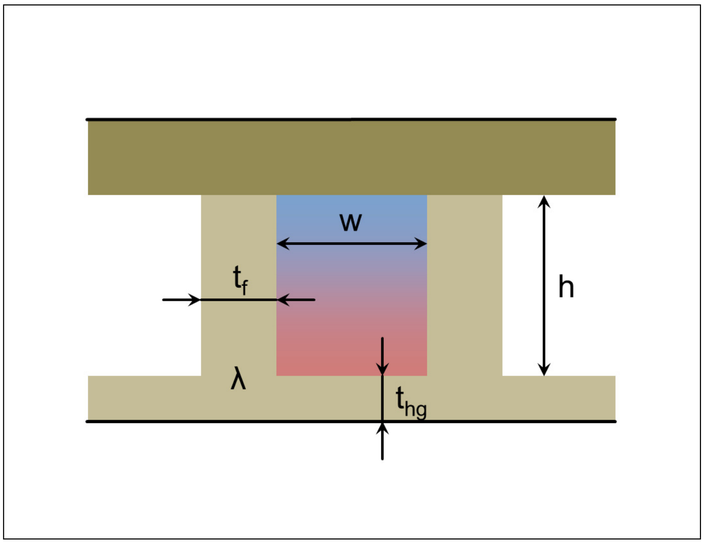

Fig. 2.13: Cross Section of Regenerative Cooled Wall

the coolant can significantly be increased by cooling channels with a high aspect ratio (cf. e.g. [47–49]).

The fin efficiency η_f correlates the transferred heat to a isothermal fin with thickness t_f. The corrected heat transfer coefficient $\alpha_{cf,f}$ results from the fin efficiency η_f and the heat transfer coefficient α_{cf} without fins.

$$\eta_f = \frac{tanh\left(\frac{h}{t_f}\cdot\sqrt{\frac{2\cdot\alpha_{cf}\cdot t_f}{\lambda}}\right)}{\sqrt{\frac{2\cdot\alpha_{cf}\cdot t_f}{\lambda}}} \tag{2.61}$$

$$\alpha_{cf,f} = \alpha_{cf}\cdot\frac{w+\eta_f\cdot 2h}{w+t_f} \tag{2.62}$$

2.3.9 Film and Transpiration Cooling

Film and transpiration cooling reduce the convective heat transfer by laying a low-energy fluid over the chamber wall. The low-energy fluid can be propellants burned at a mixture ratio considerably distinct from stoichiometric mixture ratio, pure fuel or turbine exhaust gases from e.g. a gas generator. According to this, the fluid can be a liquid, a fluid injected at trans-critical conditions with negligible enthalpy of evaporation (dense gas) or a gaseous fluid as well. If a liquid, the film fluid has first to evaporate forming a primary protected zone gaining of a high evaporation enthalpy of the coolant, before the gaseous film dissipates due to mixing and heat transfer progressing downstream.

A cooling film may be laid by special holes (Fig. 2.14(a)) or slots (Fig. 2.14(b)) as well as by the injection system, when the outer injector elements of a multi-element injector head operate at a lower mixture ratio or the characteristics of the injector element implicate the formation of a film as typical for e.g. swirl injectors. For transpiration cooling as shown in Fig. 2.15 the fluid is injected through a perforated or porous wall.

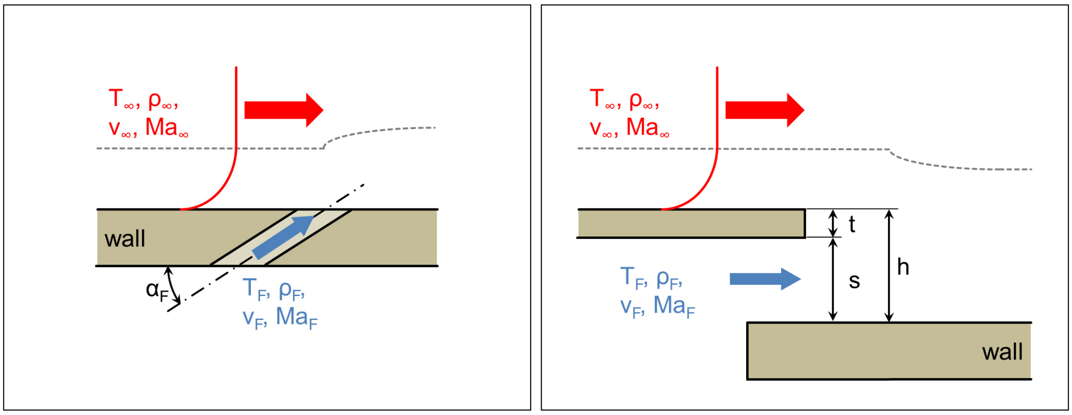

(a) hole injection (b) slot injection

Fig. 2.14: Schematic of Film Cooled Wall

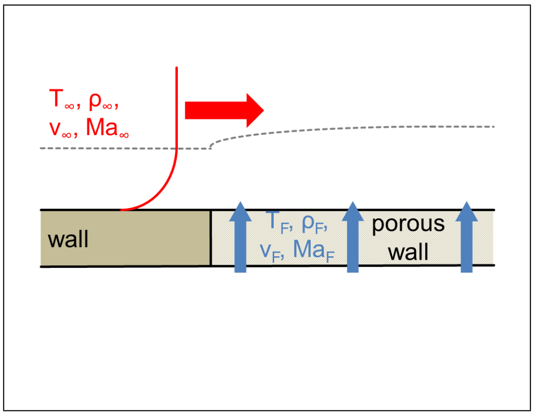

Fig. 2.15: Schematic of Transpiration Cooled Wall

Since the lower temperature of the boundary layer causes a decrease in the mean exhaust velocity and the coolant mass flow may not at all or only to some extent take part in the combustion process, film and transpiration cooling is lossy. A value to characterize the required coolant mass flow is the coolant mass flow rate μ, which correlates the fuel required for cooling to the total fuel injected. Important values to characterize the transpiration or film laying process itself are the blowing ratio F [52], which is the quotient of the coolant mass flux and the hot gas mass flux, and the momentum ratio I representing the quotient of the momentum fluxes of the coolant and the core stream.

$$\mu = \frac{\dot{m}_{Fu,F}}{\dot{m}_{Fu,F} + \dot{m}_{Fu,inj}} \tag{2.63}$$

$$F = \frac{\rho_{cool} \cdot v_{cool}}{\rho_\infty \cdot v_\infty} \tag{2.64}$$

$$I = \frac{\rho_{cool} \cdot v_{cool}^2}{\rho_\infty \cdot v_\infty^2} \tag{2.65}$$

$$\eta_{cool}(x) = \underbrace{\frac{T_{aw}(x) - T_\infty}{T_{cool} - T_\infty}}_{\text{subsonic}} = \underbrace{\frac{T_{aw}(x) - T_c}{T_{t,F} - T_c}}_{\text{supersonic}} \tag{2.66}$$

The definition of an adequate cooling effectiveness strongly depends on the state of the flow field i.e. subsonic or supersonic and the type of wall cooled. A common definition is the adiabatic film cooling effectiveness $\eta_{cool}(x)$ which compares the recovery temperature $T_{aw}(x)$ with the static film temperature (subsonic) or total film temperature (supersonic). The film cooling effectiveness is dependent of the geometry and the flow field and can be determined by experiments, semi-empirical correlations or numerical simulations. The resulting wall temperature T_w is calculated by

$$\dot{q} = \alpha_{hg} \left(T_{aw} - T_w \right) \tag{2.67}$$

where the cooling is taken into account by the recovery temperature $T_{aw} = T_{aw}(\eta_{cool})$ while the heat transfer coefficient α_{hg} is regarded unaffected. *Hartnett et. al.* [50], who investigated film cooling in wind tunnels, and others have shown that for most conditions of practical interest the difference between the local heat transfer coefficient with and without film cooling is very small and the “adiabatic wall temperature” T_{aw} derived from Eq. 2.66 for given film cooling effectiveness acts as the driving factor for heat transfer. *Parkinson and Ziebland* [52] recommend this approach also for film cooling in rocket engines.

$$\dot{q}_{cool} = \alpha_{hg,without\,Film} \cdot (T_{aw} - T_w) \tag{2.68}$$

For non-adiabatic walls the adiabatic definition of η_{cool} might not be viable to characterize cooling efficiency. In this case, cooling efficiency Θ, which correlates wall temperatures with and without film cooling, can be used [51].

$$\Theta(x) = \frac{T_{w,without\,Film}(x) - T_{w,with\,Film}(x)}{T_{w,without\,Film}(x) - T_F} \tag{2.69}$$

Film Cooling

As stated in Eq. 2.66, film cooling efficiency is commonly described as the ratio of the differences of coolant temperature and free-stream temperature as well as adiabatic wall temperature and free-stream temperature. The two common approaches to describe the film cooling effectiveness base either on the assumption that mixing takes places reducing efficiency due to the inflow of hot gas or that the film does not mix with the core stream but only heat is transferred to the film [52].
Hatch and Papell [52,53] assumed a non-mixing flow and that the heat would be conducted into the film at the same rate as into the wall in absence of a cooling film.

$$\ln \eta_{cool} = -\left(\frac{St \cdot x}{F \cdot s} - 0.04\right)\left(Re_{cool}\; Pr_{cool}\; \frac{v_\infty}{v_{cool}}\right)^{\frac{1}{8}} \tag{2.70}$$

Here, s is the slot height, x is an arbitrary point downstream the film injector and St is the Stanton number at the wall without film cooling.
Lefebvre [54, 55] gives a correlation for effectiveness basing on turbulent boundary layer model.

$$\eta_{cool} = 0.6\;\left(\frac{x}{F \cdot s}\right)^{-0.3}\;\left(Re_s\; F\; \frac{\mu_{cool}}{\mu_\infty}\right)^{0.15} \tag{2.71}$$

Thereby, F is the blowing ratio, s the slot height, x the run length, Re_s the Reynolds number based on slot conditions and μ_{cool} as well as μ_∞ is the dynamic viscosity of coolant and free stream, respectively.
Stollery and El-Ehwany [52, 56] expected a mixing process between the main stream and the cooling film. They assumed that the film would have similar velocity profiles and mixing characteristics as a ordinary boundary layer far enough downstream of the film injection.

$$\eta_{cool} = 4.09\;\left(\frac{Re_x}{Re_{cool}^{1.25}}\right)^{-0.8} \tag{2.72}$$

Since Eq. 2.72 does not satisfy $\eta_{cool} \to 1|_{x\to 0}$ *Parkinson and Ziebland* [52] give a correlation, which is at least asymptotic to Stollery and El-Ehwany for high values of x:

$$\eta_{cool} = \frac{Re_{cool}}{Re_{cool} + 0.244 \cdot Re_x^{0.8}} \tag{2.73}$$

Stechman [57, 58] developed a model applicable both for liquid and gaseous film cooling and validated his prediction to experimental results from engines using NTO/MMH and fluorine/MMH. In this approach, the heat transfer problem is broken into two parts: the heat transfer from the hot core gas to the film coolant, and the heat transfer from the film coolant to the wall. The heat transfer coefficient from hot core gas to film coolant is calculated using a modified Bartz equation while the heat transfer coefficient from the liquid film to the wall bases has been derived from a model for turbulent liquid flow on a flat plate. Since the liquid coolant flow is not assumed to be ideal but affected by an instability, an efficiency factor η_S, which is a function of the coolant Reynolds number, has

been introduced.
For the heat transfer from the main core gas and the coolant Stechman gives

$$\alpha_G = \frac{0.026 \cdot \mu_{cool,avg}}{d_{th}^{0.2}\; Pr_{cool,avg}} \left(\frac{\dot{m}_{cool}}{A_{th}}\right)^{0.8} \left(\frac{A_{th}}{A}\right)^{0.9} \left(\frac{h_{t,aw} - h_w}{T_{aw} - T_w}\right) \tag{2.74}$$

while using stability factor η_S the heat transfer coefficient between liquid film and engine wall is

$$\alpha_L = 0.0288\, \frac{c_{p,L}}{Pr_L^{0.667}\; \mu_L^{0.2}\; x^{0.2}} \left[\frac{\eta_S\, \dot{m}_L\, v_G\, \alpha_G\, Pr_G^{2/3}\, \rho_L}{\pi\, r_c\, c_{p,G}}\right]^{0.4} \tag{2.75}$$

The heat flux should be calculated using the average film temperature $T_{cool,avg}$ and the engine wall temperature T_w.
The *NASA SP-8124* [59] Annex A model assumes that turbulence effects between cooling film and core stream cause an entrainment and thus a decreasing cooling effectiveness. For a gaseous film coolant the entrainment mass flow is defined as

$$\frac{\dot{m}_e}{\dot{m}_{cool}} = \frac{\dot{m}_{all} - \dot{m}_{cool}}{\dot{m}_{cool}} \left[2 \cdot \frac{\Psi_r \cdot \bar{z}}{r_{c,i} - s_i} - \left(\frac{\Psi_r \cdot \bar{z}}{r_{c,i} - s_i}\right)^2\right] \tag{2.76}$$

Herein $\dot{m}_e$ is the entrainment mass flow, $\dot{m}_{cool}$ the coolant mass flow, s_i the film thickness at injection level and $r_{c,i}$ the chamber radius at film injection level. The variable $\bar{z}$ represents a trimmed coordinate taking into account curvature of the combustion chamber as well as effects of two-dimensional flows and turbulence caused by the injector. Finally, Ψ_r is an empiric correlation factor for entrainment within a plain film at constant velocity and mass flow.
The film cooling effectiveness can be described as a semi-empiric function of the entrainment factor $\frac{\dot{m}_e}{\dot{m}_{cool}}$:

$$\eta_{cool} = \eta \left(\frac{\dot{m}_e}{\dot{m}_{cool}}\right) \tag{2.77}$$

Assuming a non-reacting gaseous fluid, which is sufficient for high coolant mass flows and cooling film injection near the end of the combustion chamber such as the film cannot mix with the core stream before exiting the combustion chamber as well as for inert film media, the adiabatic wall temperature is defined as

$$T_{aw} = T_{t,c} - \frac{\eta_{cool} \cdot c_{p,cool}(T_{t,c} - T_{cool}) + (1 - Pr_w^{1/3})(H_{t,c} - H_{cool})}{\eta_{cool} \cdot c_{p,cool} + (1 - \eta_{cool}) \cdot c_{p,c}}. \tag{2.78}$$

Herein $T_{t,c}$ is the core stream total temperature, T_{cool} the coolant temperature, $c_{p,cool}$ respectively $c_{p,c}$ the specific heat of coolant and of the core stream, Pr is the Prandtl number and H_{cool} and $H_{t,c}$ denote coolant and total core stream enthalpy, respectively.
For a reactive gaseous film fluid the adiabatic wall temperature T_{aw} is given as a function of near-wall mixture ratio $\left(\frac{O}{F}\right)_w$ and the enthalpy of adiabatic wall H_{aw}

$$T_{aw} = T\left(\left(\frac{O}{F}\right)_w,\; H_{aw}\right) \tag{2.79}$$

where the enthalpy of adiabatic wall is

$$H_{aw} = H_{t,c} - \eta_{cool}\left(H_{t,c} - H_{cool}\right) - (1 - Pr_w^{1/3})(H_{t,c} - H_{cool}) \tag{2.80}$$

and the mixture ratio

$$\left(\frac{O}{F}\right)_w = \frac{1 + (O/F)_c}{1 + \eta_{cool} \cdot \left(\frac{1+(O/F)_c}{1+(O/F)_{cool}} - 1\right)} - 1. \tag{2.81}$$

For the modeling of liquid film coolants as described in *NASA SP-8124* [59] Annex B, a liquid film length is introduced:

$$L = \frac{1}{A}\, ln\left(1 + \frac{A \cdot \dot{m}_{Film}}{V}\right). \tag{2.82}$$

In this equation L is the liquid film length, A is the semi-empiric liquid entrainment parameter and V is the surface vaporization rate. Also the formulations for entrainment and adiabatic wall temperature are modified to take the liquid phase and the evaporation into account. More details on this can be found in Ref. [59].

Finally, *Grissom* [60] reviewed several models for gaseous and liquid films. For gaseous film he adopted the modeling of *Stollery and El-Ehwany* [56] as well as *Kutateladze* [61] for a flat plate in turbulent flow regime. Assuming that free stream mass flow and temperature are constant and radiation is negligible, a quite simple model for the adiabatic wall temperature and film efficiency with respect to the recovery temperature T_r is given:

$$T_{aw} = T_r - \eta\left(T_r - T_{cool}\right) \tag{2.83}$$

$$T_r = T_\infty - r \cdot (T_\infty - T_c) \tag{2.84}$$

where r is the recovery factor, T_∞ the static temperature of the free flow, T_c the total temperature and T_{cool} the inlet temperature of the coolant. The film cooling efficiency η is given then by

$$\eta = \left[1 + K_M\left(\frac{c_{p,\infty}}{c_{p,cool}}\right)\left(0.325 \cdot (K_t \cdot X + X_0)^{0.8} - 1\right)\right]^{-1}. \tag{2.85}$$

Hereby, $X = K \cdot x$ is the non-dimensional form of the distance x downstream of the injection point and X_0 the non-dimensional form of the fictitious edge of the film cooled plate.

$$K = \frac{\rho_\infty \cdot v_\infty \cdot \mu_\infty{}^{0.25}}{(\frac{\dot{m}_{cool}}{d_h})^{1.25}} \tag{2.86}$$

Despite the common approach to express the constant K (cf. Eq. 2.86) in terms of a coolant Reynolds number, Grissom explicit states that this should be avoided since the film injector geometry will be unimportant as long as the velocity of the injected coolant remains low. In Eq. 2.85 the factor K_t accounts for free stream turbulence and has been derived from experimental work of *Marek and Tacina* [62] as well as *Carlson and Talmor* [63]. Basing on findings of *Goldstein et al.* [64] the correction factor K_M allows for foreign gas injection introducing a power function dependence of the coolant to hot gas molecular weight ratio.

Transpiration Cooling

For a prediction of resulting solid and coolant temperatures, different situations of heat transfer between the components of the combustion chamber have to be calculated. First of all, convective heat transfer from the hot gas flow to the chamber walls is to be considered. Furthermore, heat from the chamber is absorbed and carried away by the coolant fluid. Additionally, radiative heat transfer from the chamber's outer wall to the environment may be considered. In particular, for transpiration cooling the heat exchange between hot gas stream and chamber wall is hampered by the existence of a thin coolant film, covering the wall's surface. Moreover, additional heat transfer takes place between the porous wall and the coolant flowing through it [52, 65].

Injection of a gas into the boundary layer of a gas stream leads to a thickening of the lower velocity part of the boundary layer next to the wall. If sufficient mass is injected, the boundary layer will separate, which should be avoided to prevent local hot spots at the wall when the boundary layer reattaches or vortices transport hot gases to the wall. Therefore, the most important parameter in transpiration cooling theory is the blowing rate F (cf. Eq. 2.64). One simple approach is to assume that the Stanton number St varies linearly between its value at zero blowing rate (St_0) and a minimum value when the boundary layer separates.

Hacker [52, 66] found that for $F \cdot Re_z^{1/5} \approx 0.08$, where Re_z is the local Reynolds number, the skin friction coefficient becomes zero and the boundary layer separates. Introducing $St_0 \approx 0.03 \cdot Re_z^{1/5}$ for the zero blowing rate Stanton number, he obtained the following equation:

$$St = St_0 - 0.375 \cdot F \tag{2.87}$$

Kutateladze and Leontev [52, 67] assumed that the injection into the laminar sub-layer would promote turbulence in the boundary layer leading to the limiting case where the laminar sub-layer may be disregarded. For a uniform, isothermal boundary layer they found for the ratio Ψ of the actual skin friction factor to the unaffected one that

$$\Psi \equiv \frac{C_f}{C_{f,0}} = \left(1 - \frac{b}{b_{cr}}\right) \tag{2.88}$$

where the factor $b = \frac{2F}{C_{f,0}}$, b_{cr} is the critical "blow-off" value of b and $C_{f,0}$ is the skin friction coefficient for an impermeable flat plate with same momentum thickness Reynolds number. In the simplest case b_{cr} is four. The derivation by Kutateladze and Leontev is somewhat intricate, therefore *Parkinson and Ziebland* [52] proposed the following approximation which shall agree with the exact solution within 2 %:

$$\left(\frac{C_f}{C_{f,0}}\right)_{Re_x} = (1 - 0.025b)^2 \;\; (1 + 0.25b)^{-0.5} \tag{2.89}$$

For a non-isothermal boundary layer, Kutateladze and Leontev also introduced a modified version of Eq. 2.88 [67].

Kays, Crawford and Weigand [68] introduce a heat-transfer blowing parameter B_h:

$$B_h = \frac{v_{cool}/v_\infty}{St} = \frac{\dot{m}_{cool}/(\rho u_\infty)}{St}. \tag{2.90}$$

For the same gas and constant B_h they obtain an implicit correlation for St/St_0 at the enthalpy thickness of thermal boundary layer Δ_2 which is in agreement with a wide variety of experimental data including blowing and suction as well as accelerating and decelerating free-streams:

$$\left[\frac{St}{St_0}\right]_{\Delta_2} = \left[\frac{\ln\left(1+B_h\right)}{B_h}\right]^{1.25}\left(1+B_h\right)^{0.25} \tag{2.91}$$

Furthermore, they propose different solutions to modify the equations for heat transfer in turbulent boundary layer such way that transpiration can be taken into account. Details can be found in Ref. [68].

3. Test Facility and Hardware Setup

The tests investigated in this work were conducted at the high pressure combustion test facility of TUM-LFA, which features a modular water-cooled single element rocket combustion chamber operated with kerosene Jet-A1 and gaseous oxygen GOX. In Tab. 3.1 an overview over the nominal operating point and the maximum operating conditions is given.

Chamber Pressure	$p_{c,nom}$	[MPa]	8.0
	$p_{c,max}$	[MPa]	10.0
Maximum Oxidizer Mass Flow	$\dot{m}_{Ox}$	[kg/s]	1.00
Maximum Fuel Mass Flow (total)	$\dot{m}_{Fuel}$	[kg/s]	0.60
Mixture Ratio	O/F	[-]	1.4 - 3.5
Combustion Temperature	T_c	[K]	2 300 - 3 800

Tab. 3.1: Typical Operating Conditions of TUM-LFA Test Facility

A detailed description of the test facility and the combustion chamber design was already given by *Kirchberger et al.* [6, 22, 69]. The characteristics of the secondary systems which are relevant for cooling investigations have been presented in Ref. [70]. For convenience, an overview of the test facility, the test hardware and the measurement techniques including data handling will be given here.

3.1 Test Facility Overview

In this section the most important systems of the test facility and their functionality are described. It shall provide a general idea of the required components, possibilities but also limits of the experimental setup.

3.1.1 Setup and Functional Schematic of Test Facility

A detailed schematic of the high pressure combustion test facility of the Institute for Flight Propulsion is presented in Fig. 3.1. Apart from the feed systems for oxygen and kerosene, which are described in more detail below, the test facility provides nitrogen systems for the control of dome-loaded pressure regulators as well as for purging feed lines prior to and after test (shown in green in the upper and upper left section of Fig. 3.1). The nitrogen is stored in flask bundles, containing 0.6 m^3 of gaseous nitrogen each at ambient temperature and a pressure of up to 30 MPa. The pressure feeding the dome loaded pressure regulators namely DDMK for kerosene, DDMO for oxygen and DDML for the water pressure supply air can be set individually by the spring loaded pressure regulators DMN2, DMN3 and DMN4. The same applies to the pressure regulator DMN1 which is used to set the pressure in the purge feed lines. The solenoid valves MVN1, and MVN2 are used to start and stop the flow of nitrogen purge. The check valves RüVN1 and RüVN2 in the purge lines prevent hot combustion products from damaging the armatures upstream. Pressure and temperature measurements (mainly TO41, PO41 and PO51 for oxygen, TK2, PK3 and PK5 for kerosene) are used to calculate the state of the propellant as well as in transient operation the mass flow rates.

The coolant water supply system (highlighted blue in Fig. 3.1) comprises a 0.5 m^3 storage tank, which can be pressurized up to 20 MPa. Pressurization is realized with compressed air (purple, on top part), consisting of a discrete system of two tanks of a volume of 2.1 m^3 each and an air compressor. The pressure in the water tank is controlled by the dome loaded pressure regulator DDML. A hydraulic actuated ball valve AVW is opened to lead the entire mass flow to the cooling water manifold (black lines), where it can be separated into two branches for the combustion chamber and the nozzle, respectively. Prior to division of the mass flows, a measurement of the entire mass flow rate is conducted in metering orifice DPWG. After having left the cooling water outlet manifolds of chamber and nozzle, temperature (TWK, TWD) and pressure (PWK, PWD) of the water are measured and used as input parameters for mass flow rate measurement by metering orifices DPWK and DPWD installed upstream of the exit to the ambient. Pressure level and mass flow in the cooling system are set by orifices BWK and BWD installed at the exit of the dump water cooling system.

3.1.2 Oxidizer Feed System

The gaseous oxygen is stored at 30 MPa. Up to four flask bundles with a volume of 0.6 m^3 each can be connected to the feed line system. The feed line pressure in front of the flow control valve RVO is set by a dome loaded pressure regulator DDMO. A Coriolis mass flow meter is installed after the pressure regulator. The temperature and pressure of the oxygen are measured before the pressure regulator (PO2, TO2) as well as before (PO41, TO41) and after (PO51, TO51) the flow control valve, which is operated at sonic conditions. A dynamic pressure sensor PODYN is placed downstream the flow control valve near the injector head.

3.1.3 Fuel Feed System

The kerosene is stored in a tank and pumped to a bladder feed tank pressurized with nitrogen. Upon test start, the fuel is directed to a dome loaded pressure regulator DDMK which ensures a constant pressure level in the feed line during test. After having passed a Coriolis mass flow meter, the fluid passes a flow control valve RVK, which sets the mass flow required for the operation of the chamber. A solenoid valve MVK3 direct in front of the fuel manifold is used to start or shut down the fuel flow to the injector. In an emergency shutdown or to depressurize the system, a bypass valve MVK4 is opened and the fuel is dumped back into the storage tank.

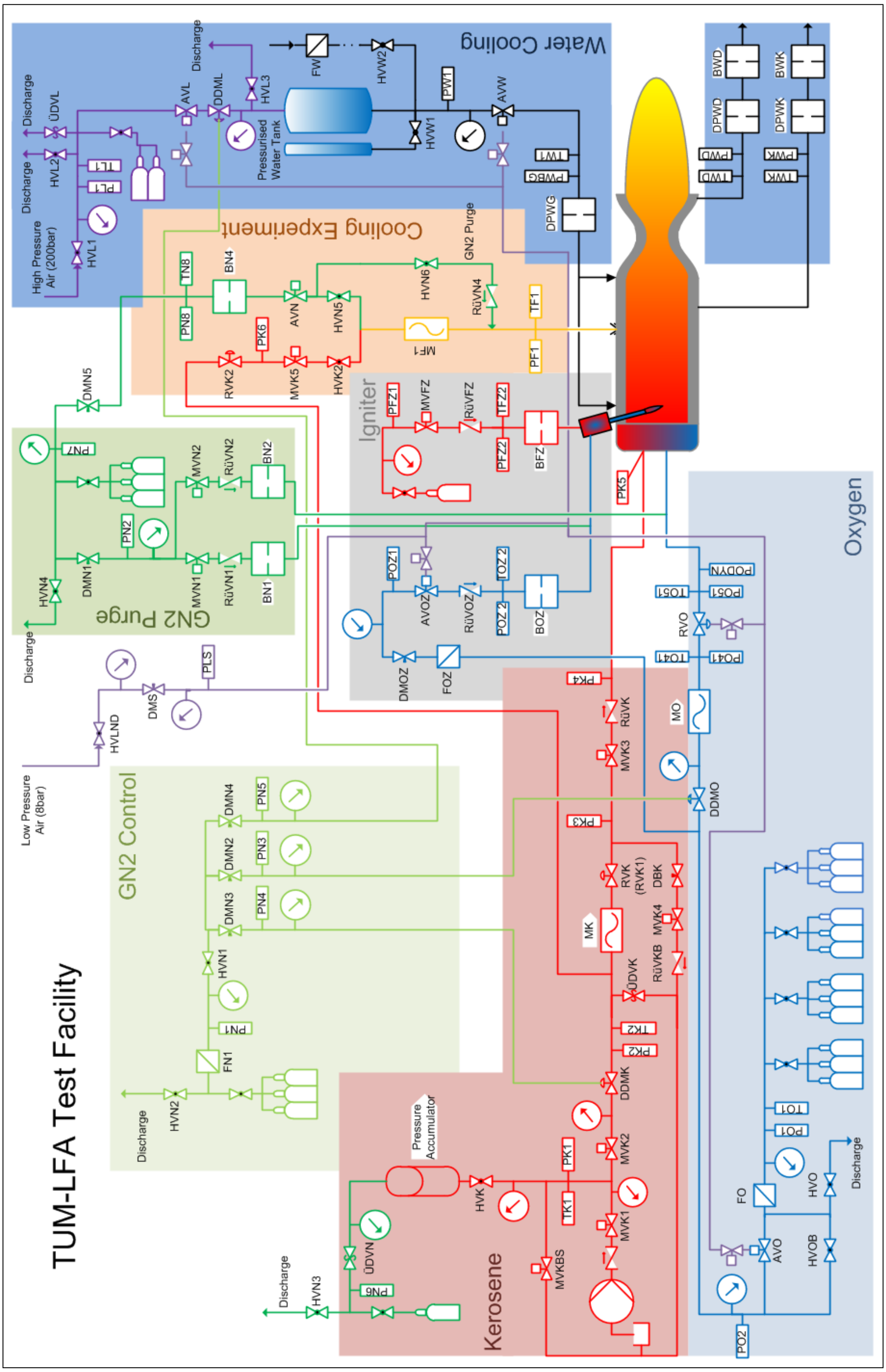

Fig. 3.1: Flow Schematic of Test Facility Feed Systems

3.1.4 Additional Cooling Feed Systems

Experiments on film and transpiration cooled devices as well as convectively cooled CMCs are conducted with gaseous nitrogen and liquid kerosene. Nitrogen used for these tests is stored in the batch of twelve 30 MPa pressure vessels also used for GN2 purge, summing up to a total storage volume of 0.6 m^3. The GN2 system pressure is set by a spring loaded pressure regulator DMN5 (see Fig. 3.1). A solenoid valve releases the GN2 flow to a calibrated sonic orifice BN4. The nitrogen mass flow is set by the primary pressure PN8 and the cross sectional area of orifice.

The kerosene cooling system is an extension of the existing kerosene feed system. The kerosene is branched off the main feed line after the dome loaded pressure regulator DDMK. Thus, the feed lines of the injector kerosene manifold and of the cooling manifold are operated at the same system pressure. The kerosene mass flow is measured in a Coriolis mass flow meter (MF1) and set by the flow control valve RVK2. The solenoid valve MVK5 gives the kerosene way to the cooling inlet manifold of the test sample.

Pressure and temperature of the cooling fluids used for film and transpiration cooling or convectively cooled CMC are recorded before entering the experiment (PF1, TF1) as well as on certain positions within the test sample. For convectively cooled CMCs an outlet pipe with additional pressure and temperature measurements (TF3, PF3) and also an additional mass flow meter (MF2) for kerosene or a calibrated orifice have been used to determinate transpiration mass flow rate or potential leakage. For this purpose, a heat exchanger has been deployed in order to keep up acceptable operating conditions for the Coriolis mass flow meter (for the type used the maximum fluid temperature is 125°C) and to maintain controllable conditions for the orifice BN5 as well as pressure control valve DBK which have been used to set the operating pressure in the dump line.

3.2 Test Hardware Components

This section presents the test hardware. Technical drawings and specifications are given here if reasonable only. For overall technical information of the hardware refer to the annex and the given references.

3.2.1 Combustion Chamber

Within project ATLLAS the subscale rocket engine facility of TUM was chosen as test rig for investigations on advanced cooling techniques as well as for tests of newly developed materials in high pressure and high temperature environments. In the past, tests were conducted using a small caloric single-element subscale rocket combustion chamber with an inner diameter of 20 mm (see Fig. 3.2). Gaseous oxygen and kerosene were used as propellants reaching chamber pressures up to 8.0 MPa typically. The heat transfer has been determined by the heat-up of the coolant within each of the three water-cooled chamber segments and the nozzle segment. Different injector elements were deployed and characterized in detail by *Soller et al.* [71–73] and *Wagner et al.* [74–76].

Due to restrictions in the manufacturing of the advanced ceramic matrix composites samples, a combustion chamber with larger inner diameter had to be designed. Therefore, a

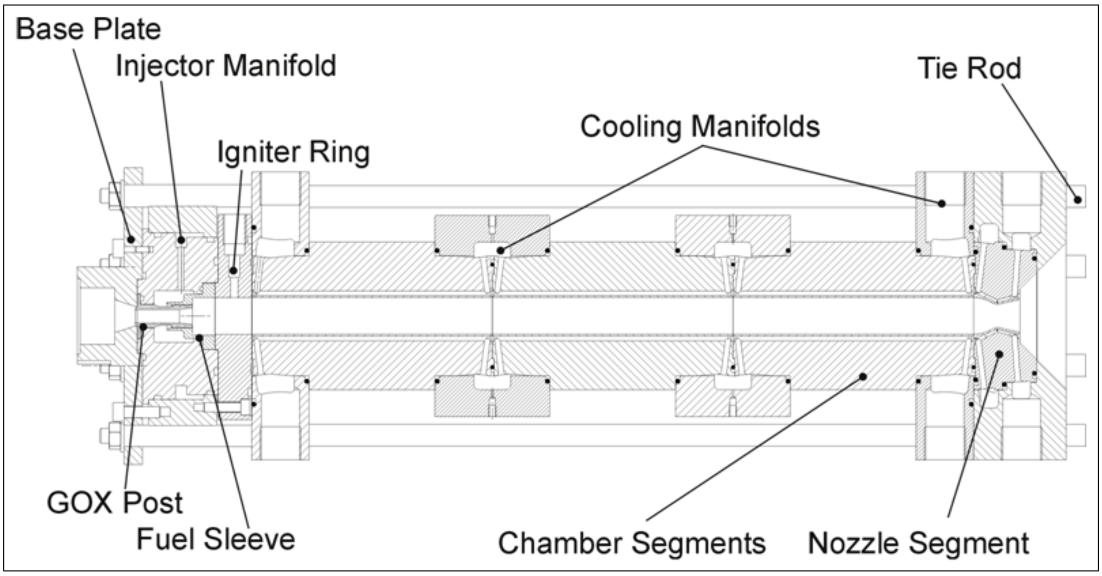

Fig. 3.2: Sketch of 20 mm Combustion Chamber (20 mm inner diameter, $\varepsilon_c = 2.5$)

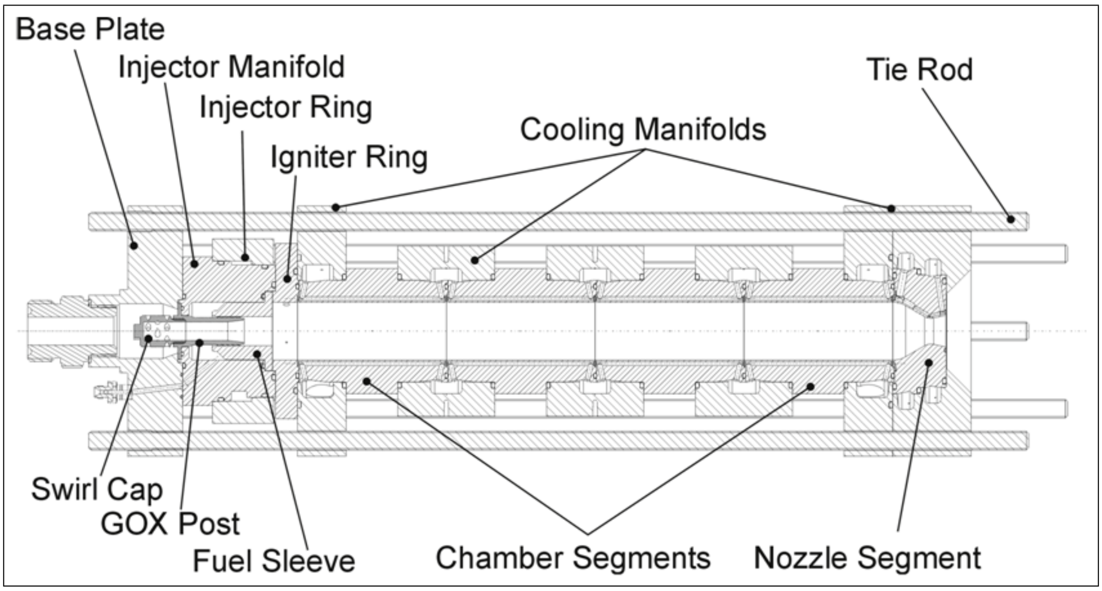

Fig. 3.3: Sketch of 37 mm Combustion Chamber (reference design, 37 mm inner diameter, $\varepsilon_c = 5.0$)

Characteristic	Symbol	Unit	Value
Chamber Diameter	d_c	[mm]	20.00
Throat Diameter	d_t	[mm]	12.65
Contraction Ratio	ε_c	[-]	2.5
Expansion Ratio	ε	[-]	1.8
Segment Length	$l_{segment}$	[mm]	130
Cylindrical Chamber Length	l_{cyl}	[mm]	404
Characteristic Length	$L*$	[m]	1.03

Tab. 3.2: Main Features of the 20 mm Combustion Chamber

Characteristic	Symbol	Unit	Value
Chamber Diameter	d_c	[mm]	37.00
Throat Diameter	d_t	[mm]	16.53
Contraction Ratio	ε_c	[-]	5.0
Expansion Ratio	ε	[-]	1.5
Segment Length	$l_{segment}$	[mm]	95
Cylindrical Chamber Length	l_{cyl}	[mm]	206 - 394
Characteristic Length	$L*$	[m]	1.10 - 2.06

Tab. 3.3: Main Features of the 37 mm Combustion Chamber

scaled water-cooled rocket combustion chamber with an inner diameter of 37 mm as well as an adapted injector and base plate was designed and manufactured. A general sketch is given in Fig. 3.3. The design and commissioning of the new combustion chamber setup has been published by *Kirchberger et al.* [69].

The chamber and nozzle segments were designed such that a transfer of existing experimental data from the small subscale chamber is viable with respect to either overall axial length or characteristic chamber length, depending on setup. The water cooling system can be operated as a serial coflow-cooling of all segments or with two independent cooling routes for the chamber and the nozzle. The main geometric parameters are depicted in Tab. 3.3.

In typical setups, film cooling experiments or CMC materials have been mounted at an axial length of 204 mm, i.e. after the first two water cooled segments. At this position, combustion is assumed to be completed and the cooling effectiveness can be investigated separately from atomization, mixing, combustion and chemical-driven acceleration of the injector gases.

3.2.2 Injector

The baseline setup comprises a single double-swirl injection element (see Fig. 3.4), which has been designed by Astrium Propulsion and Equipment, Ottobrunn. Based on the gas-jet injector type (compare to [77–79] for detail) which is one of the most commonly used design configurations in hydrocarbon/oxygen engines, it has been derived by means of scaling from the jet-swirl injector with internal mixing originally deployed in the 20 mm combustion chamber (Fig. 3.5, see Ref. [71–74]).

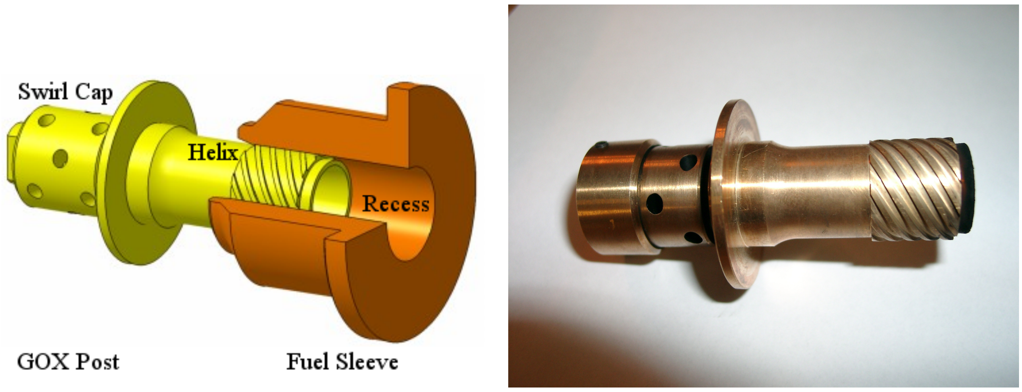

(a) Drawing (b) Photo (third row oxygen bores covered)

Fig. 3.4: Baseline Injector Element for 37 mm CC

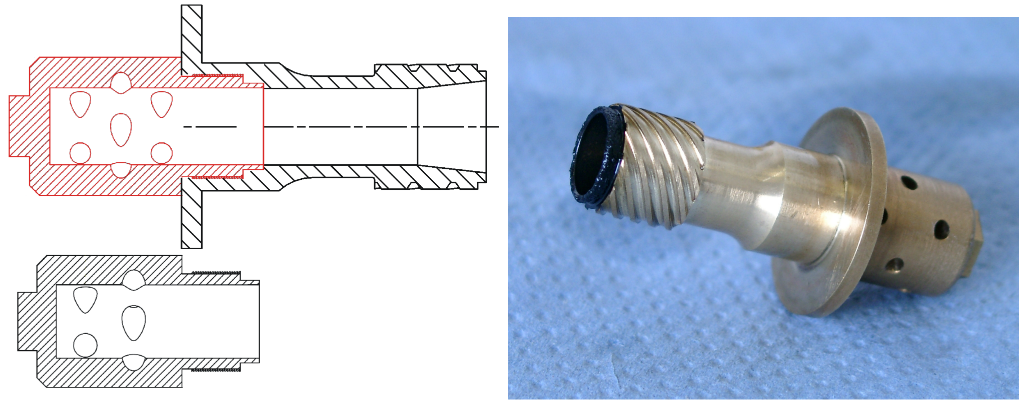

(a) Drawing (b) Photo

Fig. 3.5: Swirl Injector Element for 20 mm CC

The injector elements comprise a GOX post (yellow in Fig 3.4(a)), to which the oxygen is fed with a certain angular momentum through tangential orifices (Swirl Cap). The GOX Swirl Caps used are characterized by a large number of tangentially arranged inlet holes minimizing the pressure drop over the inlet orifices. For the 20 mm chamber configuration amongst other two elements sharing the same hydraulic flow area but differing in total number of inlet orifices of the swirl cap have been tested (twelve bores vs. eight bigger bores, see Fig. 3.5(a)). These two subconfigurations will be presented alongside. The 37 mm combustion chamber has been originally equipped with a swirl cap featuring twelve holes arranged in three rows. To improve the stability margin as well as the performance the third row has been covered during run-in tests (see Fig. 3.4(b)). Kerosene is injected via inclined slots (Helix) between Fuel Sleeve (orange) and GOX Post surrounding the central gas-jet. These inclined flow paths create a swirl on the injected kerosene, which forms a swirling liquid sheet in the recess area providing sufficient cooling. The recess area is used to enhance the mixing of the propellants and is designed such that the onset of the reaction is inside it. The optimum recess length depends on the propellant combination and the injection conditions in terms of temperature and pressure, thus the time lag of the dedicated propellant combination. The temperature increase due to pre-combustion in the recess area is estimated using the additional pressure increase at this section, comparing flow check and hot run data. The thermal throttling of the injector has been shown to be influenced by the operating parameters chamber pressure p_c and mixture ratio O/F [17]. The applied gas-swirl injectors resemble the type of open injectors where no flow path restriction exists towards the outlet. The increased circumferential velocity of the gas flow inside the element leads to higher turbulence with increased contact time and shear forces between kerosene and GOX, thus improving the mixing process in comparison to a simple gas-jet injector. Furthermore, the double-swirl injection element typically leads to an improved decoupling between the oxidizer feed system and the chamber due to the higher impedance.

3.2.3 Film Applicator

The film applicator used for the film cooling experiments is shown in Fig. 3.6. The setup consists of three parts, an outer ring (base plate) comprising the manifold and feeding system, a ring in the middle (spacer ring) which defines the film application slot height and a counterpart comprising the film lip and space for sealing. Since the spacer ring is changeable quite easily, the minimum cross section and thus the pressure drop through the film applicator can be varied by a simple variation of the middle ring (the dark green part in Fig. 3.6). Although the design of the film applicator allows different configurations, in the experiments presented here the film was always injected after two of four water cooled cylindrical chamber segments in order to decouple the processes governing the propellant injection and the film laying on one hand and on the other hand to have a sufficient measuring length available.

3.2.4 Transpiration Cooled CMC Test Specimen

For the test campaign conducted with transpiration cooled CMCs a test segment with a length of 95 mm was designed replacing the third segment of the reference design. A

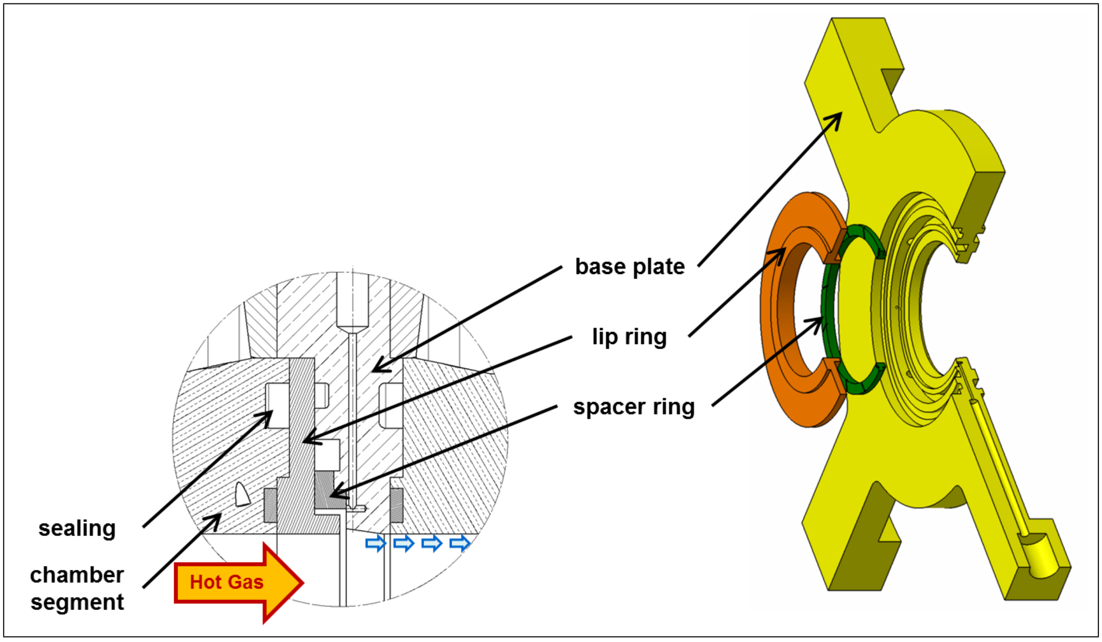

Fig. 3.6: Film Applicator Details (Sketch and 3D Cut-Away)

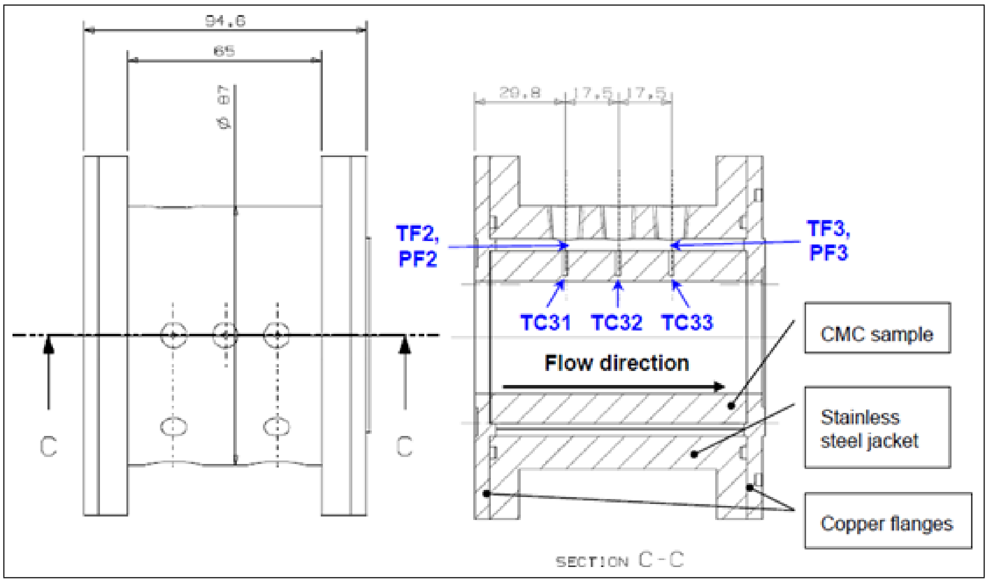

Fig. 3.7: Sketch of Transpiration-Cooled CMC Specimen and Sensors (Second Test Campaign, Courtesy of German Aerospace Center (DLR) – Institute of Structures and Design)

technical drawing is given in Fig. 3.7. The segment consists of two copper flanges, which provide the necessary interfaces to the water-cooled combustion chamber segments, a gas-tight jacket made of stainless steel and the CMC sample (tube shaped with 10 mm wall thickness) itself. Sealing between copper flanges and stainless steel jacket is achieved by Viton O-rings; between the CMC sample and the copper flanges graphite seals were placed. Apart from several bores for coolant inlet, outlet and venting, the test segment comprised three thermocouples, which have been inserted into the CMC wall with a distance of −2 mm to the hot wall.

3.2.5 Convectively-Cooled CMC Test Specimen

For ATLLAS convectively-cooled CMC chamber segments in PTAH-SOCAR technology (PSR), manufactured from $CARBOTEX^{SI}$ material, have been successfully tested at the TUM-LFA test facility [7, 80]. The PSR segment, which replaced the third and fourth chamber segment of the reference setup, has been mounted in a metallic jacket to prevent coolant leakage to the ambient as well as to carry the axial clamping force of the combustion chamber setup (see Fig. 3.8). Due to the O-ring seals used, the steady-state outlet temperature of the coolant was limited to approximately 550 K, limiting the operating domain of the test setup.

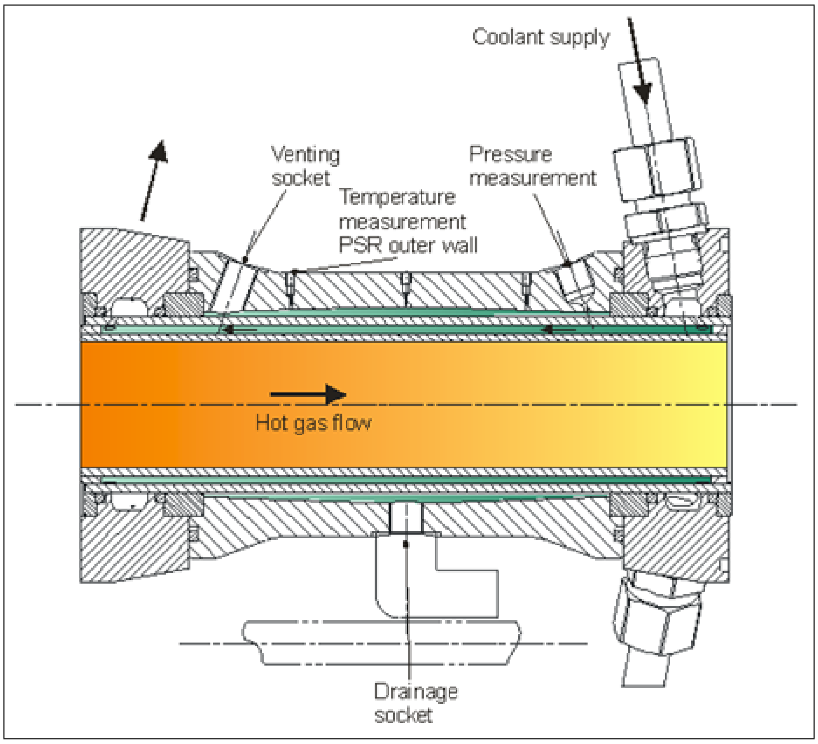

Fig. 3.8: Convectively-Cooled CMC Specimen in Metallic Jacket (Courtesy of Astrium Space Transportation)

The coolant is fed to the CMC/PSR module through two inlet pipes into an annular manifold, which is located in the jacket. The fluid enters the CMC coolant duct through 18 circumferential orifices and passes the chamber segment in counter-flow with the hot gas in the chamber. A certain amount of fluid transpires through the CMC chamber wall and serves as coolant. The coolant flow rate to the combustion chamber is amongst others influenced by the pressure drop between coolant duct and combustion chamber and the temperature-dependent permeability of the CMC material. For the samples tested, the transpiration mass flow rate has been very low.

3.3 Test Configurations and Data Acquisition

In this section the different configurations investigated in ATLLAS are presented. Additionally, an overview of the measurements applied is given.

3.3.1 Reference Setup and Common Measurements

The reference tests have been conducted with a configuration comprising of four water-cooled combustion chamber segments and a water-cooled nozzle. A schematic of the setup and the available measurements is given in Fig. 3.9. The measurements include amongst other the propellant mass flow rates (MK or MKV and MO), the combustion chamber pressure at different axial positions (PC0 ... PC4), thermocouples flush mounted with the combustion chamber wall (prefix THW, some tests only) as well as the coolant pressure (PWK1 ... PWK5, PWD1 ... PWD2) and temperature (prefix TWK and TWD) of the water cooling system. The water may pass through the combustion chamber and nozzle in separate cycles (water mass flows MWK and MWD) or in a single cycle (mass flow MWG). The water mass flow, coolant pressure and temperature are used to evaluate the heat pick-up thus heat flux to the chamber wall. Using the propellant mass flow rates and inflow conditions as well as the combustion chamber pressure the combustion efficiency is assessed.

An overview over the general and reference test specific DAQ channels recorded, sensor accuracy as well as evaluated data common for all configurations is given in Tab. A.1 throughout Tab. A.3 within the annex.

3.3.2 Setup for Film Cooling Experiments

The setup and sensor locations for steady-state film cooling tests are presented in Fig. 3.10. The film applicator has been mounted between segment 2 and segment 3 at a chamber position where the combustion process is assumed to be completed. The mass flow MF1 of the film coolant, kerosene or nitrogen, is determined in the feed line and temperature and pressure are measured in the feed line (TF1, PF1), in the coolant manifold (TF2, PF2) and immediately before entering the combustion chamber (TF3, PF3). To assess the cooling efficiency especially the thermocouples flush mounted in the hot gas wall of the third and fourth segment (THW3xy, THW4xy) and the water heat pick-up in the third and fourth segment have been used (cf. 3.4.3 and 3.4.5).

An overview over all film cooling specific DAQ channels and evaluated data is given in Tab. A.4 alongside associated accuracy of selected sensors in Tab. A.5.

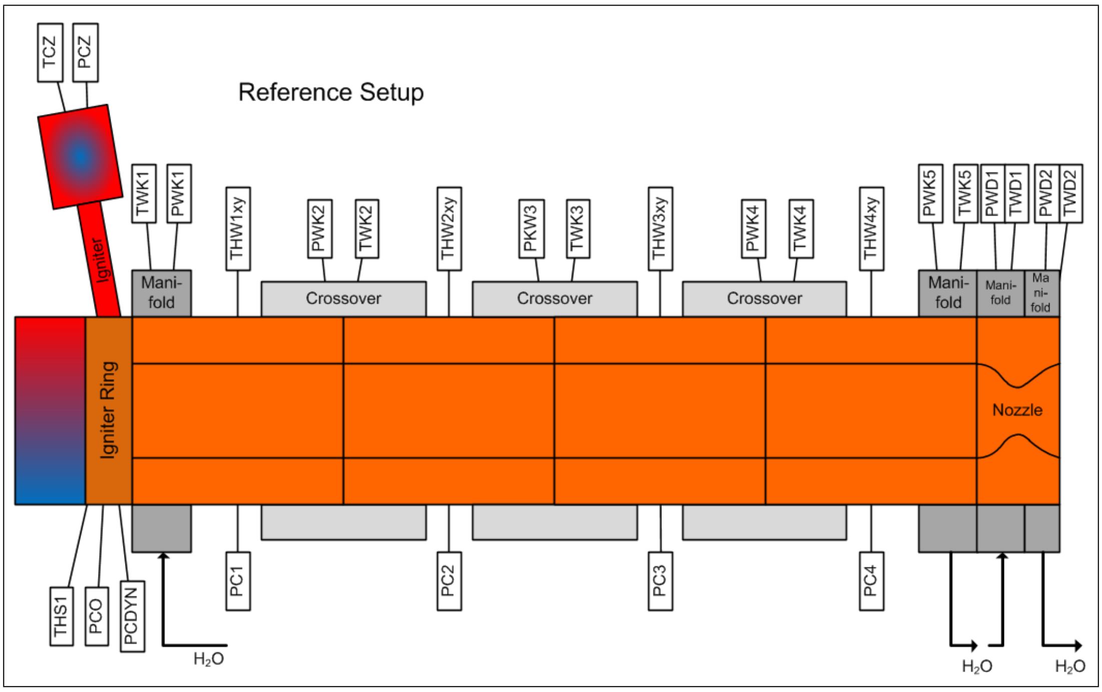

Fig. 3.9: Sensor Locations in Reference Setup

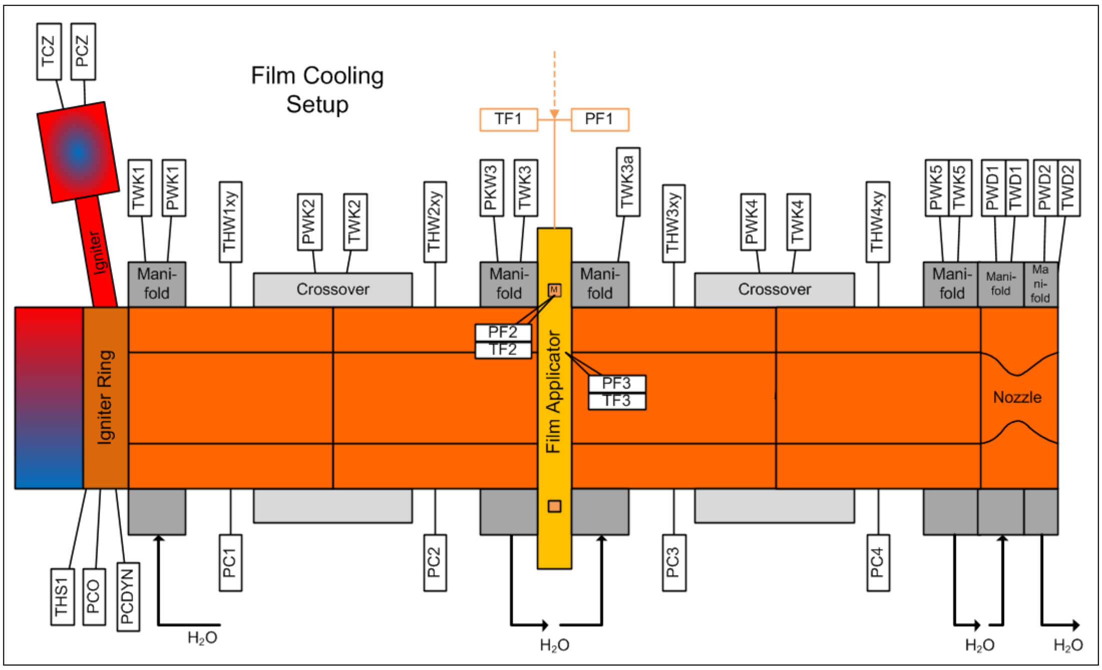

Fig. 3.10: Sensor Locations in Film Cooling Setup

3.3.3 Configuration with Transpiration Cooled CMC

The setup and available sensors for transpiration-cooled CMC test campaign are depicted Fig. 3.11. The CMC test sample has been installed instead of the third water cooled combustion chamber segment. Test specific sensors include the temperatures and pressures in the coolant manifold upstream (TF2, PF2) and downstream (TF3, PF3). As mentioned before, three thermocouples TC31...TC33 have been glued into the CMC part with a distance of 2 mm to the hot wall but were suffering from mounting tolerances and bad thermal contact. The water cooled segment downstream of the CMC segment has been used as an indicator for the cooling effect of the film generated by the transpiration cooling. An overview of test specific DAQ channels as well as is the accuracy of selected sensors used are given in Tab. A.6 and Tab. A.7 of the annex.

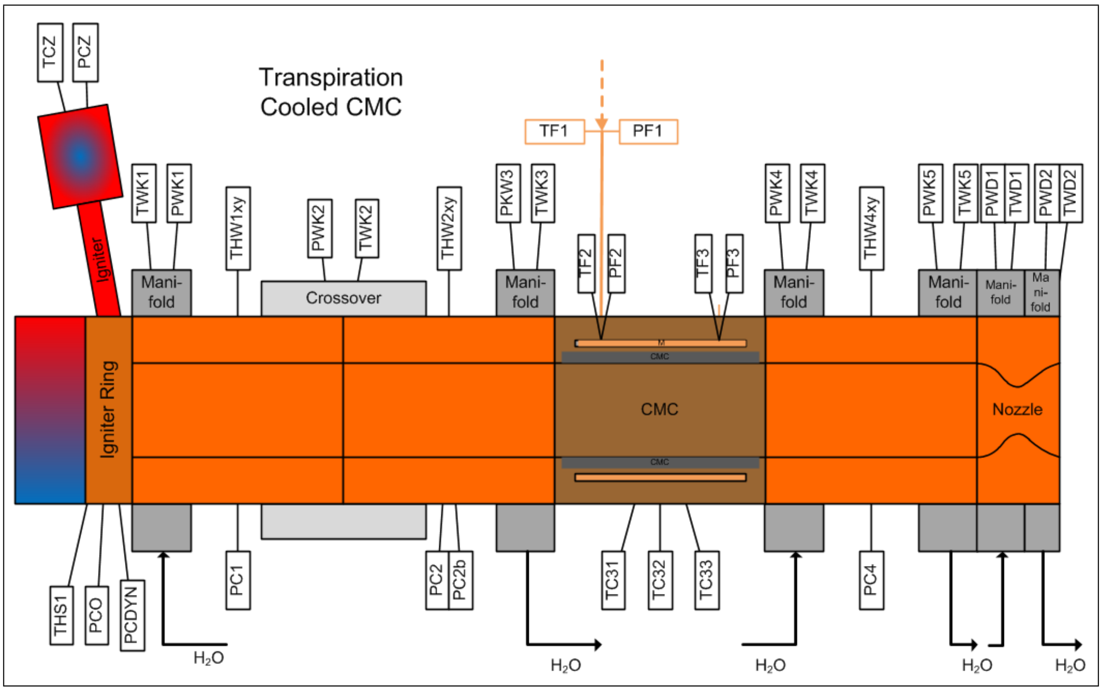

Fig. 3.11: Sensor Locations in Setup with Transpiration Cooled CMC

3.3.4 Configuration with Convectively Cooled CMC

In Fig. 3.12 the setup and available sensors for convectively-cooled CMC are shown. The PSR replaces the third and fourth water cooled segments of the reference combustion chamber setup and the cooling of the segment is counter-flow to the hot chamber gases. The coolant temperatures and pressures are measured in the feed line (TF1, PF1), in the dump line (TF3, PF3) as well as in the inlet (TF2a, PF2a) and outlet manifold (TF2c, PF2c). Additional sensors (PF2b, TPW1...TPW3) have been used to monitor the function and integrity of the test assembly. Since the coolant mass flow has been measured in front (MF1) and after the CMC segment (MF2), any transpiration mass flow or leakage could be detected.

For convenience, an overview of all test specific DAQ channels and the accuracy of selected sensors is given in the annex in Tab. A.8 and Tab. A.9.

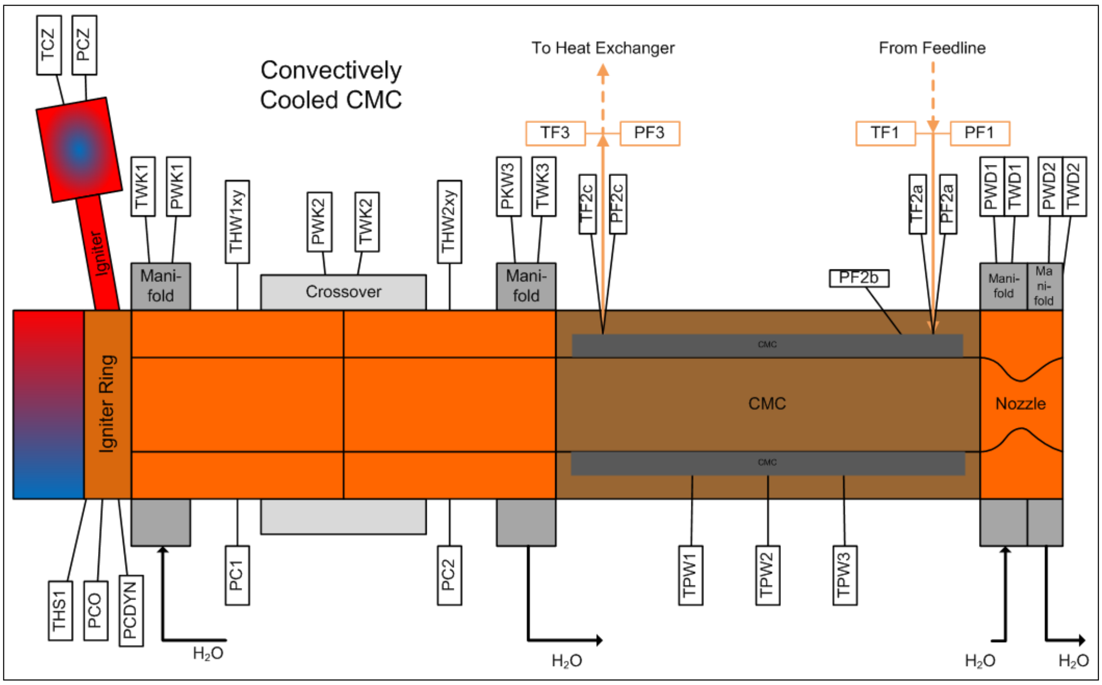

Fig. 3.12: Sensor Locations in Setup with Convectively Cooled CMC

3.4 Data Processing and Accuracy

In this section the data preparation performed on the raw test data is introduced as far as necessary for understanding of this work. The data processing includes e.g. averaging, calculation of heat pick-up and heat flux, the determination of the combustion efficiency, the evaluation of the dynamic pressure transducers and determination of specimen specific values.

3.4.1 Data Handling and Averaging

Test data are recorded by two 64 channel DAQ cards using LabVIEW [81] by National Instruments and stored as raw information in a proprietary binary format. The data rate is usually 1 500 Samples per second for standard channels and 10 000 Samples per second for the dynamic pressure transducers. The test operation implies that each load point is hold for approximately 10 seconds in order to ensure steady-state conditions.
On evaluation the raw data are converted to physical values using the calibration file and a zero balance is performed if applicable. A window near the end of the load point with a typical length of two to three seconds is chosen and the average value is determined for each channel. Further analysis and calculation of dependent values are performed on base of these average values.

3.4.2 Combustion Efficiency

The combustion efficiency has been calculated as the ratio of the experimentally determined characteristic velocity c^*_{exp} and a theoretical c^*_{theo} for that operating point.

$$\eta_{c^*,inj} = \frac{c^*_{exp,inj}}{c^*_{theo,inj}} \tag{3.1}$$

$$OF = \left(\frac{O}{F}\right)_{inj} = \frac{\dot{m}_{inj,Ox}}{\dot{m}_{inj,Fu}} \tag{3.2}$$

$$c^*_{exp,inj} = \frac{p_{t,th} \cdot A_{th}}{\dot{m}_{inj,Ox} + \dot{m}_{inj,Fu}} \tag{3.3}$$

$$c^*_{theo,inj} = f\left(p_c,\ \left(\frac{O}{F}\right)_{inj},\ h_{t,Ox,inj},\ h_{t,Fu,inj}\right) \tag{3.4}$$

For the experiments with film and transpiration cooling the algorithm has been extended in order to take into account the additional kerosene or nitrogen mass flow injected through the film applicator or the transpiration cooled CMC. The determination of the theoretical characteristic velocity as well as the experimental characteristic velocity have therefore been adapted adequately assuming a full mixing of the coolant and additional denotations have been introduced:

$$\eta_{c^*,th} = \frac{c^*_{exp,th}}{c^*_{theo,th}} \tag{3.5}$$

$$OFT = \left(\frac{O}{F}\right)_{th} = \frac{\dot{m}_{inj,Ox}}{\dot{m}_{inj,Fu} + \dot{m}_{cool}} \tag{3.6}$$

$$c^*_{exp,th} = \frac{p_{t,th} \cdot A_{th}}{\dot{m}_{inj,Ox} + \dot{m}_{inj,Fu} + \dot{m}_{cool}} \tag{3.7}$$

$$c^*_{theo,th} = f\left(p_c,\ \left(\frac{O}{F}\right)_{th},\ h_{t,Ox,inj},\ h_{t,Fu,inj},\ h_{t,cool}\right) \tag{3.8}$$

Here, the theoretical c^* is obtained with Gordon-McBride CEA computer code [24]. As CEA assumes adiabatic wall conditions, the propellants' inlet enthalpies are corrected by the convective cooling losses into the water cooling circuit (namely Q, which is determined by the total heat pick-up of the water-cooled segments). The input parameters for the code are the total pressure in the chamber, the mixture ratio (injector or throat, respectively) and the inlet conditions of fuel, oxidizer and - if applicable - film or transpiration coolant. Thereby, the film or transpiration coolant is always treated as part of the fuel mass flow. Since the coolant may not fully mix with the core stream, a comparison of the combustion efficiencies with and without taking the coolant into account can be of interest. To distinguish the combustion efficiency with the coolant considered (at throat conditions) from the injector-related combustion efficiency (at hot gas conditions) it is denoted with "T", "th" or "throat".

The experimental c^*_{exp} depends on the geometry of the throat, the total pressure (PTT or PTTT, respectively) in the throat, which can be derived from the static pressure measurement in the chamber (channel PC4 or PC3), and the overall mass flow through the throat area [76]. For the determination of the total pressure two approaches are used: Either chemical equilibrium flow is assumed (marked as "1", LFA legacy) or a frozen composition is assumed (marked as "2", proposed by *JANNAF* [83]). However, for the hardware configurations investigated the values calculated with the two different approaches hardly differ (typically mean deviation is less than 0.015 %).

Due to the small size of the combustion chamber the combustion efficiency is very sensitive to the throat diameter (0.1 mm difference in diameter results in approx. 1% deviation in combustion efficiency). Since the effective throat area is unknown, for the calculation of the throat cross sectional area the real geometric diameter of 16.515 mm for the big and 12.65 mm for the small combustion chamber have been used both for calculation of c^*_{exp} as well as total pressure in the throat in the past. Estimations using cold flow test data and a semi-empirical boundary layer model [82] showed that a boundary layer thickness of up to 0.15 mm can be assumed for tests without film or transpiration cooling. Taking the latter finding into account the combustion efficiency calculated from the geometric throat cross sectional area would be generally approximately 3.5 % too high leading sometimes to values even greater than unity. Therefore, the combustion efficiency has been recalculated using a corrected diameter of 16.232 mm and 12.467 mm.

In contrast, the change of the throat area due to thermal elongations has been neglected. For determination of this effect *JANNAF* provides a formula given in Eq. 3.9.

$$\Delta A_{th} \approx 2\pi \, r_{th} \left[\frac{r_{th} \cdot p_{stat,th}}{E} (1+\nu) - \alpha_L \cdot x \cdot \Delta T \right] \tag{3.9}$$

Here, r_{th} is the throat radius, $p_{stat,th}$ is the static pressure in the throat and x the distance between hot gas wall and the center of the cooling channel. The Young's modulus E, Poisson's ratio ν and the thermal elongation coefficient α_L are material properties. Using values of copper ($E = 115$ GPa, $\nu = 0.35$, $\alpha_L = 16.5 \cdot 10^{-6}$ K^{-1}) and a typical load point ($p_c = 6$ MPa $\rightarrow p_{stat,th} \approx 4.1$ MPa, $\Delta T \approx 350$ K) with $x = 1.85$ mm (37 mm CC), the change can be estimated as $\Delta A_{th} = -5.34 \cdot 10^{-7}$ m^2 which equals a constriction of the throat area of 0.25%.

Implausible high combustion efficiencies have been reported for mixture ratios significantly lower than 2.2 [69, 84], whereas the latter has been traced back to the effect of unburnt kerosene being considered as a fully reacting species by Gordon-McBride-Code CEA leading to a too low c^*_{theo}. Actually, this problem applies also to nitrogen, where the assumption of a fully mixed/reacting nitrogen film leads to a very low c^*_{theo}. Although one might neglect the film or transpiration mass flow for very low coolant mass flows in this case, the additional mass flow and boundary layer displacement must always be considered. Since CEA assumes full and ideal mixture of the propellants but the functional principle of film and transpiration cooling bases on the inhomogeneity of the hot combustion gases, the performance calculation comprises an imminent inaccuracy and marks always a kind of worst-case-assumption namely that the film has fully dissolved or the coolant behaves totally inert.

3.4.3 Heat Flux to Water Cooled Copper Segments

The heat flux to the copper chamber segments and the nozzle is calculated by the balance of the water's total enthalpy from inlet to outlet of each segment. Therefore, coolant temperature and pressure are measured per each segment and the coolant mass flow is determined by the differential pressure over metering orifices. The overall heat flux is defined as:

$$\dot{Q}_{Cu} = \underbrace{H_{t,cool,out}}_{f(p_{t,out},\ T_{out})} - \underbrace{H_{t,cool,in}}_{f(p_{t,in},\ T_{in})} \tag{3.10}$$

Fluid properties have been derived from Wärmeatlas [11], while the enthalpy definition is derived from Gordon-McBride CEA [24].

The determination of the heat flux is quite sensitive to measurement uncertainties especially regarding steady-state conditions and heat-up of the cooling fluid i.e. water. From the usually multiple thermo sensors installed after each of the segments, a circumferential temperature distribution is determined and for each octant of the segment the individual heat pick-up is calculated. Thereof, the mean as well as for reference the minimum and maximum value is taken. By normalizing the heat pick-up to the inner combustion chamber surface area, i.e. $1.1043 \cdot 10^{-2}$ m^2 per cylindrical segment, or the inner nozzle surface area, i.e. $2.6706 \cdot 10^{-3}$ m^2, respectively, the heat flux is established.

In general, the uncertainty of the heat flux measurements is affected by the measuring chain of each variable involved. Here, the chain comprises the sensor itself, wiring, measuring transducers and DAQ device. Thereof, the sensor usually features by far the highest measuring inaccuracy (cf. Tab. A.2). Although the error of measurement can be further decreased by appropriate measures e.g. in-situ calibration and zero offset correction, the manufacturer guaranteed accuracy may be taken as reference. For a load point of 6.0 MPa and mixture ratio 2.9 the uncertainty of the coolant mass flow measurement is in the order of 2.1%. Using a set of three thermocouples (two type K, 0.5 mm, one PT-100, 1.0 mm), the uncertainty is 0.28% for the temperature measurement and 1.5% for the pressure measurement resulting in an uncertainty of 2.1% in the determination of the specific enthalpy of the coolant water. Therefore, the heat pick-up thus the heat flux of aforementioned test case is determinable with an uncertainty of 3.7%. For lower combustion pressures and water temperatures the uncertainty will be higher. Taking into account the variation in meeting the nominal load point and the reproducibility the confidence interval of the heat flux is in the order of ±10% for the chamber segments and mixture ratios greater than 2.0 and ±20% for the nozzle segment.

3.4.4 HF Chamber Pressure Characteristics

Dynamic pressure transducers have been installed in the combustion chamber (PCDYN), in the injector kerosene feed line (PKDYN) and in the oxygen feed line (PODYN). The sensors are usually sampled at 20 kHz. In order to identify frequencies and peak amplitudes of combustion oscillations, a "Fast Fourier Transform" (FFT) has been carried out with a window size of 1024 samples. See references [85], [86] and [87] for a detailed description on the FFT.

3.4.5 Film Cooling Effectiveness

For the quantification of the film cooling effectiveness several definitions exist. Using hot wall temperature measurements, the cooling efficiency Θ can be determined as [51, 88]:

$$\Theta = \frac{T_{wall,\ withoutFilm} - T_{wall,\ withFilm}}{T_{wall,\ withoutFilm} - T_{cool}} \tag{3.11}$$

Thereby the temperature T_{cool} is the temperature of the film coolant entering the combustion chamber i.e. channel TF3. The determination of the hot wall temperature without film cooling $T_{wall,\ withoutFilm}$ is non-trivial due to the limited number of appropriate reference tests available, since hot wall temperature measurements have only been introduced after combustion chamber characterization and reference test campaign. For simplification, the highest hot wall temperature of each load point (typically at the very end of the second or fourth segment, THW22b or THW42b, respectively) has been chosen as reference temperature $T_{wall,\ withoutFilm}$.
Basing on the heat flux calculated for each segment the following definition for a heat flux based cooling effectiveness has been introduced:

$$\eta_{Film,\dot{q}} = 1 - \frac{\dot{q}\ (Segment)}{\dot{q}_{reference}\ (Segment)} \tag{3.12}$$

For the reference heat flux the heat flux correlations based on ATLLAS chamber characterization test campaign has been used [84, 89]. The effective film length can only be roughly estimated from hot wall temperature and heat flux due to the limited spatial resolution of the measurements.

3.4.6 Transpiration Mass Flow Rate

For the tests with convectively-cooled CMCs namely the PSR test samples a certain transpiration mass flow rate through the CMC chamber wall has been expected due to the permeability of the material. This transpiration mass flow has been defined as [91]:

$$\dot{m}_{Transpiration} = \dot{m}_{cool,in} - \dot{m}_{cool,out} = MF1 - MF2 \tag{3.13}$$

For the flow checks and hot tests the transpiration mass flow was estimated by measuring both the mass flow entering the PSR and the mass flow exiting the dump line.

3.4.7 Blowing Ratio

The blowing ratio has been defined as:

$$F = \frac{\rho_{cool} \cdot v_{cool}}{\rho_{\infty} \cdot v_{\infty}} = \frac{\dot{m}_{cool}}{\dot{m}_{\infty}} \cdot \frac{A_{ref,c}}{A_{ref,cool}} \tag{3.14}$$

The coolant mass flow rate $\dot{m}_{cool}$ is derived from Coriolis mass flow meter MF1 or in case of the convectively-cooled CMCs from $\dot{m}_{Transpiration} = \mathrm{MF1} - \mathrm{MF2}$. The free stream mass flow $\dot{m}_c$ is calculated from Coriolis mass flow meter MO and kerosene mass flow rate by turbine flow meter MVK or Coriolis mass flow meter MK. The cross sectional area of the combustion chamber has been used for $A_{ref,\infty}$:

$$A_{ref,c} = \frac{\pi}{4}\,(0.037\ \mathrm{m})^2 = 1.075 \cdot 10^{-3}\ \mathrm{m}^2 \tag{3.15}$$

For the transpiration cooled CMC the inner surface of the CMC sample $A_{ref,cool}$ [90] is given as:

$$A_{ref,cool} = \pi \cdot 0.037\ \mathrm{m} \cdot 0.0846\ \mathrm{m} = 9.833 \cdot 10^{-3}\ \mathrm{m}^2 \tag{3.16}$$

For the convectively cooled CMC the appropriate cooling surface is:

$$A_{ref,cool} = \pi \cdot 0.037\ \mathrm{m} \cdot 0.1915\ \mathrm{m} = 2.227 \cdot 10^{-2}\ \mathrm{m}^2 \tag{3.17}$$

For film cooling the definition of $A_{ref,cool}$ is non-trivial due to the radial inflow characteristic of the film applicator used. For evaluation the area of gap, where the coolant enters the combustion chamber, has been used:

$$A_{ref,cool} = \pi \cdot 0.037\ \mathrm{m} \cdot 5.0 \cdot 10^{-4}\ \mathrm{m} = 5.812 \cdot 10^{-5}\ \mathrm{m}^2 \tag{3.18}$$

3.4.8 Heat Flux to GN2 or H/C cooled PSR duct

The heat flux to the convectively cooled PSR ducts has been calculated based on a balance of coolant total enthalpy from inlet to outlet of the coolant duct. The enthalpy values have been calculated using NASA polynomials derived from Gordon-McBride CEA [24]. For the inlet conditions the sensors PF2a and TF2a within an effective cross section of $9.828 \cdot 10^{-4}\ \mathrm{m}^2$ have been used as well as sensors PF3 and TF3 within a cross section of $1.227 \cdot 10^{-4}\ \mathrm{m}^2$ for the outlet. The overall heat transfer rate to the nitrogen or kerosene is based on the measured outlet mass flow rate [91]:

$$\dot{Q}_{CMC} = \underbrace{H_{t,cool,out}}_{f(p_{t,out},\ T_{out})} - \underbrace{H_{t,cool,in}}_{f(p_{t,in},\ T_{in})} \tag{3.19}$$

By normalizing the heat transfer rate to the inner combustion chamber surface area, i.e. a value of $2.227 \cdot 10^{-2}\ \mathrm{m}^2$, the heat flux is determined.

4. Experimental Data and Analysis

In this chapter the measurements and key results from the experimental activities are presented. First, an overview of the reference and calibration tests is given. Afterwards, the results from film and transpiration cooling as well as experiments conducted with convectively cooled CMCs are shown. The modeling of the heat transfer presented here will be the focus of chapter 5.

4.1 Reference Tests

In this section the results of the run-in and reference tests of the 37 mm water-cooled combustion chamber using the standard double-swirl liquid/gas injector are presented and compared with the results of the older 20 mm combustion chamber using double-swirl liquid/gas-jet injectors, which were formerly presented in Ref. [69] and Ref. [75].

When analyzing the results, some differences between the two configurations allow to investigate the sensitivity of the experimental data and subsequent of the modeling on certain geometric characteristics: Firstly, the CC diameter was increased from 20 to 37 mm which results in a higher volume to surface ratio by a factor of 1.85 for the bigger combustion chamber. Secondly, the contraction ratio ϵ_c is 5 for the bigger combustion chamber compared to 2.5 of the 20 mm one resulting in a free flow Mach number of 0.12 in contrast to 0.24. The aim of this modification was to maintain the maximum combustion pressure of 10.0 MPa with the existing test facility. However, the pressure gradient along engine axis due to the acceleration of the gases, the influence of the boundary layer and the heat transfer differ as well. Determined by semi-empirical correlations [82], the boundary layer thickness in the nozzle throat is in the order of 0.142 mm for the 37 mm CC and 0.092 mm for the 20 mm CC. The lower free stream velocity effects an approximately 40% less convective heat transfer for the 37 mm chamber (cf. Eq. 2.31 et seqq.). Since the bigger combustion chamber consists of four segments of 95 mm length each while the small combustion chamber has three segments of 130 mm, the total heat-pick per segment is only about 20% smaller for the 37 mm hardware. With no major significance for the heat transfer but combustion performance, the double-swirl gas-jet injector of the 37 mm CC, which has been evolved by means of scaling, is designed for an operation point $O/F = 2.9$ at 8.0 MPa in comparison to $O/F = 2.9$ at 6.0 MPa of the smaller injector elements used in the 20 mm CC.

The main chamber parameters relevant for this work comprise the chamber pressure, which is measured at several axial positions in the chamber, the mass flow rates and other inlet conditions of oxidizer and kerosene, the coolant mass flow rate as well as the pressure loss and heat up of the coolant for each chamber segment and the nozzle segment. Based on these data characteristic values like mixture ratio, combustion efficiency and heat flux have been calculated.

4.1.1 Operating Points Investigated

The operating points investigated are summarized in Tab. 4.1 and shown in Fig. 4.1.

Characteristic	Symbol	Unit	20 mm CC	37 mm CC
Pressure	p_c	[MPa]	$3.7 \dots 8.0$	$0.9 \dots 8.2$
Mixture ratio	O/F	[−]	$2.34 \dots 3.38$	$1.36 \dots 3.33$
Reynolds number	Re_D	[−]	$1.4 \dots 3.0 \cdot 10^5$	$0.4 \dots 3.0 \cdot 10^5$
… nominal	$Re_{D,nom}$	[−]	$2.3 \cdot 10^5$	$2.9 \cdot 10^5$

Tab. 4.1: Summary of Reference Operating Points Investigated

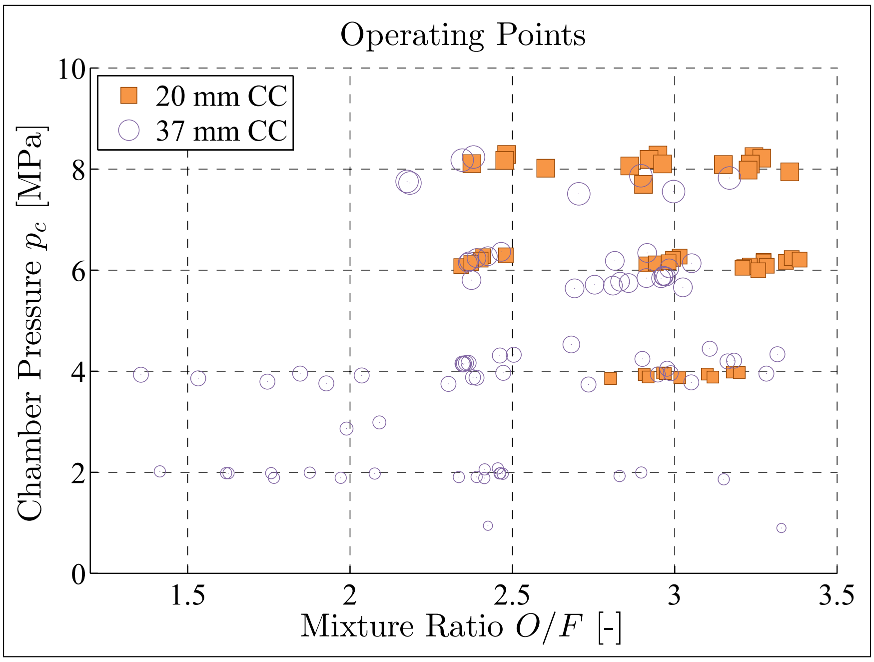

Fig. 4.1: Operating Point Investigated with Swirl Injector for 37 mm CC (hollow circles) and 20 mm CC (full squares), Symbol Size Encodes Pressure Level

A large number of different test cases has been investigated for the 37 mm combustion chamber (hollow circles) providing a quite comprehensive database for the modeling as well as for the CMC and film cooling experiments conducted later on. For the 20 mm combustion chamber (full squares) less test data is available for this injector setup and the operational envelope contains only mixture ratios from 2.4 up to 3.2 and pressures between 4.0 and 8.0 MPa, limiting the number of possible points for comparison of both chamber configurations. The corresponding Reynolds number based on the combustion chamber diameter, which is relevant for the heat transfer modeling, is comparable for both configurations.

4.1.2 Combustion Efficiency

The combustion efficiency with respect to mixture ratio and pressure is presented in Fig. 4.2. The values for the 37 mm combustion chamber are generally higher than for the 20 mm which can obviously be traced back to overall better mixing and atomization of the new double-swirl injector element as well as the higher contraction ratio, which yields a longer residence time of propellants in the bigger chamber. The 37 mm combustion chamber has a characteristic length $L^* = 2.06$ m twice as long as the smaller combustion chamber since it was not scaled to retain L^* but to keep overall length constant and to ensure that the combustion process is completed at the location where the cooling experiments are located. Unfortunately, the available data does not facilitate a detailed attribution of performance gains to the longer residence time and less total pressure losses due to the lower velocity or additional friction losses due to larger wetted area for the 37 mm CC.

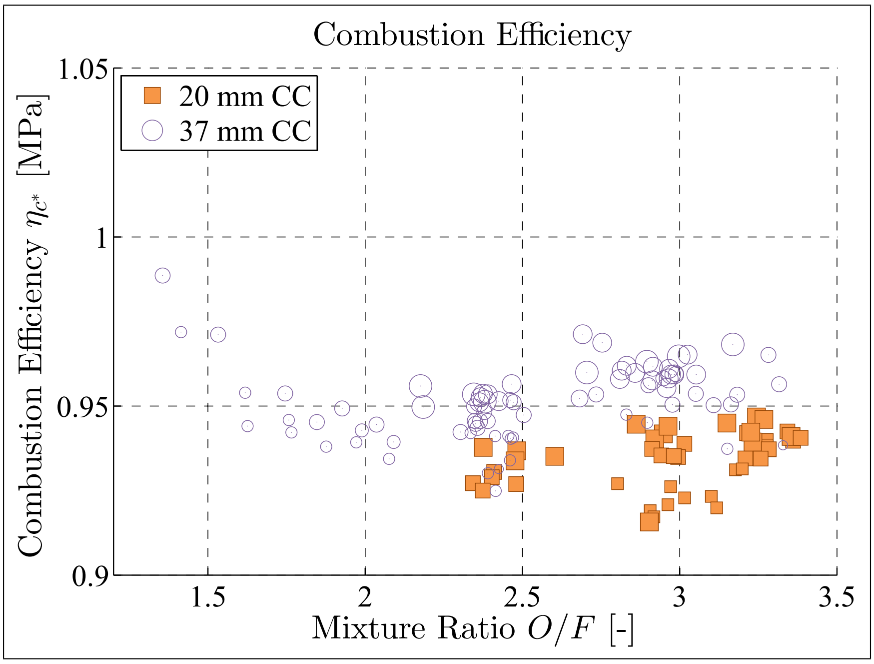

Fig. 4.2: Combustion Efficiency of Swirl Injector for 37 mm CC (hollow circles) and 20 mm CC (full squares), Symbol Size Encodes Pressure Level

Although results show a high variance especially for lower pressure levels (data points with small symbols), the pressure dependency of the combustion efficiency is quite obvious for both configurations. With increase of the mixture ratio from 2.0 to stoichiometric conditions ($O/F = 3.4$) a slight increase in combustion efficiency can be found as expected. In contrast, the increase of combustion efficiency at mixture ratios smaller than 2.0 is quite odd. An analysis on this behavior using the CEA code [24] showed that for mixture ratios smaller 2.0 the temperature gradient and the gradient of characteristic velocity over mixture ratio becomes quite high, leading to large changes in c^*_{theo} for small differences in the mixture ratio O/F. Since the swirl injector is known to create a propellant film on the chamber under specific operating conditions, a plausible reason for the behavior at low mix-

ture ratios is the formation of a kerosene film on the chamber wall (compare to [17]). This probably induces an inhomogeneous gas composition at the nozzle throat where a layer of fuel-rich gases surrounds a more oxidizer-rich than average core leading to a increased characteristic velocity $(\dot{m}_{core} \cdot c^*_{core} + \dot{m}_{fuel-rich} \cdot c^*_{fuel-rich}) > (\dot{m}_{core} + \dot{m}_{fuel-rich}) \cdot c^*_{fully-mixed}$ and to the particular increase of combustion efficiency towards lower mixture ratios. Although CFD simulations show stratification effects in the combustion chamber giving an evidence for a kerosene film at the wall [92], this behavior could not be quantified in experiment so far.
In order to handle different operating conditions and to provide an easy approach for comparisons and numerics, a correlation for the combustion efficiency has been established:

$$\eta_{c^*}\,[-] = a \cdot OF^b \cdot PCC\,[bar]^c \tag{4.1}$$

Due to the multiple difference in geometry and test configuration, a single parameter set for the big and the small combustion chamber was not realizable. For the 37 mm combustion chamber the parameters a, b and c are given in Tab. 4.2. Thereby, the correlation describes the evaluated combustion efficiency with a mean accuracy of ±0.0035 within the area of validity comprising pressures between 2 MPa and 6 MPa and mixture ratios between 1.9 and 3.3.

Parameter	Value	Comment
a	0.892912	Multiplier
b	0.018138	Influence of mixture ratio
c	0.012481	Influence of combustion pressure

Tab. 4.2: Correlation for Combustion Efficiency of 37 mm CC

Similarly, the correlation has been applied to the combustion efficiency of the 20 mm combustion chamber. The parameters are summarized in Tab. 4.3. The mean accuracy of the approximation is ±0.0025 within a pressure level of 4 MPa up to 8 MPa as well as mixture ratios between 2.4 and 3.4.

Parameter	Value	Comment
a	0.803291	Multiplier
b	0.034723	Influence of mixture ratio
c	0.027673	Influence of combustion pressure

Tab. 4.3: Correlation for Combustion Efficiency of 20 mm CC

From the parameters, the higher combustion efficiency of the bigger compared to the smaller injectors (factor a) and a less distinctive dependency on mixture ratio (factor b, indicator for the injector velocity ratio) and pressure (factor c, affected by injector momentum ratio) of the bigger combustion chamber are apparent. In the modeling of the heat transfer the correlations are used to take the influence of incomplete combustion on the recovery temperature into account.

4.1.3 Heat Flux

The heat flux density for different mixture ratios, pressures and axial positions is given in Fig. 4.3 to Fig. 4.6. Higher mixture ratios yield an overall increase of heat flux for all test cases up to a mixture ratio of approximately 3.1. For the pressure dependency a linear or near-linear correlation can be found.

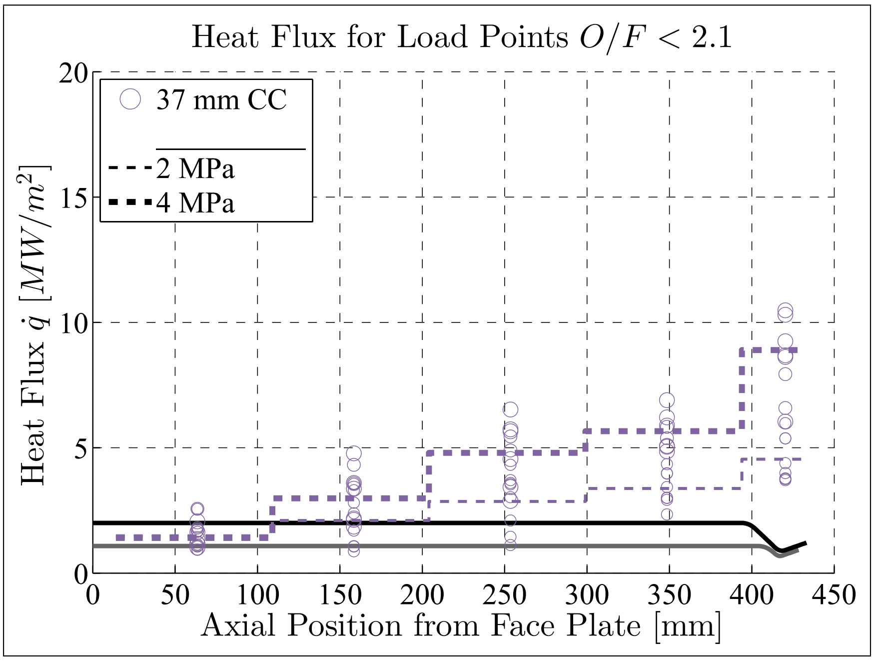

Fig. 4.3: Evolution of Heat Flux for 37 mm CC (lilac circles) at MR below 2.1 (Symbol Size Encodes Pressure Level, Different Scale)

The heat flux shows for the first segment a lower pressure dependency of the double-swirl liquid/gas-jet injector applied in the 37 mm CC than for the more downstream segments, which is best illustrated in Fig. 4.4 where the heat fluxes in the first segment are similar. In contrast, the injector elements of the 20 mm combustion chamber show in segment 1 a similar pressure dependency as in the segments 2 and 3 – lines representing mean values neither converge nor diverge. This can be traced back on the larger chamber contraction ratio ε_c of the 37 mm setup, which causes a larger recirculation zone compared to the 20 mm chamber. Also, the longer segment length for the smaller chamber may cause a blurring of the back flow effects near the face plate on the axial heat flux distribution.

The heat flux of the smaller combustion chamber setup only slightly increases from the middle segment 2 to the last chamber segment 3, which indicates that combustion can be considered completed somewhere in the second segment, especially for mixture ratios higher than 2.6 at which evidently less kerosene is deposited by the injector swirl. Although the reactants have already accumulated a longer residence time at the end of the second segment in the 37 mm combustion chamber, there the heat flux still distinctly increases from segment 2 to segment 3. Comparing the different heat fluxes between the 20 mm and the 37 mm combustion chamber, it can be found that the values correlate roughly by factor 1.85 in the middle and the last segments. This coincides exactly with the volume to

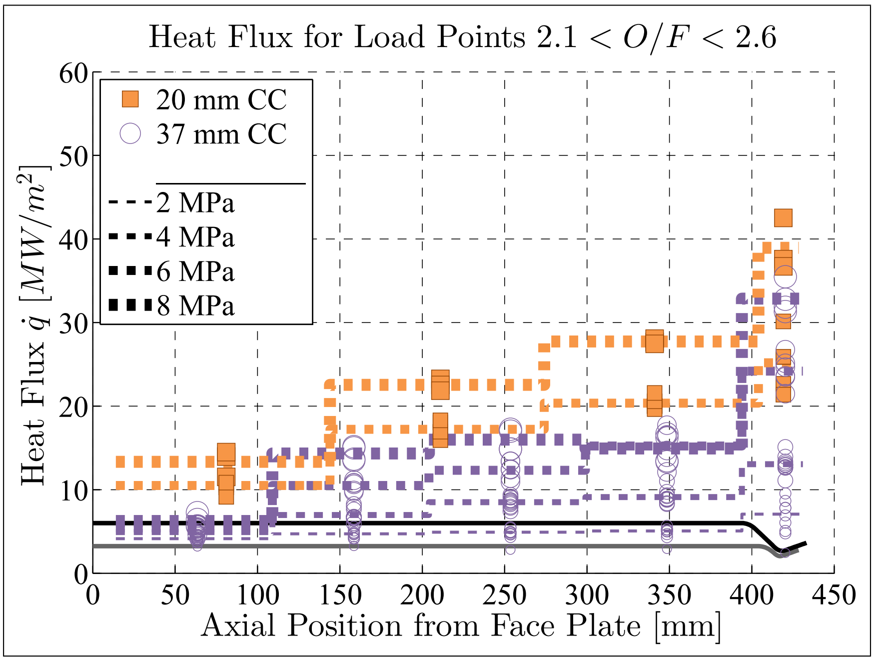

Fig. 4.4: Evolution of Heat Flux for 37 mm (lilac circles) and 20 mm CC (orange squares) at MR between 2.1 and 2.6 (Symbol Size Encodes Pressure Level)

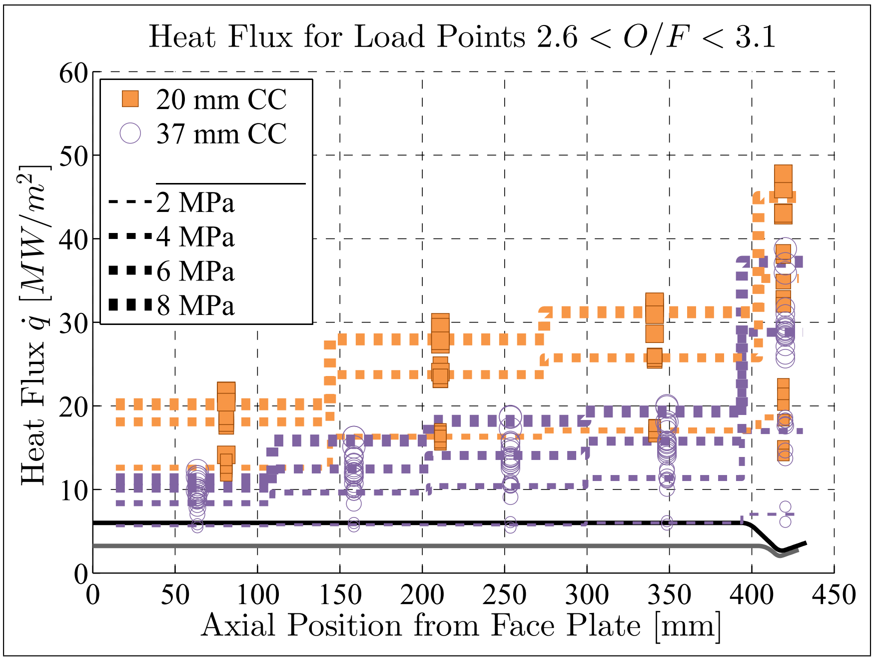

Fig. 4.5: Evolution of Heat Flux for 37 mm (lilac circles) and 20 mm CC (orange squares) at MR between 2.6 and 3.1 (Symbol Size Encodes Pressure Level)

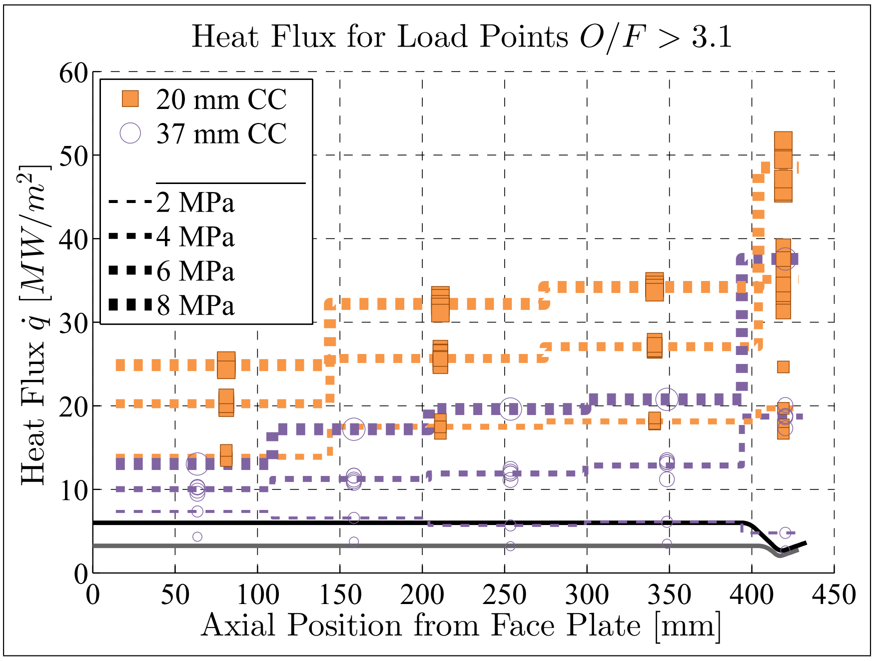

Fig. 4.6: Evolution of Heat Flux for 37 mm (lilac circles) and 20 mm CC (orange squares) at MR above 3.1 (Symbol Size Encodes Pressure Level)

surface area ratio between the two different chambers, which represents the energy release to heat transfer ratio.

Between the third and the fourth segment of the 37 mm CC the heat flux remains almost constant, so that the combustion is assumed to be completed at the end of the third segment. For higher pressure levels even a slight decrease of the heat flux can be found for certain tests, which can be explained by the growth of the boundary layer in this area.

Already in the past a segment-wise correlation for the heat flux of the reference combustion chamber configuration has been introduced [89–91]. It uses three parameters in order to describe the heat flux as function of mixture ratio and combustion pressure:

$$\dot{q}\left[\frac{W}{m^2}\right] = a \cdot OF^b \cdot PCC\,[bar]^c \tag{4.2}$$

The adequate factors determined by regression analysis and updated with the latest findings are given in Tab. 4.4. These factors have been found valid for pressures between 2 MPa and 6 MPa and mixture ratios between 1.9 and 3.3. The mean deviation of the correlation to measured data is between 4.3 % (3rd and 4th segment) and 9.4 % (1st segment) for the chamber segments as well as approximately 10.4 % for the nozzle segment, which is roughly in the same order of magnitude as the measurement uncertainty.

Obviously, the heat flux in the first combustion chamber segment is mostly driven by effects related to mixture ratio i.e. injection, evaporation and mixture of the propellants rather than the combustion pressure. This can be traced back to recirculation as well as generation of a fuel-rich film on the hot gas chamber wall by the swirl injector used. Within the remaining chamber segments the influence of the mixture ratio, which is linked to the injector velocity ratio, seems to decrease more downstream, while the overall heat

Parameter	1st CC Segment	2nd CC Segment	3rd CC Segment	4th CC Segment	Nozzle Segment	Comment
a	93565	132591	140865	158353	61416	Multiplier
b	2.1017	1.4408	0.9086	1.0065	0.9053	Influence of mixture ratio
c	0.6043	0.7387	0.8961	0.8650	1.2606	Influence of combustion pressure

Tab. 4.4: Correlation for Heat Flux of 37 mm CC

flux (multiplier “a”, indicator for completeness of combustion) increases and the pressure dependency “c” soon reaches the typical value of 0.9 (cf. [1]). Otherwise, the heat flux in the nozzle segment is significantly influenced by the combustion pressure albeit the measurement accuracy and reproducibility thus quality of the correlation is worse than for the combustion chamber segments due to the more complex geometry, axial heat conduction and a low overall heat pick-up amplifying measuring errors. However, the presented behavior can be found for all tests conducted with the 37 mm combustion chamber.

Parameter	1st CC Segment	2nd CC Segment	3rd CC Segment	Nozzle Segment	Comment
a	103616	224805	293836	92174	Multiplier
b	1.9892	1.2420	0.8303	0.8528	Influence of mixture ratio
c	0.7143	0.7968	0.8611	1.1998	Influence of combustion pressure

Tab. 4.5: Correlation for Heat Flux of 20 mm CC

The parameters for the 20 mm combustion chamber are summarized in Tab. 4.5. The correlation is valid for mixture ratios between 2.4 and 3.4 and for combustion pressures of 4 MPa up to 8 MPa. Mean deviation between correlation and measurement is between 2.1 % (3rd segment) and 4.7 % (1st segment) for the cylindrical part and 9.7 % for the nozzle segment.

For special purposes also a correlation with eight factors has been developed for the 37 mm combustion chamber which extends the area of validity up to a pressure of 8 MPa and down to a mixture ratio of approximately 1.6 [1]. This approach also overcomes some shortcomings of the three-factor-correlation, which are caused by influences of the water cooling mass flow rates (see Ref. [84] for details).

---

[1] S. Blank: *Auswertung und Modellierung von Experimenten zur Charakterisierung des Wärmeübergangs in einer Raketenbrennkammer*, Diploma Thesis [in German], Institute of Flight Propulsion (LFA), Technische Universität München, Munich, 2009

4.2 Film Cooling

4.2.1 Test Objectives

During the chamber characterization and reference tests as presented in chapter 4.1, an extensive test envelope has been investigated with the 37 mm combustion chamber, which in the following serves as reference configuration and data base for comparisons with different cooling techniques. The operating points (pressure-mixture ratio-pairings) of all test conducted within the film cooling test campaign are shown in Fig. 4.7 with respect to injector mixture ratio. Fig. 4.8 gives an overview of the film coolant mass flow rates applied during the tests and Fig. 4.9 the corresponding blowing ratios. Reference tests with film applicator installed but without film mass flow rate have been limited to one load point of a nitrogen test only due to a potential overheating and damage of the test setup for such conditions. Assigned reference experiments were performed without film applicator oder dummy device installed hence a 9 mm (length of film applicator) shorter combustion chamber. These tests are illustrated by lilac circles in Fig. 4.7 to Fig. 4.9.

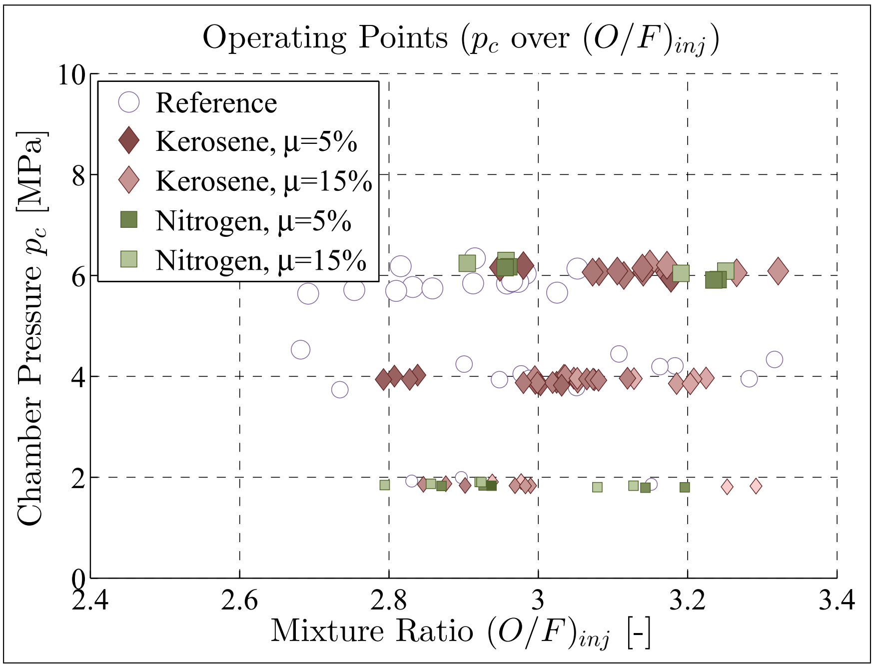

Fig. 4.7: Overview of Load Points Investigated in Film Cooling Campaign (Color Brightness Encodes Film Mass Flow Ratio)

With the coolant nitrogen, tests with an injector mixture ratio of 2.9 and 3.2 at 2 MPa and 6 MPa have been conducted. Nitrogen mass flows between 3 g/s ($\mu = 5$ % at 2 MPa) and approximately 30 g/s ($\mu = 15$ % at 6 MPa) have been investigated. The accuracy and reproducibility of the test has been found satisfying i.e. in the same order of magnitude as the measurement uncertainties are (cf. section 3.4.3 and Tab. B.5 in the annex).
With kerosene, tests at pressure level of 2 MPa, 4 MPa and 6 MPa have been performed. Two approaches have had been traced: Firstly, tests with a constant injector mixture ratio of 3.2 and film mass flow ratio of 5 %, 10 % and 15 % resulting in throat mixture ratios of

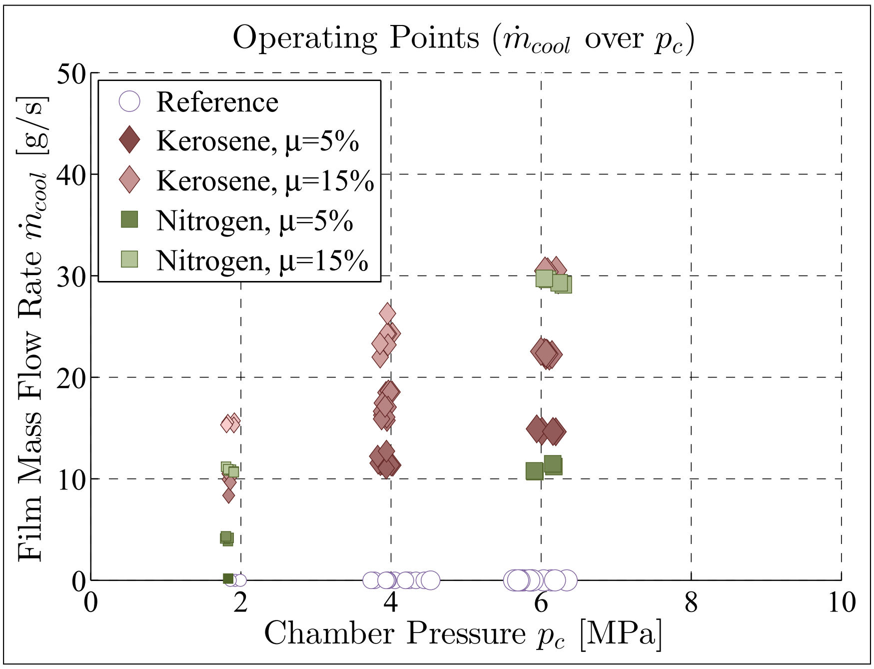

Fig. 4.8: Overview of Film Mass Flow Rates Investigated (Color Brightness Encodes Film Mass Flow Ratio)

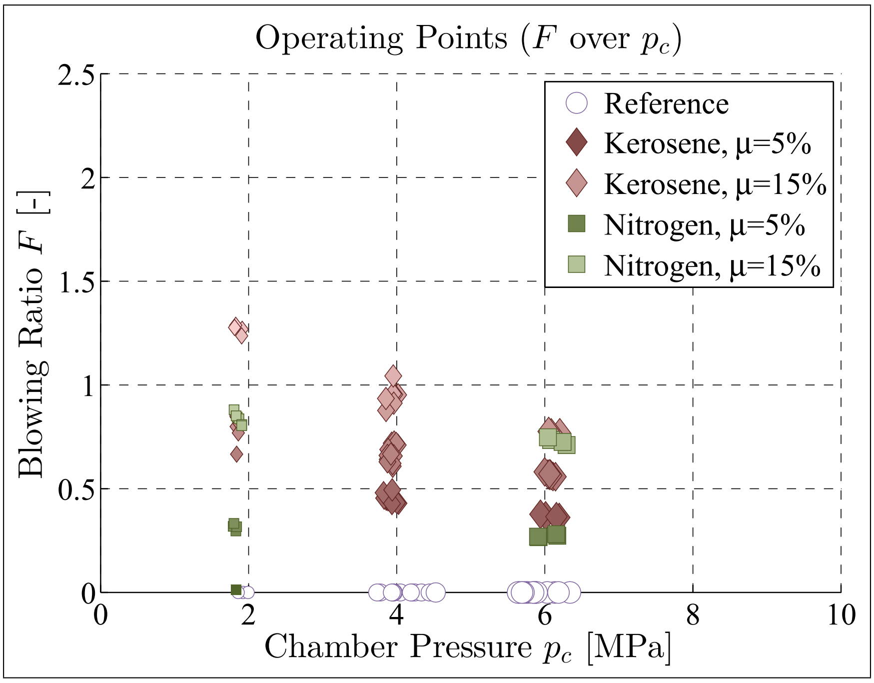

Fig. 4.9: Overview of Blowing Ratio Investigated (Color Brightness Encodes Film Mass Flow Ratio)

3.05, 2.88 and 2.72 have been conducted. Secondly, tests with a constant throat mixture ratio of 2.9 but variable injector mixture ratio (3.05, 3.22 and 3.41, respectively) have been performed. However, for tests with coolant kerosene a significant scatter has been apparent. The small kerosene and oxygen mass flow differences from load point to load point have been challenging with respect to the sequencing of the control valves. Also, for the kerosene film cooling the minimum mass flow rate was limited to about 8 g/s by the characteristics of the control valve used and the feed pressure required. Therefore, the evaluation of the test results has been performed in such way that all test points have been analyzed with respect to pressure, mixture ratio and film part regardless of an originally planned load case and have been assigned to pressure levels 2 MPa, 4 MPa and 6 MPa, injector mixture ratios 2.9 ± 0.15 and 3.2 ± 0.15 as well as film mass flow ratio μ. For each class mean values as well as root mean square deviations have been determined (see Tab. B.3 in the annex).

The film cooling test campaign has been affected by HF oscillations caused by the injector assembly and linked with the oxygen inlet temperature. Measures e.g. pre-cooling of the oxygen feed line and exchange of the oxygen swirl cap have been undertaken in order to reduce the possible impact. However, influences of the HF oscillation on e.g. the mass flow measurement accuracy and boundary layer thus the heat transfer could not be excluded (cf. section 4.2.3).

4.2.2 Film Applicator Pressure Drop and Coolant Heat-Up

The pressure drop over the film applicator and the associated discharge coefficients are shown in Fig. 4.10 and Fig. 4.11. Additionally, in Fig. 4.12 the film coolant temperature at the chamber inflow (“slot”) is given.

For the compressible gas nitrogen the influence of the pressure i.e. fluid density is clearly visible e.g. by the left-bend of the trendline ($\Delta p_{Film} \propto \dot{m}^2$ and $\Delta p_{Film} \propto 1/\rho$). For the approximately incompressible kerosene a good agreement of the pressure drop with theory ($\rho = const.$, $\Delta p_{Film} \propto \dot{m}^2$ only) is apparent for lower pressures and film coolant mass flow rates. For higher combustion pressures an increasing deviation from the trend has been found. This behavior is traced back to higher temperature of the cooling fluid flowing through the film applicator at the higher combustion chamber pressure thus heat load (compare to Fig. 4.12). Similarly, the discharge coefficient of the film applicator (Fig. 4.11) is affected by the thermal effects.

The analysis of the film inlet temperature increase in Fig. 4.12 thus film coolant heat up in the film applicator shows a high dependency from the coolant mass flow rate for nitrogen and a slight dependency for kerosene. The temperature is higher for nitrogen than kerosene due to the lower heat capacity and most probably higher heat transfer coefficient of the nitrogen cooling due to the higher volume flow. Also, the higher combustion chamber pressure thus heat loads are reflected more for the nitrogen case than for kerosene. The overall temperature levels have been non-negligible but uncritical for the safe operation of the film applicator assembly. Regarding a possible coking or decomposition of the kerosene within the film applicator, neither critical temperatures arose nor have any indications for coking been found on the film applicator during visual inspection after test.

The knowledge of the film inlet temperature is a prerequisite for the evaluation of the film cooling effectiveness Θ as defined in Eq. 2.69, which is presented in section 4.2.7. The

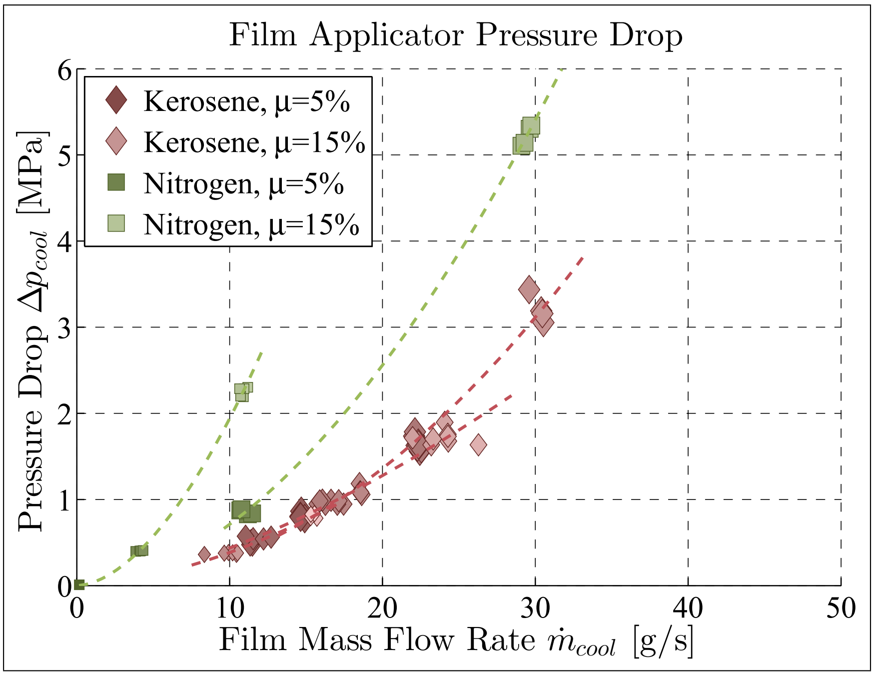

Fig. 4.10: Pressure Drop over Film Applicator (Color Brightness Encodes Film Mass Flow Ratio, Symbol Size Represents Pressure Level)

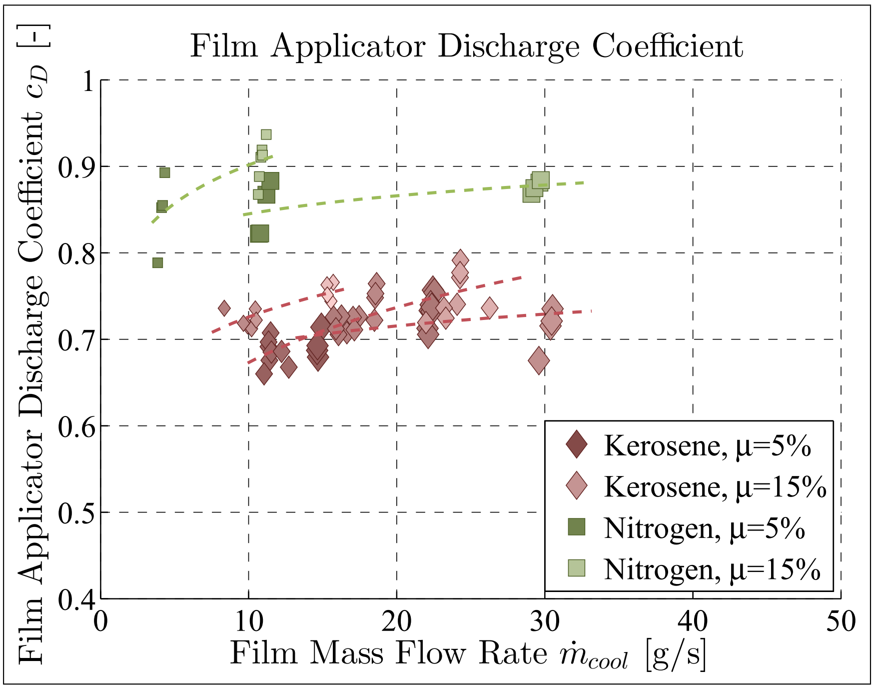

Fig. 4.11: Discharge Coefficient of Film Applicator (Color Brightness Encodes Film Mass Flow Ratio, Symbol Size Represents Pressure Level)

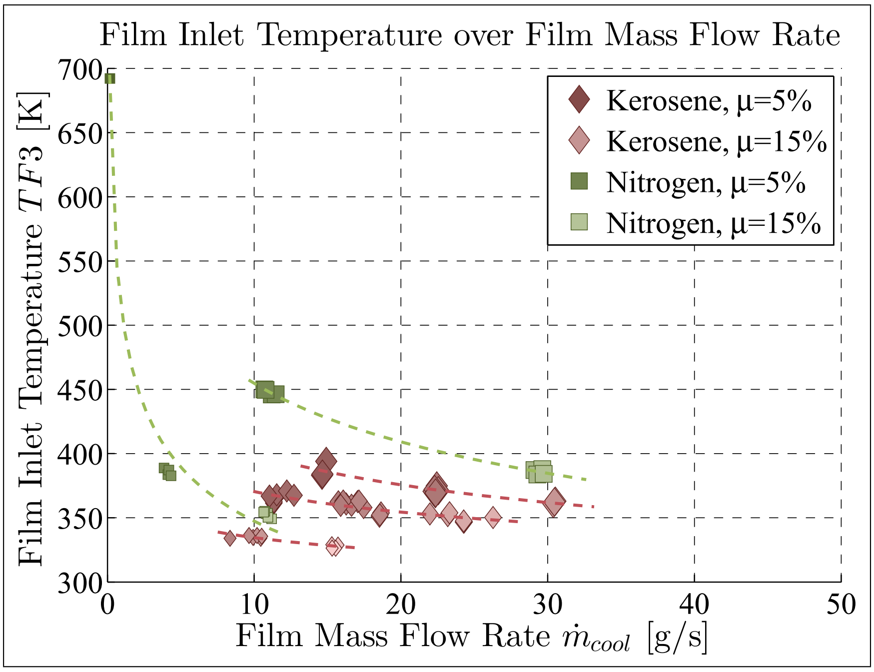

Fig. 4.12: Film Inlet Temperatures (Color Brightness Encodes Film Mass Flow Ratio, Symbol Size Represents Pressure Level)

coolant heat pick-up may also be used to estimate the heat load on the film applicator although this method is error-prone due to the complex geometry of the film device.

4.2.3 Combustion Oscillations

The examination of the dynamic behavior is of importance in order to assess the results with respect to plausibility and reliability. While no significant LF amplitudes i.e. oscillations with frequencies below 1 kHz caused by interactions between combustion chamber and feed lines have been observed, problems with rough combustion due to HF oscillations (coupling of propellant injection or combustion with combustion chamber acoustics) caused or enforced by specifics of the injection assembly used have occurred during the film cooling experiments.

The relative amplitudes of the HF oscillations with respect to associated frequencies are given in Fig. 4.13. A rough combustion (i.e. relative amplitudes higher than 5 %) can be found in the combustion chamber for several tests. In most cases, higher amplitudes appear for lower combustion pressures. The frequency of the peaks at approximately 1300 Hz or multiplies thereof coincide with the first longitudinal mode $L1$ of the combustion chamber, as comparative calculations using the model of a gas-filled cylinder showed. As obvious from Fig. 4.14, no apparent dependency of combustion pressure, film fluid or film mass flow rate is evident. Fig. 4.15 shows the HF oscillations with respect to the oxygen inlet temperature for film cooling tests and the reference tests, where higher amplitudes are found for higher oxygen temperature, but in general a high scatter exists. Further experiments have linked the HF oscillations with an instability of the injector system connected with

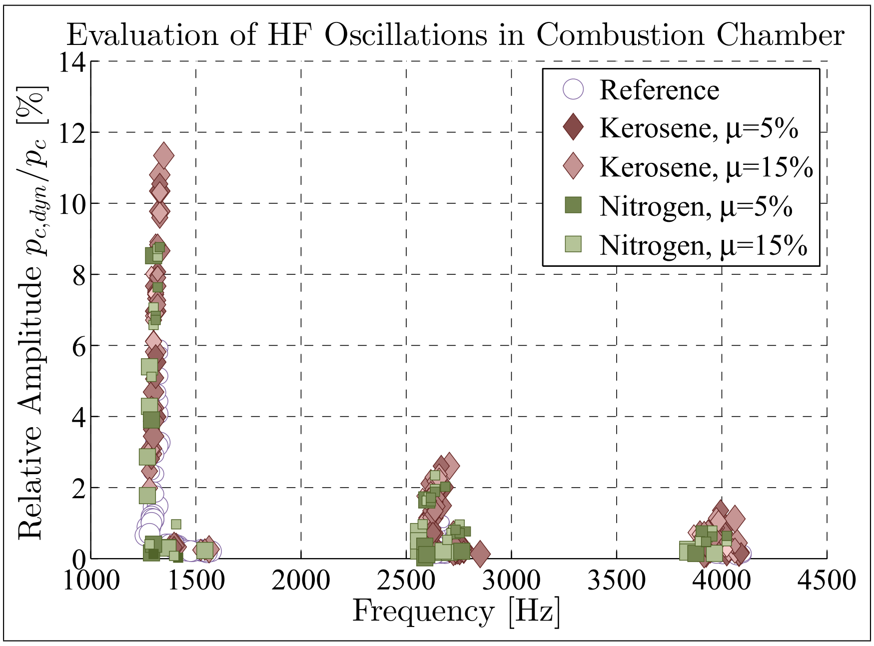

Fig. 4.13: HF Oscillations in Combustion Chamber over Peak Frequency (1st to 4th peak frequency only; Color Brightness Encodes Film Mass Flow Ratio, Symbol Size Represents Pressure Level)

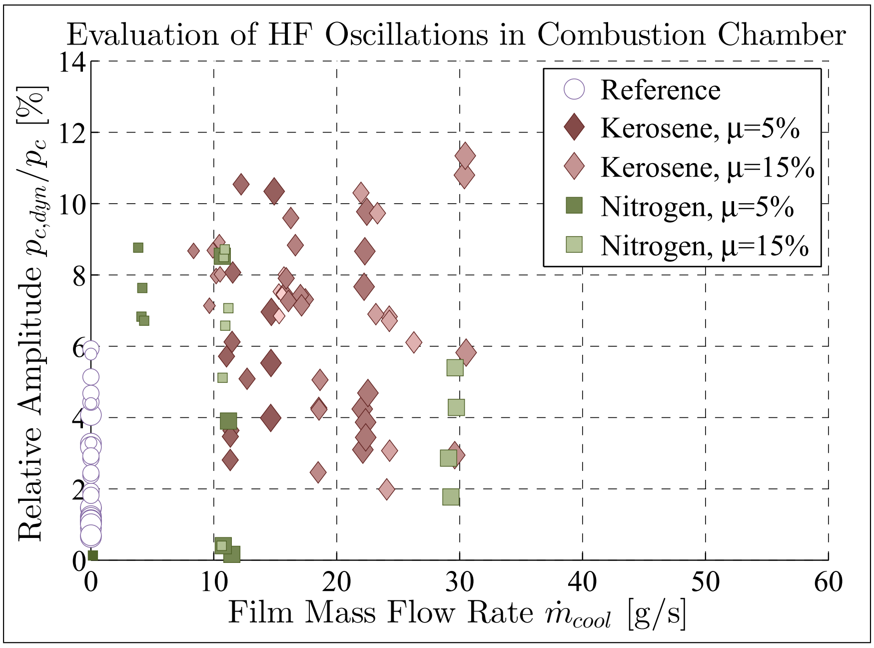

Fig. 4.14: HF Oscillations in Combustion Chamber over Film Mass Flow Rate (Color Brightness Encodes Film Mass Flow Ratio, Symbol Size Represents Pressure Level)

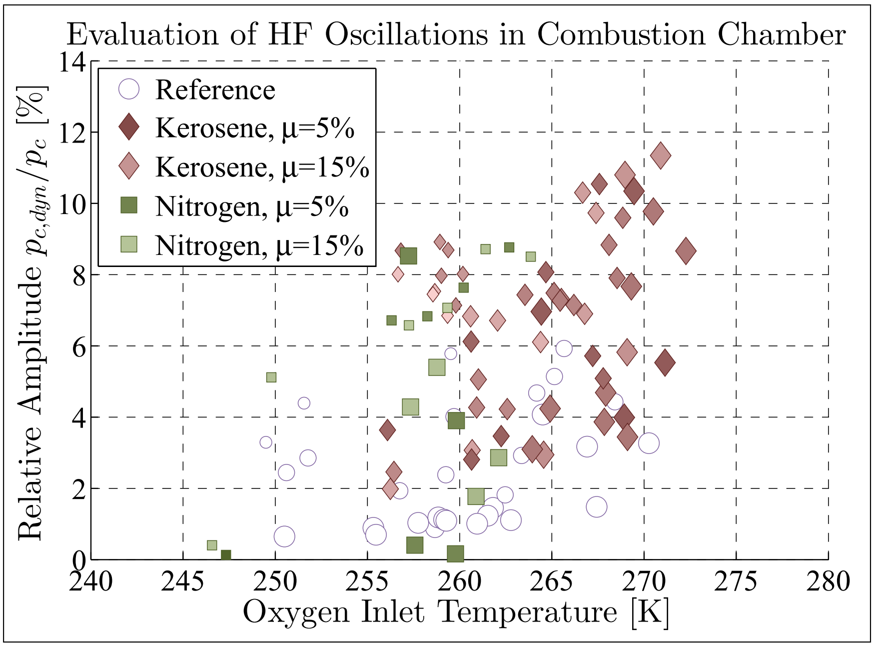

Fig. 4.15: HF Oscillations in Combustion Chamber over Oxygen Inlet Temperature (Color Brightness Encodes Film Mass Flow Ratio, Symbol Size Represents Pressure Level)

or influenced by the oxygen inlet temperature [93]. Since the rough combustion have been observed for reference and both for nitrogen and kerosene film tests, an influence of e.g. the film applicator cavity or film injection on the stability behavior could not be investigated independently. Also, data of combustion efficiency, heat transfer and film effecitveness may have been affected resulting in higher uncertainties for the film modeling [94].

4.2.4 Performance

In Fig. 4.16 and Fig. 4.17 the combustion efficiency calculated at throat conditions (cf. Eq. 3.5 et seqq.) are presented over injector mixture ratio and blowing ratio, respectively. Injector-based combustion efficiency has been calculated during analysis, but has shown values significantly higher than unity due to the non-negligible film mass flow rates. Therefore, the throat-based combustion efficiency which however assumes a fully and perfect mixture of the core gas stream and the cooling film is used for analysis.
The combustion efficiency is mainly dependent of the combustion chamber pressure as can be seen from the dashed lines calculated from the correlation presented in Tab. 4.2 for reference conditions at 2 MPa, 4 MPa and 6 MPa. Within the range investigated, the influence of the injector mixture ratio is apparently marginal. The comparison of combustion efficiency for film cooled tests with the reference tests and the correlated data shows a significantly lower efficiency for all film tests at 2 MPa (small symbols). Thereby, the tests with nitrogen feature apparently a slightly lower combustion efficiency than comparable tests with kerosene, but these differences are less than 1 % and therefore roughly in the same order of magnitude as the measurement uncertainty. No substantive relationship

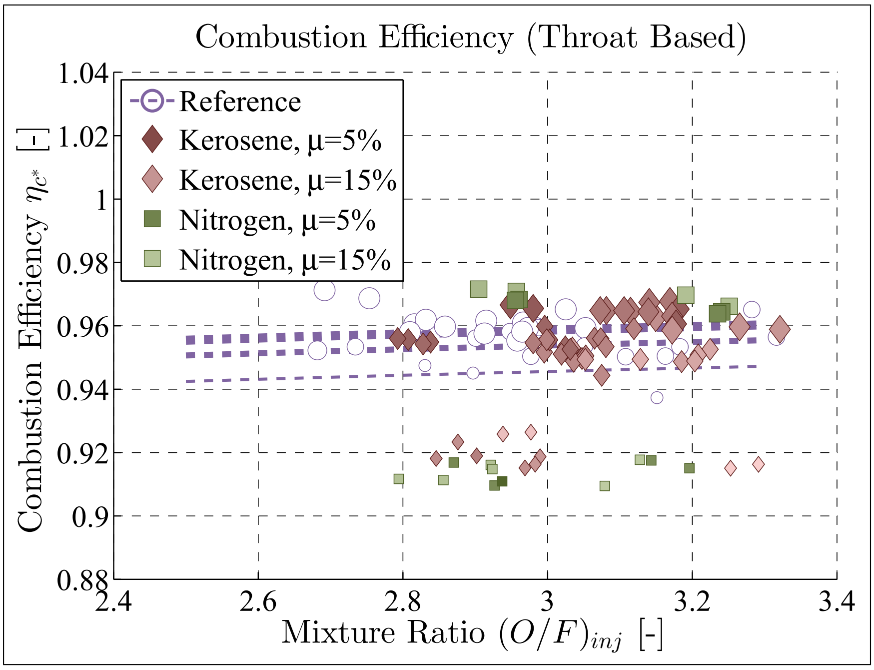

Fig. 4.16: Overview of Combustion Efficiency for Film Cooling (Color Brightness Encodes Film Mass Flow Ratio, Symbol Size Represents Pressure Level)

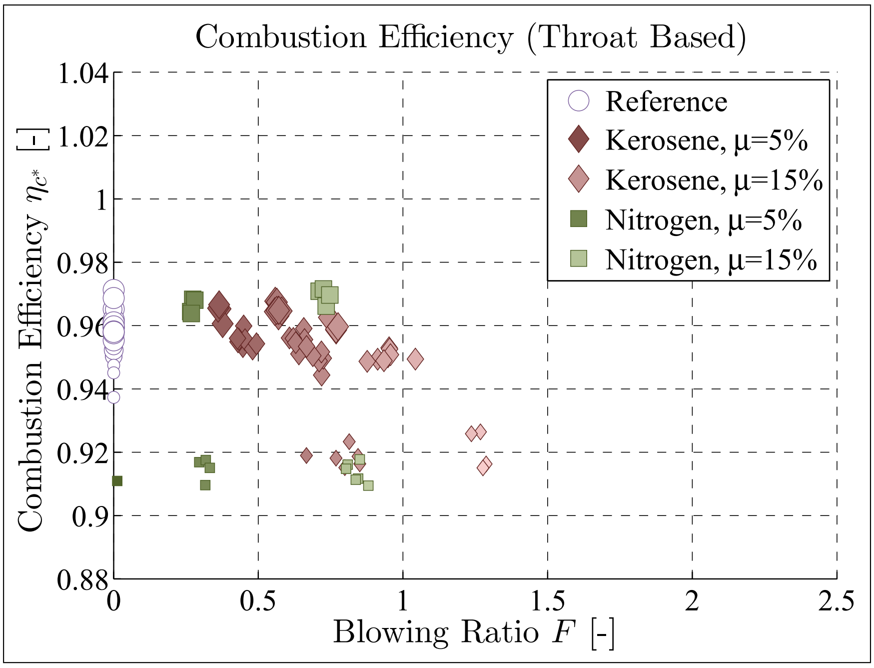

Fig. 4.17: Dependency of Combustion Efficiency from Blowing Ratio (Color Brightness Encodes Film Mass Flow Ratio, Symbol Size Represents Pressure Level)

between the combustion efficiency at 2 MPa and film fluid, film mass flow rate (brightness of colors), blowing ratio or even evaluation approach (throat, injector) could be identified suggesting that this finding is connected to the film applicator hardware although no root cause could be determined.

For tests at 4 MPa (medium sized symbols) the performance with film cooling is approximately the same as expected for tests without film cooling (best seen in Fig. 4.17). For tests at 6 MPa the performance is higher for tests with film compared to tests without. This indicates that either the effective throat area is smaller than assumed e.g. by displacement of the boundary layer by the film inflow or the theoretic characteristic velocity $c^*_{theo,th}$, which is calculated assuming a perfect mixture of gases, is too low, as in test the additional nitrogen or kerosene does not fully mix up with the core flow (compare to section 4.1.2).

Generally, the differences between different cooling mass flow rates and fluids are rather small and often within measurement accuracy. An influence of the HF oscillations is detectable but also significantly lower than 1 %. The lower combustion efficiencies for the tests at 2 MPa are non-negligible and must be carefully considered in the film cooling modeling.

4.2.5 Heat Fluxes

Averaged heat fluxes and associated root mean square values for the four water-cooled chamber segments and the water-cooled nozzle segment are given in Tab. 4.6 for the tests with kerosene film cooling and in Tab. 4.7 for nitrogen film injection. Hereby, different load cases with film (dependent of p_c, $(O/F)_{inj}$, and μ) are compared with appropriate reference cases without film cooling. For convenience, the heat fluxes are also graphically presented for the different pressure levels in Fig. 4.18 throughout Fig. 4.20 [89,94]. Hereby, the correlations for the reference cases as defined by Eq. 4.2 have been added (lilac lines).

p_c $[MPa]$	$(O/F)_{inj}$ $[-]$	μ $[\%]$	Segment 1 $[MW/m^2]$	Segment 2 $[MW/m^2]$	Segment 3 $[MW/m^2]$	Segment 4 $[MW/m^2]$	Nozzle $[MW/m^2]$
1.8	2.98	15.2	7.1 ± 0.1	6.7 ± 0.2	2.9 ± 0.1	5.9 ± 0.2	8.0 ± 0.3
1.8	3.27	22.8	7.3 ± 0.1	6.0 ± 0.1	1.9 ± 0.0	5.4 ± 0.1	7.8 ± 0.1
3.9	2.94	9.7	10.0 ± 1.2	12.6 ± 0.4	5.6 ± 1.0	10.4 ± 0.6	20.3 ± 1.1
4.0	3.07	14.6	10.3 ± 0.9	12.9 ± 0.3	4.1 ± 0.7	9.0 ± 0.9	19.3 ± 1.2
3.9	3.19	18.0	11.0 ± 0.8	13.0 ± 0.3	3.5 ± 0.4	8.8 ± 0.7	19.6 ± 0.8
6.2	2.96	7.2	13.2 ± 0.0	18.1 ± 0.4	9.6 ± 0.5	16.9 ± 1.0	32.7 ± 0.8
6.1	3.14	10.5	14.6 ± 1.5	18.3 ± 0.5	8.5 ± 1.9	15.6 ± 1.4	31.5 ± 1.0
6.2	3.23	14.9	16.2 ± 2.4	19.1 ± 0.7	5.8 ± 0.9	14.1 ± 1.7	32.7 ± 0.9
1.9	2.96	N/A	6.2 ± 1.0	6.1 ± 0.5	5.7 ± 0.3	6.0 ± 0.2	6.3 ± 1.6
4.1	2.92	N/A	8.6 ± 1.0	9.9 ± 0.9	10.7 ± 0.9	11.6 ± 1.0	17.4 ± 2.1
5.9	2.90	N/A	10.2 ± 0.9	12.5 ± 1.0	14.1 ± 1.1	15.8 ± 1.3	28.8 ± 1.7

Tab. 4.6: Experimental Heat Fluxes for Film Cooling With Kerosene (Average±RMS)

Generally speaking, heat fluxes vary from 1.8 MW/m^2 up to 38.0 MW/m^2 within the operating conditions investigated. The main driving factor for different heat fluxes is the combustion pressure. Within the test envelope, the influence of the mixture ratio is

p_c $[MPa]$	$(O/F)_{inj}$ $[-]$	μ [%]	Segment 1 $[MW/m^2]$	Segment 2 $[MW/m^2]$	Segment 3 $[MW/m^2]$	Segment 4 $[MW/m^2]$	Nozzle $[MW/m^2]$
1.8	2.90	6.1	7.2 ± 0.1	6.4 ± 0.1	5.3 ± 0.1	6.4 ± 0.0	8.9 ± 0.1
1.9	2.91	15.0	6.9 ± 0.3	6.5 ± 0.2	4.7 ± 0.1	5.8 ± 0.3	8.1 ± 0.4
1.8	3.17	6.8	7.0 ± 0.1	6.2 ± 0.2	5.1 ± 0.1	6.0 ± 0.0	8.6 ± 0.1
1.8	3.11	16.1	7.0 ± 0.1	6.3 ± 0.3	4.4 ± 0.1	5.6 ± 0.2	7.8 ± 0.4
6.2	2.96	5.6	12.2 ± 0.0	17.9 ± 0.3	15.4 ± 0.1	18.6 ± 0.1	38.0 ± 0.0
6.3	2.93	13.2	11.9 ± 0.4	18.1 ± 0.8	13.2 ± 0.2	16.8 ± 0.5	33.6 ± 1.2
5.9	3.24	5.8	15.6 ± 0.4	18.6 ± 0.2	15.8 ± 0.2	18.6 ± 0.1	34.9 ± 0.2
6.1	3.22	14.5	14.1 ± 1.1	18.8 ± 0.6	13.4 ± 0.3	16.8 ± 0.5	32.0 ± 0.7
1.9	2.96	N/A	6.2 ± 1.0	6.1 ± 0.5	5.7 ± 0.3	6.0 ± 0.2	6.3 ± 1.6
5.9	2.90	N/A	10.2 ± 0.9	12.5 ± 1.0	14.1 ± 1.1	15.8 ± 1.3	28.8 ± 1.7

Tab. 4.7: Experimental Heat Fluxes for Film Cooling With Nitrogen (Average±RMS)

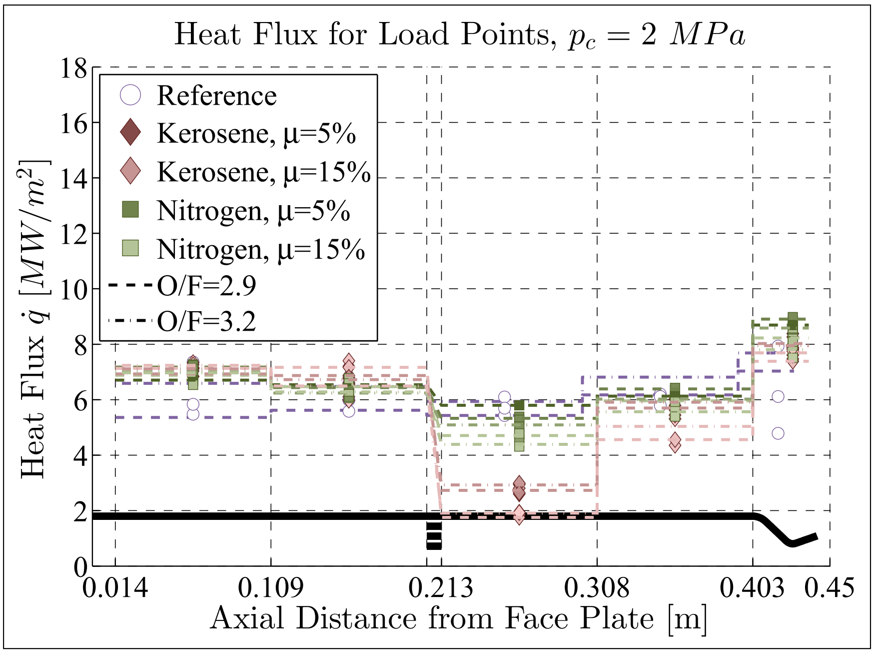

Fig. 4.18: Heat Flux as Function of Axial Position (p_c = 2 MPa – Color Brightness Encodes Film Mass Flow Ratio, Symbol Size Represents Pressure Level)

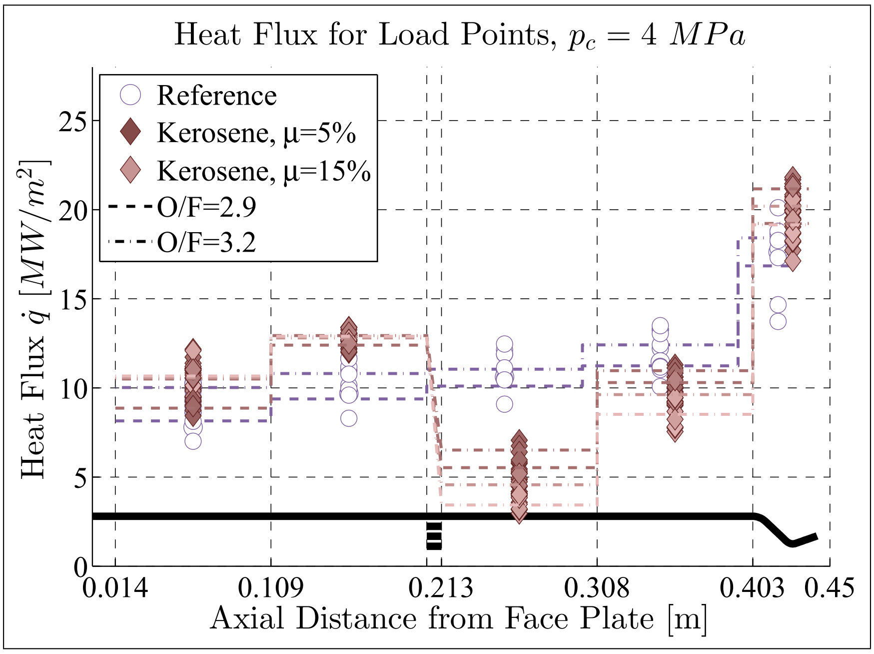

Fig. 4.19: Heat Flux as Function of Axial Position (p_c = 4 MPa – Color Brightness Encodes Film Mass Flow Ratio, Symbol Size Represents Pressure Level)

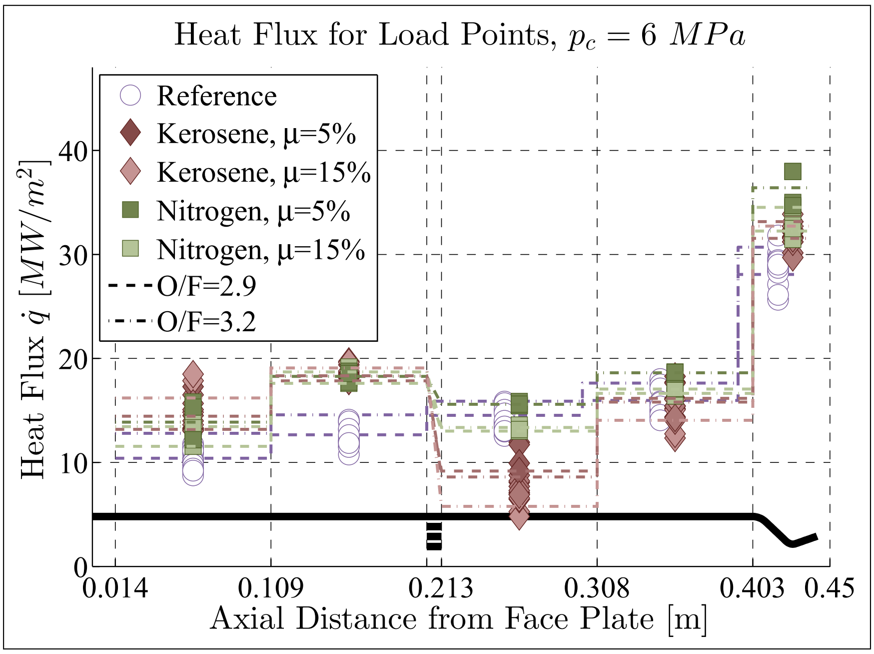

Fig. 4.20: Heat Flux as Function of Axial Position (p_c = 6 MPa – Color Brightness Encodes Film Mass Flow Ratio, Symbol Size Represents Pressure Level)

approximately in the same order as the heat flux uncertainties are (approx. 10 %). As expected, higher film coolant mass flow rates lead to lower heat fluxes in the third and in some parts in the fourth chamber segment, but hardly in the nozzle segment. Unexpectedly, the heat fluxes in the first and second segment, which are not film cooled, are higher than in appropriate reference tests. Since an influence of the film injection on the pressure level and the heat soak back of the uncooled film applicator on the neighboring water-cooled segments can only partly be accounted, the heat flux increase most likely originates from the rough combustion observed in the film cooling tests.

For tests at 2 MPa (see Fig. 4.18) the reproducibility of all film tests is better than 7.5 % albeit the heat flux in the first and partly second segment is slightly higher than expected from the heat flux correlations and the reference tests. For nitrogen film cooling the heat flux is approximately 5 to 30 % lower than reference for the third, but rather the same or higher for the fourth and nozzle segment. For kerosene film cooling the heat flux is decreased up to 70 % in the third segment, but the heat flux quickly increases in the fourth and nozzle segment.

For tests at 4 MPa, which were conducted with kerosene film only, a clear stepping between the different mass flow rates is visible (Fig. 4.19). The heat fluxes are up to 70 % lower in the third and up to 30 % lower than reference in the fourth segment. The heat fluxes in the nozzle segment are roughly in the same order of magnitude as the reference tests, but the heat fluxes in the in segments upstream of the film applicator are unusually high.

For 6 MPa (shown in Fig. 4.20) the heat fluxes in the first and second segment are also significantly higher than expected from the reference data. For low nitrogen mass flow rates the heat flux in the third and fourth segment roughly agrees with the data from the case without film cooling. For higher nitrogen mass flows the heat flux is lowered by approximately 10 % in the third segment. For kerosene the heat flux is lower up to 60 % compared to the reference for the third and up to 10 % for the fourth segment. For the nozzle even higher than reference heat fluxes are observed.

The heat fluxes, additionally to hot wall temperature measurements, are used to assess the film cooling effectiveness. This topic will be discussed in section 4.2.7.

4.2.6 Wall Temperatures

The hot wall temperature measurements using thermocouples flush-mounted with the hot chamber wall are presented in this section. These measurements have a higher spatial resolution than the heat flux measurements but suffer from limited accuracy due to local soot depositions, mounting tolerances and the high thermal and mechanical loads leading to degrading and failure of the thermocouples. Therefore, temperature deviation averages up to 20 %. The measured wall temperatures are graphically presented over the engine axis for different load cases in Fig. 4.21 to Fig. 4.23. Hereby, the temperatures vary from 328 K up to 871 K. These data are used to assess the film cooling efficiency Θ (see Eq. 2.69).

For tests at 2 MPa the hot wall temperatures are generally quite low. The data scatter is low (mostly less than 3 %) leading to a good reproducibility of the results. However, mounting tolerances are visible as the mean temperatures deviate from the virtual temperature progression determined by least square method (dashed and chain dotted lines). This is best seen in the second segment where the thermocouples at 146.5 mm and 166.0 mm differ constantly by 50 K. A steady temperature increase is apparent from the film applicator up to the last temperature measurement indicating a decreasing cooling effectiveness.

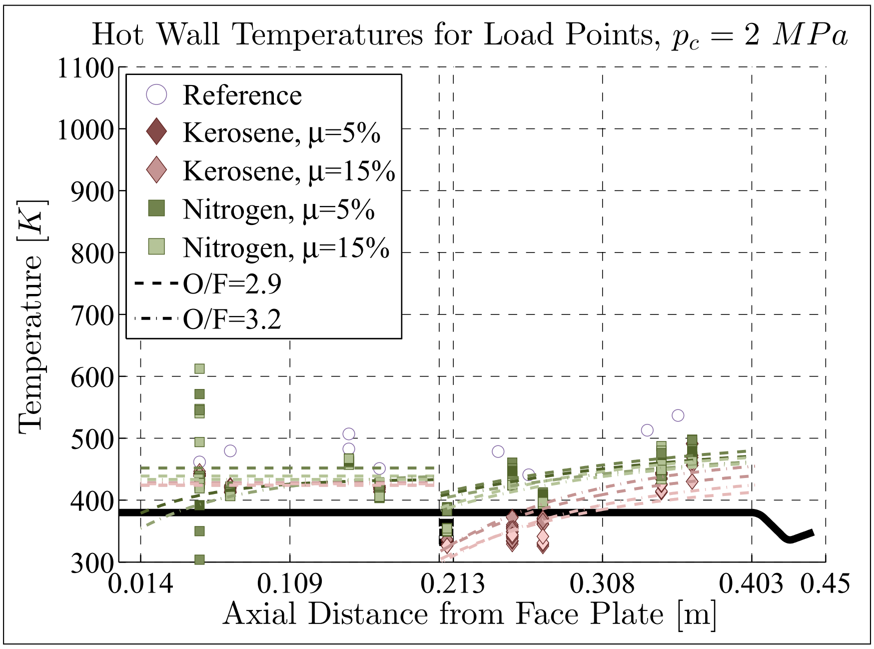

Fig. 4.21: Hot Wall Temperature as Function of Axial Position (p_c = 2 MPa – Color Brightness Encodes Film Mass Flow Ratio)

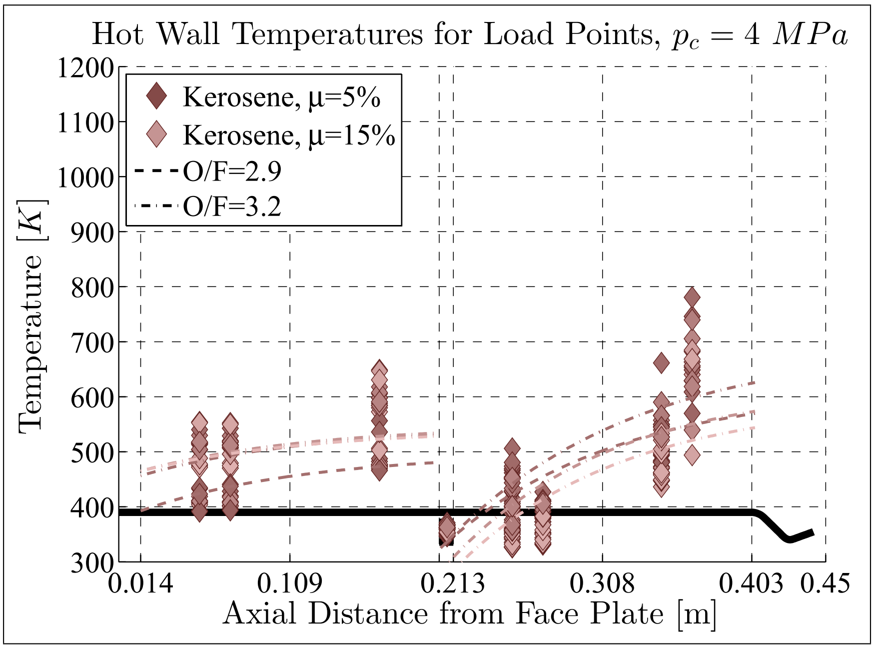

Fig. 4.22: Hot Wall Temperature as Function of Axial Position (p_c = 4 MPa – Color Brightness Encodes Film Mass Flow Ratio)

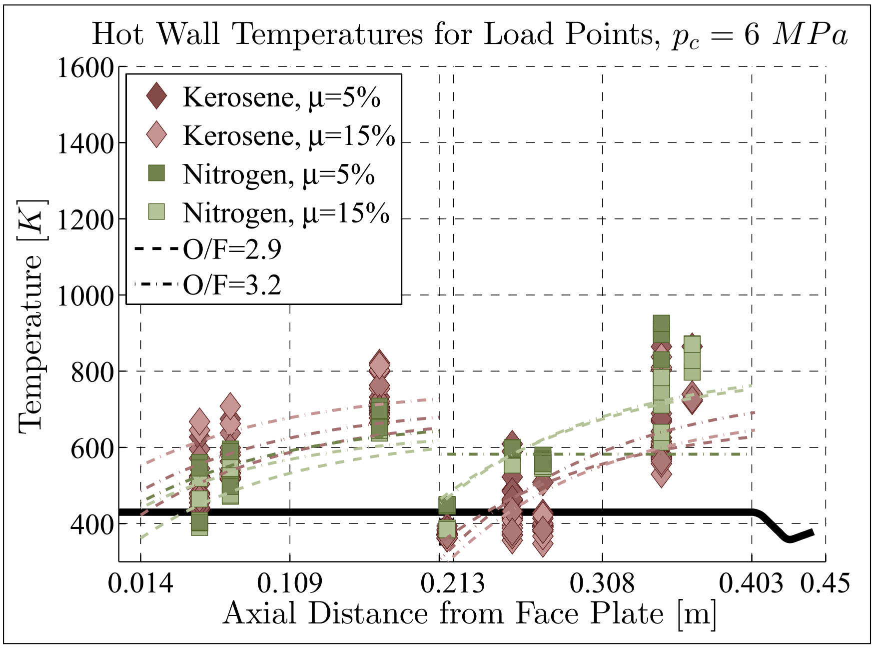

Fig. 4.23: Hot Wall Temperature as Function of Axial Position (p_c = 6 MPa – Color Brightness Encodes Film Mass Flow Ratio)

A liquid cooling film of up to 60 mm length exists for high kerosene mass flow rates as the wall temperatures at the 250.5 mm and 270.0 mm mesuring positions remain constant and near film inlet temperature TF3 (at 211 mm).

A slightly higher data scatter (approx. up to 12 %) exists for the tests at 4 MPa. This especially applies to the measurements upstream of the film applicator. A liquid kerosene film exceeding 60 mm is obervable. A cooling-down of the injected film by the water-cooling is apparent for some load points. The film seems to quickly dissolve in the fourth segment.

The hot wall temperature measurements at 6 MPa show a high scattering (partly exceeding 20 %). Either the high HF oscillation amplitudes or the challenging thermal and mechanical loads had a negative impact on the accuracy of the temperature measurement. For nitrogen hardly any film effect is identifiable. A noticable film cooling effect is still detectable for kerosene 60 mm downstream of the film applicator.

4.2.7 Evaluation of Film Cooling Effectiveness

Two approaches to assess the film cooling efficiency have been investigated within the film cooling test campaign in the past [89]. Firstly, the changing of the heat fluxes, which are measured by the coolant heat up of the water-cooled chamber segments, was evaluated. These data yield a high accuracy but the spatial resolution is limited by the chamber segment length (i.e. 95 mm). Secondly, the wall temperature measurements using thermocouples flush-mounted with the hot chamber wall have been used to determine the so-called cooling efficiency Θ. The hot wall temperature measurements have a higher spatial resolution but suffer on limited accuracy due to mounting tolerances and the high thermal and mechanical loads leading to degrading and failure of the thermocouples.

The cooling effectiveness as ratio of the heat fluxes with and without film cooling is presented in Fig. 4.24 to Fig. 4.26 with respect to film coolant mass flow rate. Thereby, the heat flux correlations (compare to Eq. 4.2) have been used as reference for the heat flux without film but corrected by the ratio of actually measured and predicted heat flux in the second segment in order to take the increased heat transfer by the rough combustion into account (cf. section 4.2.5). Due to the definition of the heat flux based cooling efficiency "$1-(\dot{q}_{cool}/\dot{q}_{corr})$" this approach may sometimes lead to negative values. Generally speaking, the assessment of a cooling effectiveness basing on heat flux shows a plausible behavior although the film cooling effect seems to be smeared by the relatively long segment length.

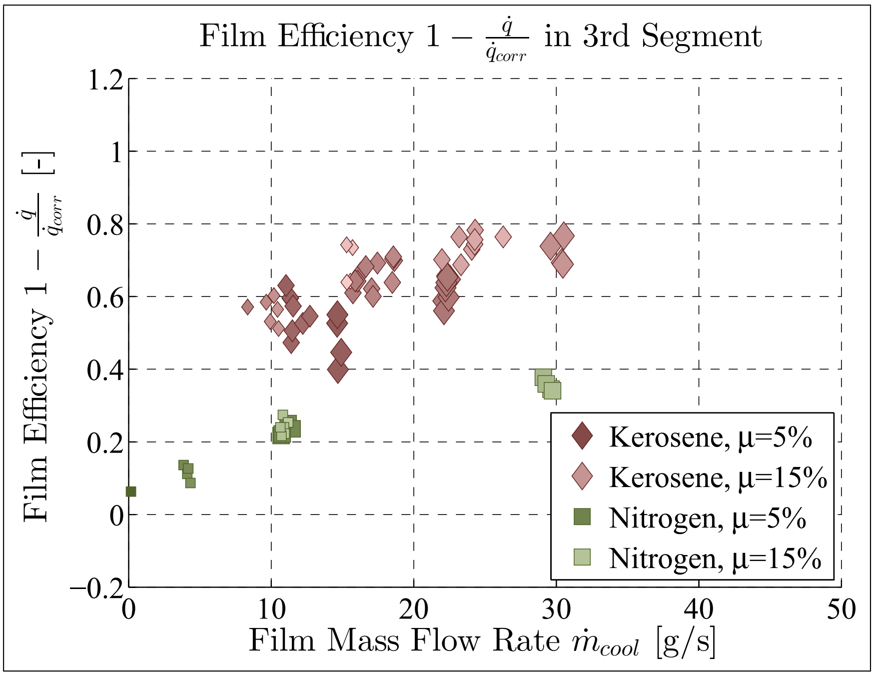

Fig. 4.24: Film Efficiency (based on Heat Flux Correlation) in 3rd Segment (Color Brightness Encodes Film Mass Flow Ratio, Symbol Size Represents Pressure Level)

The effectiveness of nitrogen film cooling is apparently moderate for the third segment (up to approx. 100 mm after film injection, Fig. 4.24) and low in the fourth segment (approx. 100 mm up to 190 mm after film injection, Fig. 4.25) within the mass flow rates investigated. For the conducted tests and pressures, comparable nitrogen mass flow led to roughly similar heat flux reductions. The same trend applies to the tests with kerosene albeit the heat flux reduction by kerosene film is significant in the third segment and still remarkable in the fourth segment. For the nozzle segment in Fig. 4.26 the results are less clear and reliable. Only a low film cooling effect seems to persist and cooling efficiency is for all tests at 2 MPa near or even below zero. This indicates that for this conditions the near-throat boundary layer thus the heat transfer in the nozzle is negatively affected by the film inflow albeit measurements in the nozzle are less reliable than in the chamber.

The cooling efficiency Θ (see Eq. 2.69) determined using available hot wall temperature

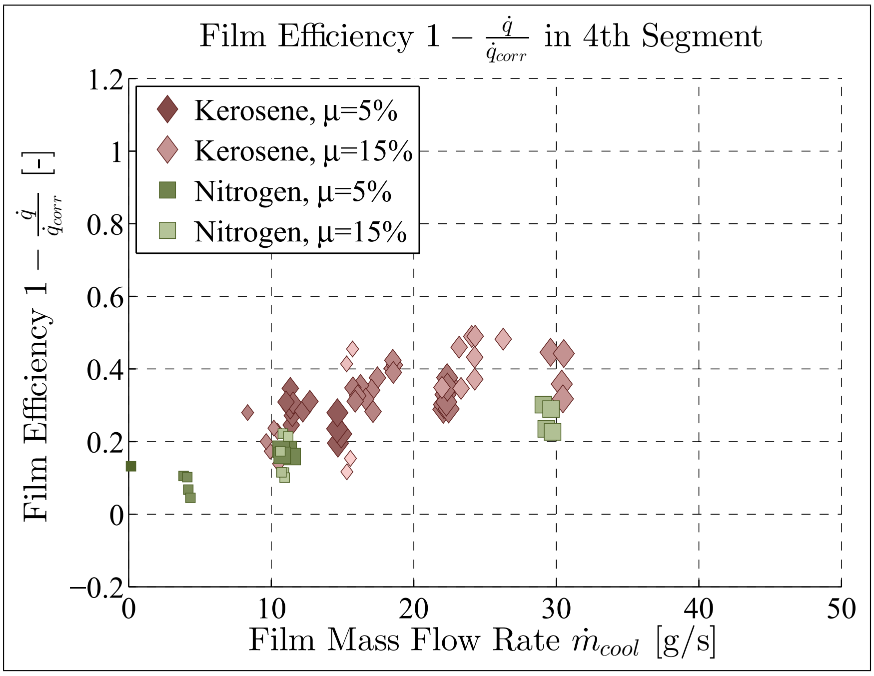

Fig. 4.25: Film Efficiency (based on Heat Flux Correlation) in 4th Segment (Color Brightness Encodes Film Mass Flow Ratio, Symbol Size Represents Pressure Level)

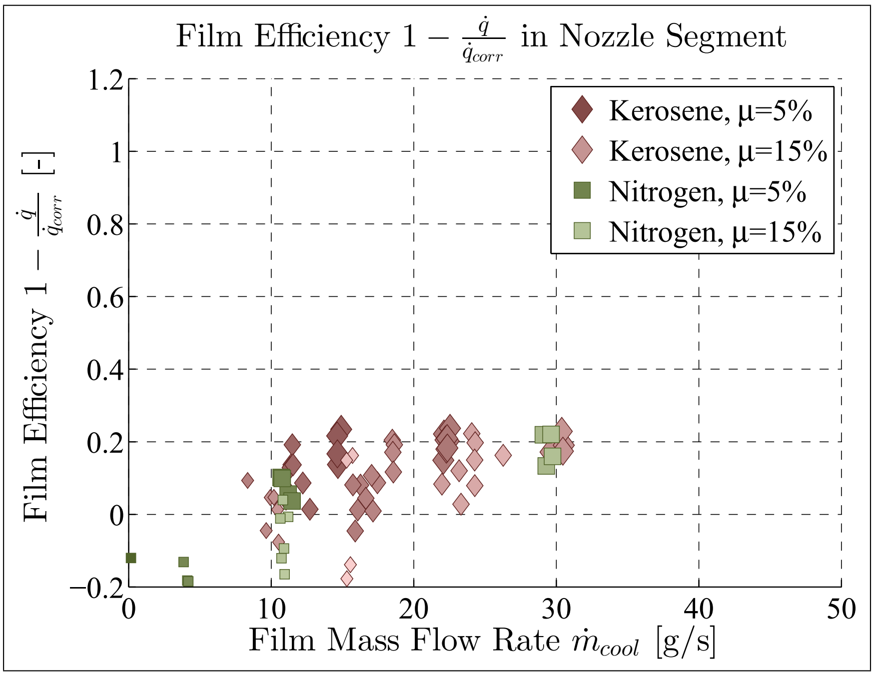

Fig. 4.26: Film Efficiency (based on Heat Flux Correlation) in Nozzle Segment (Color Brightness Encodes Film Mass Flow Ratio, Symbol Size Represents Pressure Level)

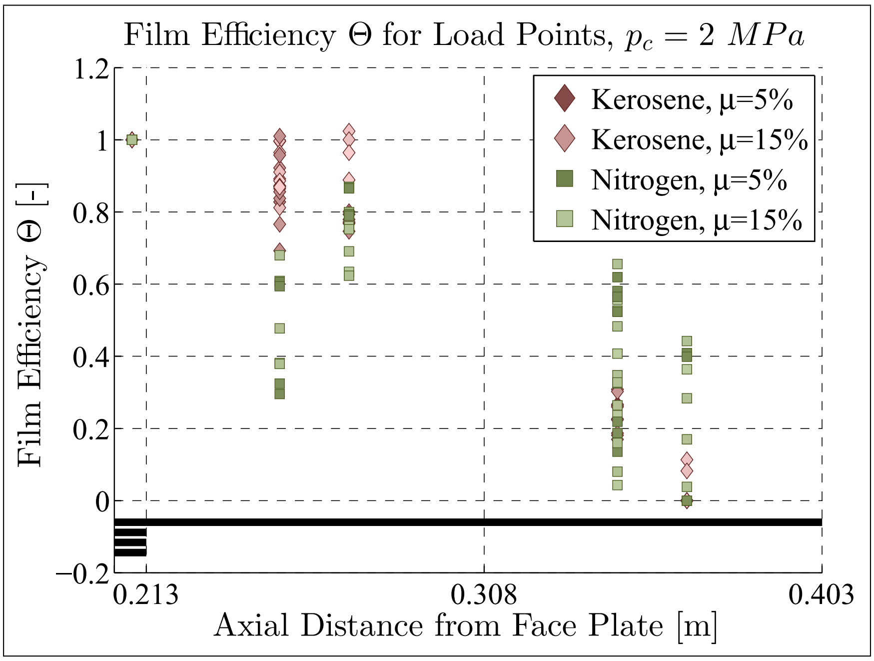

Fig. 4.27: Film Efficiency Θ over Axial Position ($p_c = 2$ MPa – Color Brightness Encodes Film Mass Flow Ratio)

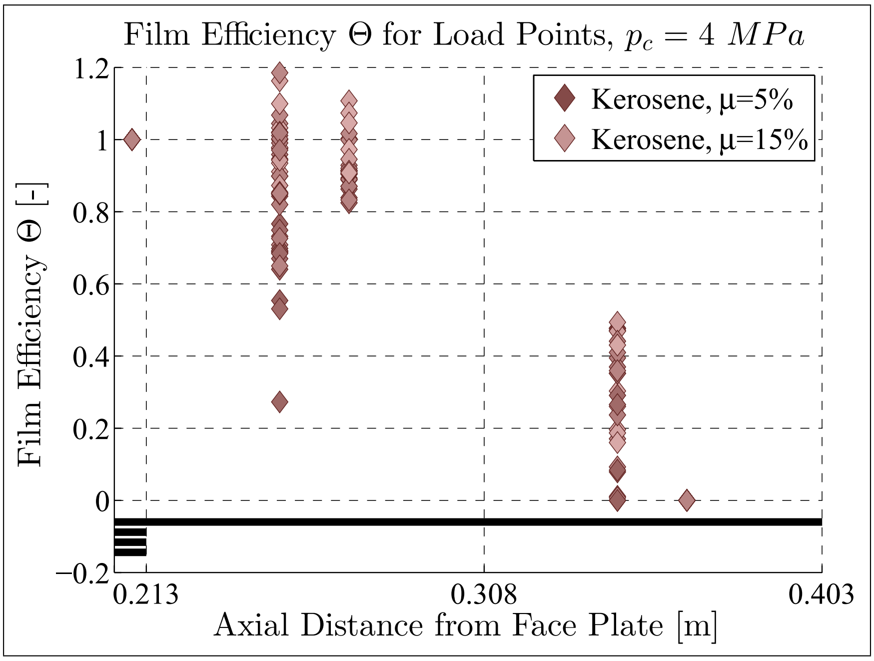

Fig. 4.28: Film Efficiency Θ over Axial Position ($p_c = 4$ MPa – Color Brightness Encodes Film Mass Flow Ratio)

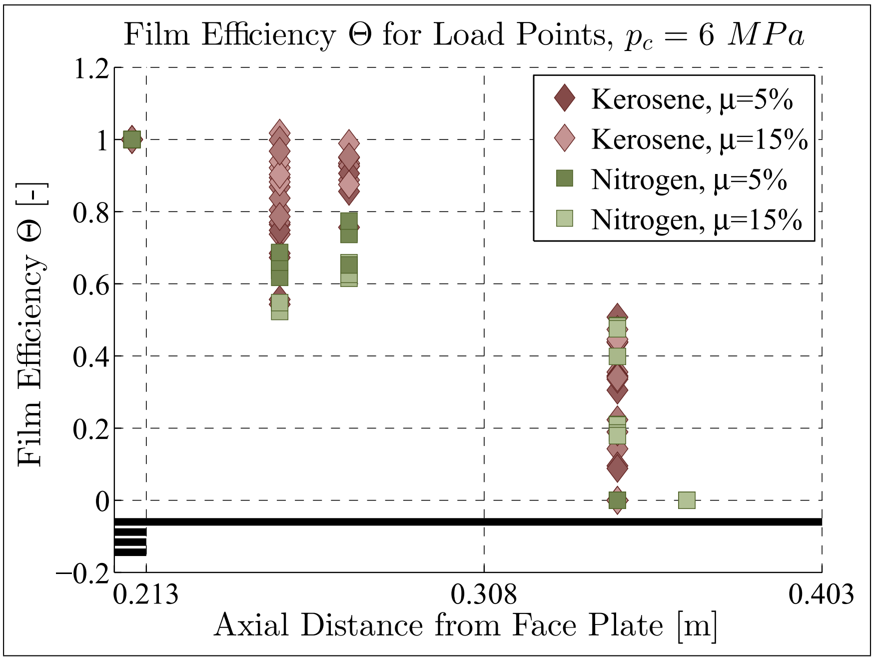

Fig. 4.29: Film Efficiency Θ over Axial Position (p_c = 6 MPa – Color Brightness Encodes Film Mass Flow Ratio)

measurements is shown in Fig. 4.27 to Fig. 4.29 over the engine axis. As stated in Eq. 2.69, the hot wall temperature without any film cooling, which is used as reference, is of great importance and has been derived as the hottest wall temperature measured in the combustion chamber here.

For the fourth segment the results from heat flux based and wall temperature based assessment of cooling effectiveness are roughly in the same order of magnitude. In the third segment the cooling effectiveness on heat flux data are significantly lower than the wall temperature based data. With respect to spatial resolution this indicates high gradients within the third combustion chamber segment.

4.3 Transpiration Cooled CMC

4.3.1 Test Objectives

The load points (combinations of combustion pressure and mixture ratio) of tests conducted within the transpiration cooling test campaign are shown in Fig. 4.30. Thereby, experiments with one material sample each of C/C, WHIPOX and OXIPOL have been performed [90]. As anchor and run-in load point for the investigations a mixture ratio of 1.8 at 2 MPa has been chosen. Additionally, tests with C/C and kerosene cooling have been performed at the mixture ratio 2.4/ 2 MPa and mixture ratio 3.2/ 2 MPa. Since the tests at low mixture ratios result in a heavy soot deposition, the tests with the OXIPOL sample have been conducted at mixture ratio 3.2 but 1 MPa instead.

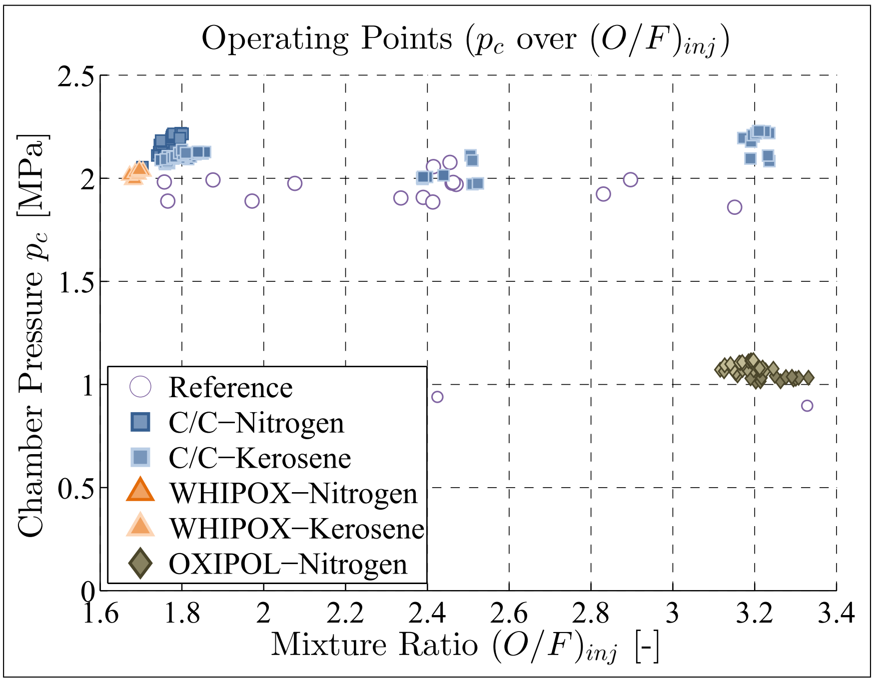

Fig. 4.30: Overview of Load Points Investigated in Transpiration Cooling Campaign (Color Brightness Encodes Blowing Ratio)

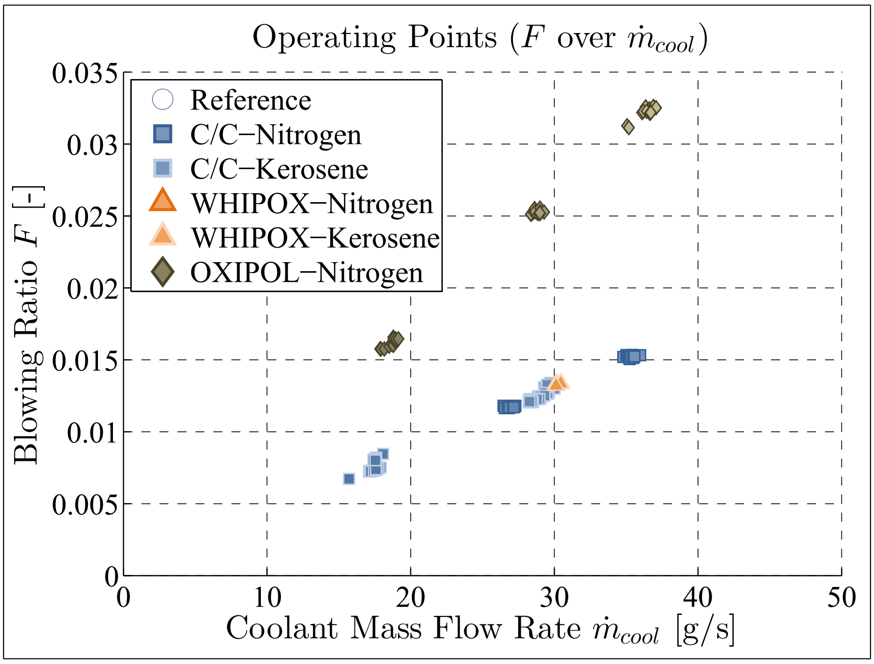

Fig. 4.31: Blowing Ratio over Coolant Mass Flow in Transpiration Cooling Tests (Symbol Size Represents Pressure Level)

The transpiration mass flow rates as well as corresponding blowing ratios are presented in Fig. 4.31. The blowing ratios are mostly comparable between the tests with C/C and WHIPOX both for kerosene and nitrogen cooling. Only the tests with OXIPOL feature a significant higher blowing ratio since these tests have been conducted at a different combustion chamber pressure but with identical overall mass flow rates as the other test samples. The test campaign has been impacted by problems due to a difficult environment for the measurements and a lack of maturity of the manufacturing process of the CMC samples itself. This led to an early failure of the test specimens and uncertain solid properties.

4.3.2 Combustion Oscillations

The peak HF amplitudes with respect to the frequencies are given for the dynamic chamber pressure in Fig. 4.32. An excessive (i.e. higher than 5 %) pressure amplitude can be found for the reference tests without CMC only. Otherwise, no significant HF oscillations are observable. Also no obvious dependency of the HF oscillations from the blowing ratio has been found (see Fig. 4.33). Since the conditions of e.g. the injection have been similar to the one of the film cooling test campaign where a very rough combustion has been detected, all applied CMC samples seemingly feature a kind of damping capacity.

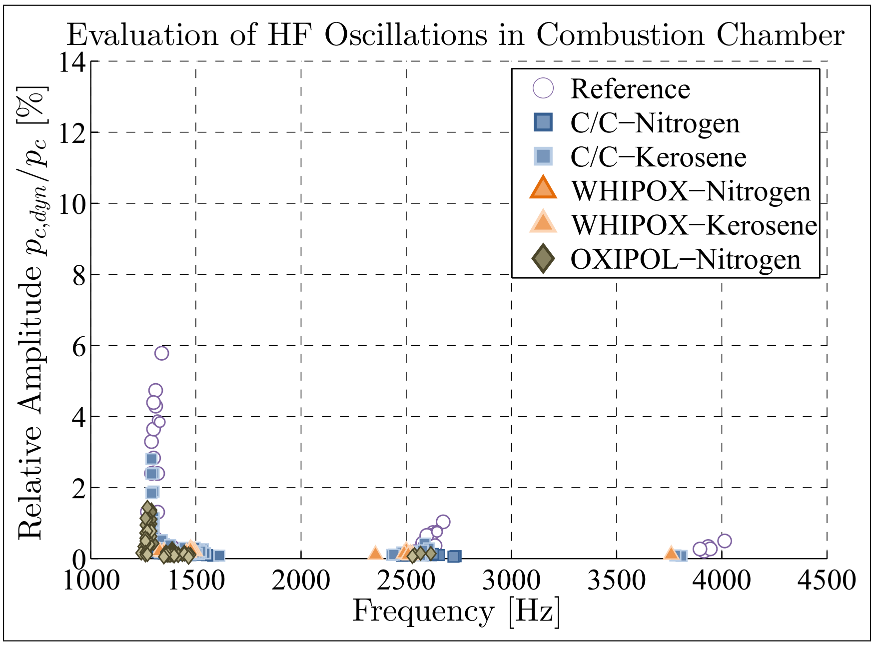

Fig. 4.32: HF Amplitudes in Combustion Chamber as Function of Frequency (1st to 4th peak only – Color Brightness Encodes Blowing Ratio, Symbol Size Represents Pressure Level)

The peak LF amplitudes in the combustion chamber with respect to the associated frequencies are given in Fig. 4.34. In a rocket combustion chamber, LF oscillations usually occur if the pressure drop over the injector is very low. In general, no noteworthy tendency for LF oscillation can be found excluding for two exceptions: tests with OXIPOL as well as some tests with C/C and coolant kerosene.

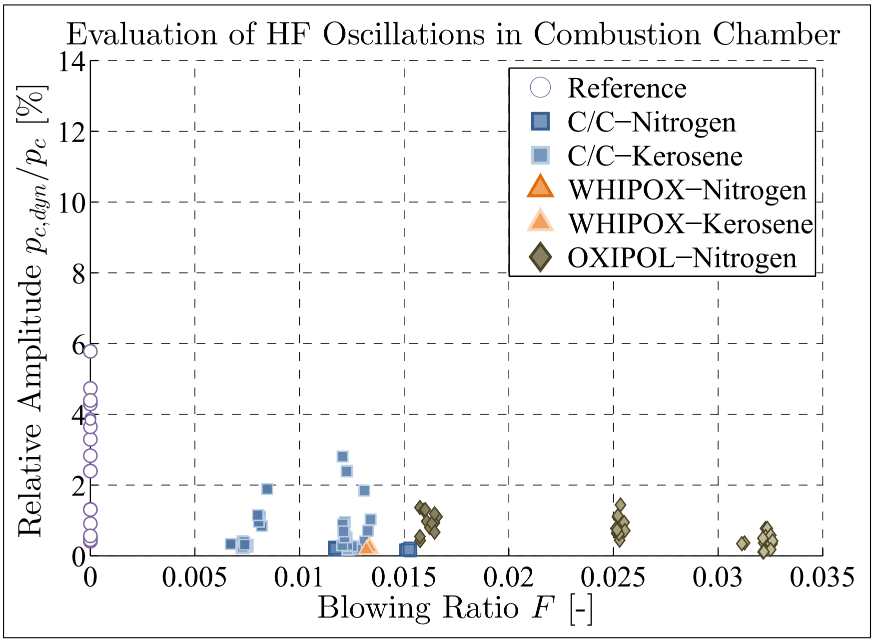

Fig. 4.33: HF Amplitudes in Combustion Chamber as Function of Blowing Ratio (Symbol Size Represents Pressure Level)

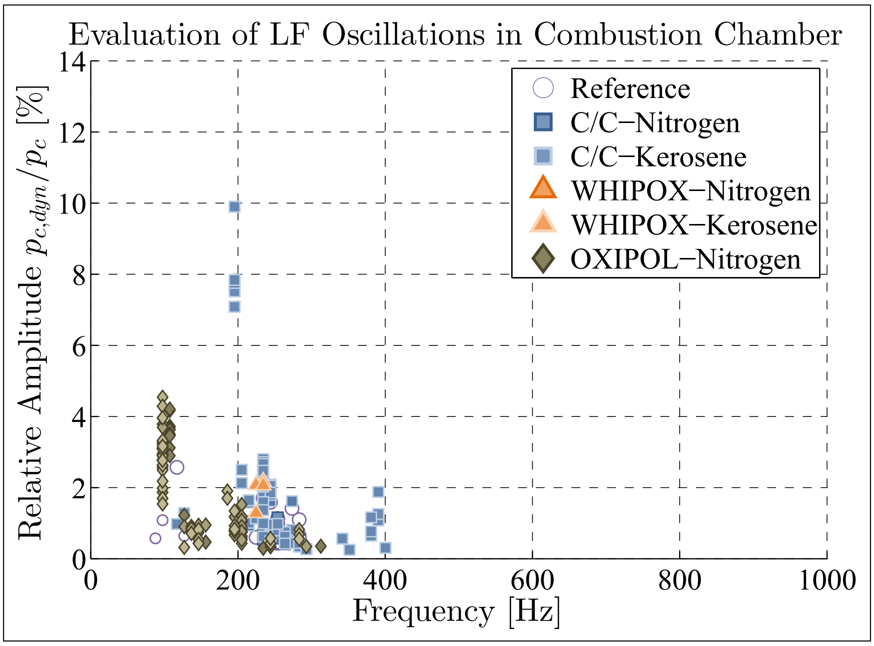

Fig. 4.34: LF Amplitudes in Combustion Chamber as Function of Frequency (1st to 4th peak only – Color Brightness Encodes Blowing Ratio, Symbol Size Represents Pressure Level)

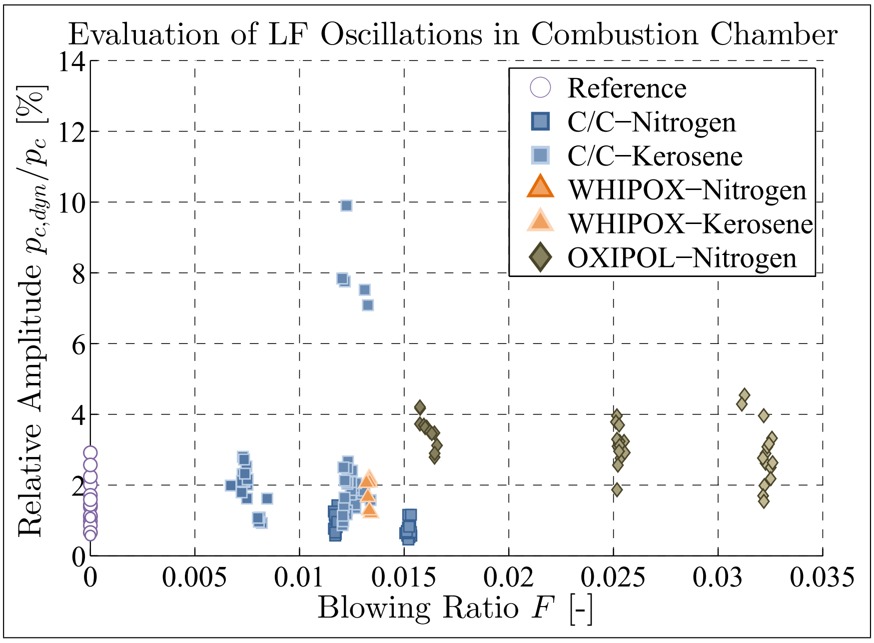

Fig. 4.35: LF Amplitudes in Combustion Chamber as Function of Blowing Ratio (Symbol Size Represents Pressure Level)

For the test with OXIPOL different operating conditions i.e. a mixture ratio of 3.2 at 1 MPa instead of mixture ratio 1.8 at 2 MPa have been applied. Due to the low combustion pressure and the relatively oxidizer-rich load point, the kerosene mass flow rate was quite low leading to smaller than usual pressure losses in the injector assembly. These low pressure losses, which have been in the order of 5 % of the combustion chamber pressure only, abetted LF oscillations in the injector kerosene feed line and subsequently in the combustion chamber itself at 117 Hz in the order of 5 % of the mean combustion chamber pressure. However, these oscillations had no major effect on the tests conducted and do not need to be considered in the modeling.

For the tests with C/C and coolant kerosene a labile LF oscillation was found at 195 Hz with a relative amplitude up to 13 % in the kerosene feed system and up to approximately 10 % in the combustion chamber. A detailed analysis has indicated that the LF oscillation has its origin in the test sample kerosene feed line or the CMC manifold itself where a feed pressure fluctuation of approximately 0.3 MPa at a rate of aforementioned 195 Hz has been detected. Although the fluctuation may be linked to some local burnouts of the test sample, the mechanism of the excitation was not clearly identified.

4.3.3 Performance

The combustion efficiency of the experiments performed is presented in Fig. 4.36 and Fig. 4.37, whereas the evaluation of the combustion efficiency with respect to the mixture ratio is given in Fig. 4.36 and the combustion efficiency with respect to the blowing ratio F is shown in Fig. 4.37, respectively. Since the data base is limited especially for tests with WHIPOX and OXIPOL and the performance calculation is affected by the problems described in 3.4.2 (e.g. combustion efficiency greater than unity because of unknown effective throat sectional area and existence of unburnt fuel), no final conclusion should be drawn. However, tendencies are clearly visible.

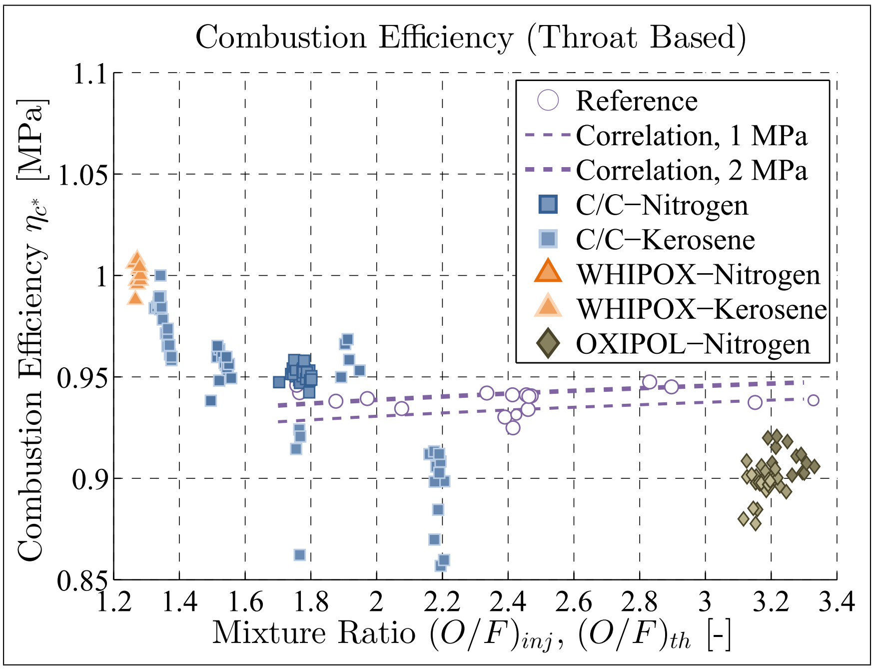

Fig. 4.36: Overview of Combustion Efficiency for Transpiration Cooling ($(O/F)_{th}$ for kerosene, $(O/F)_{inj}$ for nitrogen – Color Brightness Encodes Blowing Ratio, Symbol Size Represents Pressure Level)

For tests with nitrogen transpiration cooling at low mixture ratios and moderate pressures i.e. mixture ratio 1.8 and 2 MPa the transpiration cooling apparently has only a minor effect on combustion efficiency and results in a slight increase of combustion efficiency compared to reference data probably due to higher turbulence thus better mixing. Likewise for tests with kerosene transpiration cooling at the same mixture ratio and pressure the combustion efficiency seems to be slightly increased by higher transpiration mass flow rates, but the evaluation of combustion efficiency is generally error-prone at such low mixture ratios. Also the effect is overlaid with a significant scatter for the tests with C/C and kerosene, which is linked to the LF oscillations observed (see section 4.3.2).
The tests with C/C with kerosene at injector mixture ratio 3.2/ 2 MPa (corresponds to $(O/F)_{th} \approx 2.2$) as well as OXIPOL with nitrogen at 3.2/ 1 MPa show that combustion efficiency has been significantly lowered by transpiration mass flow at higher mixture ratios due to the unfavorable injector operating conditions and extensive inflow of coolant whereas the tests with OXIPOL even clearly give a correlation between transpiration mass flow rate and combustion efficiency for the given load point and coolant (Fig. 4.37).

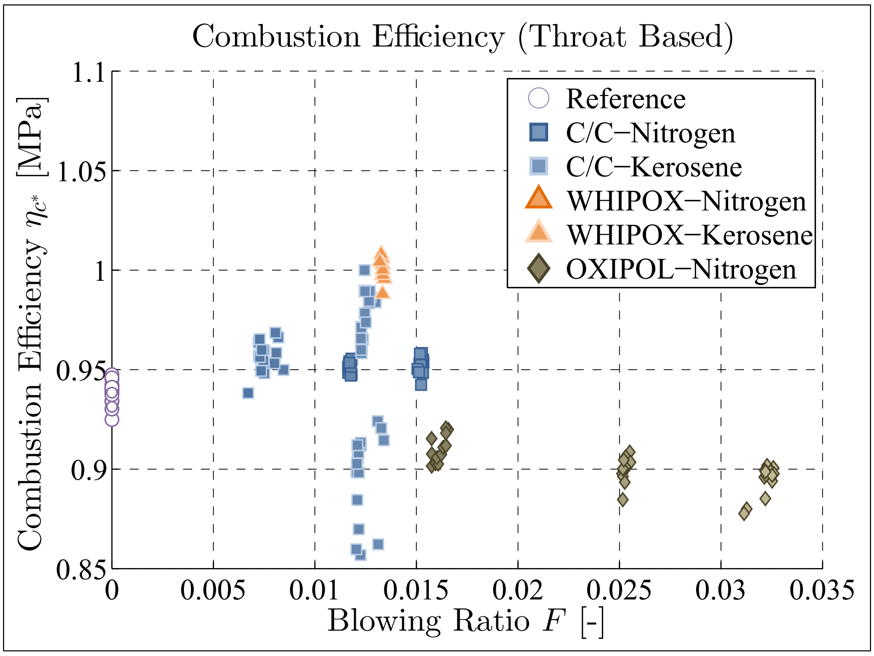

Fig. 4.37: Influence of Blowing Ratio on Combustion Efficiency (Color Brightness Encodes Blowing Ratio, Symbol Size Represents Pressure Level)

4.3.4 Heat Flux

The heat flux with respect to the distance from face plate is presented in Fig. 4.38 and Fig. 4.39. The CMC test samples replaced segment 3, allowing further assessment of downstream flow conditions by the water heat up in the fourth and nozzle segment. The tests at 1 MPa (Fig. reffig:ExpTransQAZ1) comprise the experiments with the OXIPOL and nitrogen only. The heat fluxes of the tests with at 2 MPa and variable mixture ratio are shown in Fig. 4.39 alongside appropriate reference test and correlated heat fluxes.

For tests with nitrogen heat flux is almost the same or slightly higher for WHIPOX and moderately higher for C/C than for the adequate reference test. Otherwise the heat flux is slightly lower for the tests of C/C with kerosene. The latter finding is also true for the tests at 2.4/ 2 MPa and 3.2/ 2 MPa where a significant film effect and resulting heat flux decrease can be found for the downstream fourth segment whereas the heat flux in the nozzle segment is only slightly lower and almost comparable in value to the reference test. Subsequently, the tests with OXIPOL and nitrogen at 3.2/ 1 MPa show a comparable behavior, although the heat flux seems to be notedly lower than in the reference test for the nozzle segment.

The heat flux with respect to the blowing ratio F is shown in Fig. 4.40 to Fig. 4.43. Due to the limited data base no quantitative conclusion can be drawn, but the tendencies are clearly visible. For all test samples being tested at different transpiration cooling mass flow rates i.e. C/C with kerosene and the OXIPOL test sample with nitrogen a more or less decreased heat flux can be observed at the downstream fourth chamber segment and the nozzle segment for an increased coolant mass flow.

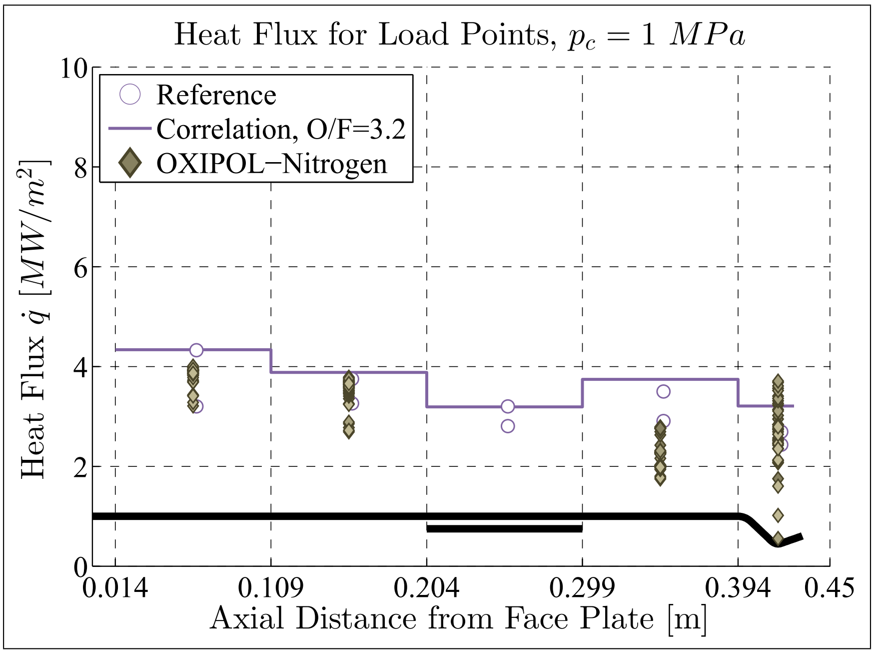

Fig. 4.38: Heat Flux over Axial Position (p_c = 1 MPa – Color Brightness Encodes Blowing Ratio)

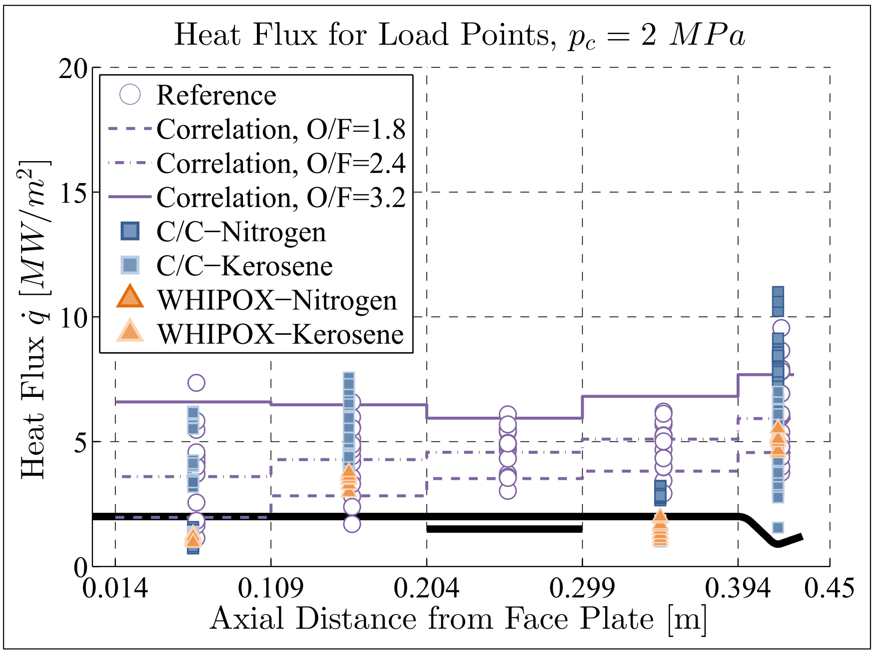

Fig. 4.39: Heat Flux over Axial Position (p_c = 2 MPa – Color Brightness Encodes Blowing Ratio)

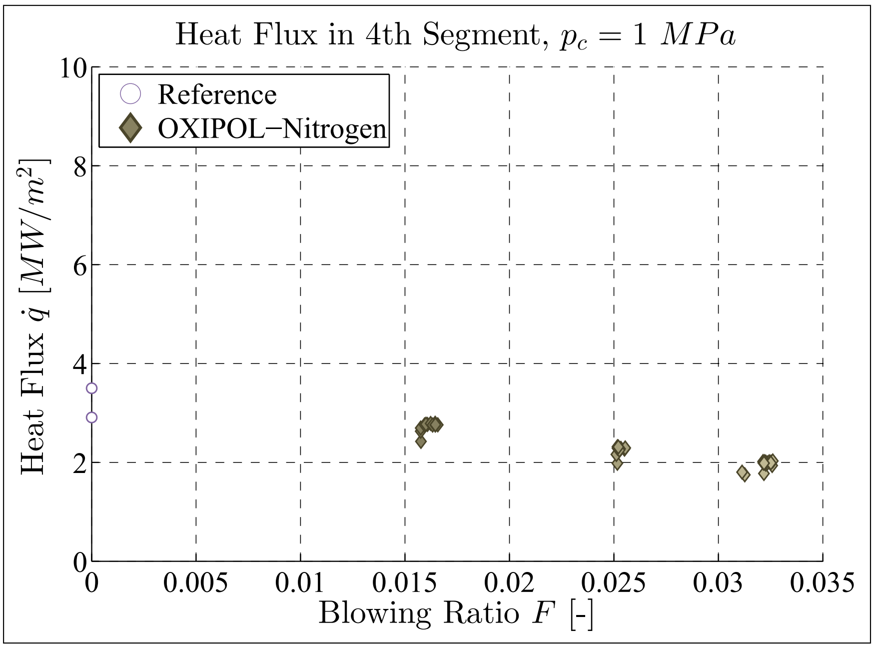

Fig. 4.40: Influence of Blowing Ratio on Heat Flux (4th Segment, $p_c = 1$ MPa)

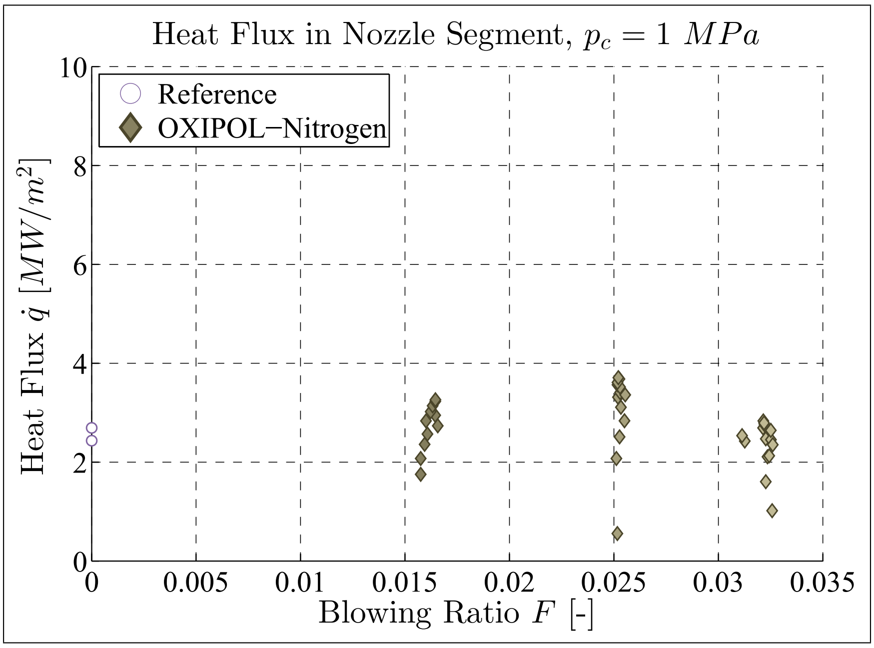

Fig. 4.41: Influence of Blowing Ratio on Heat Flux (Nozzle, $p_c = 1$ MPa)

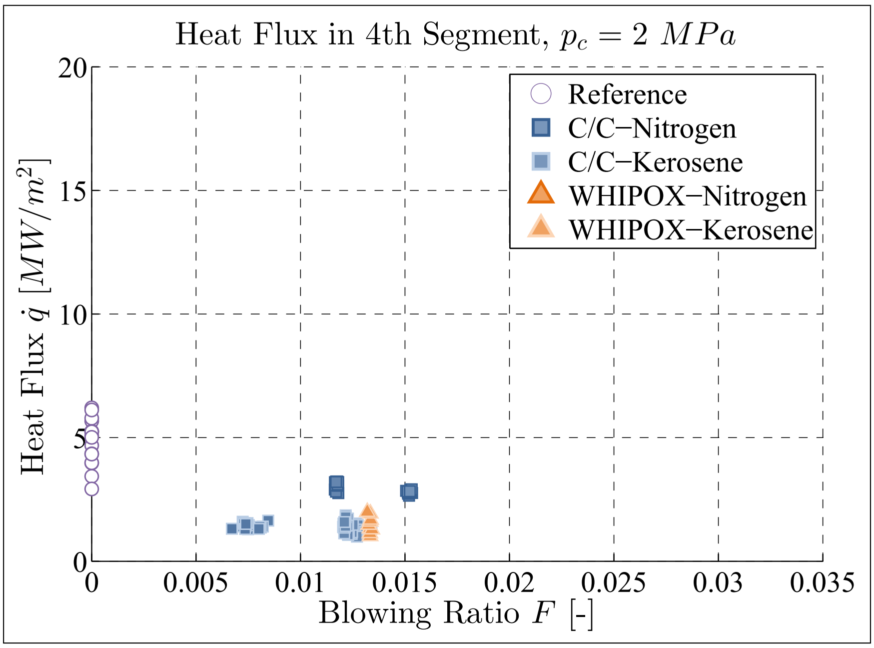

Fig. 4.42: Influence of Blowing Ratio on Heat Flux (4th Segment, $p_c = 2$ MPa)

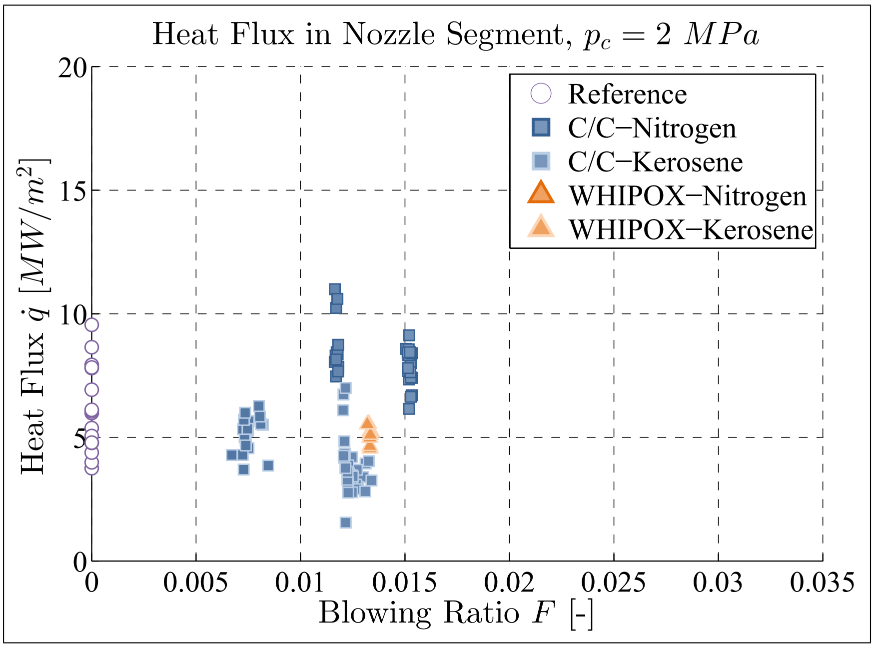

Fig. 4.43: Influence of Blowing Ratio on Heat Flux (Nozzle, $p_c = 2$ MPa)

4.3.5 Hot Wall Temperature Measurements

Wall temperature measurements of the water-cooled chamber segment downstream of the CMC segment have initially not been foreseen but have been installed after a change of the test sample configuration. Although the measured wall temperatures are subject of discussions regarding accuracy and reliability, they can serve as additional source of information.

The hot wall temperatures measured by thermocouples flush-mounted with the inner chamber wall are presented in Fig. 4.44 and Fig. 4.45. A comparison of the hot wall temperatures and the heat fluxes shows a good agreement between these two measuring techniques with respect to overall behavior and trends. These temperature measurements are therefore used as an additional source of validation for simulations.

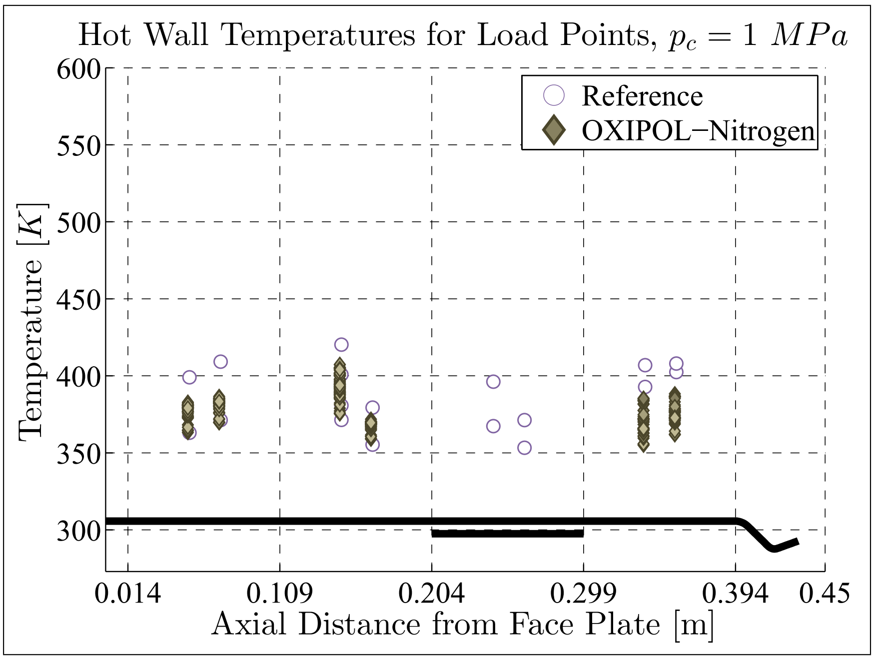

Fig. 4.44: Hot Wall Temperature over Axial Position (p_c = 1 MPa – Color Brightness Encodes Blowing Ratio)

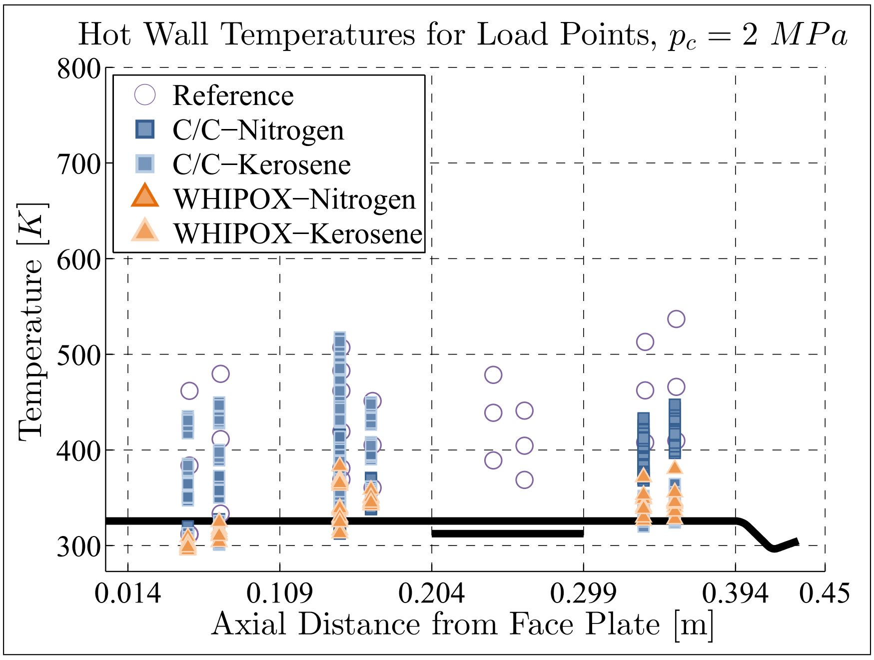

Fig. 4.45: Hot Wall Temperature over Axial Position (p_c = 2 MPa – Color Brightness Encodes Blowing Ratio)

4.4 Convectively Cooled CMC

4.4.1 Test Objectives

The load points (O/F-p_c-pairings) of all tests conducted with two convectively cooled CMC test samples namely PSR0 and PSR1 are shown in Fig. 4.46 [91]. Load points with a mixture ratio 2.3 at 1 MPa and 1.8 at 2 MPa have been chosen as anchor points for the investigations. For tests with coolant nitrogen (green markers) a good reproducibility of the load points has been achieved. For the tests with coolant kerosene (red markers) a slightly higher scatter is apparent.

4.4.2 Combustion Oscillations

Due to problems with HF oscillations caused by the injection assembly used, the examination of the dynamic behavior has been of importance in order to check plausibility and reliability of the experimental results. The relative peak HF amplitudes in the combustion chamber with respect to the associated frequencies are given in Fig. 4.47. A rough combustion i.e. amplitudes higher than 5 % are found at a frequency of approximately 1300 Hz (L1 mode of the combustion chamber) for the tests with nitrogen and some of the reference tests. This observation corresponds to an anticipated HF oscillation dependancy on the ambient temperature thus the oxygen inlet temperature, which was roughly 20 K higher during the test with nitrogen compared to the tests with kerosene [91].

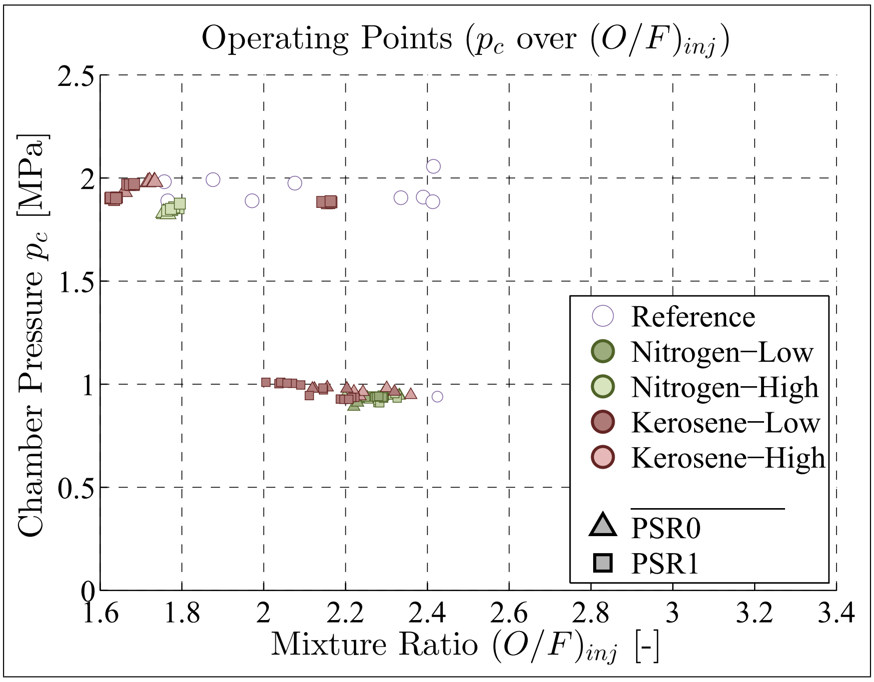

Fig. 4.46: Overview of Load Points Investigated with Convectively Cooled CMC (Color Brightness Encodes Coolant Mass Flow)

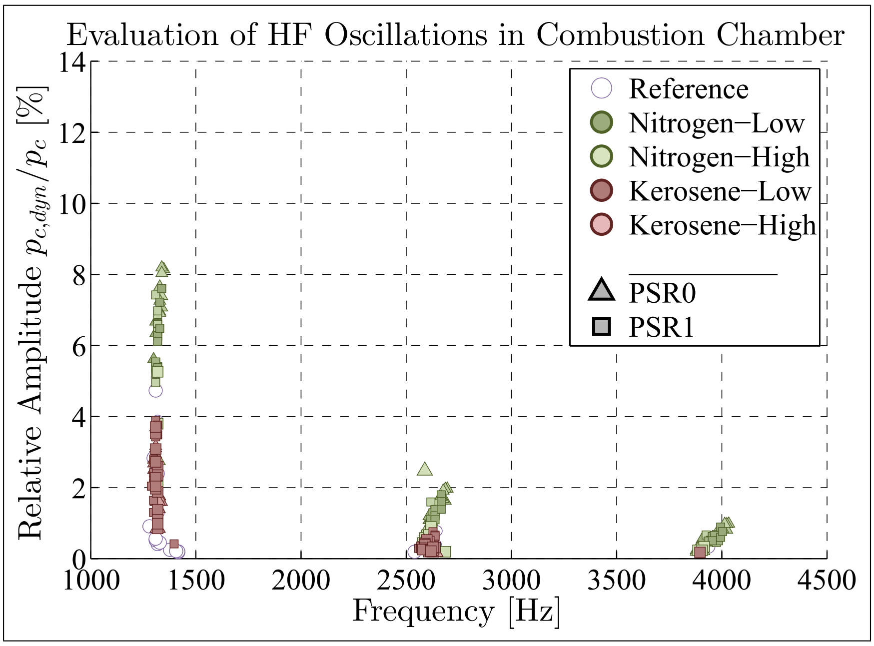

Fig. 4.47: HF Oscillations in Combustion Chamber over Peak Frequency (1st to 4th peak frequency only – Color Brightness Encodes Coolant Mass Flow, Symbol Size Represents Pressure Level)

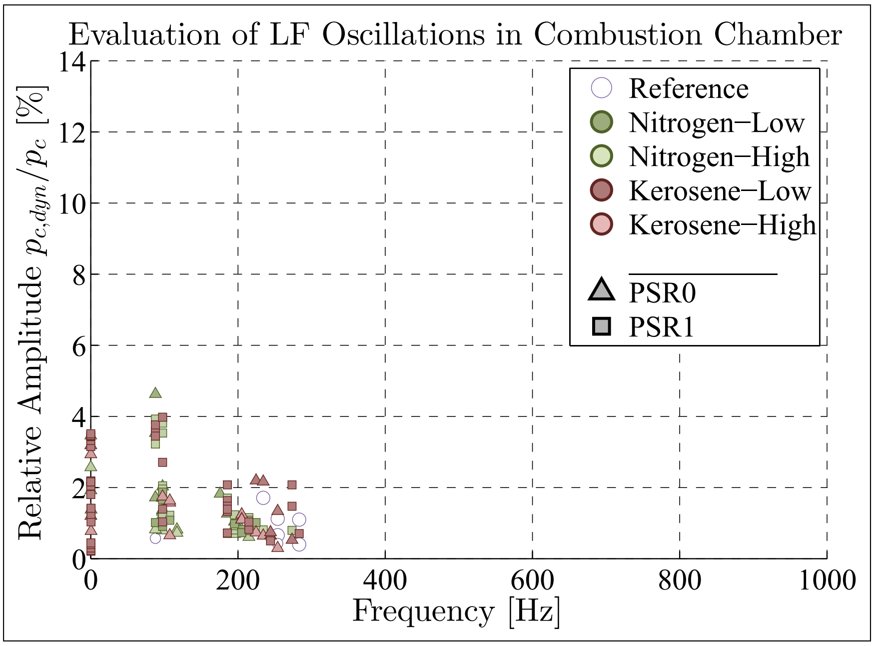

Fig. 4.48: LF Oscillations in Combustion Chamber over Peak Frequency (1st to 4th peak frequency only – Color Brightness Encodes Coolant Mass Flow, Symbol Size Represents Pressure Level)

The relative peak LF amplitudes with respect to frequency are given in Fig. 4.48. In general, no noteworthy tendency for LF oscillation can be found.

4.4.3 Performance

The combustion efficiency of the experiments performed with the two convectively cooled CMC test samples is presented in Fig. 4.49 along with associated reference data. Additionally, the combustion efficiency correlation (Eq. 4.1) is given. The tests with coolant nitrogen feature for a mixture ratio of 2.3 and a combustion pressure of 1 MPa (small greenish symbols) a up to approximately 5 % lower combustion efficiency as comparable reference tests. The data significantly scatters and shows no clear dependancy regarding the specific test sample, differential pressure over the CMC wall or the coolant mass flow rate. The unclear trend applies also to load case 1.8/ 2 MPa both for nitrogen and kerosene albeit the data is less scattered. Hereby, the overall combustion efficiency is roughly the same as in the reference tests.
For tests with kerosene and PSR0 at 1 MPa and mixture ratio 2.3 (small reddish triangles) the combustion efficiency is higher than for the reference tests, which can be linked to a non-negligible transpiration mass flow rate observed during these tests (cf. Fig 4.50). This is supported by the results for PSR1 at 2.3/ 1 MPa (small reddish squares), where for an increasing transpiration mass flow rate a significant increase of the calculated combustion efficiency has been found. For tests with PSR1 at 2 MPa and mixture ratio 2.3 (big red squares) the combustion efficiency agrees with the reference tests.

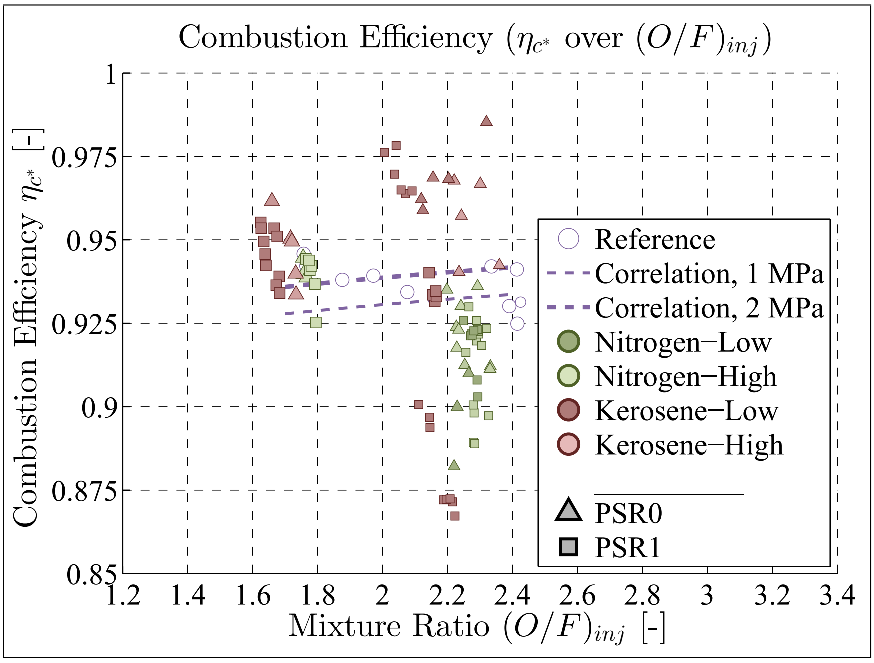

Fig. 4.49: Overview of Combustion Efficiency for Convectively Cooled CMC (Color Brightness Encodes Coolant Mass Flow, Symbol Size Represents Pressure Level)

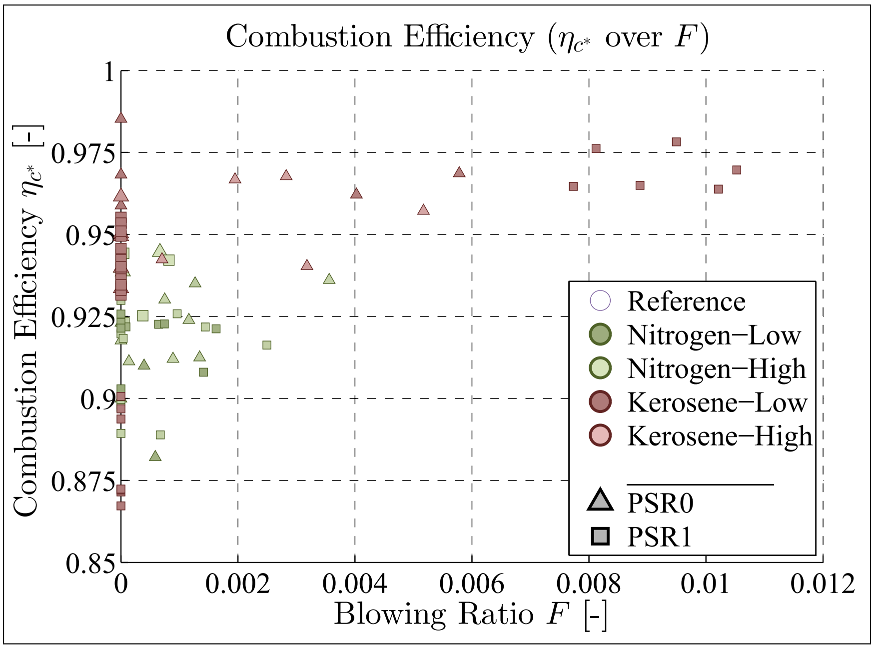

Fig. 4.50: Dependency of Combustion Efficiency from Blowing Ratio (Color Brightness Encodes Coolant Mass Flow, Symbol Size Represents Pressure Level)

4.4.4 Heat Flux

The heat flux with respect to the distance from the face plate is presented for load cases 2.3/ 1 MPa, for 1.8/ 2 MPa and for 2.3/ 2 MPa in Fig. 4.51, Fig. 4.52 and Fig. 4.53. Compared to the reference tests a decrease in the heat flux can be observed for the CMC segment (position ≈ 300 mm of face plate). For the nozzle the heat flux significantly scatters. Phenomena like the disturbance of the boundary layer due to the rougher CMC chamber surface or the cooling effect by the transpiration mass flow are hardly assessable due to the general measurement uncertainty in the nozzle segment.

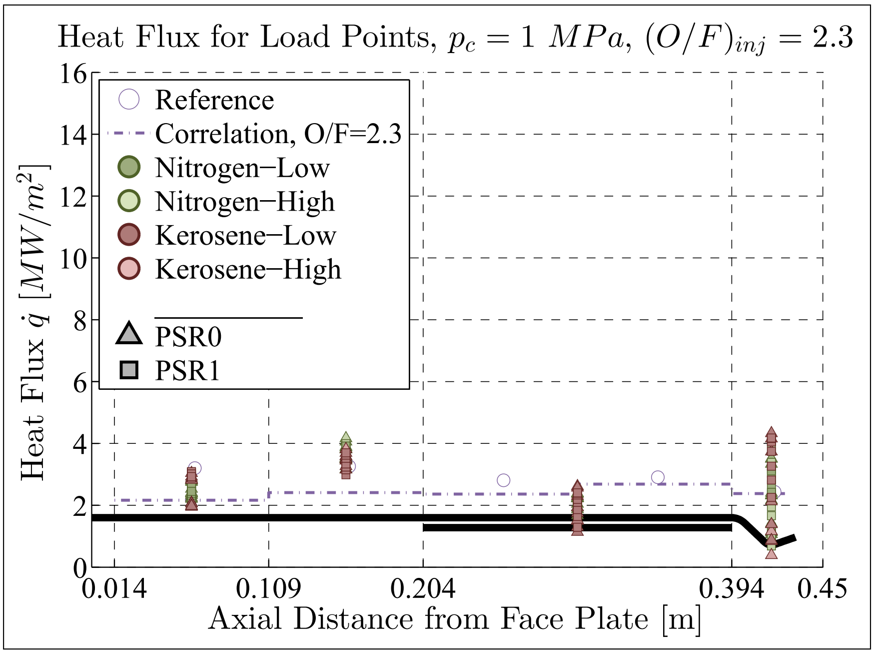

Fig. 4.51: Heat Flux over Axial Position ($p_c = 1$ MPa, $(O/F)_{inj} = 2.3$ – Color Brightness Encodes Coolant Mass Flow)

An influence of the burning time thus the CMC temperature has been found resulting in a slight drift of the data points in Fig. 4.51 et seqq. A longer burning time thus higher CMC temperature leads to an increase in heat flux of the CMC and nozzle segment until steady-state conditions are reached. The time till steady-state varies from approximately 10 s for nitrogen at 2.3/ 1 MPa up to more than 50 s for some kerosene test cases. Furthermore, analyses on the heat flux in the second segment indicates a extensive axial heat transfer from the upstream flange of the CMC segment to the adjoining water-cooled segment. This characteristic has to be considered in the modeling of the heat transfer.

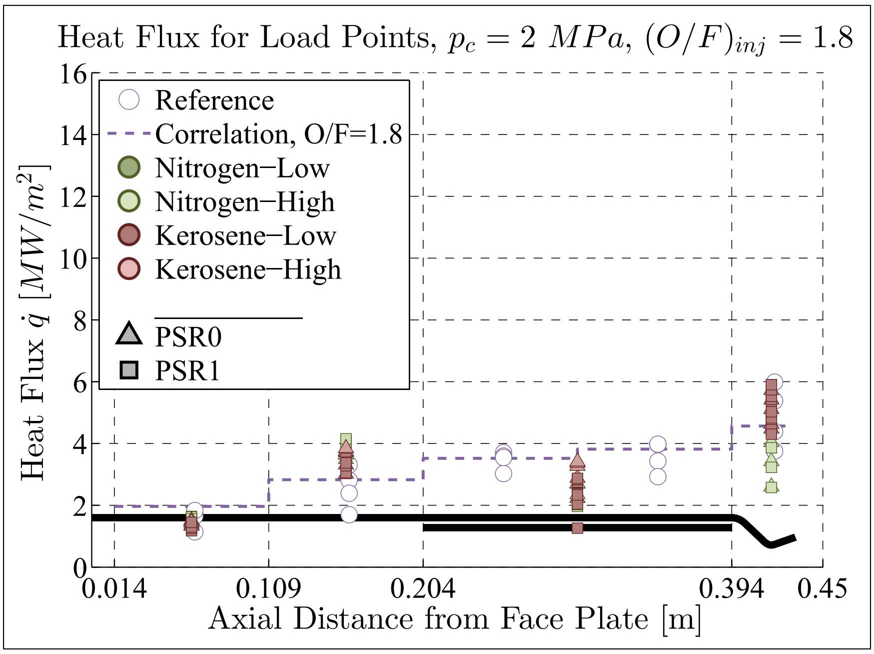

Fig. 4.52: Heat Flux over Axial Position (p_c = 2 MPa, $(O/F)_{inj}$ = 1.8 – Color Brightness Encodes Coolant Mass Flow)

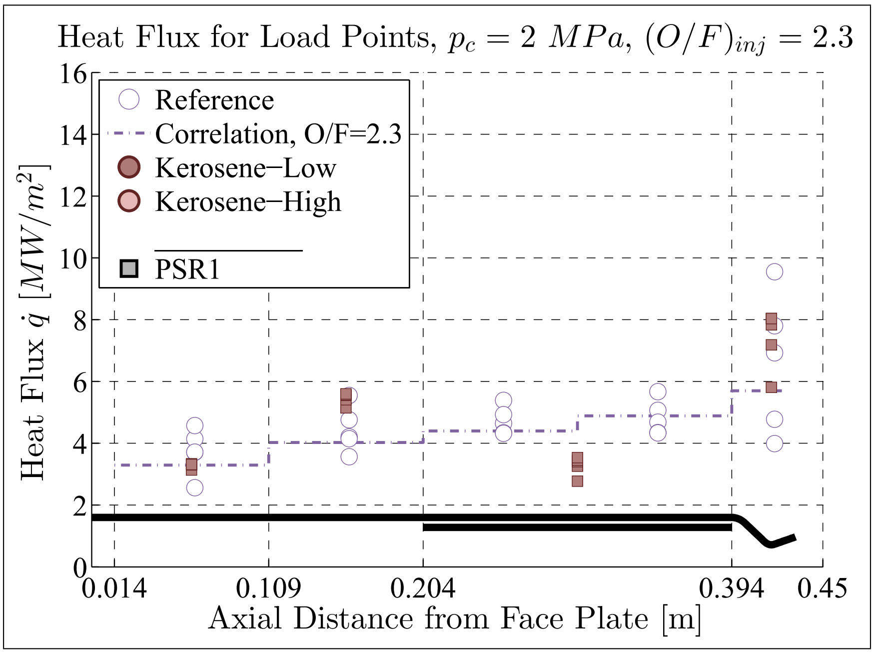

Fig. 4.53: Heat Flux over Axial Position (p_c = 2 MPa, $(O/F)_{inj}$ = 2.3 – Color Brightness Encodes Coolant Mass Flow)

5. Modeling of Heat Transfer

In this chapter the methods of correlation-based heat transfer modeling as well as its application to the experimental results introduced in chapter 4 are presented. The so-called “Common Approach” as described in section 5.1 was implemented in the TUM-LFA in-house engineering tool THERMTEST and has been used for preparation of the ATLLAS test campaigns conducted at the high pressure test facility of the Institute for Flight Propulsion, Technische Universität München [6, 22, 70, 94]. With experimental data available, a detailed post-test analysis and model validation has been performed. In section 5.2 the measurements from the 37 mm reference configuration as well as the 20 mm combustion chamber are compared to results from calculations using the “Common Approach” and other models reviewed in section 2.3.1. In the sections thereafter, modeling approaches for film cooling, transpiration cooled CMC and convectively cooled CMC are applied and their general practicability is investigated.

5.1 TUM/ATLLAS Common Approach

5.1.1 Motivation

The need for a reliable prediction of the thermal behavior of the chamber and of the heating of the cooling water has led to the programming of the simulation tool THERMTEST at TUM. This program was first developed with Mathworks Matlab in 2004[1] and gradually enhanced since then [96]. With THERMTEST it is possible to simulate the steady and transient thermal behavior of cooled or uncooled structures as well as a wide variety of different chamber materials and cooling fluids as used in small rocket engines e.g. in the institute’s subscale rocket thrust chamber. While the heat conduction inside the chamber material is solved by a 3D finite difference method (see Fig.5.1(b) for mesh detail), the convective heat transfer is implemented by empirical Nusselt correlations (compare to Fig. 5.1(a) for cooling channel). The advantage of this approach is a satisfying accuracy maintaining a reasonably fast simulation of the coupled heat transfer from the hot gas into the cooling fluid.

At the beginning of the ATLLAS program, each of the partners involved in the analyses of the experiments performed at TUM computed the expected heat fluxes and wall temperatures with their own in-house engineering tools and semi-empirical methods. These programs, namely NANCY by MBDA [97], and THERMTEST respectively, have been designed with different objectives. While NANCY was intended to predict heat transfer in actively cooled CMCs for ramjet applications, THERMTEST was primarily designed

---

[1] C. Kirchberger: *Gestaltung einer Raketenbrennkammer aus faserverstärktem Siliziumcarbid*, Diploma Thesis [in German], Institute for Flight Propulsion, Technische Universität München, 2004

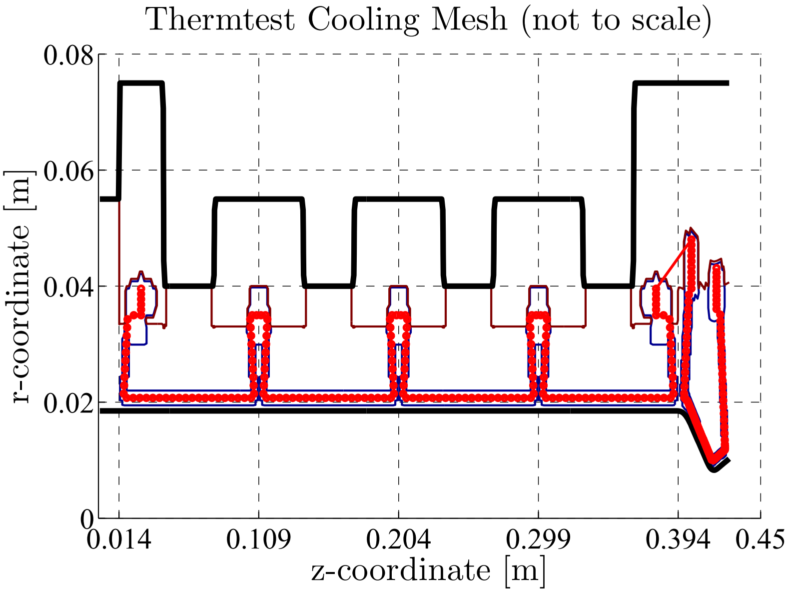

(a) 1D Cooling Channel (Red)

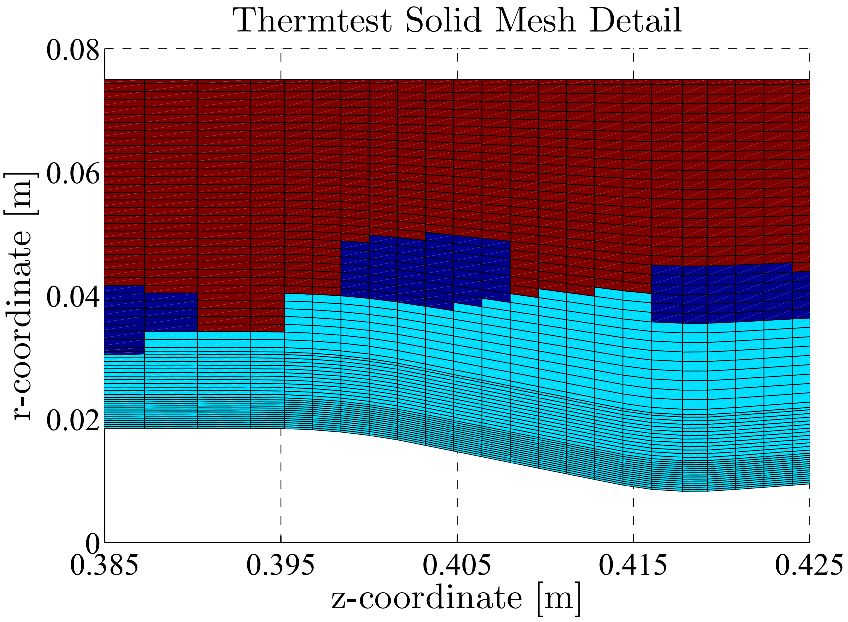

(b) Detail of 3D Solid Mesh near Nozzle (Light Blue: Copper, Dark Blue: Cooling Channel/ Manifold, Dark Red: Stainless Steel)

Fig. 5.1: Example of THERMTEST Mesh Representation

to predict the heat transfer of the water-cooled metallic rocket combustion chamber of TUM. However, the tools have been steadily improved and extended so that the original limits have been overcome. Facing the task of commonly preparing a test setup, several discrepancies were found, most noticeable the overall heat flux differing almost by a factor of 1.5. Although cross-checks with results from more detailed computational tools are always favored, NANCY and THERMTEST are preferably used for test preparations and test analysis when time for a more detailed computation is not available. This led to detailed exchange of data and mutual understanding of the different algorithms, resulting in a commonly agreed method, which is described in the next section. Further information on THERMTEST and the "Common Approach" as well as a comparison with experimental data and calculations from commonly available CFD code has already been published [6, 22, 70, 92].

5.1.2 Implementation into THERMTEST

The common approach utilizes one-dimensional hot gas representation along combustion chamber axis acquired from the NASA computer program "Chemical Equilibrium with Applications" (short CEA2) of *Sanford Gordon and Bonnie McBride* [24]. The temperature of the fluid and the ideal characteristic velocity are calculated using the built-in rocket problem. The "injector" level used in this problem case is implied to be right at the injector face plate and "combustion end" at the end of the cylindrical chamber section. The evolution of temperature caused by atomization, mixing and reaction kinetics is generally neglected as it is not taken into account in CEA2. The fluid properties needed for heat transfer calculations near the wall are calculated assuming an equilibrium composition temperature-pressure-problem within CEA2.

The convective heat transfer from the hot gas to the inner wall as well as from the wall to the coolant is modeled using Nusselt correlations. The hot wall heat transfer coefficient is calculated from a modified formulation of the *Sinyarev* correlation as presented in Eq. 2.40 [34]:

$$Nu = 0.0162 \cdot (Re \cdot Pr)^{0.82} \left(\frac{T_{aw}}{T_w}\right)^{0.35} \tag{5.1}$$

$$\alpha_{hg,conv} = 0.01975 \cdot \frac{\lambda^{0.18} \cdot (\dot{m} \cdot c_p)^{0.82}}{d_h^{1.82}} \cdot \left[\frac{T_{aw}}{T_w}\right]^{0.35} \tag{5.2}$$

However, values of viscosity, specific heat and conductivity are computed at a mean temperature $T = (T_{aw} + T_w)/2$ rather than hot wall temperature T_w as in the original formula. Temperature T_{aw} denotes the recovery temperature taking into account imperfect combustion as well as incomplete heat recovery:

$$T_{aw} = T_\infty + r \cdot \left(T_{c,theo} \cdot \eta_{c^*}^2 - T_\infty\right) \tag{5.3}$$

Hereby the recovery factor r is an empiric value varying from 0.7 to 0.9, depending on the gas Prandtl number and on the boundary layer status. The value used here is 0.80, which was found to be conservative but realistic in the past. In the typical temperature regime the influence of the recovery factor chosen on the heat transfer coefficient is well below 1 % for the combustion chamber and will also not exceed 5 % for the nozzle. Therefore, no detailed analysis on the recovery factor is necessary. Due to local overspeed and effects of turbulence the heat transfer coefficient in the throat is corrected with an empirical factor. Evaluations concerning the influence of hot gas radiation on the heat transfer led to the conclusion that radiation might be of significance especially if the wall temperature is high. This is true e.g. for CMC-based combustion chambers. Therefore, the formulas as given by Eq. 2.49 and 2.50 have been implemented. The gas composition is assumed to be equilibrium and is calculated using CEA2.

For the calculation of the heat transfer to the coolant, the models of *Kraussold* [41], *McAdams* [42] and *Gnielinski* [33] have been implemented in THERMTEST. Fluid properties of water have been derived from Ref. [11]. Correction factors mentioned by e.g. *Kraussold* [41] for curvature of the cooling channel or starting and stratification have been generally neglected.

For further applications like CMC structures the model has to be capable of calculating the cold external wall heat transfer coefficient taking into account natural convection as well as heat transfer by radiation. The necessary formulations are usually well known and do not need to be presented here in detail.

A method for modeling the influence of a cooling film on the hot gas side has been a main focus of the research activities of the Institute for Flight Propulsion. The models by *Stechman* [57, 58], *Hatch/ Pappel* [53] and *Stollery/ El-Ehwany* [56] as introduced in section 2.3.9 had already been implemented into THERMTEST in the past but showed dissatisfying agreement with measured data obtained from experiments deploying cooling film laying swirl injectors [96]. Therefore the models presented in *NASA SP-8124* (Eq. 2.76 et seqq., [59]) have been investigated during ATLLAS research project[2].

The non-reacting formulations of both NASA cooling film models, gaseous and liquid, have been implemented in THERMTEST and several calculations and parameter variations have been performed[3]. Thereby, the liquid film model is defined for test conditions below critical point only (for kerosene 684.3 K and 2.34 MPa [13]), although it might be applicable for "trans-critical" conditions as well. Comparisons of THERMTEST simulation results and measurements from film cooling experiments have been presented in References [70,94,95].

For simulation of transpiration cooled CMC, the model of *Hacker* [66] has been implemented in THERMTEST and several calculations have been performed. Results of these investigations[4] have been published in [98].

5.1.3 Limitations of "Common Approach"

The validation and improvement of the "common approach" has been and still is a continuous process. Thereby, several factors influencing the results of the simulation have been identified and investigated in the past.

---

[2] S. Zawadzki: *Untersuchung der Kerosin-Filmkühlung in einer Subscale-Raketen-Brennkammer*, Semester Assignment [in German], Institute for Flight Propulsion (LFA), Technische Universität München, Munich, Germany, 2007

[3] A. Galbiati: *Predictions and Analysis of Film Cooling Experiments at a Subscale Rocket Combustion Chamber*, Diploma Thesis, Institute for Flight Propulsion (LFA), Technische Universität München, Munich, Germany, 2008

[4] S. Bickelmaier: *Prediction and Analysis of Transpiration Cooling Experiments on a Subscale Rocket Combustion Chamber*, Semester Assignment, Institute for Flight Propulsion (LFA), Technische Universität München, Munich, Germany, 2009

The wall temperature is of great importance for the heat transfer in the combustion chamber. On one hand the difference of near-wall gas temperature and wall temperature is directly proportional to the heat flux, and on the other hand the wall temperature has a significant effect on the heat transfer coefficient in two ways. Firstly, as stated in Eq. 2.40 and Eq. 5.2, the wall temperature is reciprocal to the heat transfer coefficient, meaning that a higher wall temperature will lower the coefficient. Secondly, the effect of the reference temperature used to compute the hot gas physical properties (see section 2.3.3) increases or decreases the heat transfer coefficient and thus the heat transfer depending on gas composition and temperature regime.

Otherwise, the heat transfer coefficient is directly proportional to heat flux and therefore the accuracy of the formula used is very important. The preferred *Sinyarev* correlation (cf. Eq. 5.2) was developed for and validated on metal-based combustion chambers from low to moderate wall temperatures. This model neglects effects like the boundary layer evolution at the upstream part of the combustion chamber and the increase of the boundary layer thickness with chamber length. Also one has to keep in mind that the Nusselt correlations neglect effects like deposition of soot on the chamber wall, chamber materials featuring low thermal conductivity and high wall temperatures as typical for the CMCs. Also e.g. wall roughness or porous walls which may have an influence on turbulence and the boundary layer are usually modeled insufficiently or completely ignored. In such cases the calculated heat transfer coefficient will significantly differ from experimental results. These limitations in the heat transfer model can only be overcome by explicitly modeling the influences neglected.

For the calculation of the hot gas temperature and fluid properties the effects of mixing, atomization and reaction kinetics are not considered since they are neglected in the program CEA2 [24], which has been used to determine hot gas conditions. This usually causes an overprediction of heat transfer and wall temperatures in the first segments of the combustion chamber. To overcome this problem, CEA2 may be replaced by the computer codes TDK, CHEMKIN or CANTERA [25–27] in the future.

An increasing deviation between prediction and test was observed for mixture ratio decreasing from mixture ratio 2.6 in the past. In the face of an operating envelope comprising mixture ratios of 2.3 and below this inaccuracy has been quite unsatisfying [6, 22]. The following aspects have been considered to have an influence:

- General limitations of the Sinyarev heat transfer correlation: The Sinyarev model seems not to be able to represent correctly the influence of the mixture ratio for a small hydrocarbon/oxygen engine. An assessment on possible empirical or semi-empirical corrections is given in section 5.2.

- Limitations in the prediction of hot gas fluid properties from Gordon-McBride-Code CEA2: The computed values of the characteristic velocity c^* from CEA2 show an increasing deviation from experimental data for mixture ratios below 1.8 as known from experience of Astrium and LFA. It is also known from LOX/methane testing, that the deviations in c^* values increase for computations assuming chemical equilibrium, if the mixture ratio is far in the fuel rich regime. This behavior is caused by the occurrence of combustion products with slow reaction kinetics e.g. soot.

- Soot: The deposition of soot on the cold chamber wall in more fuel-rich regimes significantly lowers the heat transfer. This comprises especially the regime below a mixture ratio of 2.6. To deal with this issue a simple static model for the decomposition of soot has been developed. However, experiments conducted at a mixture ratio of 1.8 and a combustions pressure of 2 MPa showed that the deposition and flaking of soot is a highly unsteady process where wall temperatures can vary by more than 150 K.

- Fuel film on chamber wall: The application of a fuel cooling film is characteristic for the kind of injectors used in the single-element chamber. Comparison between data calculated with THERMTEST and different experimental values showed evidence that the injector type has an influence on the deviation. Modeling of a possible film cooling has been tested but the results have not been satisfying since the lower heat fluxes near the face plate could not be clearly attributed to a film deposition or to the general atomization and mixing process.

Specific work has also been done in order to estimate the influence of radiation between the hot gases and the cylindrical chamber wall. The results are presented in section 5.2.

5.2 Reference Setup

The reference setup tests comprises all experiments conducted with a standard water cooled combustion chamber with 37 mm inner diameter as presented in subsection 3.2.1. The adequate modeling of the reference test cases is a prerequisite for further investigations on e.g film and transpiration cooling, as it is important to correctly represent the heat release mechanism and injector footprint for the latter one. Thereby, the wide operating envelope containing mixture ratios between 1.4 and 3.4 at pressure levels between 1.0 and 8.0 MPa in 81 distinctive load points is challenging for a unique modeling approach since different physical effects influence different areas of the overall envelope.

For comparison, the results of the simulations for the 45 load points from five tests conducted with the 20 mm hardware are given likewise where appropriate and applicable. These data cover a limited operational envelope of mixture ratios between 2.4 and 3.4 at pressure levels between 4.0 and 8.0 MPa.

5.2.1 Influence of Hot Gas Heat Transfer Model

The determination of the hot gas heat transfer is expected crucial but complicated due to a limited knowledge on the processes dominating in a rocket combustion chamber. For CFD a model for each of the processes e.g. atomization, mixing, combustion, turbulence and wall treatment has to be applied. Here, a more general model is used for the sake of simplicity and speed. The modified Sinyarev model (Eq. 2.40) used by the “Common Approach” is considered as reference. With more experimental data available, the measurements are evaluated and compared to results from calculations using different heat transfer models and the prior selection of the Sinyarev model is reviewed.

The results using Bartz heat transfer model as described by Eq. 2.33 are depicted in Fig. 5.2 for the 37 mm combustion chamber and in Fig. 5.3 for the smaller 20 mm combustion chamber (see Tab. C.1 and Tab. C.2 in the annex for details). The mean deviation between experimentally determined heat flux and simulation for each segment and different load

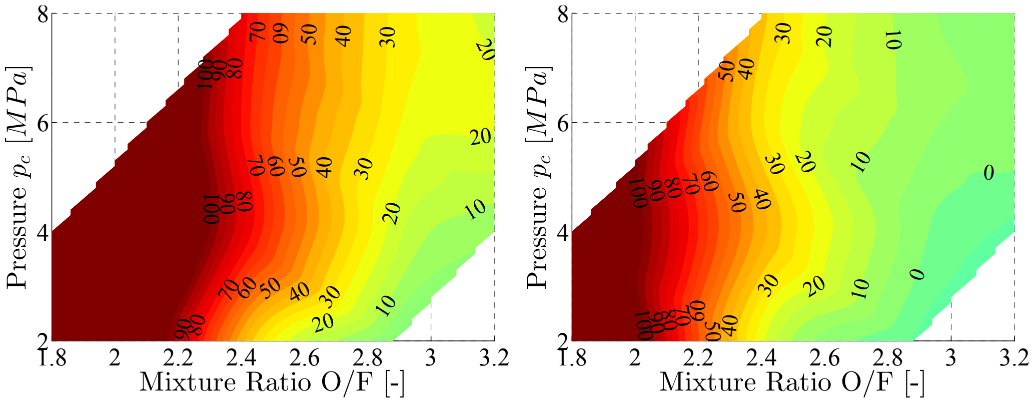

(a) Segment 1 (b) Segment 2

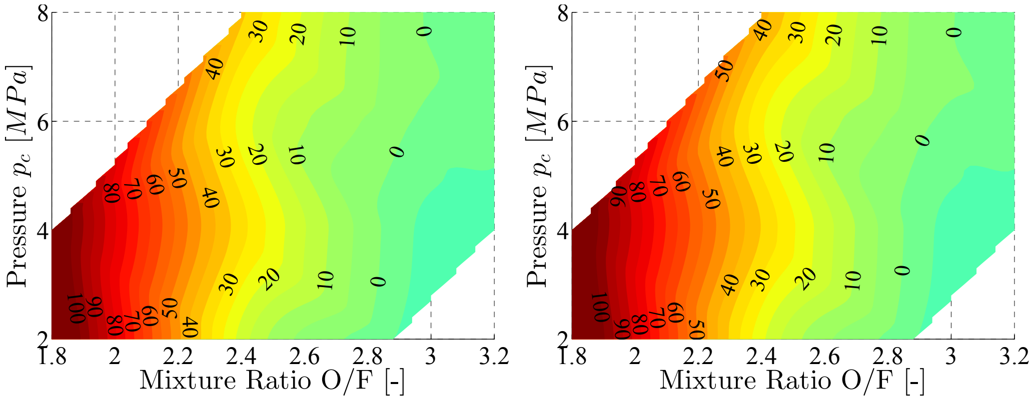

(c) Segment 3 (d) Segment 4

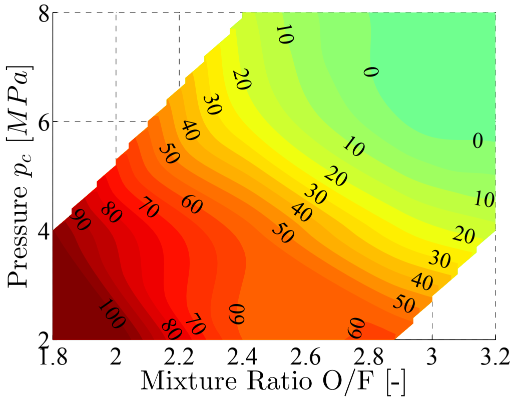

(e) Nozzle Segment

Fig. 5.2: Deviation of Heat Flux Prediction from Measurements for 37 mm Combustion Chamber Using Bartz Model isolines in [%]; "-" underprediction–blue, "+" overprediction–red, agreement–green)

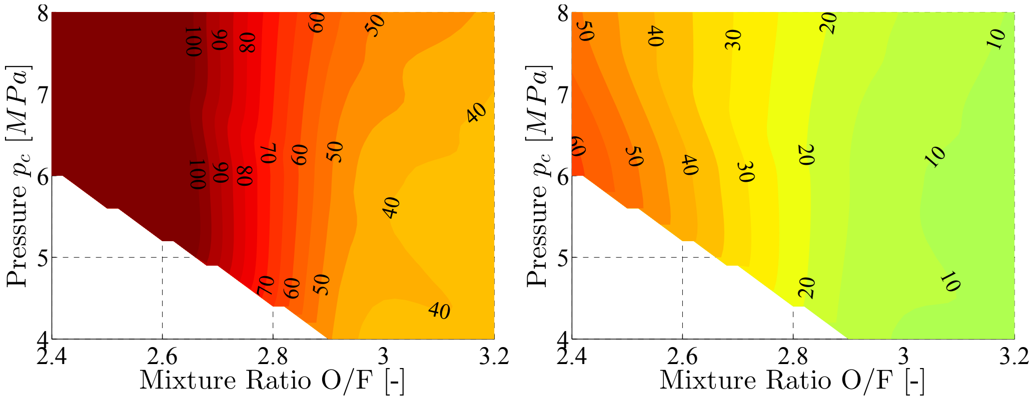

(a) Segment 1

(b) Segment 2

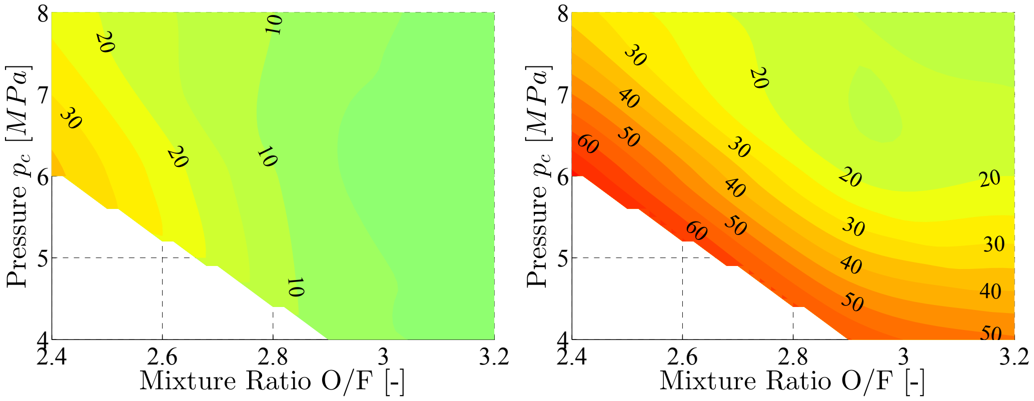

(c) Segment 3

(d) Nozzle Segment

Fig. 5.3: Deviation of Heat Flux Prediction from Measurements for 20 mm Combustion Chamber Using Bartz Model (isolines in [%]; "-" underprediction–blue, "+" overprediction–red, agreement–green)

case classes (levels of pressure and mixture ratios) is given. In the 37 mm chamber the simulations agree with measurements within 10% accuracy for mixture ratios above 2.6 and all but the first segment. For high mixture ratios and high pressure levels also the heat fluxes in the nozzle segment match well. At lower pressures and especially at lower mixture ratios the Bartz fomula significantly overpredicts the heat fluxes. The increasing deviation for lower mixture ratios is attributed to an increasing amount of imperfectly chemically reacting kerosene remaining in the exhaust gas and the increased production of soot. This general behavior is found both for the 37 mm combustion chamber featuring a Mach number of 0.12 as well as for the 20 mm with a Mach number of 0.24. However, the Bartz approach generally overpredicts the heat flux in the 20 mm chamber. Although the Bartz model is often used as reference model for a wide variety of operational conditions, configurations and propellants, it was regarded unsuitable for the investigated test case in the past [6, 22]. This opinion based yet on simulations performed with an erroneous representation of the hot flow properties and can be revoked due to the latest findings.

Using the model of Gnielinski the heat fluxes in the chambers are usually underpredicted (see Fig. 5.4 et seq. as well as Tab. C.3 et seq. in the annex). Since Gnielinski is a correlation for general pipe flow, it misses corrections for the combustion-caused turbulence which is a characteristic of rocket combustion chambers. Accordingly, the shortcomings of the model have been traced back to representation of the axial velocity profile (derived from Gordon-McBride CEA2) and the calculation of an appropriate Reynolds number. As with Bartz and Sinyarev two suitable correlations have been available, no further optimizations on the Gnielinski model have been carried out, although much better agreement might be achieved by using a different data base for the hot gas properties or a modified Reynolds number.

Finally, the deviation between experimental data and simulation using the modified Sinyarev model (Eq. 2.40) is given in Fig. 5.6 and Fig. 5.7 (also compare to Tab. C.5 and Tab. C.6 in the annex). Generally speaking, the agreement of measurements and calculations is very good (better ±20%) for moderate up to high pressure levels and mixture ratios above 2.4. For very high mixture ratios and high pressure levels the simulation tends to slightly underpredict the heat fluxes. At low pressures and especially at low mixture ratios the model significantly overpredicts the heat fluxes. The quality of the prediction improves for downstream chamber segments since the used correlation does not feature corrections which take into account atomization and mixing processes or an increase of the boundary layer thickness. The agreement of simulation and measurement is also satisfying for the nozzle segment. The prediction of the heat transfer within the nozzle is usually quite challenging due to the complex geometry of the coolant circuit and the steep gradients in the flow conditions. The increasing deviation for lower mixture ratios is ascribed again to imperfect combustion of kerosene and soot.

A comparison of the heat flux profile along chamber axis of the different hot wall heat transfer models is given for selected load points with the 37 mm combustion chamber in Fig. 5.8, Fig. 5.9 and Fig. 5.10 and with the 20 mm combustion chamber in Fig. 5.11 and Fig. 5.12. Beside the developing of the heat flux also the average flux per segment is shown by the symbols. Apparently the best qualitative and quantitative agreement between simulation and experiment is achieved using the modified Sinyarev model tightly followed by the Bartz model. Basing on these findings the modified Sinyarev model remains the reference heat transfer model for the hot gas side. In the following sections the influence of the coolant heat transfer and heat transfer by radiation is cross-checked.

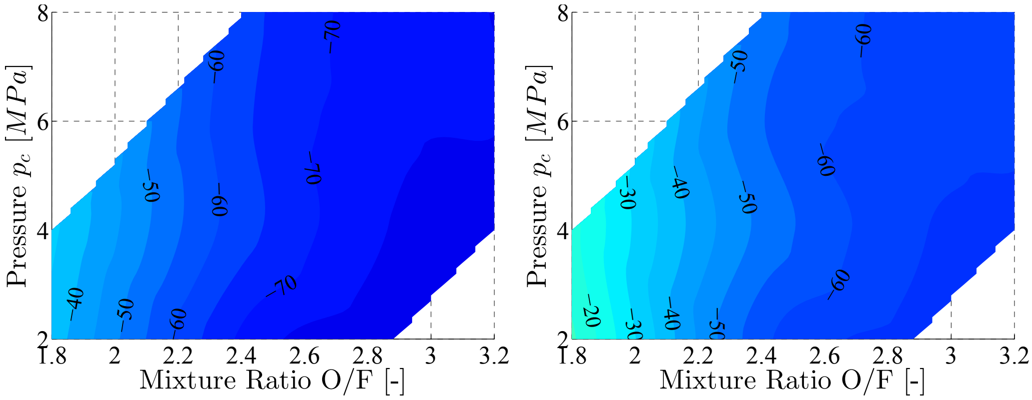

(a) Segment 1 (b) Segment 2

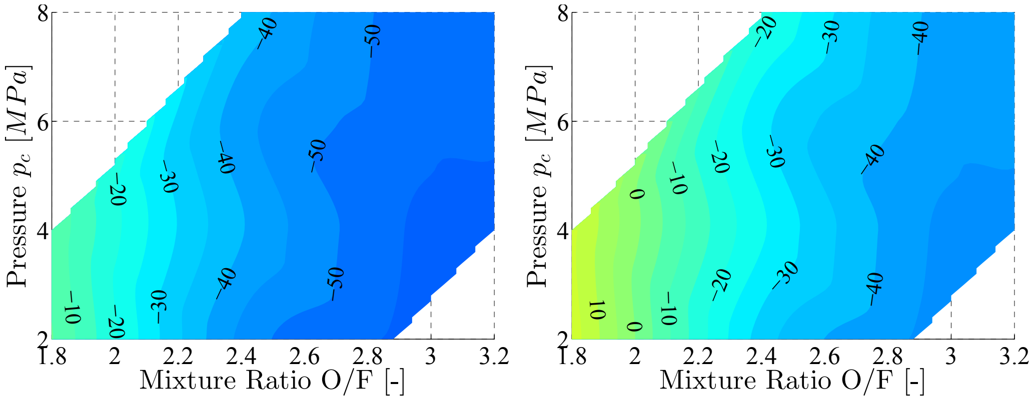

(c) Segment 3 (d) Segment 4

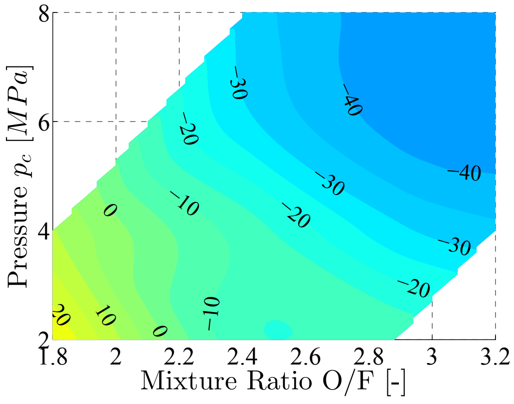

(e) Nozzle Segment

Fig. 5.4: Deviation of Heat Flux Prediction from Measurements for 37 mm Combustion Chamber Using Gnielinski Model (isolines in [%]; "-" underprediction–blue, "+" overprediction–red, agreement–green)

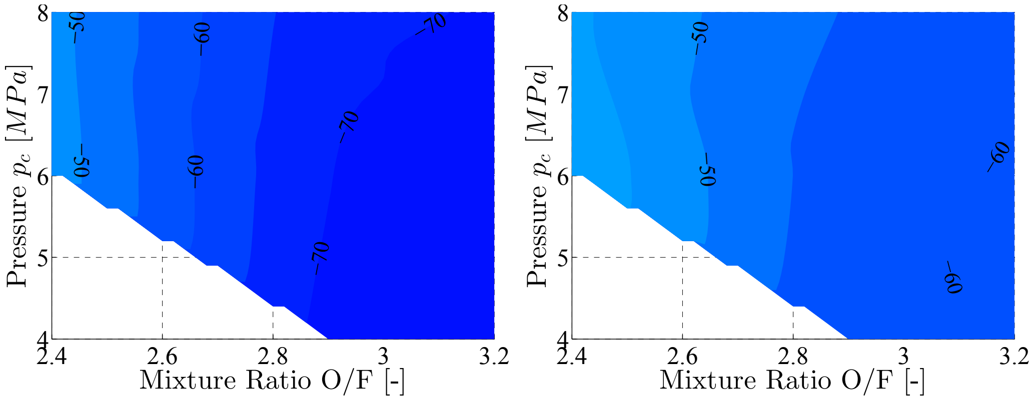

(a) Segment 1 (b) Segment 2

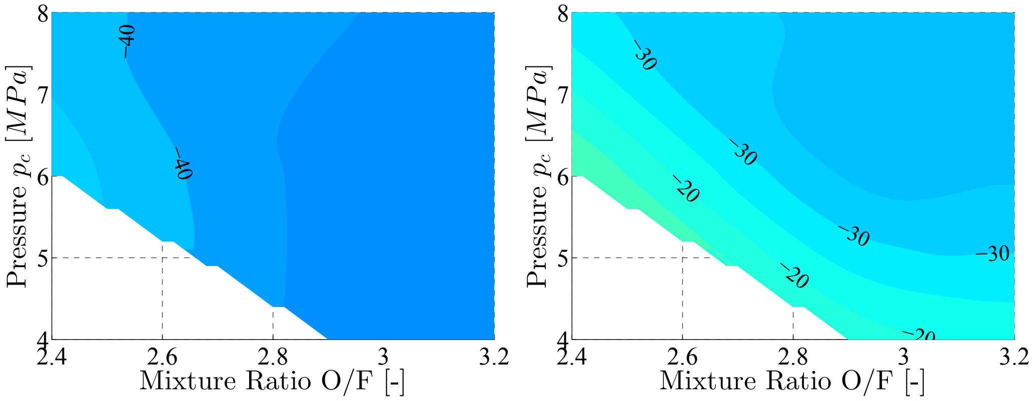

(c) Segment 3 (d) Nozzle Segment

Fig. 5.5: Deviation of Heat Flux Prediction from Measurements for 20 mm Combustion Chamber Using Gnielinski Model (isolines in [%]; "-" underprediction–blue, "+" overprediction–red, agreement–green)

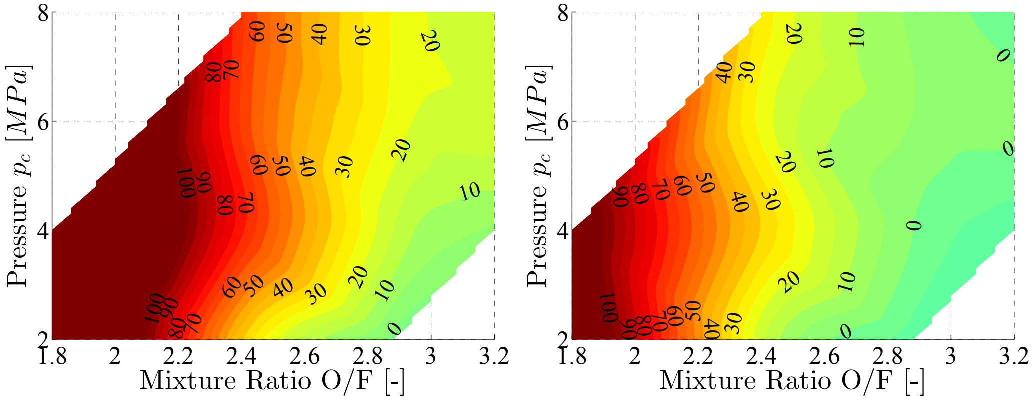

(a) Segment 1 (b) Segment 2

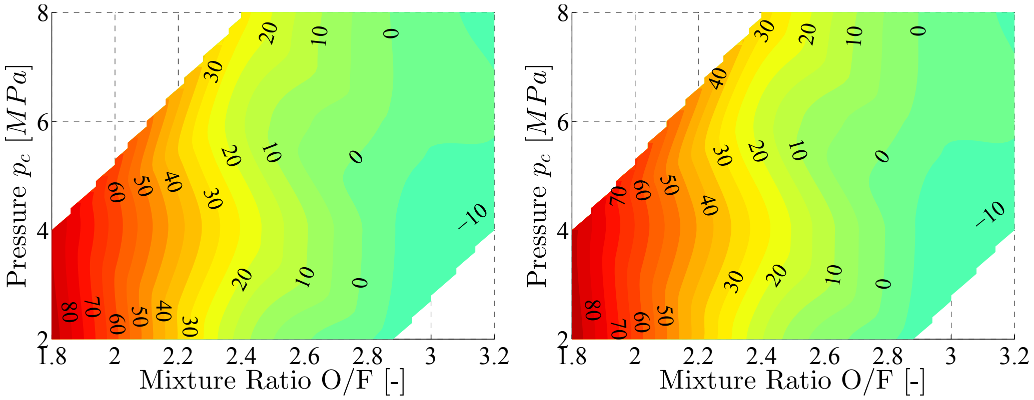

(c) Segment 3 (d) Segment 4

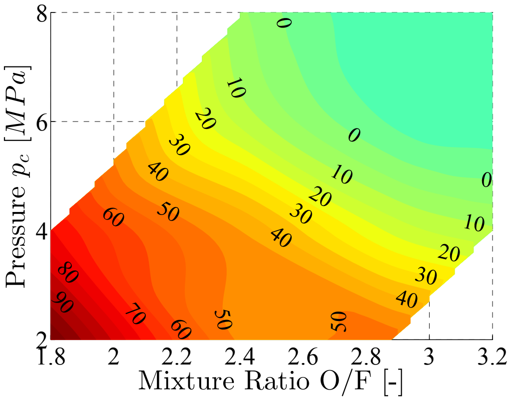

(e) Nozzle Segment

Fig. 5.6: Deviation of Heat Flux Prediction from Measurements for 37 mm Combustion Chamber Using Modified Sinyarev Model (isolines in [%]; "-" underprediction–blue, "+" overprediction–red, agreement–green)

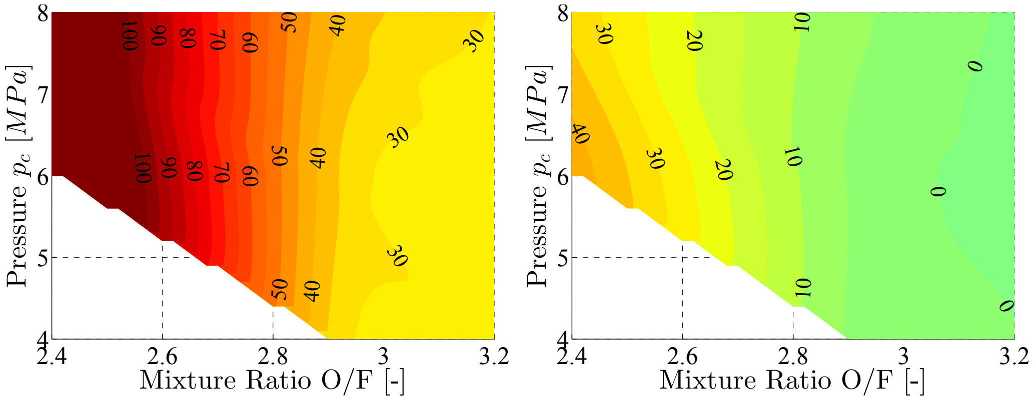

(a) Segment 1 (b) Segment 2

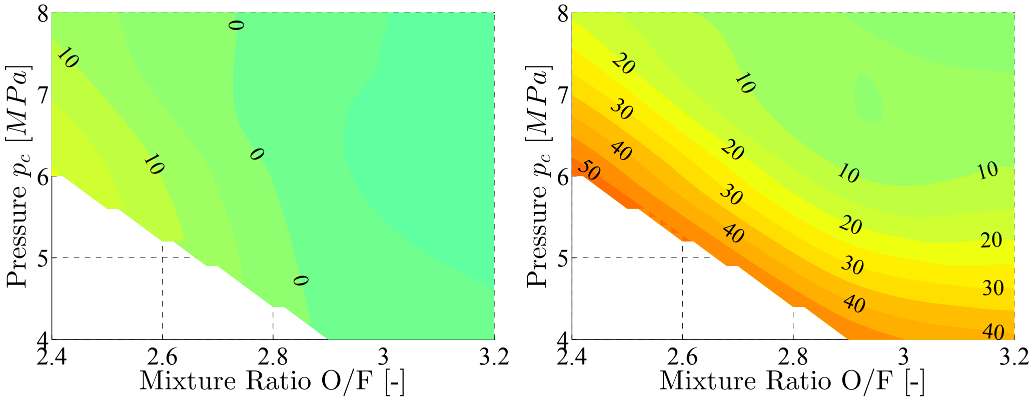

(c) Segment 3 (d) Nozzle Segment

Fig. 5.7: Deviation of Heat Flux Prediction from Measurements for 20 mm Combustion Chamber Using Modified Sinyarev Model (isolines in [%]; “-” underprediction–blue, “+” overprediction–red, agreement–green)

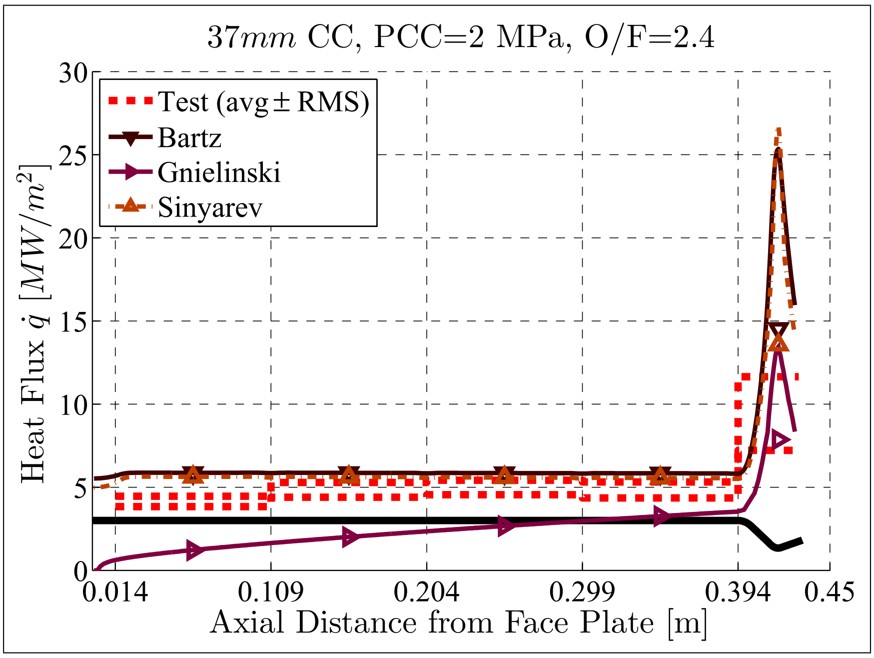

Fig. 5.8: Comparison of Hot Wall Heat Transfer Models for Test with 37 mm CC at Low Mixture Ratio and Low Combustion Pressure (dashed red line represents integral heat flux by experiment, symbols represent the segment-wise integral value of simulation)

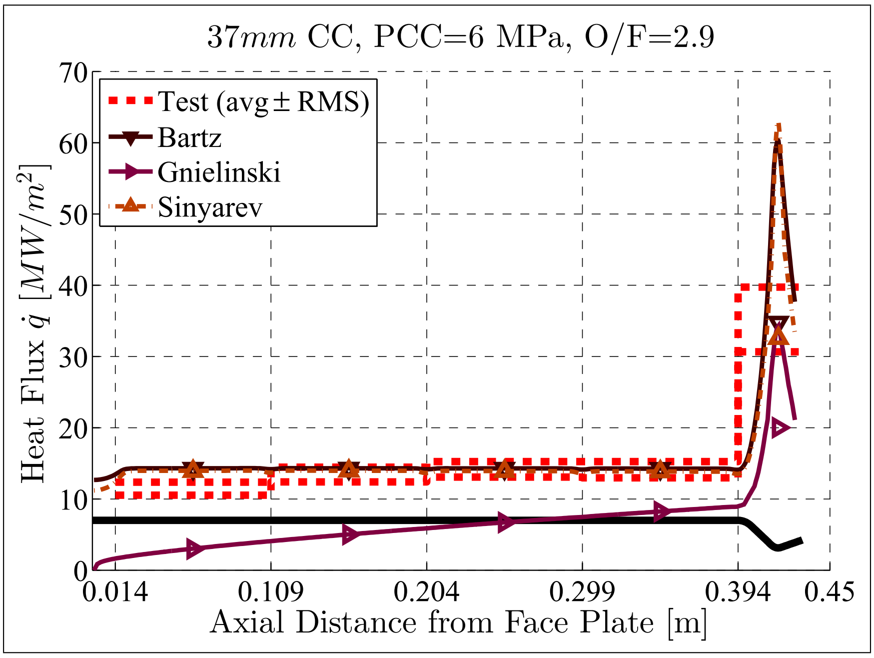

Fig. 5.9: Comparison of Hot Wall Heat Transfer Models for Test with 37 mm CC at Design Load Point (dashed red line represents integral heat flux by experiment, symbols represent the segment-wise integral value of simulation)

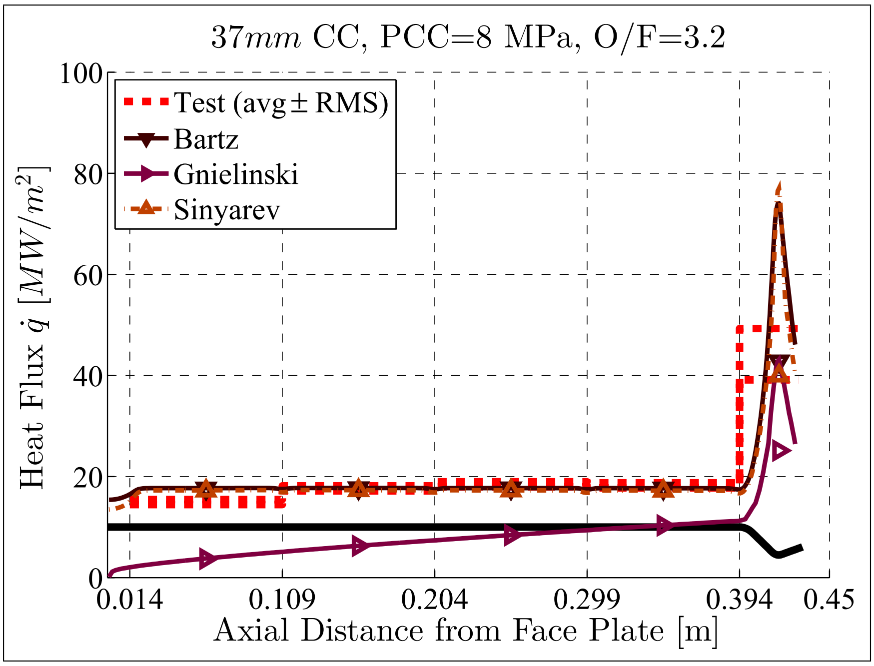

Fig. 5.10: Comparison of Hot Wall Heat Transfer Models for Test with 37 mm CC at High Mixture Ratio and High Combustion Pressure (dashed red line represents integral heat flux by experiment, symbols represent the segment-wise integral value of simulation)

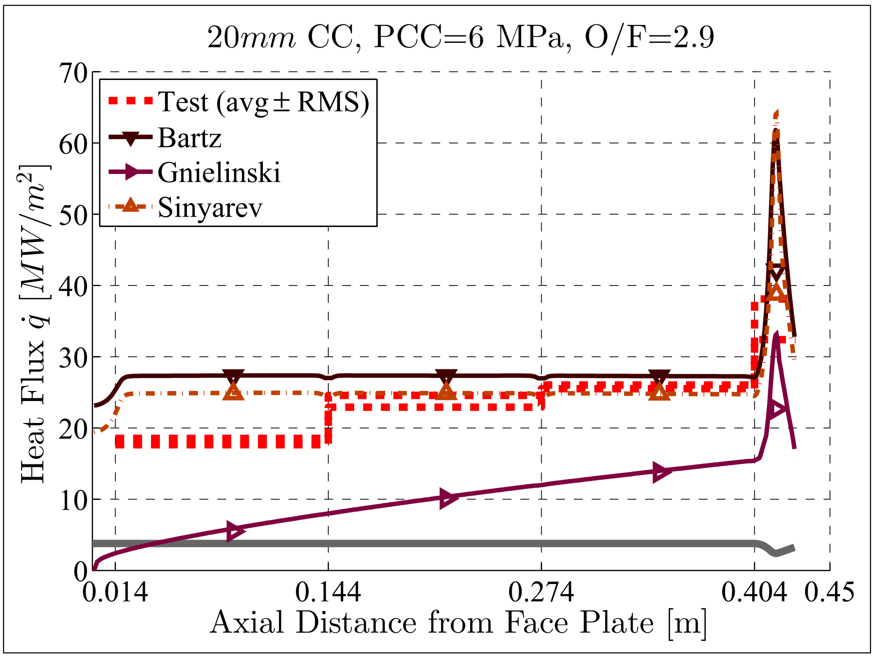

Fig. 5.11: Comparison of Hot Wall Heat Transfer Models for Test with 20 mm CC at Design Load Point (dashed red line represents integral heat flux by experiment, symbols represent the segment-wise integral value of simulation)

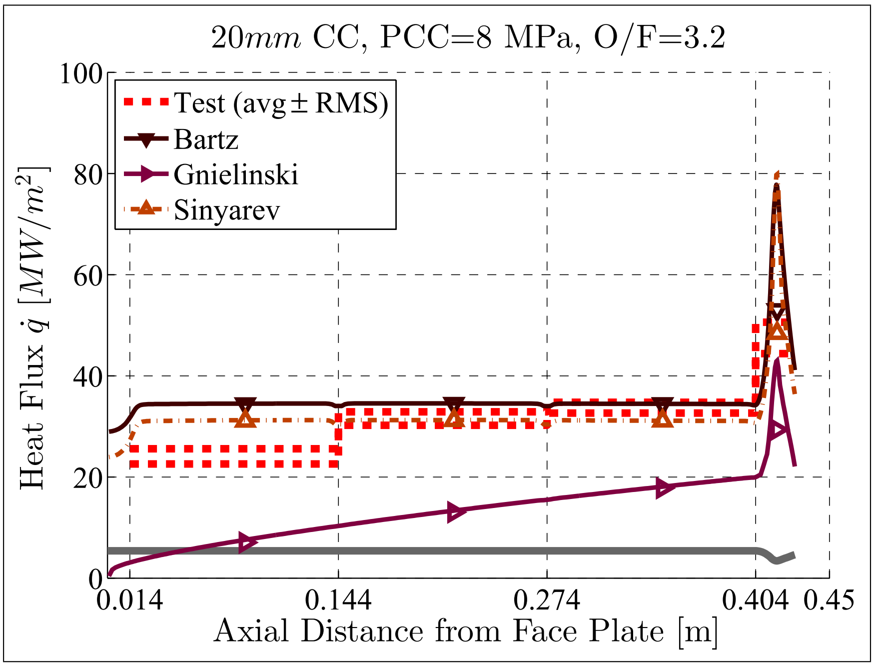

Fig. 5.12: Comparison of Hot Wall Heat Transfer Models for Test with 20 mm CC at High Mixture Ratio and High Combustion Pressure (dashed red line represents integral heat flux by experiment, symbols represent the segment-wise integral value of simulation)

5.2.2 Influence of Hot Gas Radiation

The influence of the hot gas radiation on the overall hot gas side heat transfer is assumed to be at least one order of magnitude smaller than the heat transfer by convection (see e.g. Ref. [1]) and is therefore often neglected. However, the main exhaust gases of a hydrocarbon rocket combustion chamber, water vapor and carbon dioxide, are known as strong radiators. In order to asses the influence of radiation, Eq. 2.49 and Eq. 2.50 have been applied to the hot gas composition along the chamber axis as provided by CEA2.

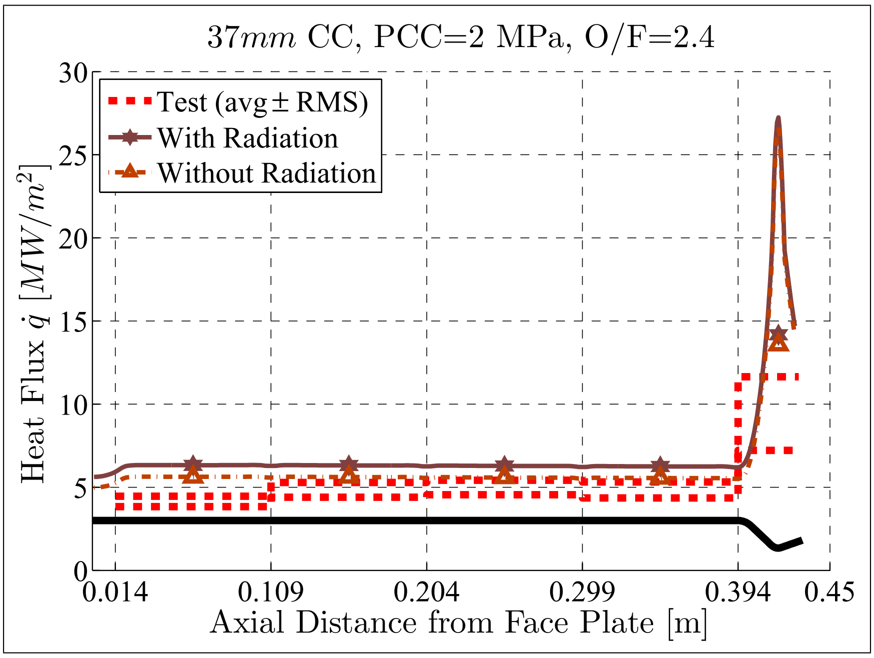

Fig. 5.13: Influence of Radiation for Test with 37 mm CC at Low Mixture Ratio and Low Combustion Pressure (dashed red line represents integral heat flux by experiment, symbols represent the segment-wise integral value of simulation)

A comparison of the heat flux profile along chamber axis of simulations with and without hot gas radiation is given for different load cases of the 37 mm combustion chamber in Fig. 5.13, Fig. 5.14 and Fig. 5.15 and for two load cases of the 20 mm combustion chamber in Fig. 5.16 and Fig. 5.17. As expected, the effect on the heat transfer in the chamber segments is mostly in the order of 3% to 8% but can increase up to 20% for very low mixture ratios. Since the CEA2 code does not represent the atomization and mixing processes but assumes a fully combusted gas already near the face plate, no noteworthy evolution of the combustion products and hot gas temperatures thus the heat transfer by radiation can be determined in the cylindrical chamber segments by the radiation model. Similarly, a propellant film on the chamber wall e.g. deposited by the swirl injector element blocking radiation locally may not be detected in any way.

In summary, neither a positive nor a negative trend on the quality of the heat transfer modeling can be amounted for the radiation model since the changes are in the order of the measuring accuracy as well as the confidence level of the convective heat transfer model. Although from this point of view a special treatment of the radiative heat transfer

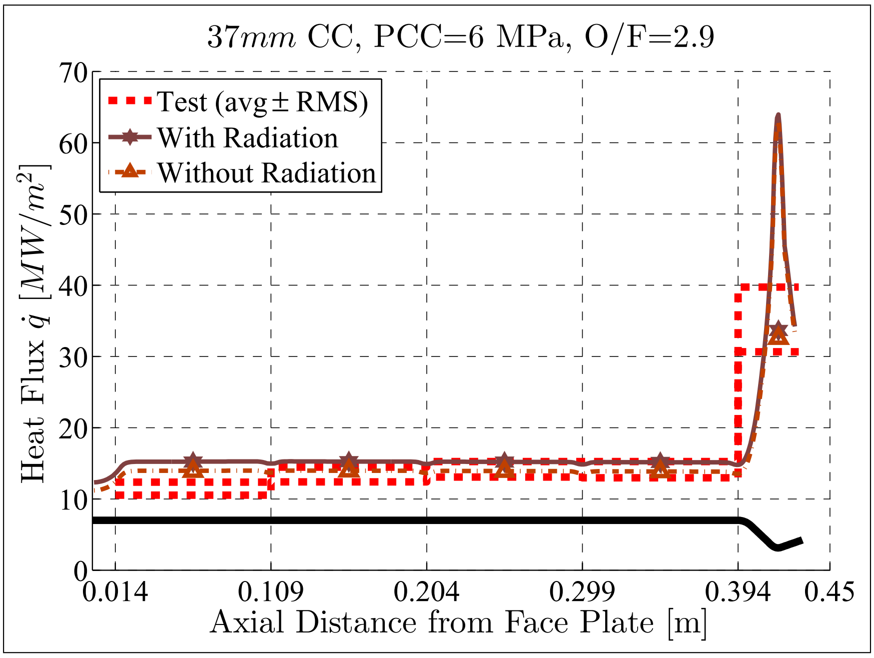

Fig. 5.14: Influence of Radiation for Test with 37 mm CC at Design Load Point (dashed red line represents integral heat flux by experiment, symbols represent the segment-wise integral value of simulation)

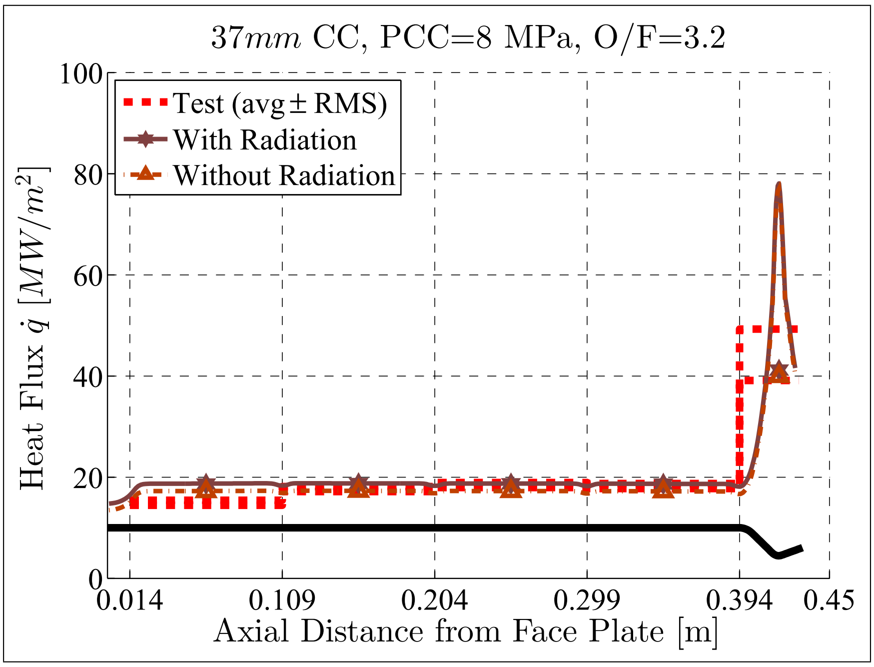

Fig. 5.15: Influence of Radiation for Test with 37 mm CC at High Mixture Ratio and High Combustion Pressure (dashed red line represents integral heat flux by experiment, symbols represent the segment-wise integral value of simulation)

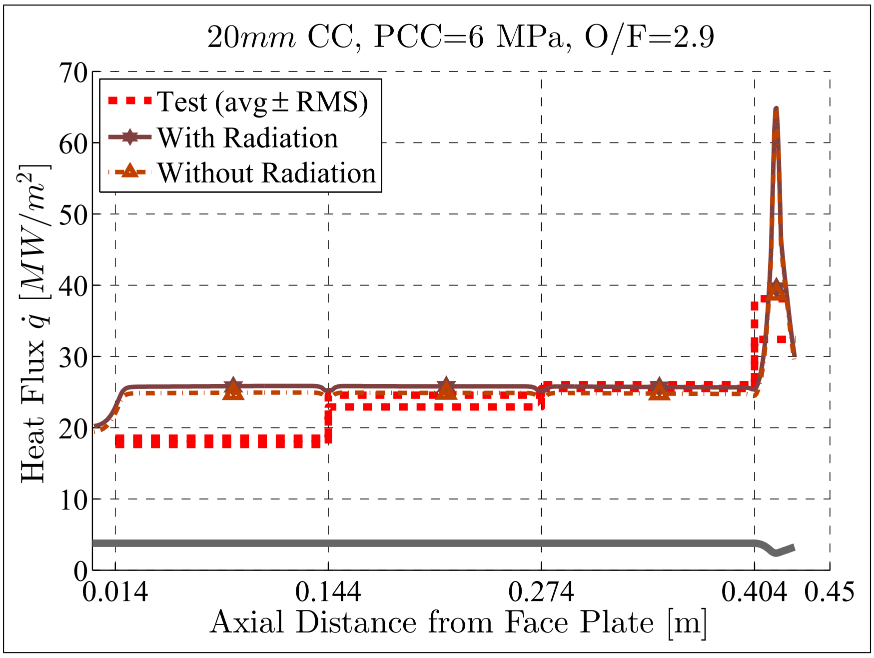

Fig. 5.16: Influence of Radiation for Test with 20 mm CC at Design Load Point (dashed red line represents integral heat flux by experiment, symbols represent the segment-wise integral value of simulation)

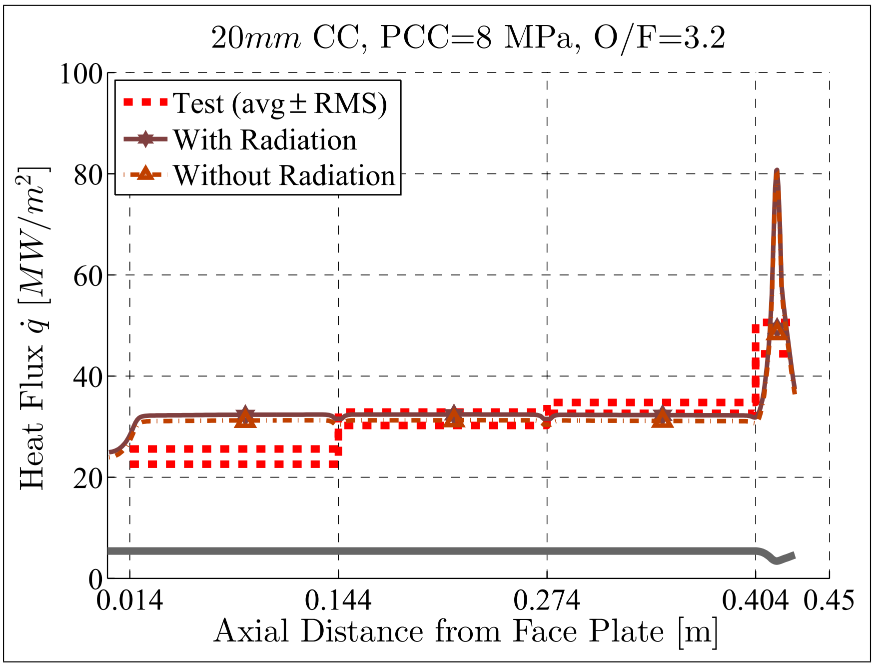

Fig. 5.17: Influence of Radiation for Test with 20 mm CC at High Mixture Ratio and High Combustion Pressure (dashed red line represents integral heat flux by experiment, symbols represent the segment-wise integral value of simulation)

seems to be unnecessary, for the investigated film cooling and CMC experiments, which were conducted at low mixture ratios, the heat transfer by radiation has been considered.

5.2.3 Influence of Coolant Heat Transfer Model

Since the heat transfer coefficient for the heat flux into the coolant is usually one order of magnitude higher than the heat transfer coefficient for the hot gas side, the influence of the coolant heat transfer model is expected to be low in most cases. Also, the investigated models of Kraussold (Eq. 2.58) and McAdams (Eq. 2.60) are both basing on bulk conditions (quasi-one-dimensional) in the cooling channel and use similar parameters. More sophisticated modeling like it is presented by *Woschnak* [99] is beneficial in case of e.g. stratification of the flow within the cooling channel but would otherwise increase modeling efforts and computational times.

In Fig. 5.18 throughout Fig. 5.22 the simulated heat fluxes using the baseline Kraussold model, the Kraussold model with correcting factors and the correlation by McAdams are given together with experimental results for different load cases. For the combustion chamber segments the results of the models investigated are virtually identical (deviations less than 5%). For the nozzle segment the correcting factors of the extended Kraussold model imply a slightly higher heat flux due to the start-up of the flow and the curvature of the cooling channel. However, the effect can be considered marginally.

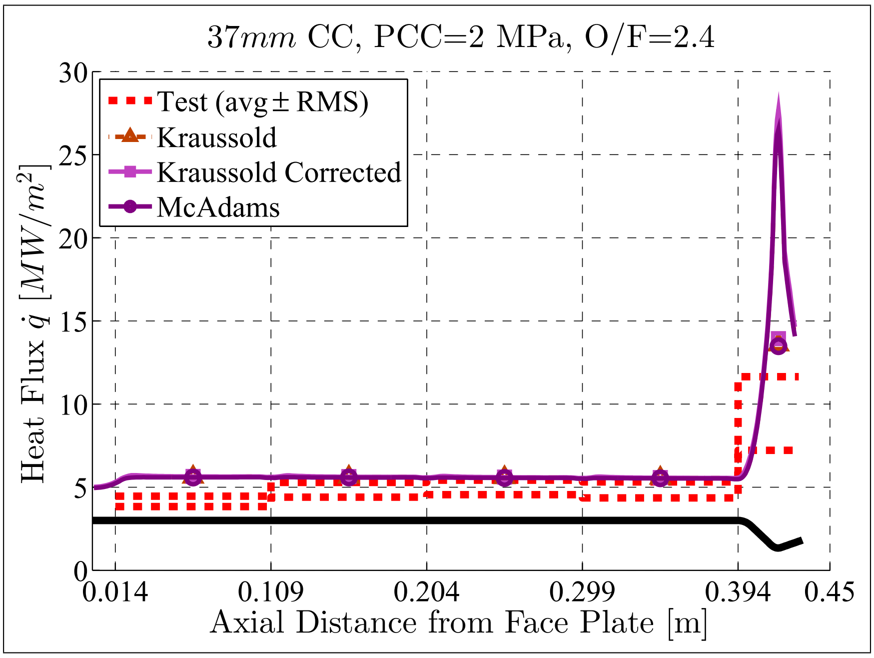

Fig. 5.18: Comparison of Coolant Heat Transfer Models for Test with 37 mm CC at Low Mixture Ratio and Low Combustion Pressure (dashed red line represents integral heat flux by experiment, symbols represent the segment-wise integral value of simulation)

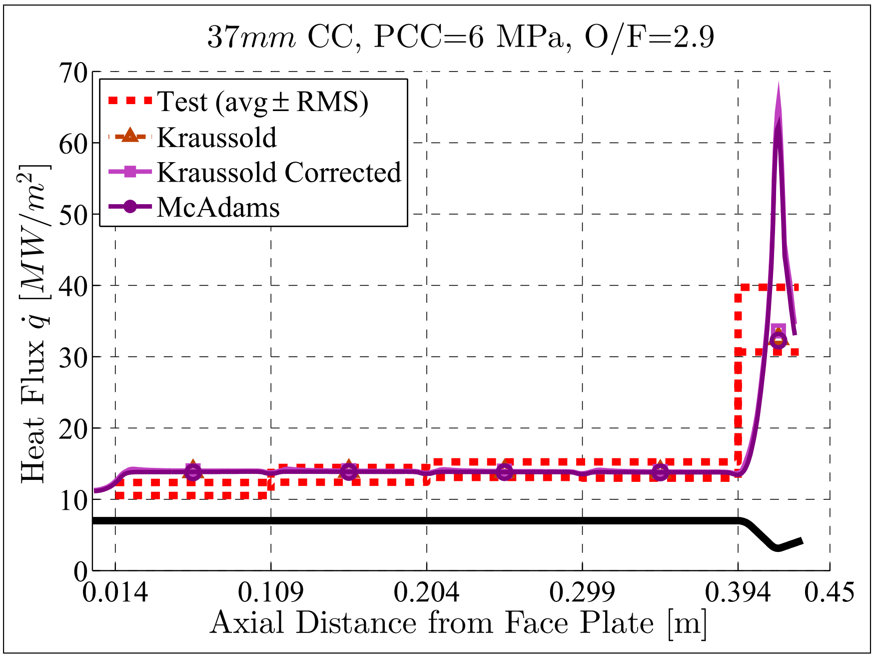

Fig. 5.19: Comparison of Coolant Heat Transfer Models for Test with 37 mm CC at Design Load Point (dashed red line represents integral heat flux by experiment, symbols represent the segment-wise integral value of simulation)

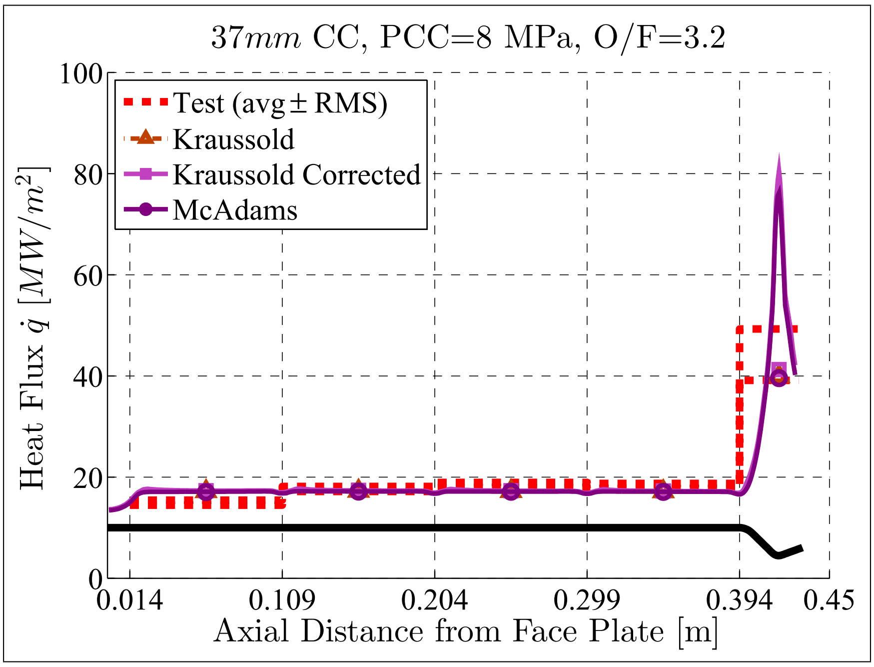

Fig. 5.20: Comparison of Coolant Heat Transfer Models for Test with 37 mm CC at High Mixture Ratio and High Combustion Pressure (dashed red line represents integral heat flux by experiment, symbols represent the segment-wise integral value of simulation)

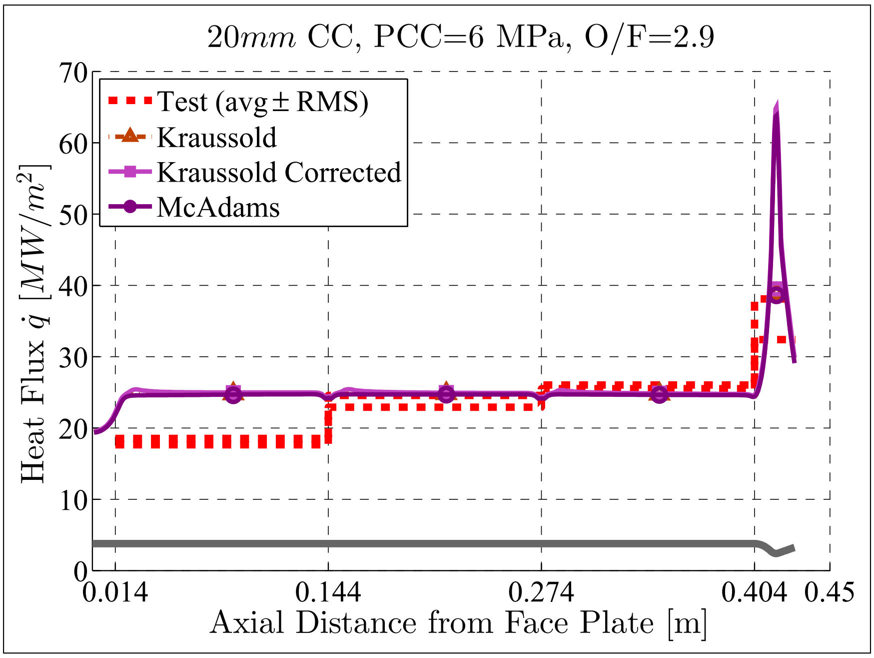

Fig. 5.21: Comparison of Coolant Heat Transfer Models for Test with 20 mm CC at Design Load Point (dashed red line represents integral heat flux by experiment, symbols represent the segment-wise integral value of simulation)

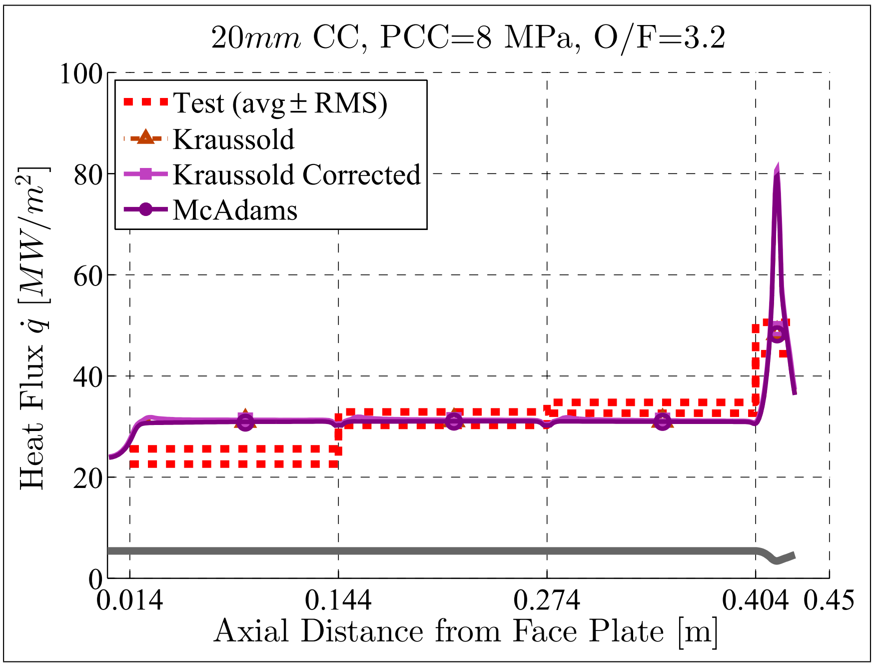

Fig. 5.22: Comparison of Coolant Heat Transfer Models for Test with 20 mm CC at High Mixture Ratio and High Combustion Pressure (dashed red line represents integral heat flux by experiment, symbols represent the segment-wise integral value of simulation)

5.2.4 Optimization of Sinyarev Model Parameters

Basing on the modified Sinyarev model (cf. Eq. 5.2) an optimization has been carried out in order to determine the optimum parameters of the generalized Sinyarev model as given in Eq. 5.4. Thereby, the deviation between predicted and measured heat flux in the fourth and nozzle segment has been minimized for 30 load points at or near nominal operational point of the combustion chamber in order to achieve full agreement here.

$$\alpha_{hg,conv,opt} = C_1 \cdot \frac{\lambda^{C_2} \cdot (\dot{m} \cdot c_p)^{(1-C_2)}}{d_h^{(2-C_2)}} \cdot \left[\frac{T_{aw}}{T_w}\right]^{C_3} \tag{5.4}$$

The parameters found are presented in Tab. 5.1. The deviation between experimental data and simulation using the such optimized Sinyarev model is given in Fig. 5.23 (cf. Tab. C.15) and the improvement (or worsening) of the simulation results compared to the uncorrected Sinyarev model (cf. Tab. C.5) is summarized in Tab. 5.2. In Fig. 5.24, Fig. 5.25 and Fig. 5.26 the simulated heat fluxes using optimized and baseline Sinyarev model are given aside experimental results.
Albeit the optimized correlation has no physical meaning in a close sense, the offset of the factors provide an insight into the constraints of the Sinyarev model. The increase of the temperature dependence C_3 indicates that the influence of the hot gas temperature (T_aw) is not sufficiently considered. This is in agreement with prior findings that the variation of the mixture ratio O/F is usually not modeled correctly [6, 22]. The change of sign for C_2 enhances the impact of the mass flux $\dot{m}/d_h^2$ thus density, which allows a better adaption of the pressure dependency, but (inadvertently) also upvaluates the importance of the enthalpy flow $\dot{m} \cdot c_p$. The factor C_1 compensates the variation of the values which are associated with units.

	C_1	C_2	C_3
Original	$1.9750 \cdot 10^{-2}$	0.18	0.35
Optimized	$1.0839 \cdot 10^{-6}$	-0.4693	1.2151

Tab. 5.1: Optimized Sinyarev Model Parameters (37 mm CC)

Although the parameters are significantly altered, the changes in heat flux for the 37 mm combustion chamber near nominal conditions are low and the general trend – overprediction for low mixture ratios and upstream segments, underprediction for high mixture ratios – is preserved. A slight improvement in the representation of the load points for $O/F = 2.4$ at $p_c = 6.0$ MPa and $O/F = 3.2$ at $p_c = 8.0$ MPa is apparent. Otherwise, if the parameter set is applied to lower combustion pressures, in the chamber segments deviations between simulation and measurement are decreased for lower mixture ratios but increased for moderate and higher mixture ratios. For the nozzle segment the modeling is generally improved although neither for the chamber segments nor for the nozzle segment a satisfying agreement i.e. deviation less than 20% between simulation and measurement can be achieved for major parts of the operational envelope. A similar behavior can be found for the 20 mm when applying the same set of coefficients (cf. Fig. 5.27 et seq., Fig. 5.29, Tab. 5.3 and Tab. C.16 in the annex).

p_c [MPa]	O/F [−]	Segment 1 [%]	Segment 2 [%]	Segment 3 [%]	Segment 4 [%]	Nozzle [%]
2.0	1.8	+115.7	+90.6	+69.1	+73.8	+67.4
2.0	2.4	+26.0	−6.2	−13.3	−8.9	+34.3
2.0	2.9	−25.5	−29.1	−29.6	−29.9	+41.7
4.0	1.8	+70.2	+52.5	+46.2	+47.4	+26.6
4.0	2.4	+27.3	+21.5	+20.5	+21.5	+12.8
4.0	2.9	+6.7	−8.3	−10.8	−11.2	+7.3
4.0	3.2	−4.2	−11.4	−11.3	−11.7	+4.9
6.0	2.4	+8.8	+6.4	+6.5	+7.3	−0.7
6.0	2.9	+3.3	+0.7	−0.5	−0.5	+1.0
6.0	3.2	+2.7	−0.5	−1.5	−1.7	+1.1
8.0	2.4	−2.7	−2.6	−2.3	−1.9	−3.6
8.0	2.9	−5.0	−3.7	−1.0	−1.1	+1.7
8.0	3.2	−5.6	−0.8	+4.8	+4.4	−0.6

Tab. 5.2: Improvement of Heat Flux Prediction from Reference Model for 37 mm Combustion Chamber Using Optimized Sinyarev Model Parameters ("-" worsening, "+" improvement)

p_c [MPa]	O/F [−]	Segment 1 [%]	Segment 2 [%]	Segment 3 [%]	Nozzle [%]
4.0	2.9	+27.5	−12.2	−18.4	+23.9
4.0	3.2	+23.8	−17.5	−19.0	+19.9
6.0	2.4	+28.5	+17.6	+15.1	+11.2
6.0	2.9	+13.8	−1.2	−10.0	+2.1
6.0	3.2	+12.6	−8.6	−9.7	+3.2
8.0	2.4	+13.9	+8.0	+6.6	+1.6
8.0	2.9	+7.3	+3.7	−2.8	+0.3
8.0	3.2	+6.1	−1.6	−2.7	+0.1

Tab. 5.3: Improvement of Heat Flux Prediction from Reference Model for 20 mm Combustion Chamber Using Optimized Sinyarev Model Parameters ("-" worsening, "+" improvement)

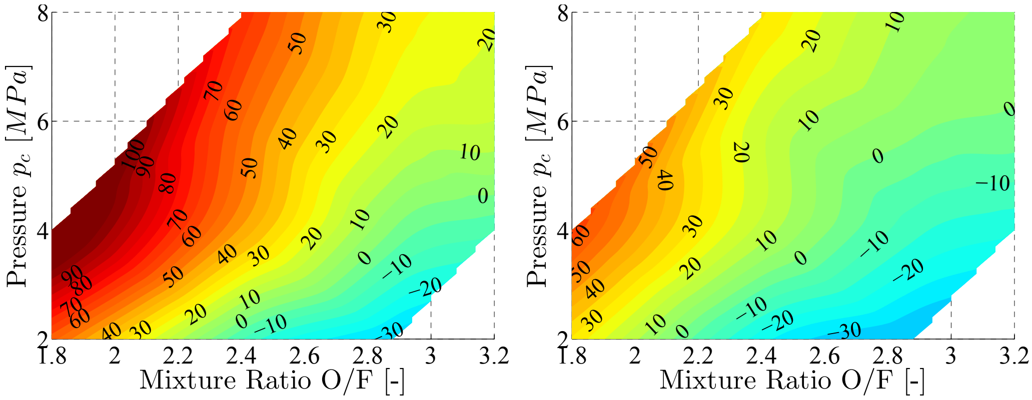

(a) Segment 1

(b) Segment 2

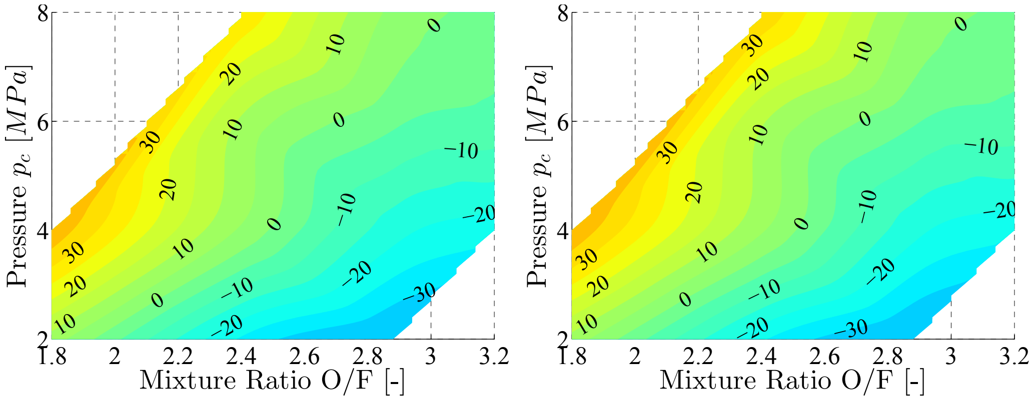

(c) Segment 3

(d) Segment 4

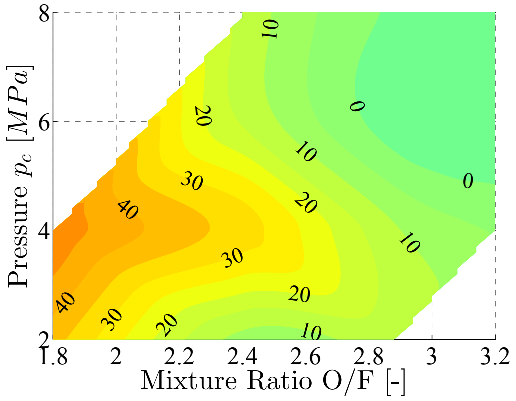

(e) Nozzle Segment

Fig. 5.23: Deviation of Heat Flux Prediction from Measurements for 37 mm Combustion Chamber Using Optimized Sinyarev Model Parameters (isolines in [%]; "-" underprediction–blue, "+" overprediction–red, agreement–green)

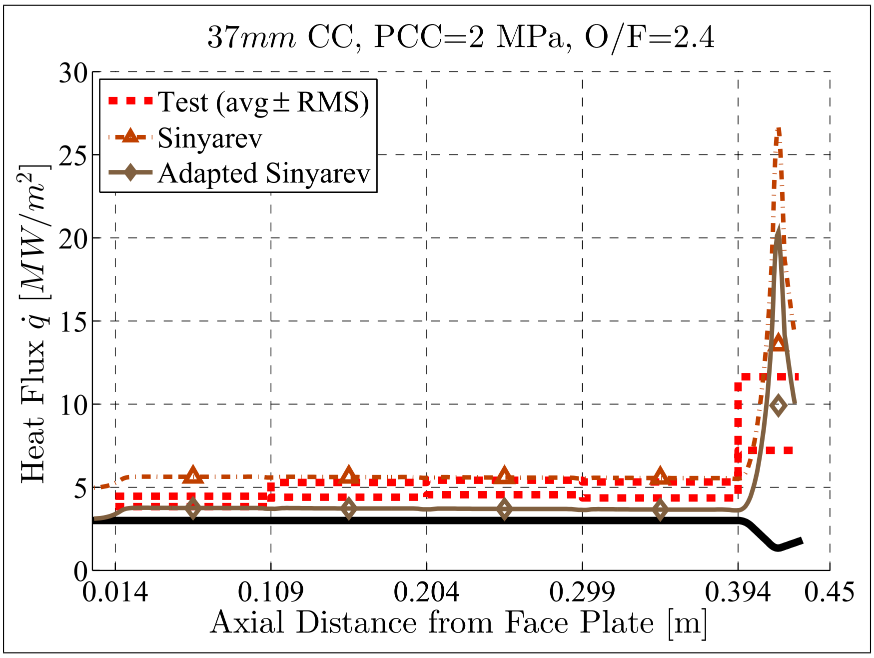

Fig. 5.24: Heat Flux Profile with Optimized Sinyarev Parameters for Test with 37 mm CC at Low Mixture Ratio and Low Combustion Pressure (dashed red line represents integral heat flux by experiment, symbols represent the segment-wise integral value of simulation)

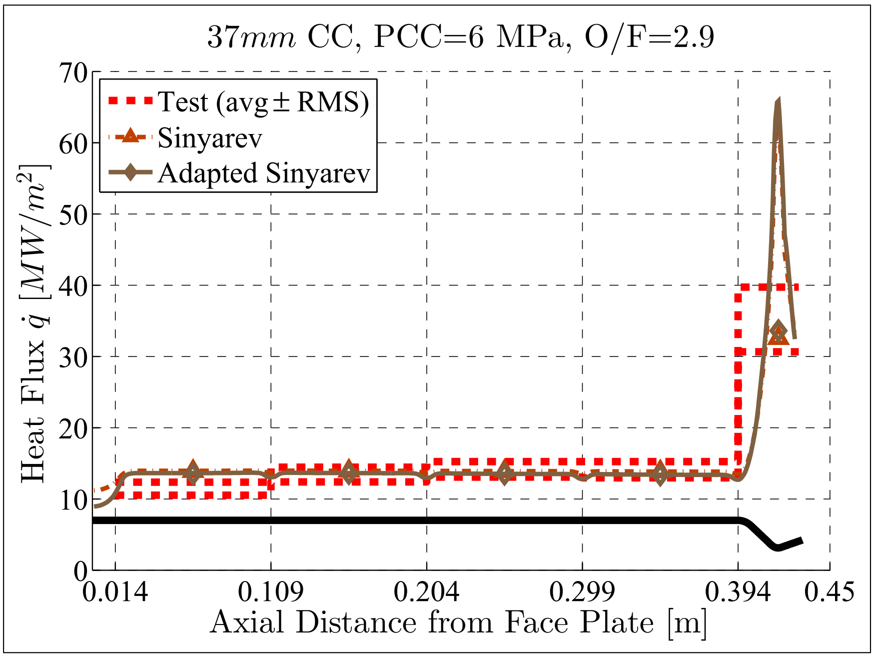

Fig. 5.25: Heat Flux Profile with Optimized Sinyarev Parameters for Test with 37 mm CC at Design Load Point (dashed red line represents integral heat flux by experiment, symbols represent the segment-wise integral value of simulation)

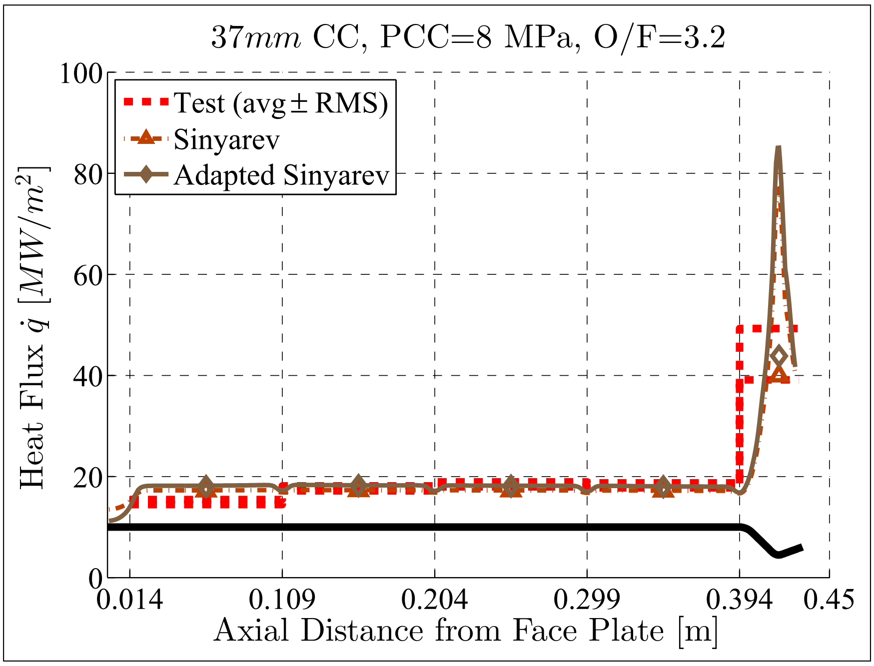

Fig. 5.26: Heat Flux Profile with Optimized Sinyarev Parameters for Test with 37 mm CC at High Mixture Ratio and High Combustion Pressure (dashed red line represents integral heat flux by experiment, symbols represent the segment-wise integral value of simulation)

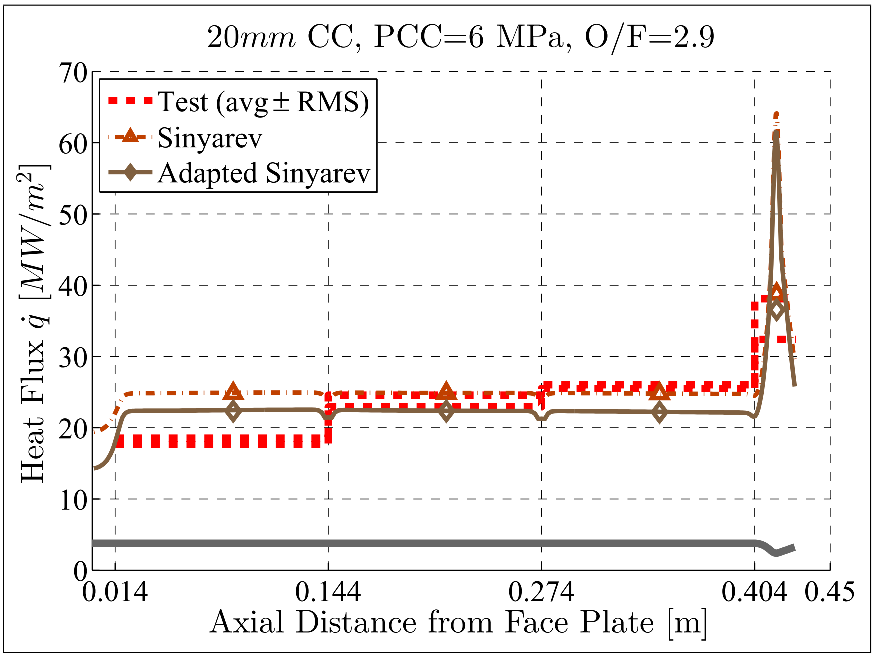

Fig. 5.27: Heat Flux Profile with Optimized Sinyarev Parameters for Test with 20 mm CC at Design Load Point (dashed red line represents integral heat flux by experiment, symbols represent the segment-wise integral value of simulation)

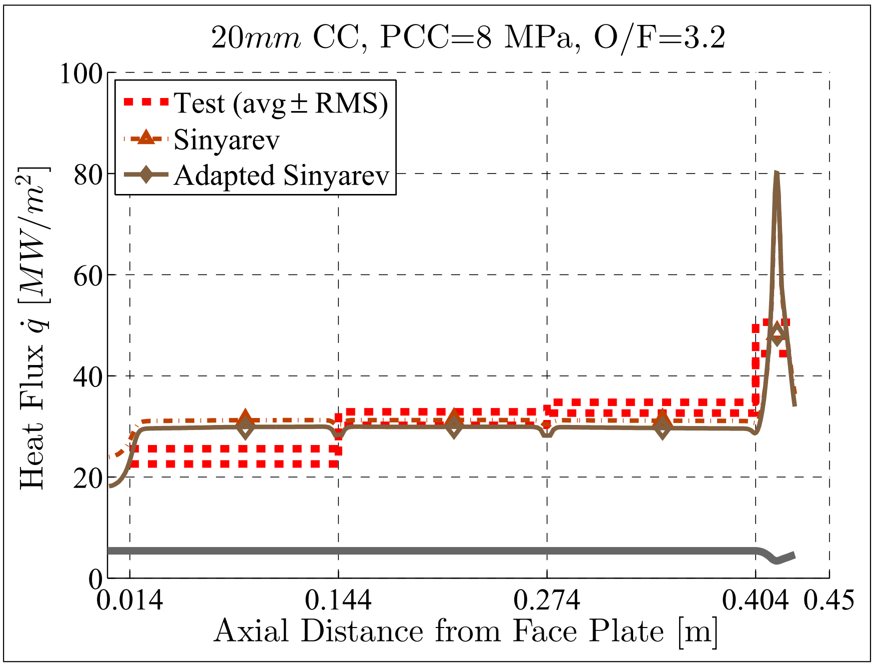

Fig. 5.28: Heat Flux Profile with Optimized Sinyarev Parameters for Test with 20 mm CC at High Mixture Ratio and High Combustion Pressure (dashed red line represents integral heat flux by experiment, symbols represent the segment-wise integral value of simulation)

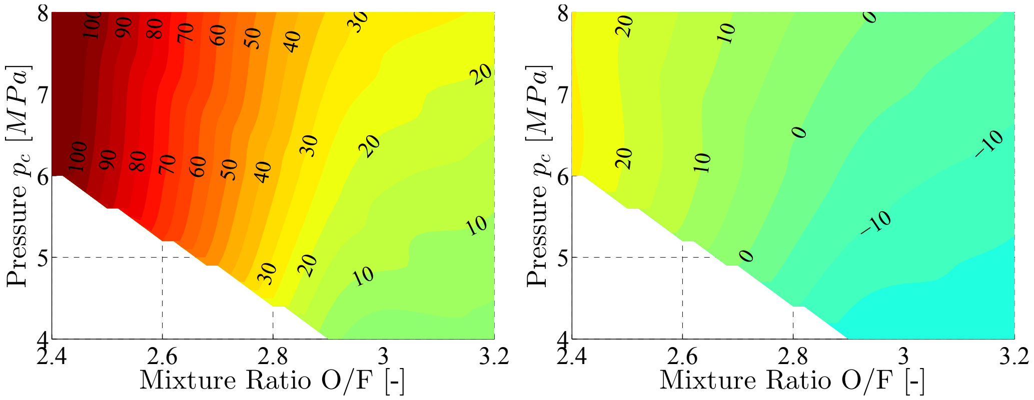

(a) Segment 1 (b) Segment 2

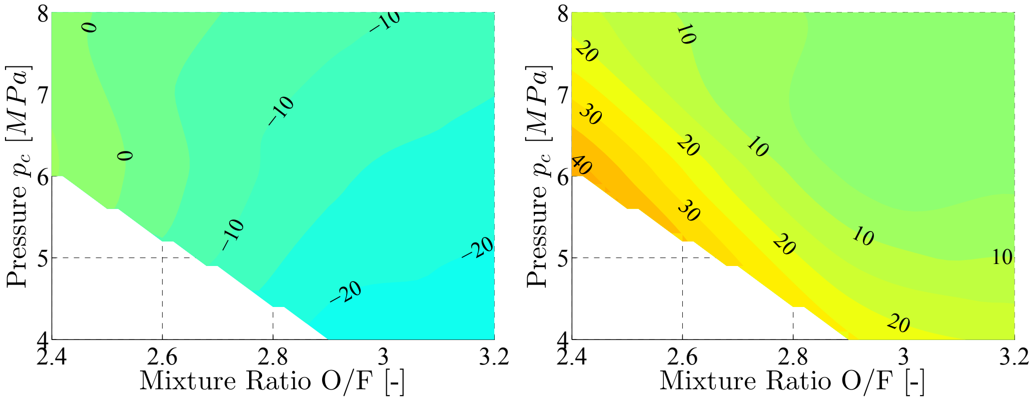

(c) Segment 3 (d) Nozzle Segment

Fig. 5.29: Deviation of Heat Flux Prediction from Measurements for 20 mm Combustion Chamber Using Optimized Sinyarev Model Parameters (isolines in [%]; "-" underprediction–blue, "+" overprediction–red, agreement–green)

The optimization of the Sinyarev model parameters shows the potential to improve the simulation. An independent variation of mass flux and enthalpy flow as well as additional correction factors for density, Mach number or hot gas temperature are recommendable. However, for representing the slope of the heat flux along the engine axis extensive modeling efforts comprising correlations for e.g. injection (number and type of injector, velocity ratio, Weber number) would be necessary. This is out of scope and therefore a general adaption of the Sinyarev model parameters is not constructive for this work.

5.2.5 Adaption of Local Adiabatic Wall Temperature

Swirl injector elements as used in the reference setup are known to lay a propellant film i.e. a kerosene film in the present case on the combustion chamber wall. The modeling of this film using common film models is problematic due to a lack of experimental data regarding droplet size, deposition and entrainment rates or initial film thickness or film velocity. Therefore, the existence of a fuel rich boundary layer is assumed represented by Eq. 5.5 resulting in reduced local gas temperatures due to the mixture ratio shift and the decrease in combustion efficiency, which is modeled by Eq. 5.6 (cf. section 4.1.2).

$$\left(\frac{O}{F}\right)_s = \left(\frac{O}{F}\right)_{inj} - \left(\left(\frac{O}{F}\right)_{inj} - 1\right) \cdot \exp\left(-s \cdot C_I \cdot \left(\frac{O}{F}\right)_{inj}^{C_{II}} \cdot \left(\frac{p_c}{10^5}\right)^{C_{III}}\right) \tag{5.5}$$

$$\eta_{c^*} = 0.892912 \cdot \left(\frac{O}{F}\right)_s^{0.018138} \cdot \left(\frac{p_c}{10^5}\right)^{0.012481} \tag{5.6}$$

The specific parameters as depicted in Tab. 5.4 have been determined for the 37 mm combustion chamber by method of least squares using a data set of 36 out of 81 load points representing the full operational envelope. The final parameter optimization required 250 iterations and approx. 2 million CPU seconds (three days). In Fig. 5.30, Fig. 5.31 and Fig. 5.32 the simulated heat fluxes using a fuel rich boundary layer, the results using reference model and experimental data are presented for the 37 mm combustion chamber.

C_I	C_{II}	C_{III}
4.9408	0.17053	0.77838

Tab. 5.4: Parameters for Adaption of Adiabatic Wall Temperature (37 mm CC)

Detailed analysis shows that the local recovery temperature is substantially altered by the method described but the effect of the lowered hot gas temperature is compensated or even overcompensated by phenomena affecting the determination of the hot wall heat transfer coefficient (see Fig. 5.33). According to this, no satisfying parameter set could be found in the optimization. The consideration of the fuel rich boundary layer necessarily requires additional modeling efforts regarding e.g film deposition, the entrainment and potential pyrolysis of the fuel. Therefore, this approach has not been continued.

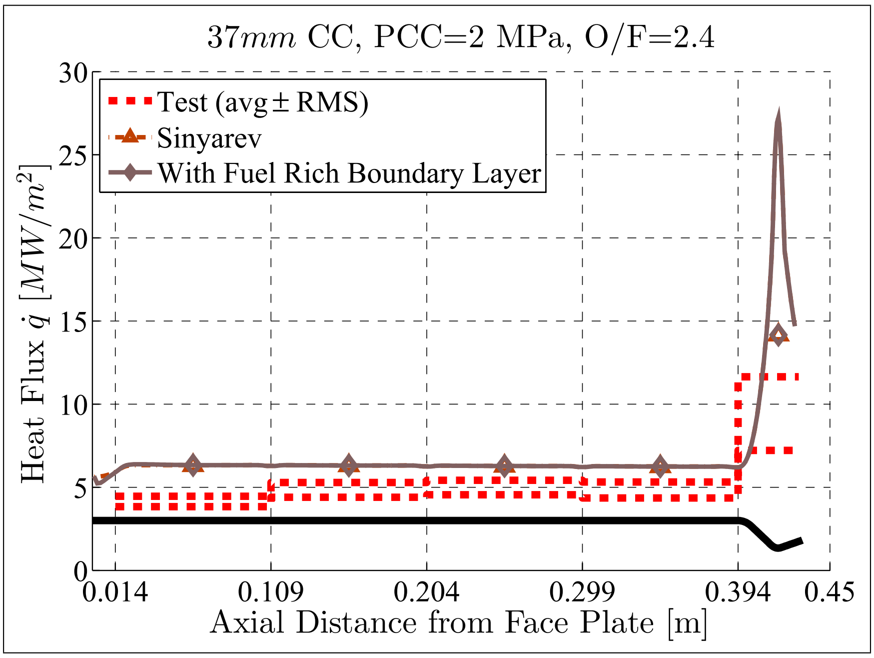

Fig. 5.30: Fuel Rich Boundary Layer for Test with 37 mm CC at Low Mixture Ratio and Low Combustion Pressure (dashed red line represents integral heat flux by experiment, symbols represent the segment-wise integral value of simulation)

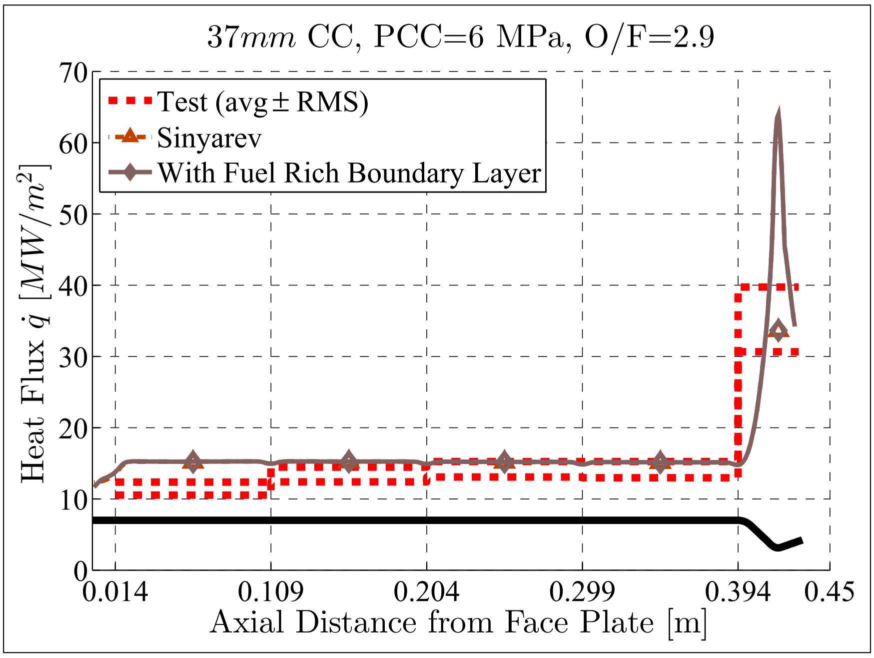

Fig. 5.31: Fuel Rich Boundary Layer for Test with 37 mm CC at Design Load Point (dashed red line represents integral heat flux by experiment, symbols represent the segment-wise integral value of simulation)

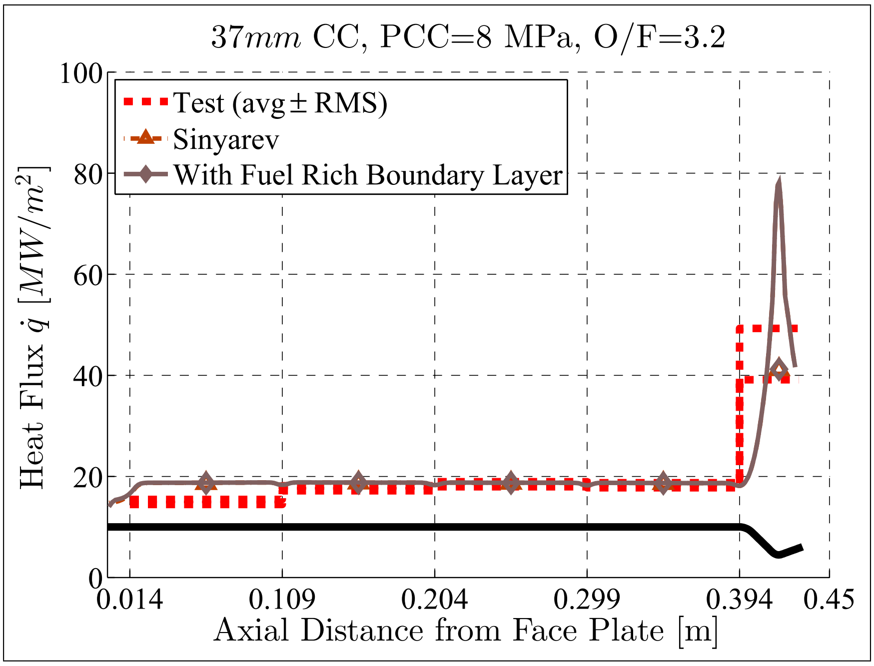

Fig. 5.32: Fuel Rich Boundary Layer for Test with 37 mm CC at High Mixture Ratio and High Combustion Pressure (dashed red line represents integral heat flux by experiment, symbols represent the segment-wise integral value of simulation)

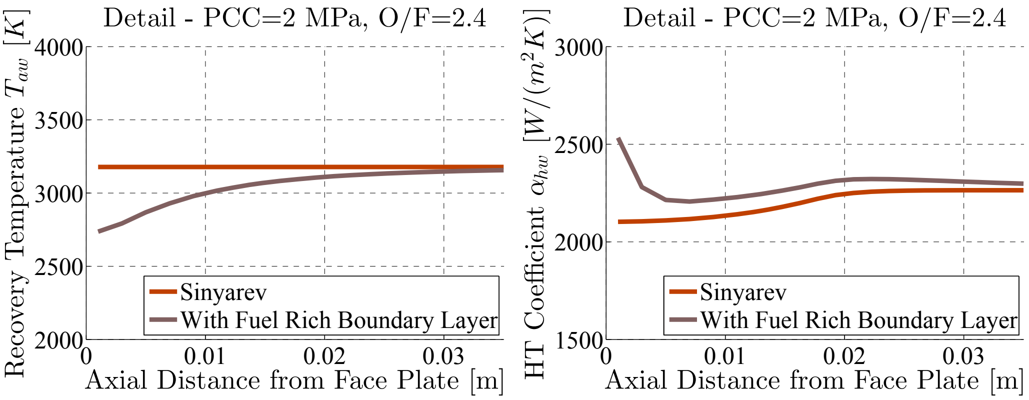

(a) Recovery Temperature (b) Heat Transfer Coefficient

Fig. 5.33: Influences on Heat Transfer of Fuel Rich Boundary Layer Model for 37 mm Combustion Chamber

5.2.6 Adaption of Heat Transfer Coefficient

Taking into account the heat flux correlation as presented in Eq. 4.2 it has been assumed that $\dot{q} \propto \alpha_{hg}$ for $T_{aw} \approx const.$ and therefore the hot gas side heat transfer coefficient provided a by semi-empirical correlation might be corrected and adapted to experimental data using the following approach

$$\alpha_{hg}|_s \left[\frac{W}{m^2 \cdot K}\right] = C_x|_s \cdot OF^{C_y|_s} \cdot PCC\,[bar]^{C_z|_s} \cdot \alpha_{hg,Sinyarev}|_s \tag{5.7}$$

where s is any point along the engine axis and $C_x|_s$, $C_y|_s$ and $C_z|_s$ are the correction factors at position s. This procedure is different to traditional approaches where the corrective terms are applied to the adiabatic wall temperature T_{aw} but allows e.g. the application of the same set of corrections to different hardware configurations as long as the injector characteristics remain unchanged. Using for computational cost issues a reduced dataset of 36 out of 81 load points, which represent the full test envelope, the parameters as given in Tab. 5.5 have been determined by the method of least squares. The carried out optimization required in the order of 25 million CPU seconds.

	Segment 1	Segment 2	Segment 3	Segment 4	Nozzle
C_x	0.1604	0.1904	0.1988	0.1930	0.0138
C_y	2.1812	1.5731	1.3633	1.5173	1.0289
C_z	−0.1651	−0.0216	0.0262	−0.0158	0.7846

Tab. 5.5: Parameters for Empiric Correction of Modified Sinyarev Model (37 mm CC)

The deviations between measured and empirically corrected heat fluxes and the improvement of the simulation results compared to the uncorrected Sinyarev model (cf. Tab. C.5 in the annex) are summarized in Fig. 5.34 and Tab. 5.6, respectively. For most parts of the test envelope a good agreement (better ±10%) is achieved. Some shortcomings remain for load points with a low mixture ratio where soot and incomplete mixing may play a major role and in the nozzle segment where the complex flow conditions hardly allow the application of such a simple empiric correction.

A comparison of the heat flux profiles along chamber axis of simulations with and without the empiric correction is given for different load cases in Fig. 5.35, Fig. 5.36 and Fig. 5.37. The simulated integral heat fluxes (symbols) match the confidence level of the measured heat fluxes well. However, some waviness is created at the segment interfaces caused by the absence of reliable reference data for the numerical optimization of the supporting points required at these positions. Similarly, the absolute peak heat flux in the nozzle throat is influenced by assumptions made for the heat flux at begin of the convergent part ($\dot{q} \approx \dot{q}_{4th\ Segment}$) and nozzle exit ($\dot{q} \approx 0.9 \cdot \dot{q}_{4th\ Segment}$). The correction itself is configuration specific. The application of the same empiric correction to the 20 mm combustion chamber failed as it leads to an increased deviation between simulated and measured heat flux. An empiric correction specific to the 20 mm chamber was not further investigated due to the very high computational costs for this approach.

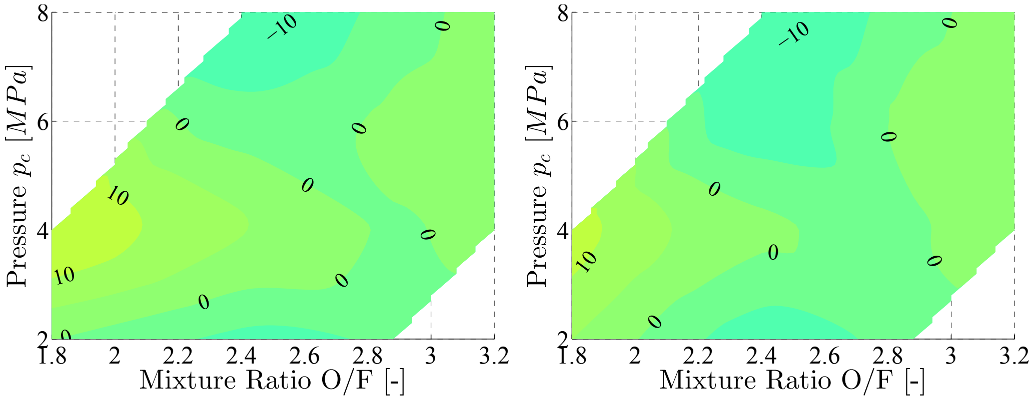

(a) Segment 1 (b) Segment 2

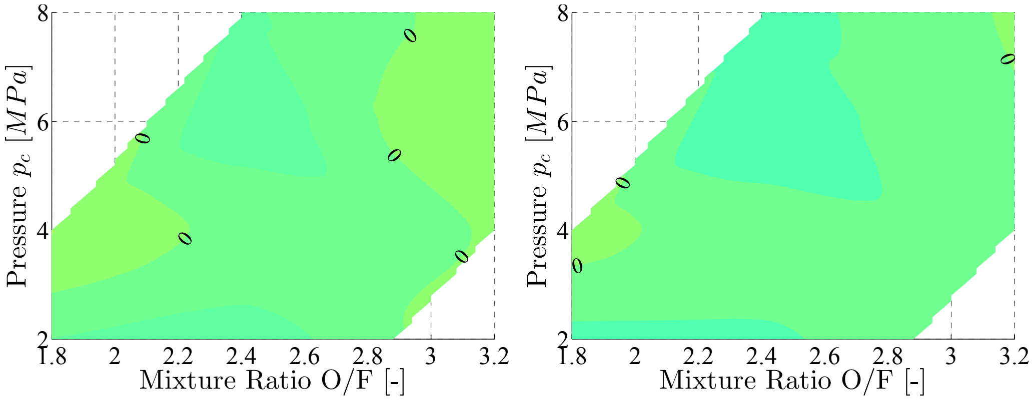

(c) Segment 3 (d) Segment 4

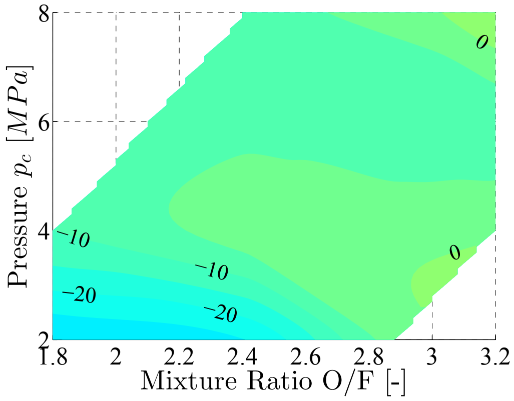

(e) Nozzle Segment

Fig. 5.34: Deviation of Heat Flux Prediction from Measurements for 37 mm Combustion Chamber Using Modified Sinyarev Model with Empiric Corrections (isolines in [%]; “-” underprediction–blue, “+” overprediction–red, agreement–green)

p_c [MPa]	O/F [−]	Segment 1 [%]	Segment 2 [%]	Segment 3 [%]	Segment 4 [%]	Nozzle [%]
2.0	1.8	+165.7	+108.4	+74.4	+78.4	+74.3
2.0	2.4	+29.4	+8.8	+4.6	+8.9	+23.9
2.0	2.9	+4.3	+6.5	+5.8	+5.0	+45.5
4.0	1.8	+174.8	+103.5	+80.2	+85.2	+65.5
4.0	2.4	+65.5	+32.4	+22.9	+24.2	+39.0
4.0	2.9	+11.9	+4.8	+5.8	+4.7	+11.0
4.0	3.2	+1.4	+5.4	+8.7	+8.6	+5.9
6.0	2.4	+60.0	+15.1	+8.1	+8.5	+6.8
6.0	2.9	+17.3	+2.6	+0.9	+0.8	−1.2
6.0	3.2	+12.1	+0.9	+0.7	+1.0	+0.1
8.0	2.4	+54.0	+16.4	+21.7	+27.1	−3.0
8.0	2.9	+21.0	+2.2	+1.5	+0.6	−0.0
8.0	3.2	+11.6	−1.0	+3.5	+3.1	−4.1

Tab. 5.6: Improvement of Heat Flux Prediction from Reference Model for 37 mm Combustion Chamber Using Modified Sinyarev Model with Empiric Corrections ("-" worsening, "+" improvement)

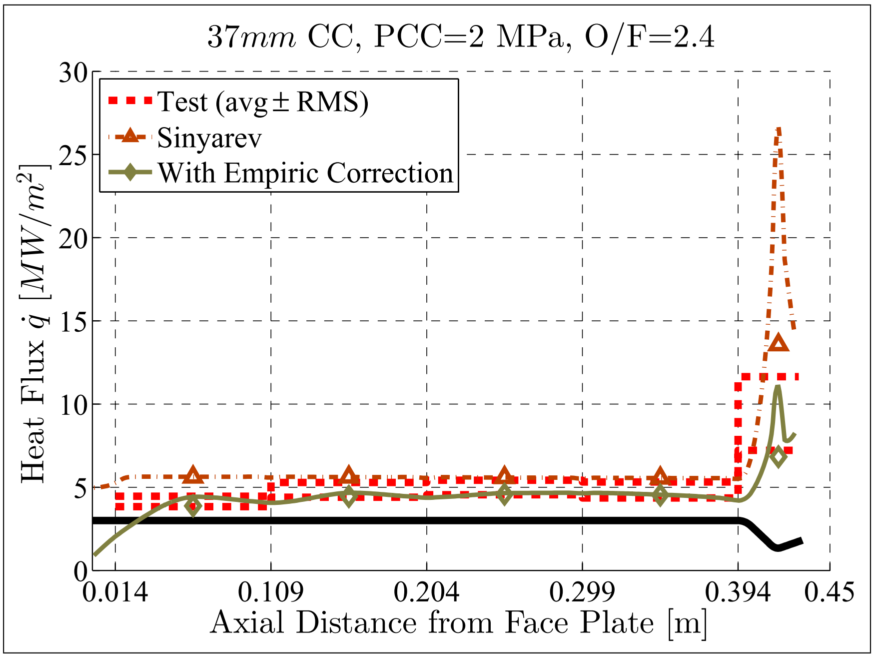

Fig. 5.35: Empiric Corrected Sinyarev for Test with 37 mm CC at Low Mixture Ratio and Low Combustion Pressure (dashed red line represents integral heat flux by experiment, symbols represent the segment-wise integral value of simulation)

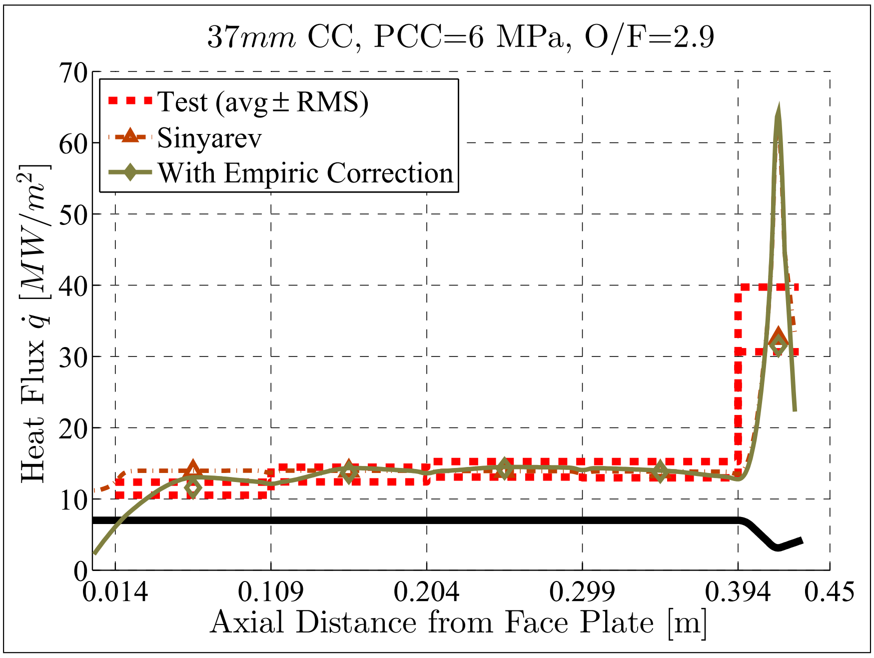

Fig. 5.36: Empiric Corrected Sinyarev for Test with 37 mm CC at Design Load Point (dashed red line represents integral heat flux by experiment, symbols represent the segment-wise integral value of simulation)

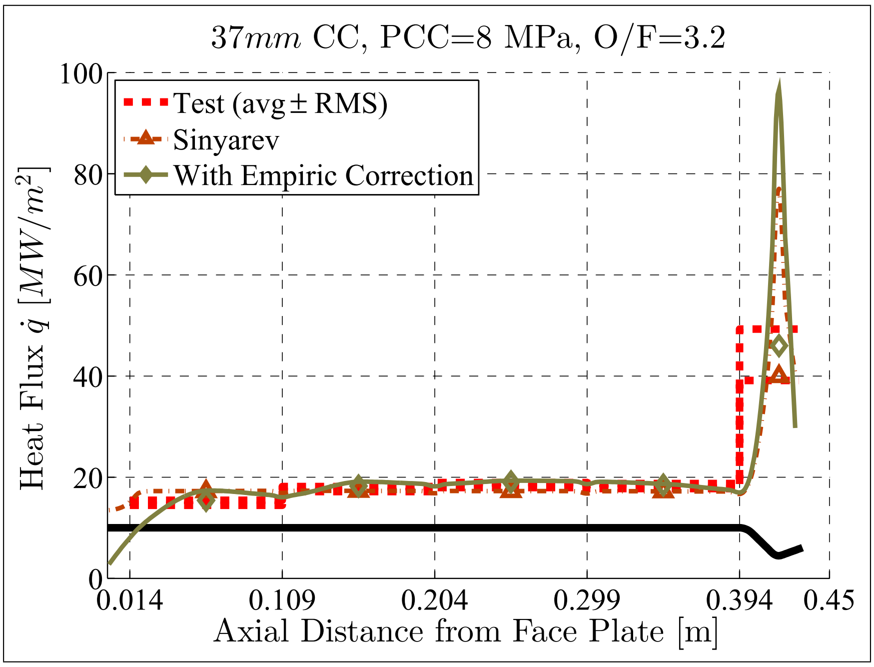

Fig. 5.37: Empiric Corrected Sinyarev for Test with 37 mm CC at High Mixture Ratio and High Combustion Pressure (dashed red line represents integral heat flux by experiment, symbols represent the segment-wise integral value of simulation)

5.2.7 Implementation of a Simple Injector Correction

The introduction of an empiric adaption to the heat transfer model as presented in section 5.2.6 is quite accurate but requires both a comprehensive experimental database and several iterations during the optimization processes. It cannot easily be applied to the 20 mm combustion chamber configuration and an injector element change would render the corrections useless as combustion characteristics will change. Therefore, for daily use a simplified approach would be beneficial.

Representing the characteristics of the employed swirl injectors by a film model led to unsatisfying results in the past [96]. Based on work of *Ponomarenko* [100] and *Kudryavtsev* [101] on the “Yevlev Method”, a corrective function for the heat load characteristic of a generic injector element near the face plate, which is presented in Eq. 5.8, has been developed and applied on a CH4/GOX coaxial single injector heat sink hardware [102].

$$\dot{q}_{w,corr} = \dot{q}_w \cdot C_a \cdot \left((1 - C_b) + C_b \cdot tanh\left(\frac{s}{l_{max}} \pi \right) \right) \tag{5.8}$$

The only parameters are an initial heat transfer $1-C_2$, the axial coordinate s, the maximum combustion length l_{max} and a multiplier C_a. Thereby, the arrangement of the parameters allows an easy implementation into a constrained multivariable optimizer.

Using the reduced dataset of 36 out the of 81 load points, which represent the full test envelope, the parameters have been determined by the method of least squares as $C_a = 0.746$, $C_b = 0.999$ and $l_{max} = 0.154\ m$, which only represented a slight improvement compared to the modified Sinyarev model. Performing an load point dependent optimization the parameters as shown in Tab. 5.7 for the 37 mm combustion chamber and Tab. 5.8 for the 20 mm CC have been found. The deviations between experimental data and simulation using these parameters are given in Fig. 5.38 and Fig. 5.39. Though the simplicity of the correction, a good agreement (better ±20%) between simulation and experiment has been achieved throughout a wide part of the operational envelope. The improvement or worsening of the simulation compared to the modified Sinyarev model is summarized in Tab. 5.9 and Tab. 5.10, respectively.

Finally, profiles along chamber axis are given for the simulated heat fluxes using startup correction aside the experimental results in Fig. 5.40 et seqq. and Fig. 5.43 et seqq.

A general and universally valid injector correction could not be found, since the local improvements would always provoke worsening in other parts of the test range. However, for a narrow band of mixture ratios and pressures the simple injector correction can be very helpful to fit simulation results to experimental data at a fraction of the computational costs which the adaption of heat transfer coefficient model requires.

p_c [MPa]	O/F [−]	C_a [−]	C_b [−]	l_{max} [m]
2.0	1.8	0.41985	1.000	0.167
2.0	2.4	0.63669	1.000	0.113
2.0	2.9	0.69482	1.000	0.075
4.0	1.8	0.44759	0.986	0.250
4.0	2.4	0.60200	1.000	0.152
4.0	2.9	0.79830	1.000	0.118
4.0	3.2	0.85644	1.000	0.114
6.0	2.4	0.73676	1.000	0.210
6.0	2.9	0.91814	1.000	0.177
6.0	3.2	0.94476	1.000	0.173
8.0	2.4	0.75037	0.988	0.243
8.0	2.9	0.93746	1.000	0.190
8.0	3.2	0.95960	1.000	0.168

Tab. 5.7: Parameters for a Simple Injector Correction (37 mm CC)

p_c [MPa]	O/F [−]	C_a [−]	C_b [−]	l_{max} [m]
4.0	2.9	0.86984	1.000	0.194
4.0	3.2	0.91393	1.000	0.191
6.0	2.4	0.76632	0.966	0.500
6.0	2.9	1.03525	0.958	0.353
6.0	3.2	1.05240	0.992	0.259
8.0	2.4	1.04489	0.956	0.797
8.0	2.9	1.08609	0.937	0.460
8.0	3.2	1.11424	0.957	0.366

Tab. 5.8: Parameters for a Simple Injector Correction (20 mm CC)

p_c [MPa]	O/F [−]	Segment 1 [%]	Segment 2 [%]	Segment 3 [%]	Segment 4 [%]	Nozzle [%]
2.0	1.8	+167	+114	+73.8	+75.9	+89.7
2.0	2.4	+24.9	+4.1	−2.9	+2.3	+32.9
2.0	2.9	−18.2	−17.3	−17.3	−17.2	+37.2
4.0	1.8	+186	+108	+78.1	+80.5	+65.5
4.0	2.4	+64.7	+27.2	+11.2	+15.4	+38.8
4.0	2.9	+1.3	−4.5	−6.5	−6.4	+11.4
4.0	3.2	−10.1	−4.5	−4.2	−4.1	+6.0
6.0	2.4	+58.9	+21.5	+12.4	+15.7	+5.7
6.0	2.9	+14.8	+2.0	+1.2	+1.1	−2.1
6.0	3.2	+10.3	+0.3	+0.8	+0.6	−1.3
8.0	2.4	+53.0	+26.0	+24.8	+25.5	−6.3
8.0	2.9	+14.5	+0.8	+2.0	+1.7	−1.3
8.0	3.2	+6.0	+0.3	+5.1	+5.2	+0.3

Tab. 5.9: Improvement of Heat Flux Prediction from Reference Model for 37 mm Combustion Chamber Using Modified Sinyarev Model with a Startup Correction ("-" worsening, "+" improvement)

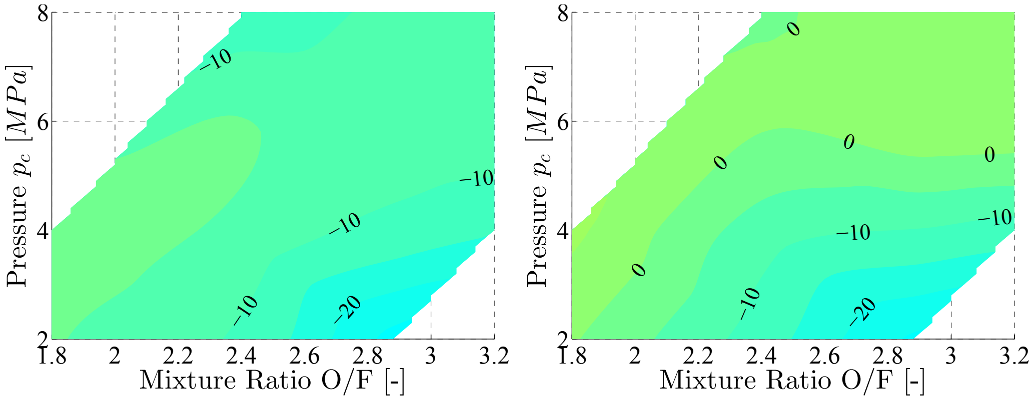

(a) Segment 1 (b) Segment 2

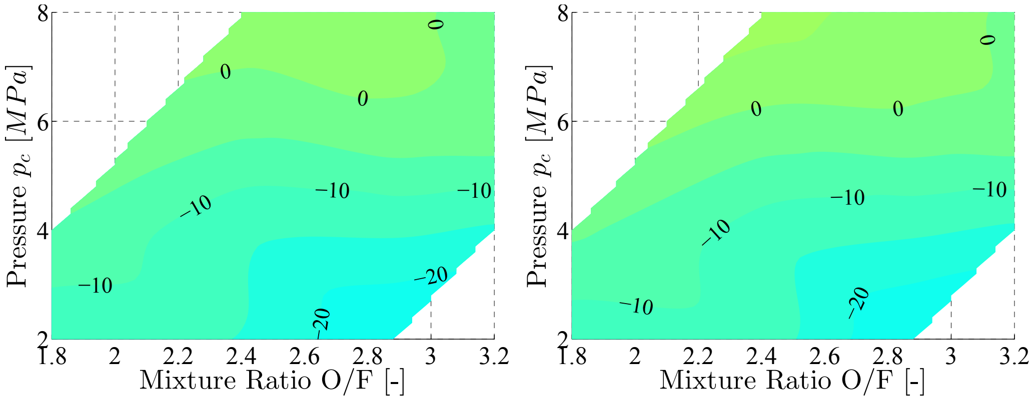

(c) Segment 3 (d) Segment 4

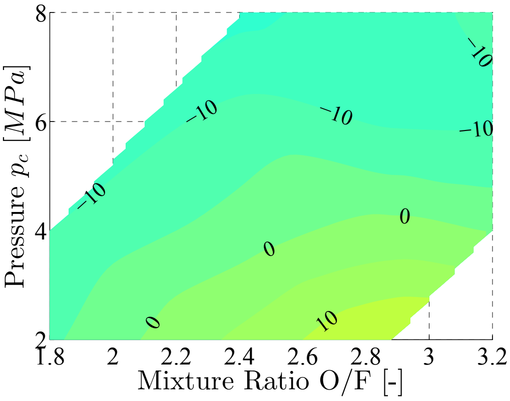

(e) Nozzle Segment

Fig. 5.38: Deviation of Heat Flux Prediction from Measurements for 37 mm Combustion Chamber Using Modified Sinyarev Model with Startup Correction (isolines in [%]; "-" underprediction–blue, "+" overprediction–red, agreement–green)

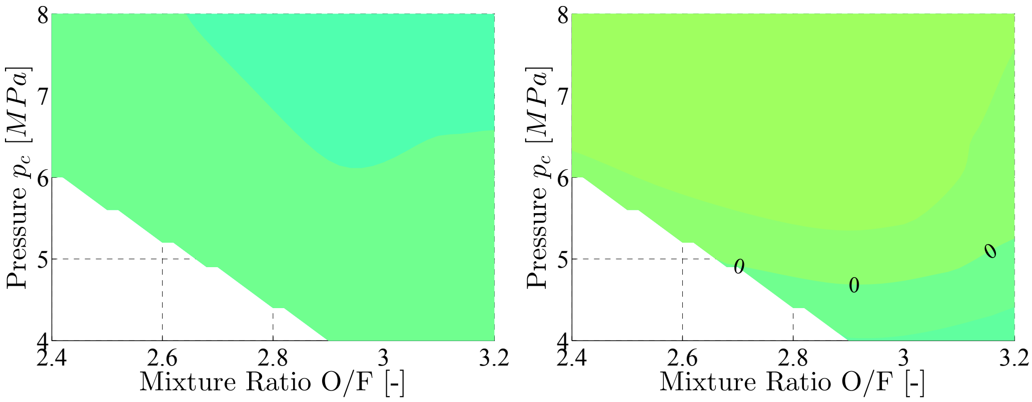

(a) Segment 1 (b) Segment 2

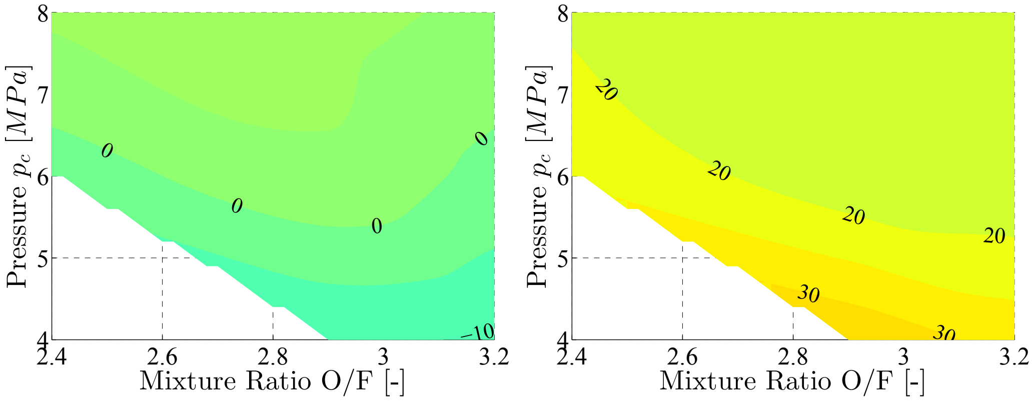

(c) Segment 3 (d) Nozzle Segment

Fig. 5.39: Deviation of Heat Flux Prediction from Measurements for 20 mm Combustion Chamber Using Modified Sinyarev Model with Startup Correction (isolines in [%]; "-" underprediction–blue, "+" overprediction–red, agreement–green)

p_c [MPa]	O/F [−]	Segment 1 [%]	Segment 2 [%]	Segment 3 [%]	Nozzle [%]
4.0	2.9	+30.1	−0.5	−6.5	+15.9
4.0	3.2	+22.4	−5.0	−6.1	+12.9
6.0	2.4	+128	+39.7	+17.0	+29.9
6.0	2.9	+32.6	−3.8	+0.5	−6.6
6.0	3.2	+20.9	+0.4	+4.9	−4.9
8.0	2.4	+122	+24.9	+3.0	−0.0
8.0	2.9	+31.6	−0.8	−0.3	−5.3
8.0	3.2	+19.1	+0.6	+6.1	−5.7

Tab. 5.10: Improvement of Heat Flux Prediction from Reference Model for 20 mm Combustion Chamber Using Modified Sinyarev Model with a Startup Correction ("-" worsening, "+" improvement)

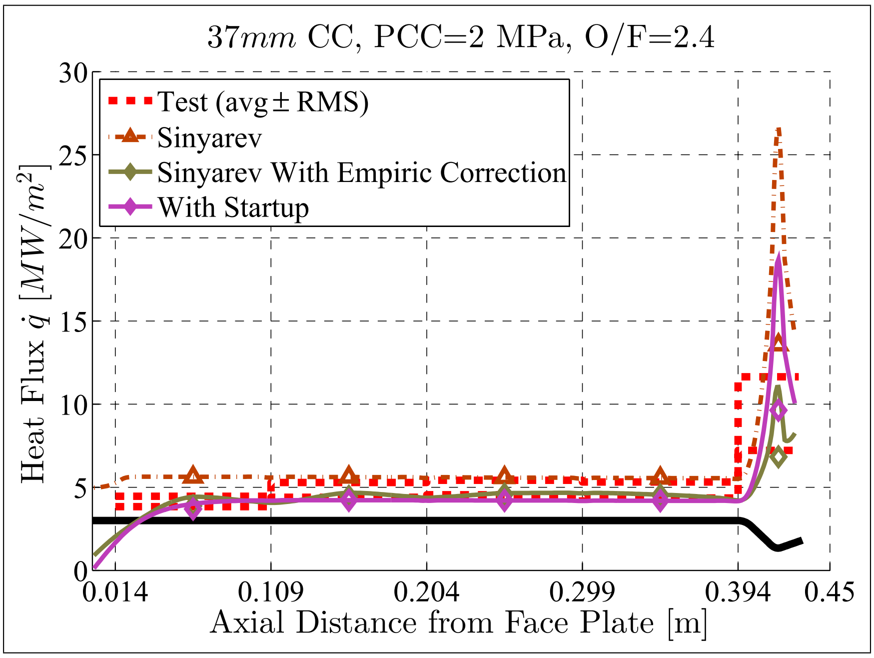

Fig. 5.40: Injector Correction for Test with 37 mm CC at Low Mixture Ratio and Low Combustion Pressure (dashed red line represents integral heat flux by experiment, symbols represent the segment-wise integral value of simulation)

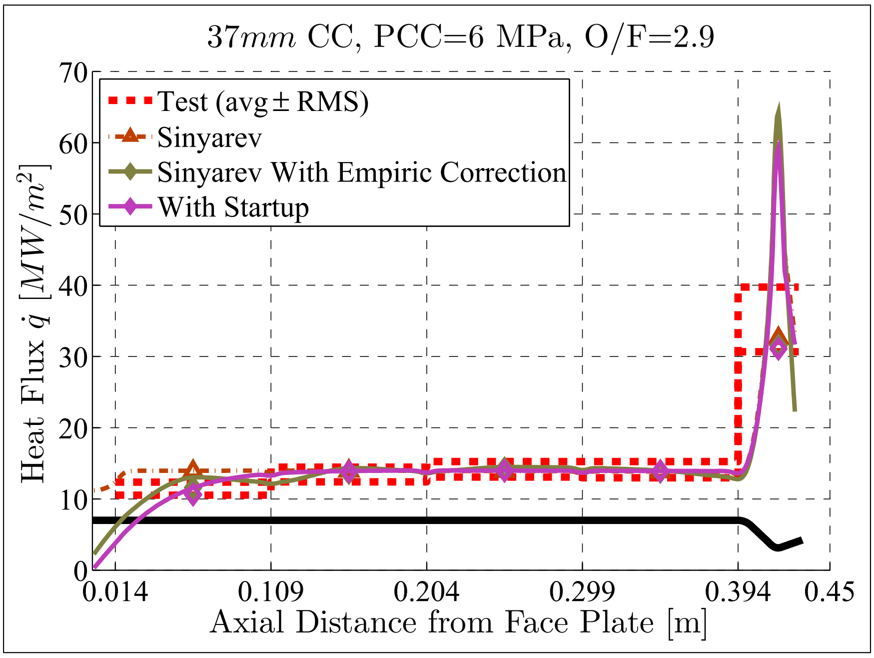

Fig. 5.41: Injector Correction for Test with 37 mm CC at Design Load Point (dashed red line represents integral heat flux by experiment, symbols represent the segment-wise integral value of simulation)

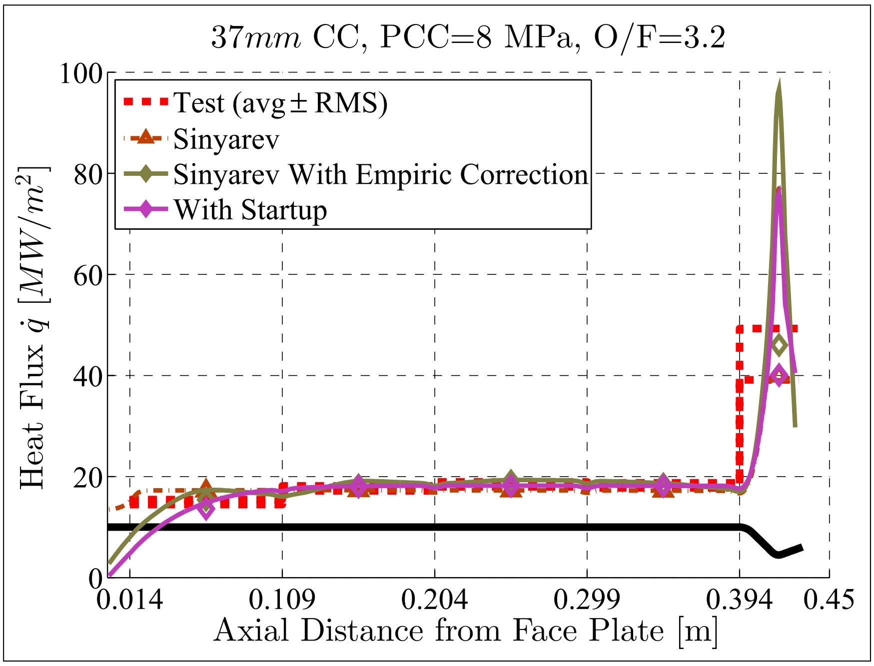

Fig. 5.42: Injector Correction for Test with 37 mm CC at High Mixture Ratio and High Combustion Pressure (dashed red line represents integral heat flux by experiment, symbols represent the segment-wise integral value of simulation)

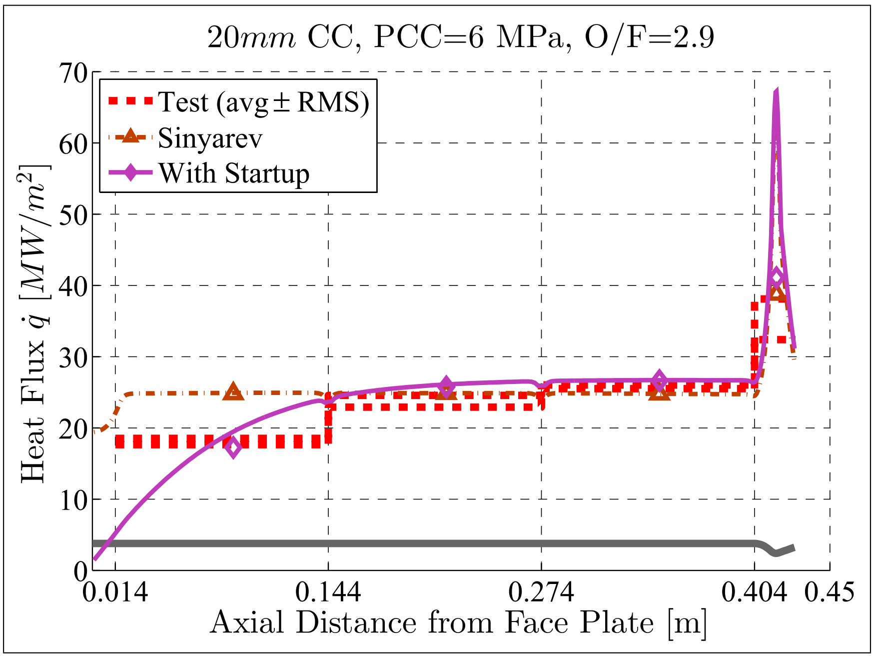

Fig. 5.43: Injector Correction for Test with 20 mm CC at Design Load Point (dashed red line represents integral heat flux by experiment, symbols represent the segment-wise integral value of simulation)

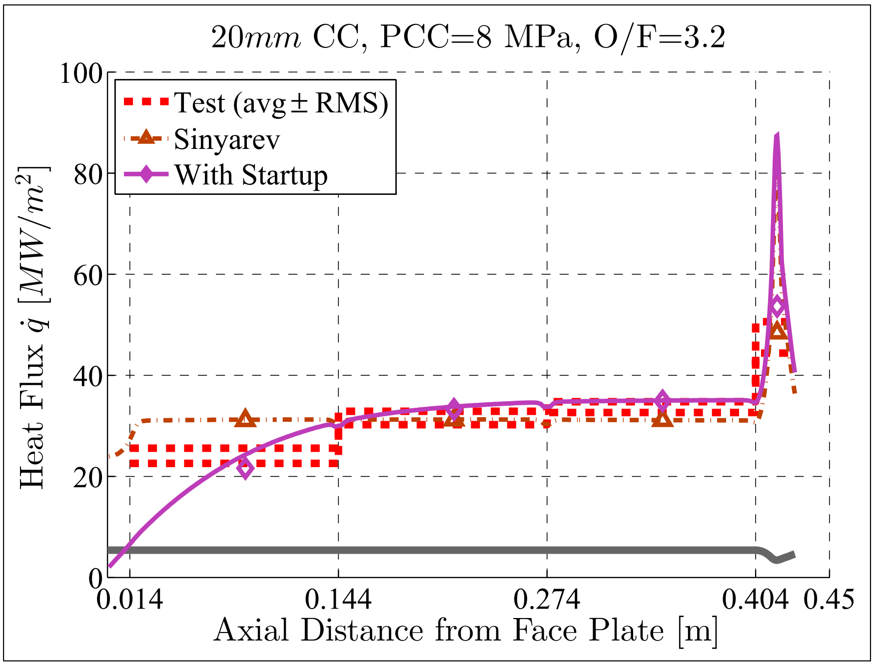

Fig. 5.44: Injector Correction for Test with 20 mm CC at High Mixture Ratio and High Combustion Pressure (dashed red line represents integral heat flux by experiment, symbols represent the segment-wise integral value of simulation)

5.3 Film Cooling Model

As aforementioned, film cooling investigations have been performed with gaseous nitrogen and kerosene (cf. chapter 4.2). Using the correlations described in Sec. 2.3.9, simulations have been performed with THERMTEST in order to better understand the film cooling experiments and to provide a proof of concept for subsequent film cooling investigations. Thereby, for kerosene both gaseous film models (NASA SP-8124 Annex A, Grissom) and liquid film models (NASA SP-8124 Annex B, Stechman) have been tested, while for nitrogen only the gaseous models have been applied. Additionally, for both coolants a modified version of NASA SP-8124 Annex A (depicted NASA-A*) replacing the definition for the adiabatic wall temperature T_{aw} Eq. 2.78 by the generic definition Eq. 2.66 has been deployed. For all simulations the heat transfer coefficient adaption as described in Sec. 5.2.6 has been applied. The test envelope comprises 54 load points with liquid and transcritical kerosene film of approx. 5%, 10%, 15% and 20% relative film mass flow rate μ at pressure levels of 2 MPa, 4 MPa and 6 MPa and 19 load points with gaseous nitrogen of approx. 5% and 15% relative film mass flow rate μ at 2 MPa and 6 MPa.

Since the film applicator inflow is radial (see Sec. 3.2.3) and with a swirl component, the boundary conditions for film modeling (often axial velocity or slot height are required) are not well defined. Assuming negligible radial velocity, which is true for kerosene ($u_{rad,Kerosene} \approx 0.3$ m/s) but may be questionable for nitrogen ($u_{rad,N2} \approx 3.7$ m/s), the initial film thickness and velocity has been determined by implying that the characteristics of the undisturbed boundary layer are impressed onto the film thus the film fluid replaces the hot gas in the near wall layer with similar dynamic conditions as the hot gas before.

The representation of the boundary layer bases on the works of *Stratford and Beavers* [82] and *Parkinson and Ziebland* [52], where the displacement thickness δ is calculated from the momentum thickness δ_2 by the 1/7-power-law (see Eq. 5.9 with $n = 7$). The momentum thickness is determined from Eq. 5.10 using a modified length z_2 (Eq. 5.11) taking into account compressibility effects.

$$\delta = \delta_2 \cdot \left(\frac{(n+1)(n+2)}{n}\right) \tag{5.9}$$

$$\delta_2 = 0.036 \cdot Re_{z_2}^{-1/5} \cdot z_2 \tag{5.10}$$

$$z_2 = \left[\frac{1+\frac{\kappa-1}{2}Ma^2}{Ma}\right]^4 \cdot \int_0^z \left[\frac{Ma}{1+\frac{\kappa-1}{2}Ma^2}\right]^4 dz \tag{5.11}$$

For comparison between simulation and measurement basically two sources of information are available: the heat flux measurements per segment and a few thermocouples flush installed with the chamber wall. While the former are known to be quite accurate but have limited spatial resolution, which is defined by the segment length of 95 mm, the latter provide additional information from the middle of each cylindrical segment but suffer on mounting tolerances and the harsh environment [103,104]. Both analyses on heat flux and temperature measurements are presented here.

5.3.1 Heat Flux Prediction for Kerosene Films

Deviations between the calculated heat flux and the measured heat flux are given for selected load cases in Tab. 5.11 for the third, in Tab. 5.12 for the fourth and in Tab. 5.13 for the nozzle segment. For reference, averaged simulated and measured heat fluxes with coolant kerosene are summarized in Fig. 5.45 et seq. for the tests at $p_c = 6$ MPa, $O/F = 3.2$ and $\mu = 15\%$, as well as in Fig. 5.47 et seq. for the tests at $p_c = 2$ MPa, $O/F = 2.9$ and $\mu = 15\%$.

p_c $[MPa]$	$(O/F)_{inj}$ [–]	μ [–]	NASA-A [%]	NASA-A* [%]	NASA-B [%]	Stechman [%]	Grissom [%]
2.0	2.90	15.0	+10.0	+12.9	+37.5	+54.0	+63.9
2.0	3.20	15.0	+5.4	+7.5	+31.3	+48.7	+59.2
6.0	3.20	15.0	+59.8	+67.1	−35.3	+80.9	+143
6.0	3.05	5.0	+4.3	+11.6	+1.1	+17.6	+34.1
6.0	3.22	10.0	+22.4	+29.0	−3.6	+38.1	+67.7
6.0	3.41	15.0	+55.5	+62.8	−38.0	+76.7	+138

Tab. 5.11: Deviation of Heat Flux Between THERMTEST Kerosene Film Modeling and Measurement in Third Segment ("-" underprediction, "+" overprediction)

Although with the heat transfer coefficient adaption a very good agreement for the reference tests has been achieved (cf. Sec. 5.2.6), the heat flux in the first and second segment, which are not film cooled at all, is especially for the 2 MPa case underpredicted i.e. higher than expected. A plausible explanation for this finding might be an increased heat transfer caused by the HF oscillations observed during these tests (compare to Sec. 4.2.3). Hence,

p_c [MPa]	$(O/F)_{inj}$ [−]	μ [−]	NASA-A [%]	NASA-A* [%]	NASA-B [%]	Stechman [%]	Grissom [%]
2.0	2.90	15.0	−36.0	−33.2	−18.4	−22.8	−23.4
2.0	3.20	15.0	−36.9	−34.5	−19.5	−23.7	−24.3
6.0	3.20	15.0	−23.6	−18.6	−10.2	−5.4	−6.3
6.0	3.05	5.0	−34.2	−27.3	−19.5	−22.0	−22.5
6.0	3.22	10.0	−29.4	−23.2	−14.1	−15.0	−15.7
6.0	3.41	15.0	−26.5	−21.7	−13.6	−8.8	−9.7

Tab. 5.12: Deviation of Heat Flux Between THERMTEST Kerosene Film Modeling and Measurement in Fourth Segment ("-" underprediction, "+" overprediction)

p_c [MPa]	$(O/F)_{inj}$ [−]	μ [−]	NASA-A [%]	NASA-A* [%]	NASA-B [%]	Stechman [%]	Grissom [%]
2.0	2.90	15.0	−28.9	−24.5	−10.9	−18.1	−18.6
2.0	3.20	15.0	−28.5	−24.4	−10.5	−17.6	−18.1
6.0	3.20	15.0	−18.6	−11.8	−1.6	−4.3	−5.0
6.0	3.05	5.0	−14.7	−5.7	+3.7	−2.1	−2.5
6.0	3.22	10.0	−14.2	−5.9	+4.2	−0.7	−1.3
6.0	3.41	15.0	−18.7	−11.8	−1.7	−4.2	−5.0

Tab. 5.13: Deviation of Heat Flux Between THERMTEST Kerosene Film Modeling and Measurement in Nozzle Segment ("-" underprediction, "+" overprediction)

the heat flux in the segments downstream of the film applicator might be affected by the rough combustion as well, but there the film processes should usually be the driving factor. In other respects, the heat fluxes below zero near the film inlet are caused by the fact that the film inflow temperatures are often higher than the local wall temperature of the water-cooled segment.

For kerosene using the gaseous film model *NASA-A* and *NASA-A** the agreement between simulation and measurement is fair (mostly better than ±35%) for the tests with sub-critical condition i.e. 2 MPa. The differences between the original and the modified representation of the adiabatic wall temperature are moderate (up to 7%). However, the heat flux is significantly overpredicted (deviation $>$ 20%) for the trans-critical load case at 6 MPa which indicates wrong startup conditions for this kind of film model (existence of quasi-liquid film, but gaseous model). The liquid film model *NASA-B* shows an heat flux overpredition in the order of +30% for subcritical conditions at 2 MPa but the quasi-liquid film in the third segment at 6 MPa is incorrectly represented leading to a too long liquid film length. In contrast, the liquid film model by *Stechman* tends to underpredict film efficiency both for low and high pressure especially in the third segment. Finally, the gaseous film model by *Grissom* significantly underpredicts film efficiency.

In conclusion for the test with kerosene, Stechman and NASA-B are the most promising models while the film efficiency more downstream thus in the fourth and nozzle segment is generally overpredicted suggesting that the kerosene film features a characteristic not properly modeled e.g. endothermic decomposition and burn-off of the film or that the heat flux is somehow increased by e.g the HF oscillations. For the NASA-A/NASA-A* model the inflow conditions (liquid, quasi-liquid or gaseous) are crucial.

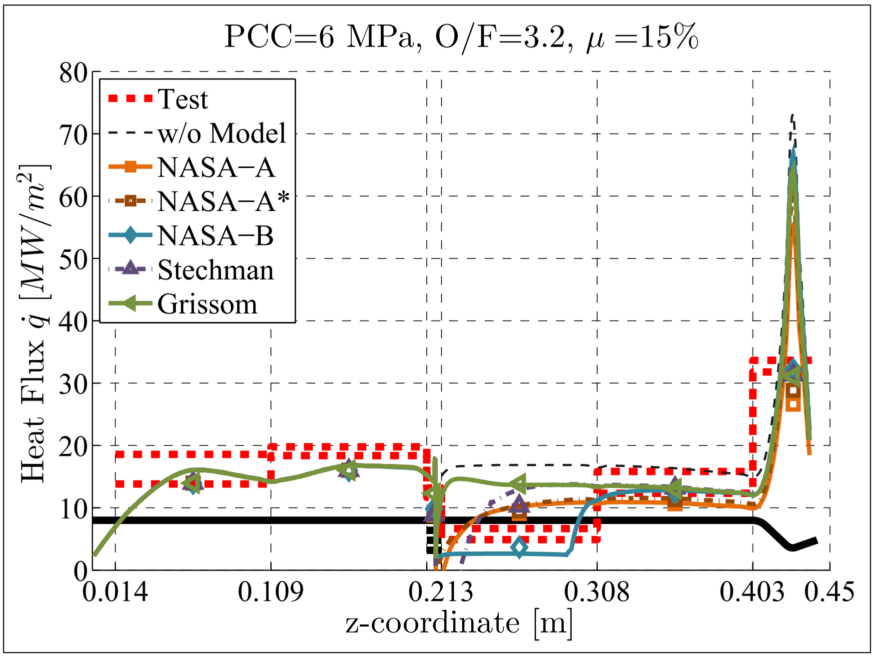

Fig. 5.45: Comparison of Film Models for 37 mm CC at Nominal Conditions with High Film Mass Flow of Kerosene (dashed red line represents integral heat flux by experiment, symbols represent the segment-wise integral value of simulation)

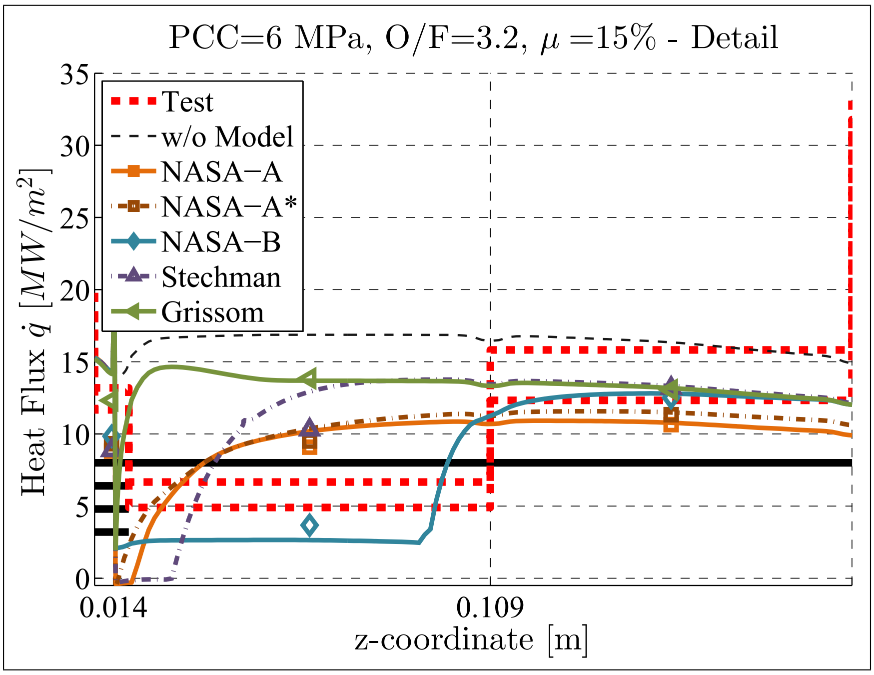

Fig. 5.46: Detail of Film Cooled Segments for Nominal Conditions with High Film Mass Flow of Kerosene (dashed red line represents integral heat flux by experiment, symbols represent the segment-wise integral value of simulation)

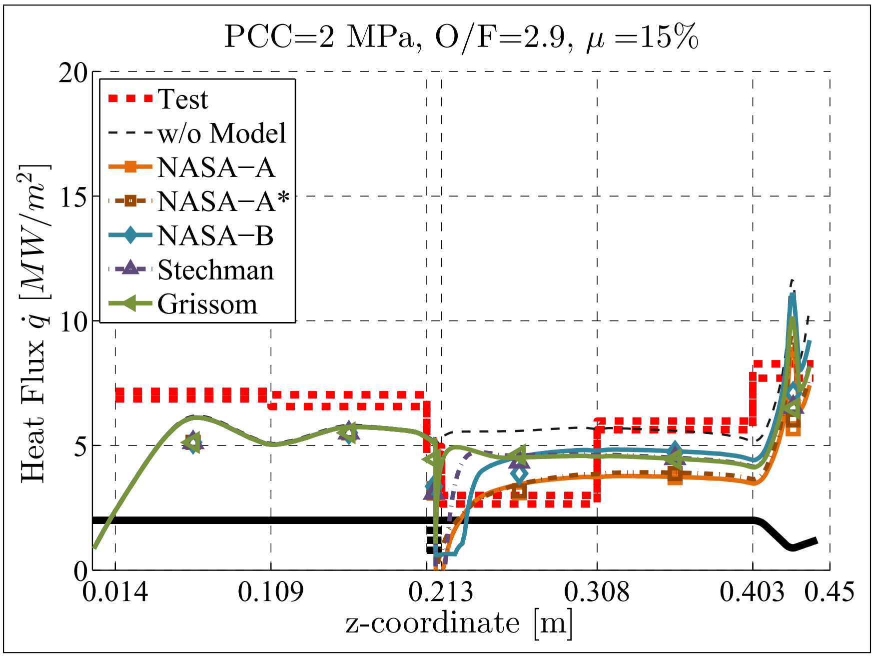

Fig. 5.47: Comparison of Film Models for 37 mm CC at Low Pressure with High Film Mass Flow of Kerosene (dashed red line represents integral heat flux by experiment, symbols represent the segment-wise integral value of simulation)

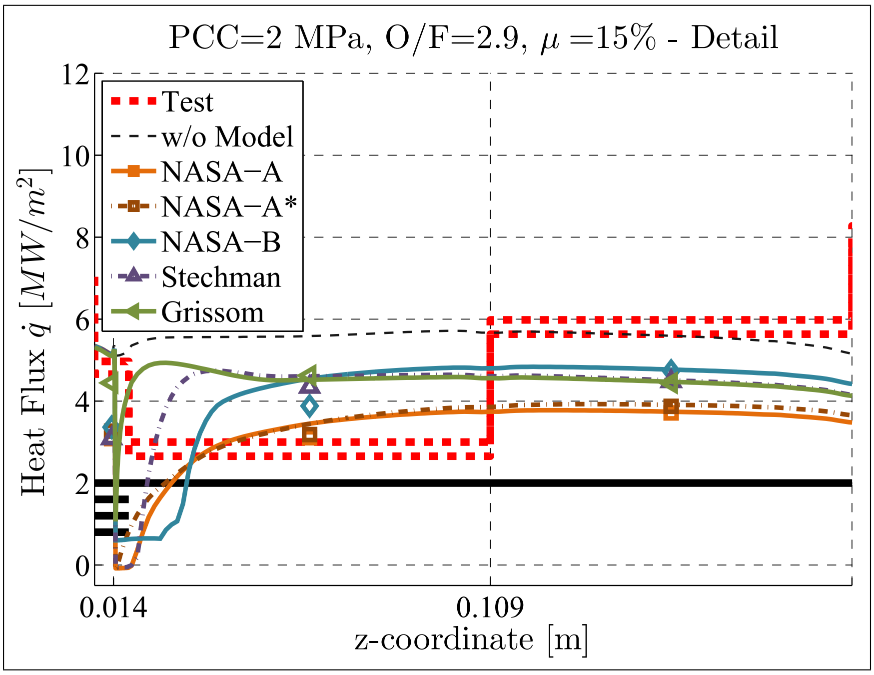

Fig. 5.48: Detail of Film Cooled Segments for Low Pressure with High Film Mass Flow of Kerosene (dashed red line represents integral heat flux by experiment, symbols represent the segment-wise integral value of simulation)

5.3.2 Heat Flux Prediction for Nitrogen Films

For nitrogen, deviations between the simulated heat flux and the measured heat flux for different load cases are given in Tab. 5.14 for the third, in Tab. 5.15 for the fourth and in Tab. 5.16 for the nozzle segment. Averaged simulated and measured heat fluxes with coolant kerosene are summarized in Fig. 5.49 for the tests at $p_c = 6$ MPa, $O/F = 3.2$, $\mu = 15\%$ and in Fig. 5.47 for the tests at $p_c = 2$ MPa, $O/F = 2.9$ and $\mu = 15\%$.

p_c $[MPa]$	$(O/F)_{inj}$ $[-]$	μ $[-]$	NASA-A [%]	NASA-A* [%]	Grissom [%]
2.0	2.90	15.0	−30.4	−34.3	+20.1
2.0	3.20	15.0	−24.0	−29.1	+31.4
6.0	3.20	15.0	−34.7	−37.1	+16.2
6.0	3.05	5.0	−23.3	−21.5	−0.6
6.0	3.41	15.0	−33.6	−36.2	+18.7

Tab. 5.14: Deviation of Heat Flux Between THERMTEST Nitrogen Film Modeling and Measurement in Third Segment ("-" underprediction, "+" overprediction)

p_c $[MPa]$	$(O/F)_{inj}$ $[-]$	μ $[-]$	NASA-A [%]	NASA-A* [%]	Grissom [%]
2.0	2.90	15.0	−24.6	−27.0	−3.8
2.0	3.20	15.0	−17.2	−20.6	+5.6
6.0	3.20	15.0	−29.1	−30.3	−7.5
6.0	3.05	5.0	−31.6	−25.8	−19.0
6.0	3.41	15.0	−27.8	−29.2	−5.7

Tab. 5.15: Deviation of Heat Flux Between THERMTEST Nitrogen Film Modeling and Measurement in Fourth Segment ("-" underprediction, "+" overprediction)

p_c $[MPa]$	$(O/F)_{inj}$ $[-]$	μ $[-]$	NASA-A [%]	NASA-A* [%]	Grissom [%]
2.0	2.90	15.0	−17.1	−15.6	−2.0
2.0	3.20	15.0	−11.5	−10.4	+4.6
6.0	3.20	15.0	−9.7	−6.2	+8.2
6.0	3.05	5.0	−18.4	−10.3	−6.3
6.0	3.41	15.0	−8.0	−4.6	+10.3

Tab. 5.16: Deviation of Heat Flux Between THERMTEST Nitrogen Film Modeling and Measurement in Nozzle Segment ("-" underprediction, "+" overprediction)

For simulations with NASA-A and NASA-A* models the heat fluxes are significantly underpredicted thus the film efficiency is overpredicted. This could once again indicate problems with the film initialization. In comparison, the heat flux prediction by Grissom model agrees well with the experimental data (mostly better ±20%). However, the simulation without film model reveals that the film cooling effectiveness using gaseous nitrogen is very low leading to a high uncertainty both for measurement and modeling. Under these

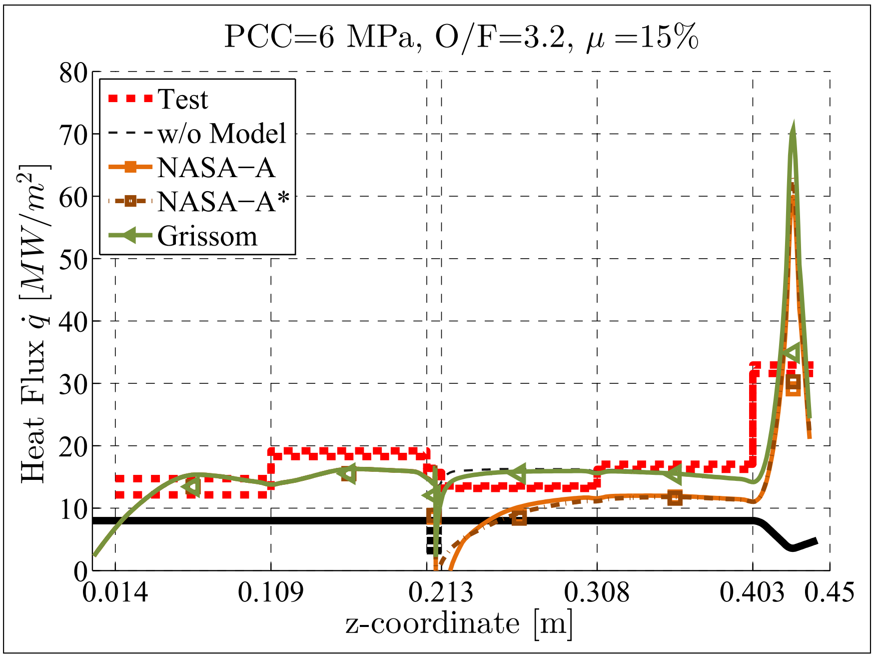

Fig. 5.49: Comparison of Film Models for 37 mm CC at High Pressure Conditions with High Film Mass Flow of Nitrogen (dashed red line represents integral heat flux by experiment, symbols represent the segment-wise integral value of simulation)

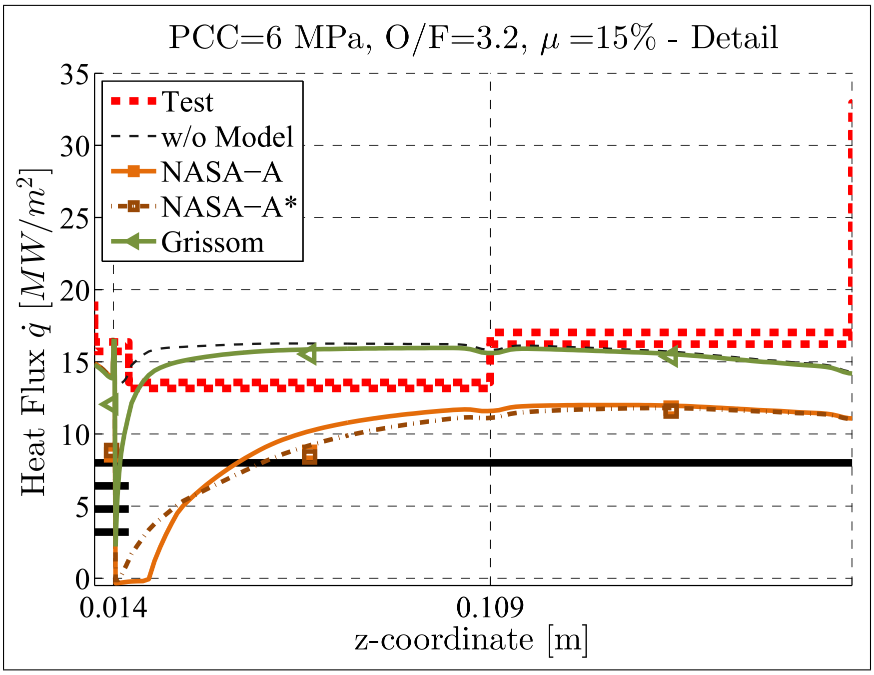

Fig. 5.50: Detail of Film Cooled Segments for Nominal Conditions with High Film Mass Flow of Nitrogen (dashed red line represents integral heat flux by experiment, symbols represent the segment-wise integral value of simulation)

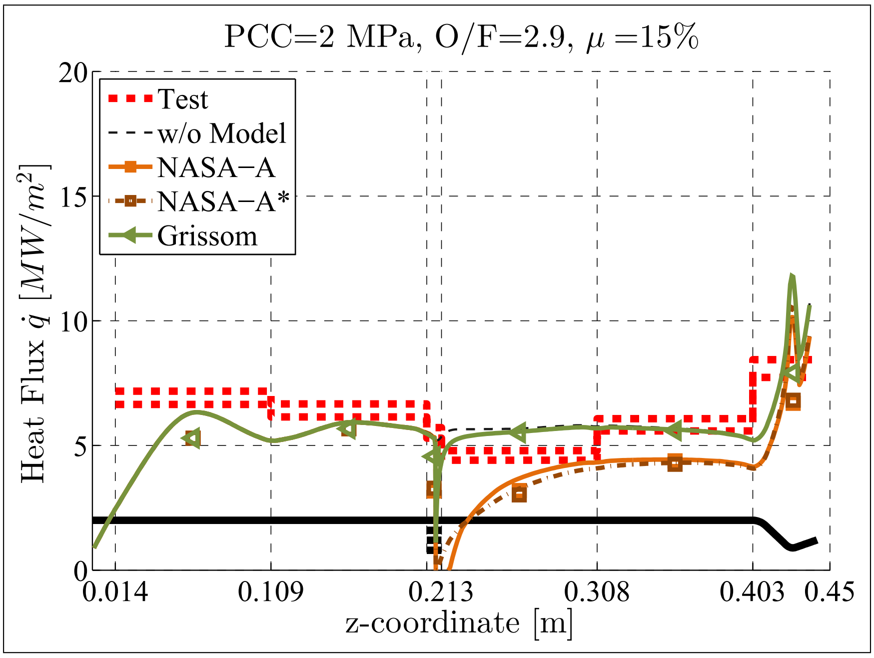

Fig. 5.51: Comparison of Film Models for 37 mm CC at Low Pressure with High Film Mass Flow of Nitrogen (dashed red line represents integral heat flux by experiment, symbols represent the segment-wise integral value of simulation)

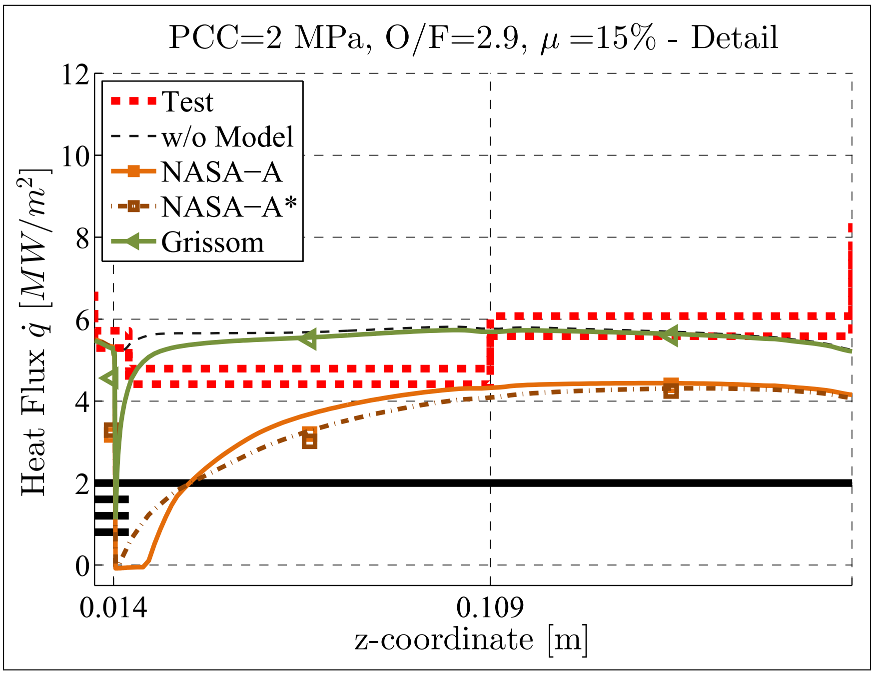

Fig. 5.52: Detail of Film Cooled Segments for Low Pressure with High Film Mass Flow of Nitrogen (dashed red line represents integral heat flux by experiment, symbols represent the segment-wise integral value of simulation)

circumstances an increase in heat transfer by e.g. HF oscillations may easily render all findings incorrect. This result finally led to a revised injector design with less tendency for oscillations as well as modifications in the setup of the experiment undertaken in the Transregio SFB-TRR40 film cooling experiments [93, 94, 103–106].

5.3.3 Analysis on Hot Wall Temperatures

Averaged hot wall temperatures calculated by THERMTEST as well as from the thermocouples flush mounted with the hot chamber wall (cf. Sec. 4.2.6) are given versus engine axis for selected load cases in Fig. 5.53 throughout Fig. 5.56. Although qualitative behavior of the measured hot wall temperatures seems to be plausible (e.g. plateau for liquid or trans-critical kerosene in third segment downstream of film applicator), the absolute values of simulation and the measurement significantly differ.

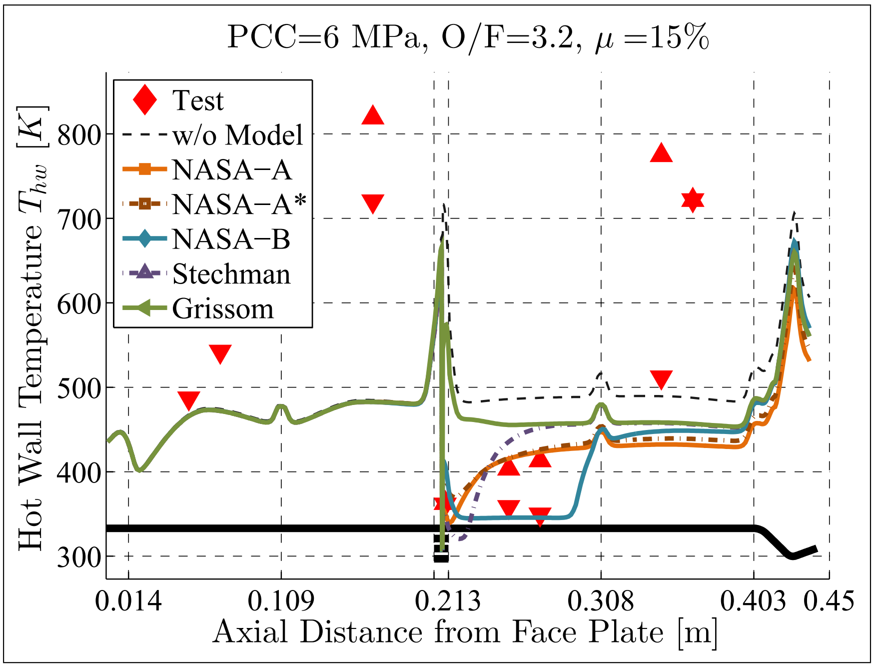

Fig. 5.53: Hot Wall Temperatures for Different Film Models in 37 mm CC at Nominal Conditions with High Film Mass Flow of Kerosene (red triangles represent upper/lower RMS of experimental data, lines represent the simulation)

By cross-checks with different numerical data bases as well as experiences regarding the thermocouples flush mounted with the chamber wall both by TUM and Astrium, the measurements have been evaluated as questionable (see Fig. 5.57). The hot wall temperature measurements are mostly reproducible, but not reliable by means of absolute values, which are required for analyzing heat transfer and film cooling effectiveness accurately. Apart mounting-related issues like gaps and tolerances due to sensor manufacturing, the different materials thus thermal conductivity of thermocouple and chamber wall has been identified a possible cause of the deviations between measured and expected hot wall temperature (see Fig. 5.58). Assuming a load point of p_c = 6 MPa and O/F = 2.9 and ideal thermal contact between thermocouple and hot wall (copper), simulations with THERMTEST

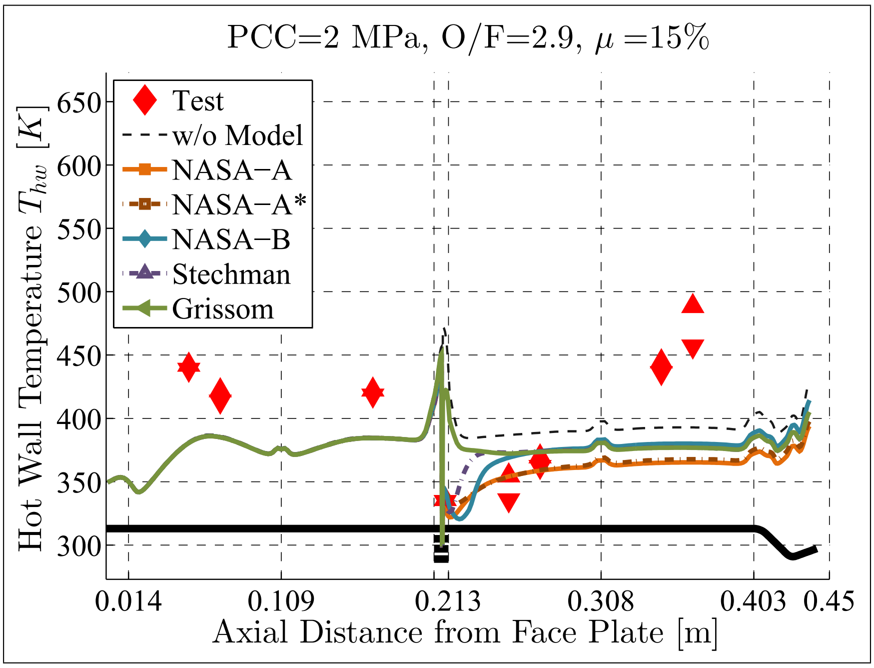

Fig. 5.54: Hot Wall Temperatures for Different Film Models in 37 mm CC at Low Pressure with High Film Mass Flow of Kerosene (red triangles represent upper/lower RMS of experimental data, lines represent the simulation)

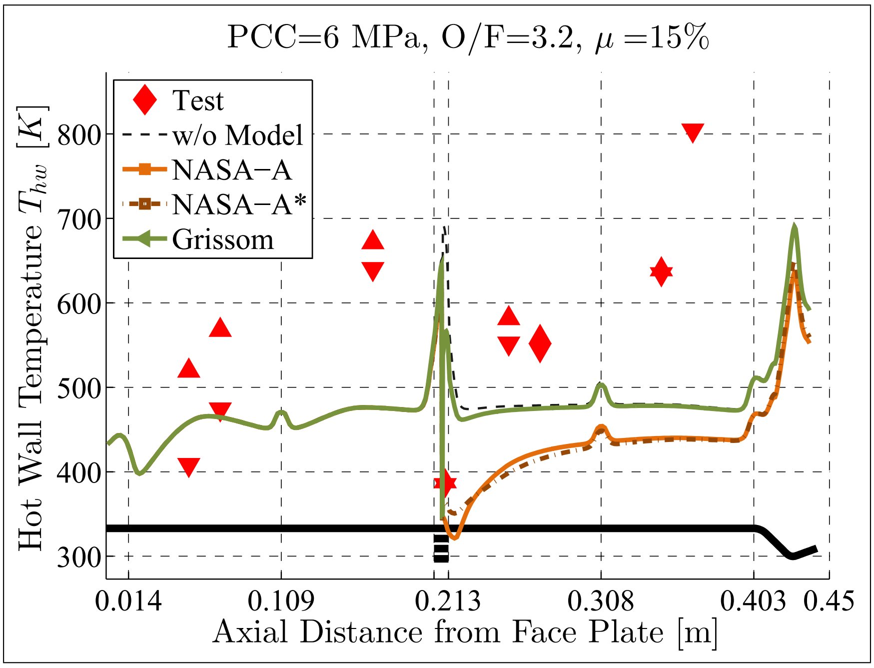

Fig. 5.55: Hot Wall Temperatures for Different Film Models in 37 mm CC at High Pressure Conditions with High Film Mass Flow of Nitrogen (red triangles represent upper/lower RMS of experimental data, lines represent the simulation)

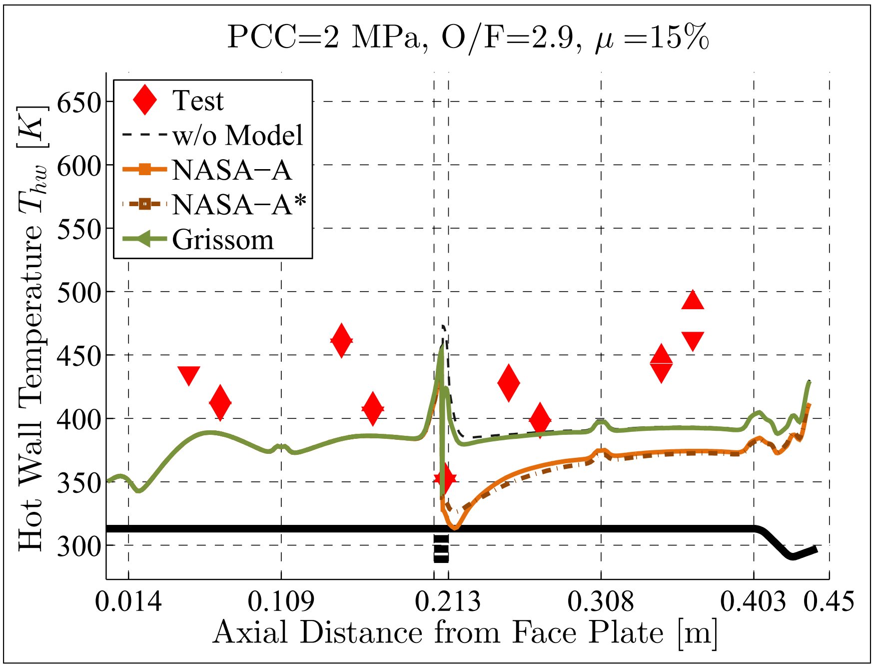

Fig. 5.56: Hot Wall Temperatures for Different Film Models in 37 mm CC at Low Pressure with High Film Mass Flow of Nitrogen (red triangles represent upper/lower RMS of experimental data, lines represent the simulation)

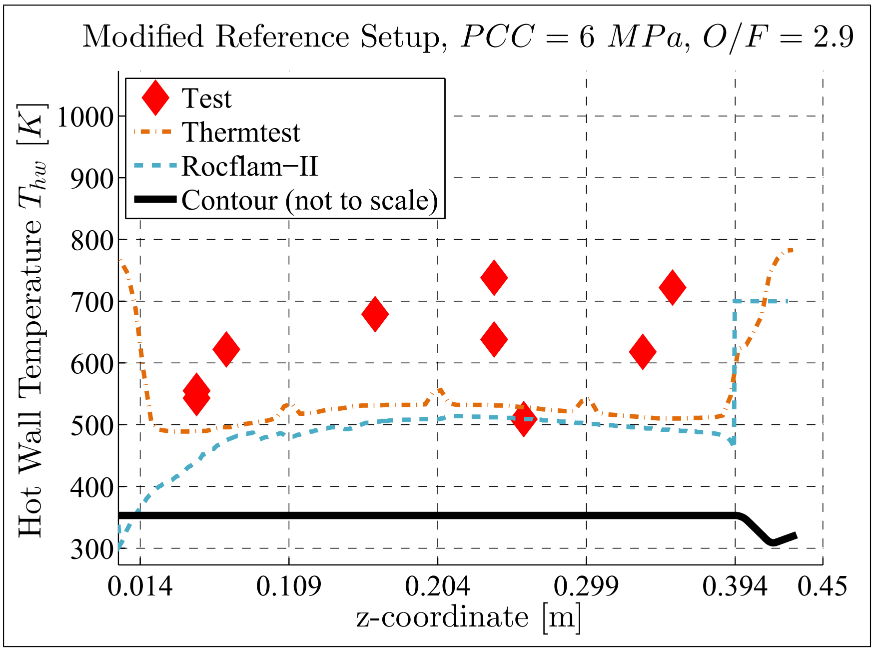

Fig. 5.57: Comparison of Measured Hot Wall Temperature and Simulation by ROCFLAM-II and THERMTEST (6 MPa, 2.9, Modified Reference Setup) [94]

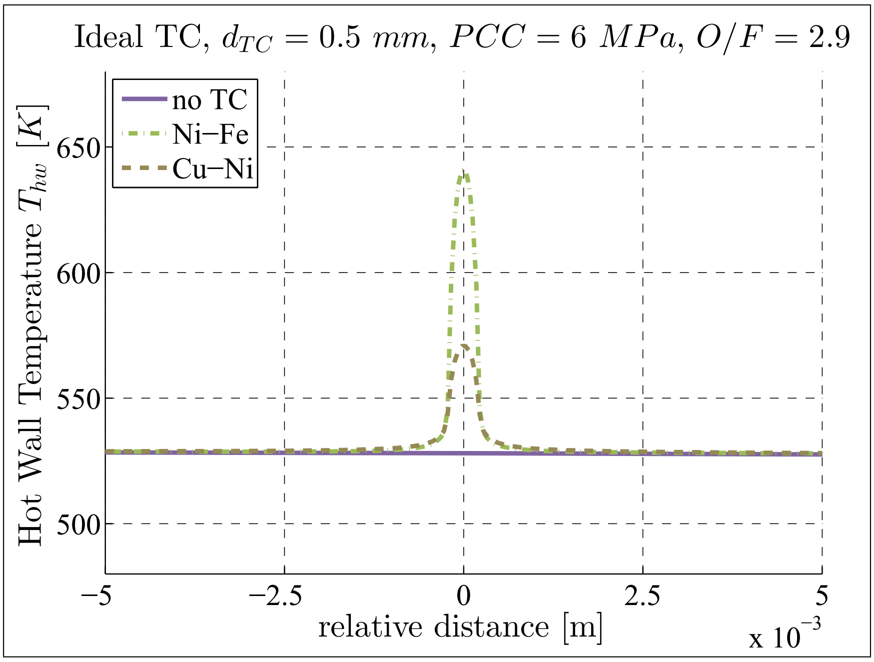

Fig. 5.58: THERMTEST Simulation of Thermocouple flush-mounted with Hot Chamber Wall (6 MPa, 2.9) [94]

show for type K thermocouples (Ni-Fe) of 0.5 mm diameter a deviation up to 110 K between wall and sensor temperature. For type T thermocouples (Cu-Ni, Medtherm) this deviation is still around 40 K [94]. This finding has been further investigated[5] and confirmed by FEM simulations. Corrective measures or correlations to the wall temperatures are imaginable but very challenging and have not be applied within the frame of this work.

5.4 Transpiration Cooling

In terms of a "proof of concept", THERMTEST simulations of the experiments with transpiration cooled CMCs (cf. Sec. 4.3) have been performed. The tests considered for evaluation comprise four runs with C/C and nitrogen, nine C/C runs with kerosene, one WHIPOX test each with nitrogen and kerosene and four OXIPOL runs with nitrogen. The simulations make use of THERMTEST's capability to perform a transient analysis where the experimental data serve directly as input for the heat transfer calculations. For modeling the transpiration cooling the model by Hacker (Eq. 2.87) is applied, albeit equilibrium thermal conditions in between porous medium and cooling fluid as well as constant properties of the solid with respect to thermal conductivity, heat capacity and porosity is assumed.

The single accessible information for benchmarking the transpiration cooling and the modeling at this point is the measurement of the intra-wall temperature. Three thermocouples

---

[5] M. Triebig: *Thermalanalyse eines Thermoelements in einer Brennkammerwand mittels FEM-Simulation*, Semester Assignment [in German], Institute for Flight Propulsion, Technische Universität München, 2011

have been installed in the CMC with a distance to the hot wall of 2 mm (see Fig. 3.7 in Sec. 3.2.4) and are embedded into a glued ceramic capillary tube. During the test campaign questions have arisen regarding positioning and thermal contact of these temperature sensors, especially after deteriorations and damages e.g. burnout of material in the vicinity of the thermocouples. Under these conditions with having a limited database and a high uncertainty of the measurements, no model validation will be performed but general findings are presented here.

The evolution of the inner wall temperature for the tests with the C/C sample and coolant nitrogen are given in Fig. 5.59. The initial temperatures in the wall ($t < 15$ s) match quite well. For the long-time run an increasing deviation can be seen which is traced back to changes in the CMC properties i.e. porosity not modeled in THERMTEST. The behavior on shutdown indicates a significant thermal capacity of the thermocouple and the ceramic tube compared to the porous medium. The very high temperatures in the second test "ATC-CB-T02-01" (colored yellow) are attributed to an erroneous measurement.

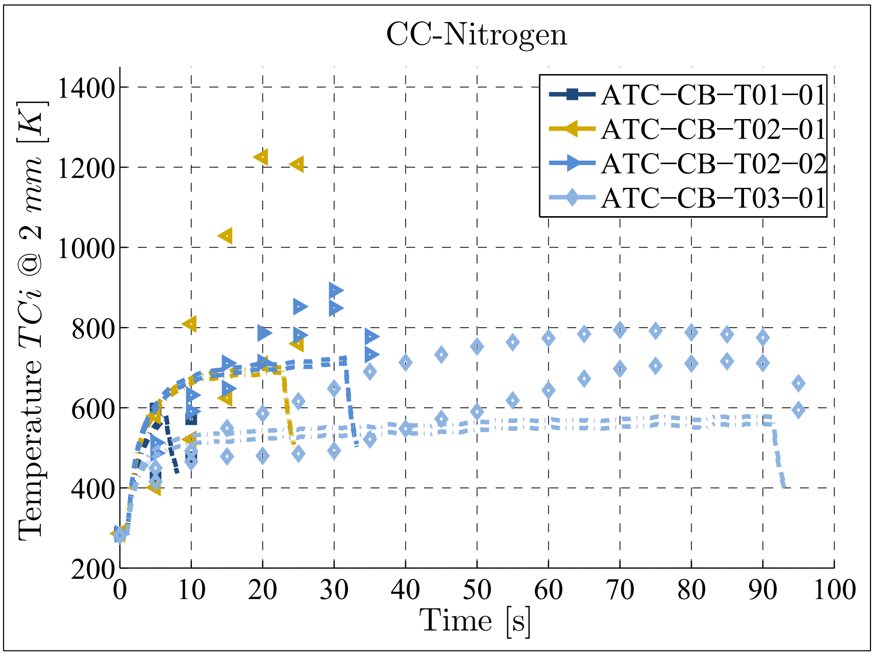

Fig. 5.59: Comparison of Intra-Wall Temperature for C/C Sample Using Nitrogen (lines represent $Mean \pm RMS$ for simulation, symbols represent $Mean \pm RMS$ for experimental data)

For C/C using kerosene as cooling fluid very low wall temperatures have been recorded (see Fig. 5.60). It is assumed that for this configuration only fluid temperature is measured and/or the assumption made that the solid and the fluid are in thermal equilibrium is not valid. Two tests are noteworthy: Firstly, the run "ATC-CB-T22-01" (colored orange) marked obviously the highest loads of all kerosene tests. At the end a deviation in the temperature data is visible and this test also marked the beginning of a LF anomaly. Secondly, in test "ATC-CB-T31-02" (magenta) the failure of the CMC is apparent from the diverging temperature measurements.

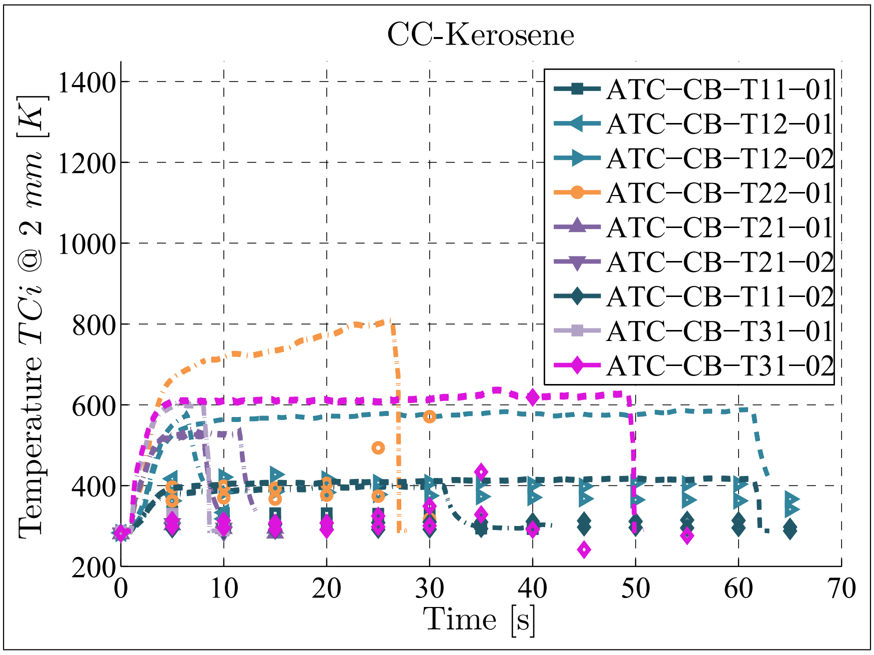

Fig. 5.60: Comparison of Intra-Wall Temperature Measurement and Simulation for C/C Sample Using Kerosene (lines represent $Mean \pm RMS$ for simulation, symbols represent $Mean \pm RMS$ for experimental data)

The two tests conducted with the WHIPOX sample are presented in Fig. 5.61 and Fig. 5.62. The test subject showed unfavorable pressure loss characteristics and a lack of fiber to matrix coherence. The comparison of THERMTEST simulations and measurements indicate that the effective thermal properties of the CMC are much lower than expected. The segment was damaged after approx. 30 s within the second test run "ATC-WB-T11-01".

In order to reduce the potential influence of soot, for the OXIPOL test sample the mixture ratio has been increased to $O/F = 3.2$, but coolant mass flow rate has been slightly increased and the combustion pressure has been reduced to $p_c = 1.0$ MPa (cf. Fig. 5.63). In principle, the segment is considerably overcooled. However, the first thermocouple TC31 suffered from hot gas infiltration due to a local leakage leading to the abort of the tests.

In general, testing and simulation has been affected by premature manufacturing technology and problems in measuring relevant data. A successful simulation of transpiration cooled CMCs seems to be feasible but requires a reproducible manufacturing process for reproducible material properties, improvements in the measurement of the characteristic values (e.g. local solid temperature and local fluid temperature) and in the modeling (e.g. temperature dependent solid properties, non-equilibrium of solid and liquid temperature in the CMC).

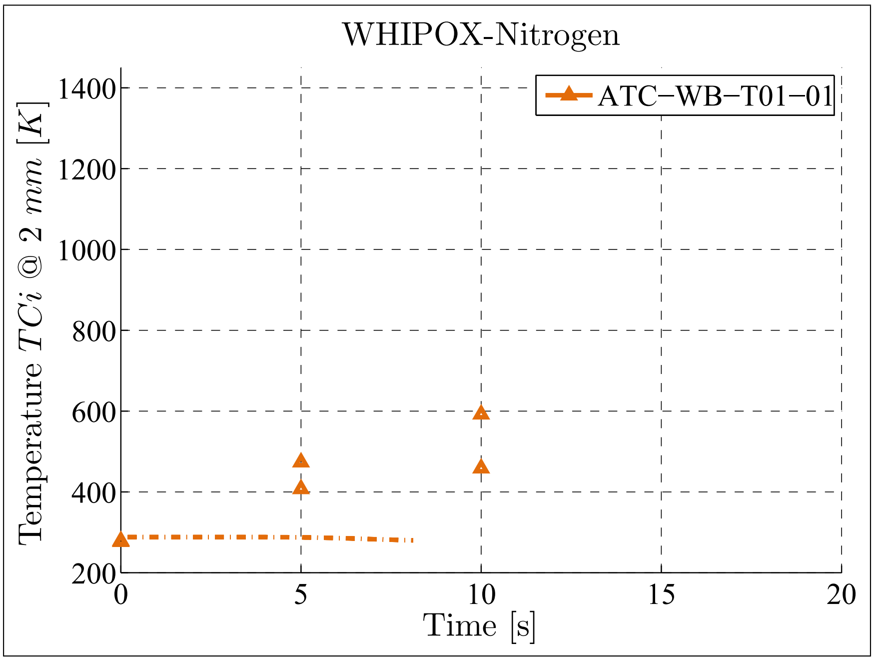

Fig. 5.61: Comparison of Intra-Wall Temperature for WHIPOX Sample Using Nitrogen (lines represent $Mean \pm RMS$ for simulation, symbols represent $Mean \pm RMS$ for experimental data)

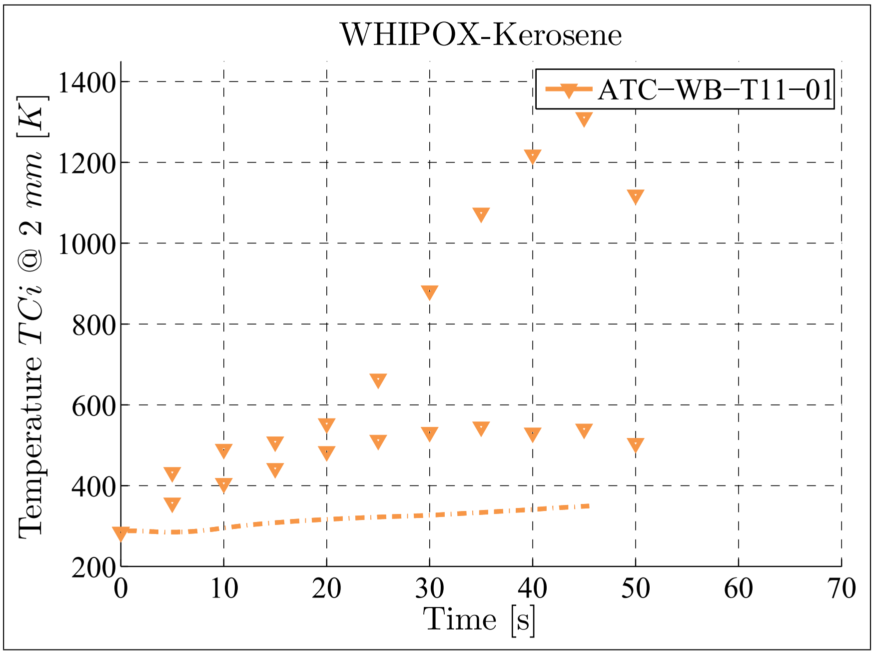

Fig. 5.62: Comparison of Intra-Wall Temperature Measurement and Simulation for WHIPOX Sample Using Kerosene (lines represent $Mean \pm RMS$ for simulation, symbols represent $Mean \pm RMS$ for experimental data)

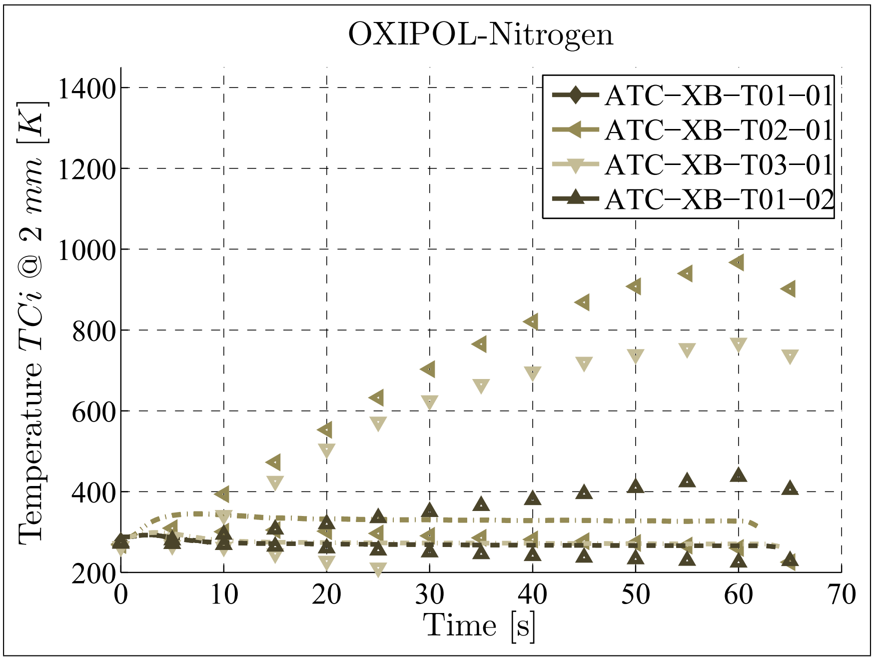

Fig. 5.63: Comparison of Intra-Wall Temperature for OXIPOL Sample Using Nitrogen (lines represent $Mean \pm RMS$ for simulation, symbols represent $Mean \pm RMS$ for experimental data)

5.5 Convectively Cooled CMC

Finally, THERMTEST simulations have been conducted for the experiments with a convectively cooled CMC (cf. Sec. 4.4). The analysis comprises 25 individual tests performed with two different samples and nitrogen as well as kerosene as coolant. Here, comparisons of the heat flux are presented.

The modeling of the CMC is challenging. The non-homogeneous characteristics of the porous and anisotropic CMC usually requires a special procedure for the determination of the effective heat transfer properties. Due to the very low porosity and special winding technology of the test samples investigated, quasi-isotropic and non-porous properties could be assumed in the simulations [107]. However, the low thermal conductivity and the heat capacity of the material requires a transient simulation. Hereby again THERMTEST's capability to perform a transient analysis with the experimental data (p_c, O/F, mass flows) as direct input for the heat transfer calculations has been very useful. The two samples have had different thermomechanical properties and showed evidence of wearing over the test campaign. The hot wall surface features a significant wall roughness which covers the expected effects caused by the high wall temperatures e.g. elevated radiation. Therefore, the hot gas side heat transfer coefficient has been increased by 20% in order to take into account the increased heat transfer by wall roughness. Also, the cooling channel requires special attention (see Fig. 5.64(a), where light green is the CMC, light blue the stainless steel jacket and the manifolds, dark blue the cooling channel and red the interweaved fibers called “pin fins”). Beside the high surface roughness of the CMC material the “pin fins” connecting the inner and the outer CMC tube have been found crucial for an accurate heat

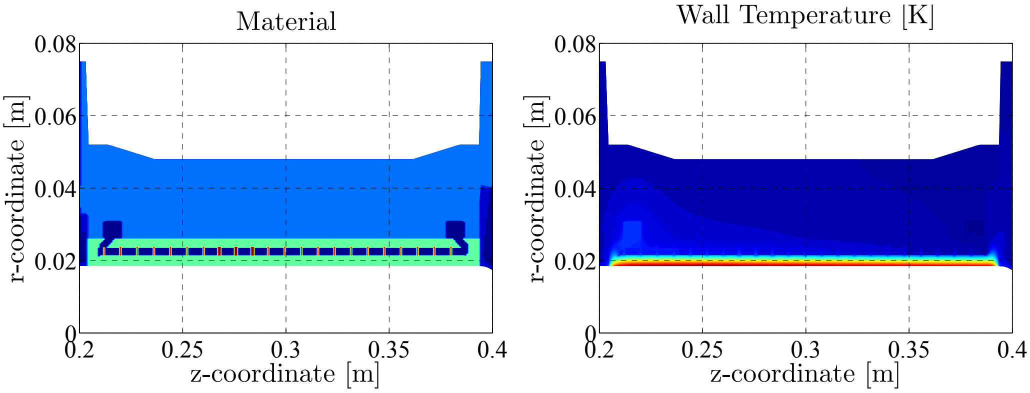

(a) Material

(b) Temperature

Fig. 5.64: Example of Representation of the Convectively Cooled CMC in THERMTEST

transfer simulation. The additional pressure losses and turbulences in the cooling channel caused by the "pin fins" are considered by a factor of 2.40 and 2.75 in the pressure loss for nitrogen and kerosene, respectively, and 2.50 for the coolant side heat transfer coefficient, which have been determined by a trial and error approach minimizing the persistent deviation between test data and simulations as well as the initial slope of the heat pick-up. The typical temperature distribution for the CMC segment is shown in Fig. 5.64(b).

Heat fluxes versus test time with coolant nitrogen are presented for the PTAH-SOCAR rocket duct number "0", short PSR0, in Fig. 5.65 and for PSR1 in Fig. 5.66. The differences between the tests are small as the deviations between experimental results and simulation are. For PSR0 a permanent overprediction of $+22\pm12\%$ exists also for long test runs. For the PSR1 the permanent deviation between simulation and experiment is within -20.4% and -3.0% (mean deviation $-10\pm9\%$), but a more significant underprediction is apparent for test time shorter than 10 s (up to 49% in test AEC-T10-17).

Heat fluxes versus test time with coolant kerosene are presented in Fig. 5.67 and for PSR1 in Fig. 5.68. For kerosene, experimental results cannot be reproduced by THERMTEST simulations. The root cause of this failing has been traced back to the complex thermal and fluid dynamic conditions in the cooling channel. Although bulk fluid temperatures at exit are in the moderate range of 300 K up to 450 K, asymmetric heating results in temperatures on the inner surface of the coolant channel in the order of 800 K. Since this will lead to two phase flow as well as decomposition of the coolant within the test sample, the assumptions made for THERMTEST (bulk temperature only, homogeneous fluid) are no longer fulfilled.

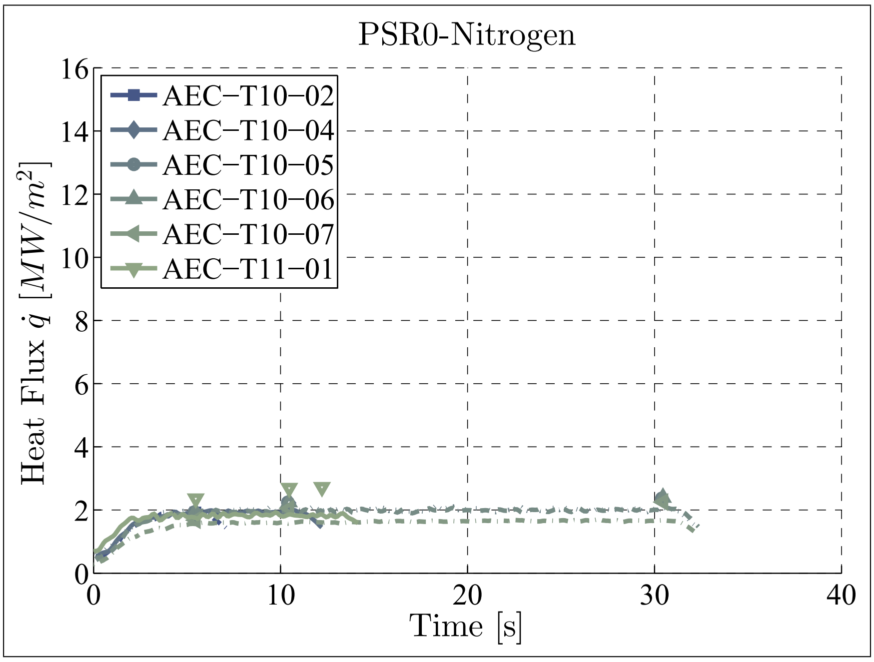

Fig. 5.65: Heat Flux in Convectively Cooled CMC PTAH-SOCAR Rocket Duct “0” Using Nitrogen (line represents simulation, symbols represent experimental data)

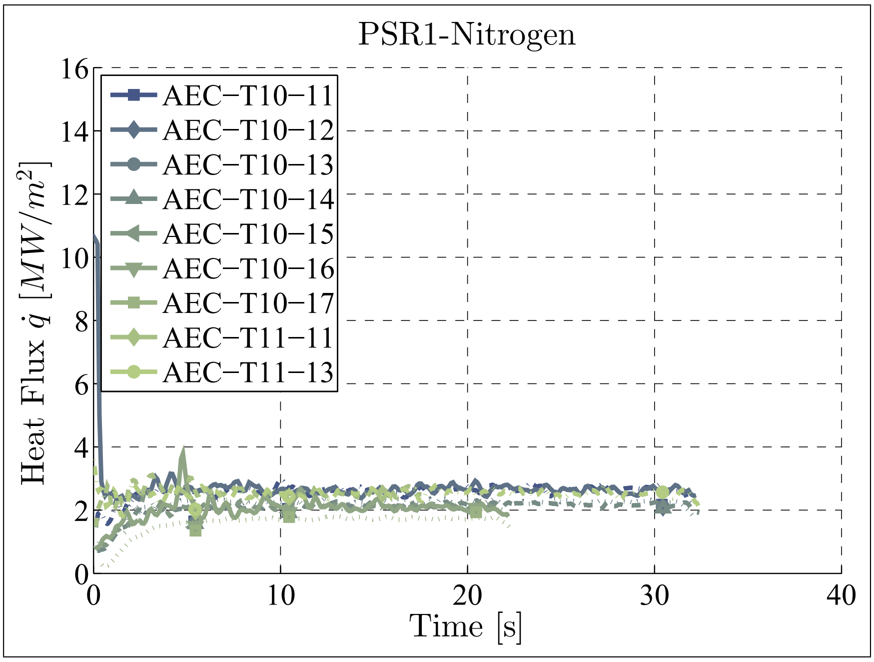

Fig. 5.66: Heat Flux in Convectively Cooled CMC PTAH-SOCAR Rocket Duct “1” Using Nitrogen (line represents simulation, symbols represent experimental data)

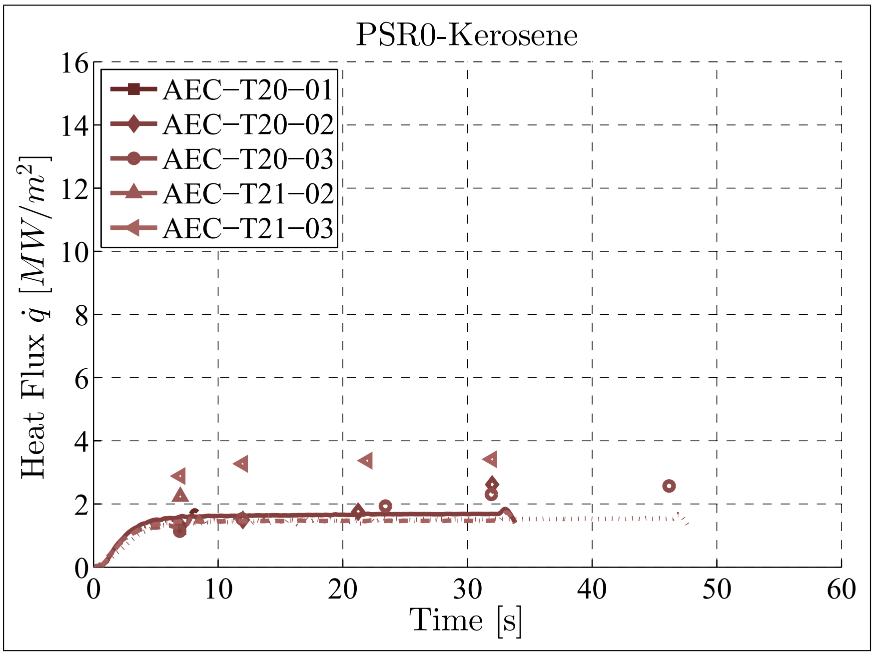

Fig. 5.67: Heat Flux in Convectively Cooled CMC PTAH-SOCAR Rocket Duct “0” Using Kerosene (line represents simulation, symbols represent experimental data)

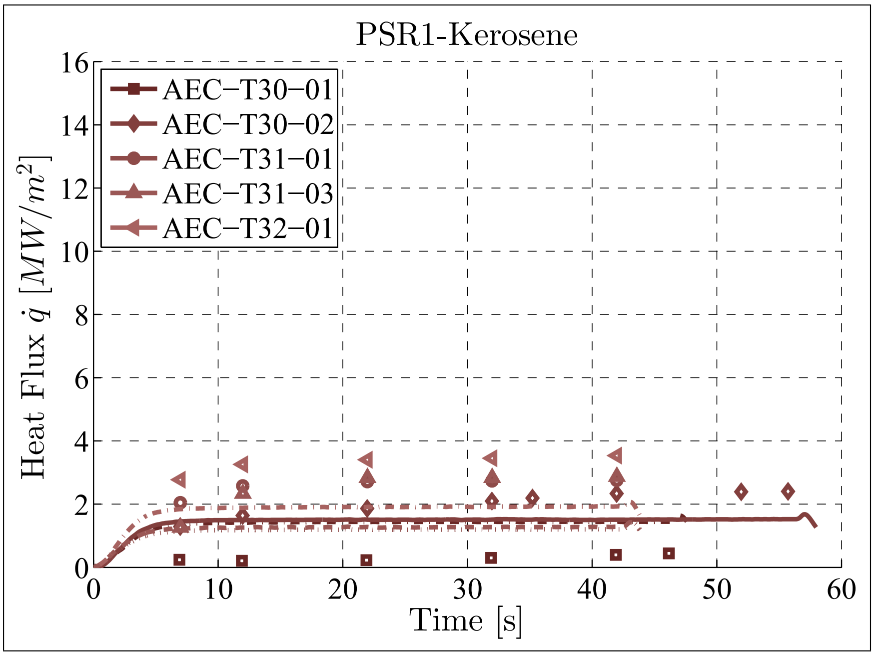

Fig. 5.68: Heat Flux in Convectively Cooled CMC PTAH-SOCAR Rocket Duct “1” Using Kerosene (line represents simulation, symbols represent experimental data)

6. Conclusion and Outlook

In the context of constrained budgets and legal requirements to substitute harmful substances the intensified use of hydrocarbon fuels i.e. kerosene and methane in rocket engines is discussed. The Institute for Flight Propulsion of Technische Universität München operates a high pressure combustion test facility enabling experiments and fundamental research on heat transfer, cooling and material compatibility at application-relevant conditions. In the EU-funded ATLLAS project, this installation served as testbed for investigations on heat transfer, film cooling as well as transpiration cooled and convectively cooled ceramic matrix composites.

For reference, hot fire tests with the propellants kerosene and gaseous oxygen have been conducted. Two different water-cooled single element combustion chambers have been used featuring different inner diameters and different contraction ratios but very similar injector elements of the double-swirl gas-jet coaxial type. Thereby, a wide operational envelope has been covered especially for the bigger chamber assembly. Due to the characteristic length doubled higher combustion efficiencies have been found for the higher contraction ratio chamber. An anomaly was observed for the combustion efficiency at mixture ratios below 2.0 which has been attributed to incomplete mixing and high gradients in the characteristic velocity in this range. The integral heat flux per segment exceeded in the nozzle 50 MW/m^2. For further use correlations describing the heat flux with respect to mixture ratio and combustion pressure have been derived.

Film cooling investigations have been performed with liquid or “trans-critical” reactive kerosene and gaseous inert nitrogen. The film applicator device was installed in the middle of the chamber where combustion is assumed to be completed enabling the investigation of the film parameters independently from chemical reactions and acceleration of the hot gases in the primary combustion zone. The design featured a radial inflow as well as inclined slots inducing swirl. The conducting of the tests was challenging leading to high data scattering. This was caused by the difficult operating conditions of the film feed system and increased high frequency oscillations observed in these tests. Performance and heat fluxes with and without film cooling have been investigated. Additionally, wall temperatures have been measured with thermocouples flush-mounted with the hot chamber wall. Heat fluxes and wall temperatures were used to determine the cooling effectiveness of the films applied.

In the test campaign on transpiration cooled CMC three different materials have been tested with cooling fluids nitrogen and kerosene. Due to a very limited number of hot runs and a reduced measuring equipment within the test samples no final result can be given.

Several hot tests with increasing loads have been performed with two CMC specimen of PTAH-SOCAR type convectively cooled with either nitrogen or kerosene. The investigations comprise data on combustion stability, performances and heat fluxes.

The experimental data have been used to determine and to validate correlations useful for engineering tools applicable to hydrocarbon fuels as well as for preliminary design. The "TUM/ATLLAS Common Approach" was defined as a set of correlations and procedures and was implemented into TUM's in-house engineering tool THERMTEST in order to analyze a variety of experiments performed at the institute's test facility. The assumptions made have been reviewed and several modifications and enhancements have been investigated.

Regarding the heat transfer modeling on the hot gas side the "Modified Sinyarev Model" is the best choice in the case under consideration although high deviations are apparent for low mixture ratios. "Bartz Model" has a similar behavior but performs slightly worse for the low contraction ratio and small diameter combustion chamber.

For low mixture ratios the heat transfer by radiation can reach 20% of the convective heat transfer, although it usually accounts only for approximately 3% up to 8% of the total heat flux.

The models for the heat transfer to the cooling channels showed no noteworthy differences in the total heat flux. However, here only one-dimensional, bulk temperature based models have been considered.

A general optimization of the parameters of the Sinyarev model was not successful. Optimization on a narrow band of operating conditions e.g. the nominal operational point led to odd parameters and a worsening off the design point. However, potential enhancements for the model e.g. a density correction have been identified.

Due to the sensitivity of the heat transfer model on temperature and mixture ratio, the assumption of a low temperature fuel rich boundary layer near the injector face plate requires additional modeling efforts. This approach could account for injector element types known to put a liquid propellant film on the chamber wall e.g. swirl injectors. For the kerosene/ oxygen setup investigated the decrease in gas temperature causes an increase in the heat transfer coefficient overcompensating the desired effect.

Best agreement between experiment and simulation has been achieved by applying an empiric correction dependent of mixture ratio, pressure and position to the Modified Sinyarev Model. The shortcomings of this approach are the high dependence on the hardware characteristics and the huge computational costs. For the sake of convenience a three-parametric correction is proposed which yet has to be adapted to each individual load point and geometry.

Several gaseous and liquid film models have been applied to tests with kerosene and with nitrogen as film fluid. For liquid kerosene the model described by NASA SP-8124 Annex B shows fair agreement but fails on trans-critical kerosene. The model by Stechman agrees fairly with experimental data for both cases. For nitrogen only the model of Grissom matches the test results. For the model described by NASA SP-8124 Annex A problems with the definition of the inflow conditions have been found. Furthermore, temperatures measured by the thermocouples flush-mounted with the hot chamber wall are not regarded as reliable source of information.

For the transpiration cooled CMC some transient simulations have been carried out using a model by Hacker. The investigations show that both the measurements within the porous medium and the modeling is not satisfying.

For the convectively cooled CMC the necessity of good geometric representation and the ability to perform transient simulations became apparent. The hot fire tests with nitrogen cooling could be simulated quite well. For kerosene two phase flow and fuel decomposition is anticipated which exceeds the capabilities of THERMTEST.

The film cooling investigations have been continued within the framework of the national research program SFB Transregio-40. As an outcome of the ATLLAS test results the thermocouples flush-mounted with the hot chamber wall have been replaced by intra cooling channel measurements in order to increased the spatial resolution of the heat flux measurements. Additionally, different cooling fluids, film inlet positions and chamber contraction ratios have been tested.

Experiments with fiber-reinforced ceramics have been successfully repeated in a bilateral project.

The test facility is currently extended for use with gaseous methane. In connection, a new rectangular five-element and a round seven-element rocket combustion chamber have been constructed. The design has been defined and optimized using THERMTEST and the correlations described in this thesis. Hot fire testing of this new hardware will start mid-2014.

Bibliography

[1] G. Schmidt:
Technik der Flüssigkeits-Raketentriebwerke,
DaimlerChrysler Aerospace, Munich, Germany, 1999

[2] J. H. Ferzinger, M. Perić:
Computational Methods for Fluid Dynamics,
3rd rev. Ed., Springer, Berlin-Heidelberg-New York, 2002.

[3] G. Hagemann, O. Knab:
Raumfahrtantriebe 2,
Lecture Notes [in German], Institute for Flight Propulsion (LFA), Technische Universität München, Munich, 2011

[4] G. Schlieben, C. Höglauer, C. Kirchberger, A. Hupfer, H.-P. Kau, O. Knab:
Further Experimental and Analytical Results of Film Cooling Investigations with a GOX/Kerosene Combustion Chamber,
Annual Report of SFB/Transregio 40 "Technological Foundations for the Design of Thermally and Mechanically Highly Loaded Components of Future Space Transportation Systems", Munich, Germany, 2010

[5] C. Höglauer, B. Kniesner, O. Knab, C. Kirchberger, G. Schlieben, H.-P. Kau:
Modeling of a GOX-Kerosene Subscale Rocket Combustion Chamber,
60. Deutscher Luft- und Raumfahrtkongress, Bremen, Germany, 27th-29th September 2011

[6] C. Kirchberger, R. Wagner, H.-P. Kau, S. Soller, P. Martin, M. Bouchez and E. Dufour:
Improved Prediction of Heat Transfer in a Rocket Combustor for GOX/Kerosene,
AIAA-2009-1214, 47th AIAA Aerospace Sciences Meeting and Exhibit, Orlando, USA, 5th-8th January 2009

[7] C. Kirchberger, S. Soller, M. Kuhn, J. Steelant:
Cooling of Ceramic Combustion Chambers,
ISABE-2009-1159, 19th International Symposium on Airbreathing Engines, Montreal, Canada, 7th-11th September 2009

[8] O. Knab, G. Hagemann:
Raumfahrtantriebe 1,

Lecture Notes [in German], Institute for Flight Propulsion (LFA), Technische Universität München, Munich, Germany, 2010

[9] G. P. Sutton:
Rocket Propulsion Elements,
6th Ed., John Wiley & Sons, New York, 1992

[10] A. Dadieu, R. Damm, E. W. Schmidt:
Raketentreibstoffe,
Springer-Verlag, Vienna-New York, 1968

[11] Verein Deutscher Ingenieure, VDI-Gesellschaft Verfahrenstechnik und Chemieingenieurwesen (Hrsg.):
VDI-Wärmeatlas,
8th Ed., Springer, Berlin-Heidelberg-New York, 1997

[12] Department of Defense, United States of America:
Performance Specification - Propellant, Methane,
MIL-PRF-32207, 10th October 2006

[13] M. Rachner:
Die Stoffeigenschaften von Kerosin Jet A-1,
Mitteilung 98-01, Institut für Antriebstechnik, Deutsches Zentrum für Luft- und Raumfahrt, Cologne, Germany, 1998

[14] Encyclopedia Astronautica:
http://www.astronautix.com/,
Internet Source, retrieved on 26th January 2011

[15] GOST 10227-86 on Website of Elarum LLC:
http://elarum.ru/info/standards/gost-10227-86/,
Internet Source, retrieved on 26th January 2011

[16] United States Air Force:
Detail Specification - Propellant, Rocket Grade Kerosene,
MIL-DTL-25576, 14th April 2006

[17] S. Soller:
Injektoren für Hauptstromtriebwerke mit oxidatorreicher Vorverbrennung,
Dissertation [in German], Institute of Flight Propulsion (LFA), Technische Universität München, Munich, Germany, 2007

[18] SpaceX:
http://www.spacex.com/,
Internet Source, retrieved on 11th March 2014

[19] STARSEM – The Modernized Soyuz:
http://www.starsem.com/soyuz/soyuzst.htm,
Internet Source, retrieved on 26th May 2014

[20] OSC "Konstruktorskoe Buro Khimavtomatiky" – RD0124 (14D23):
http://www.kbkha.ru/?p=8&cat=8&prod=51,
Internet Source, retrieved on 26th May 2014

[21] LIQUID PROPELLANT ROCKET ENGINES – NK-33:
http://www.lpre.de/sntk/NK-33/index.htm,
Internet Source, retrieved on 26th May 2014

[22] C. KIRCHBERGER, R. WAGNER, H.-P. KAU, S. SOLLER, P. MARTIN, M. BOUCHEZ AND CH. BONZON:
Prediction and Analysis of Heat Transfer in Small Rocket Chambers,
AIAA-2008-1260, 46th AIAA Aerospace Sciences Meeting and Exhibit, Reno, USA, 7th-10th January 2008

[23] D. R. BARTZ:
A simple Equation for Rapid Estimation of Rocket Nozzle Convective Heat Transfer Coefficients,
Jet Propulsion, Vol. 27 No.1, pp.49-51, 1957.

[24] S. GORDON, B. MCBRIDE:
Computer Program for Calculation of Complex Chemical Equilibrium Compositions and Applications,
NASA Reference Publication 1311, 1994.

[25] TDK'08(TM):
http://www.seainc.com/tdk.d.html,
Internet Source, retrieved on 31st March 2011

[26] CHEMKIN WEB OVERVIEW:
http://www.sandia.gov/chemkin/index.html,
Internet Source, retrieved on 31st March 2011

[27] CANTERA - AN OBJECT-ORIENTED SOFTWARE TOOLKIT FOR CHEMICAL KINETICS, THERMODYNAMICS, AND TRANSPORT PROCESSES.:
http://code.google.com/p/cantera/,
Internet Source, retrieved on 31st March 2011

[28] D. R. BARTZ:
Survey of Relationships between Theory and Experiment for Convective Heat Transfer in Rocket Combustion Gases,
in S. S. Penner (Ed.): "Advances in Rocket Propulsion", AGARD, Manchester, England, 1968

[29] D. K. HUZEL, D. H. HUANG:
Design of Liquid Propellant Rocket Engines,
NASA SP-125, 1967

[30] R. L. SCHACHT, R. J. QUENTMEYER:
Axial and Circumferential Variations of Hot-Gas-Side Heat-Transfer Rates in a Hydrogen-Oxygen Rocket.,
NASA TN D-6396, 1971

[31] E. R. G. ECKERT, R. M. DRAKE:
Heat and Mass Transfer,
McGraw-Hill Book Co., Inc., 1950

[32] W. Polifke:
Wärmetransportphänomene// Wärme- und Stoffübertragung,
Lecture Notes [in German], Lehrstuhl für Thermodynamik, Technische Universität München, Munich, Germany, 2001

[33] V. Gnielinski:
New Equation for Heat and Mass Transfer in Turbulent Pipe and Channel Flow,
International Chemical Engineering, Vol. 16, pp. 359-368, 1976

[34] G. B. Sinyarev, M. V. Dobrovolsky:
Liquid Rocket Engines - Theory and Design. [in Russian],
Moscow, USSR, 1955

[35] A. A. Gukhman and N. V. Ilyukhin:
The Doctrine of Heat Transfer in Gas Flows with High Velocity [in Russian],
Mashgiz, USSR, 1951

[36] M. H. Ostrander:
Emissivity Calculations for Carbon Monoxide,
California Institute of Technology, Pasadena, CA, USA, 1951

[37] T. L. Bergmann, A. S. Lavine, F. P. Incropera, D. P. DeWitt:
Fundamentals of Heat and Mass Transfer,
7th Ed., John Wiley & Sons, Inc., 2011

[38] A. Schack:
Der industrielle Wärmeübergang,
8th Ed., Verlag Stahleisen mbH, 1983

[39] M. Barrère, A. Jaumotte, B. F. de Veubeke, J. Vandenkerckhove:
Raketenantriebe,
Elsevier Publishing Company, 1961

[40] A. Schack, formulas quoted in D. Marty:
Conception des Véhicules Spatiaux,
Éditions Masson, p. 350, 1985

[41] H. Kraussold:
Die Wärmeübertragung an Flüssigkeiten in Rohren bei turbulenter Strömung,
Forschung auf dem Gebiet des Ingenieurwesens A, Vol. 4, Issue 1, pp. 39-44, Springer-Verlag, 1933.

[42] W. H. McAdams:
Heat Transmission,
3rd ed., McGraw-Hill Book Company, 1954

[43] P. A. Masters, C. A. Aukerman:
Deposit Formation in Hydrocarbon Rocket Fuels with an Evaluation of a Propane Heat Transfer Correlation,
NASA-TM-82911, 1982

[44] R. W. Michel:
Combustion Performance and Heat Transfer Characterization of LOX/Hydrocarbon Type Propellants,
NASA-CR-171712, 1983

[45] F. M. Kirby:
Methane Heat Transfer Investigation,
NASA-CR-171199, 1984

[46] K. Liang, B. Yang, Z. Zhang:
Investigation of Heat Transfer and Coking Characteristics of Hydrocarbon Fuels,
in "Primary, Upper-Stage, and On-Board Propulsion for Space Transportation", Proceedings of the Third International Symposium on Space Propulsion, The Chinese Society of Astronautics, Beijing, China, 11th-13th August 1997

[47] M. F. Wadel:
Comparison of High Aspect Ratio Cooling Channel Designs for a Rocket Combustion Chamber With Development of an Optimized Design,
NASA TM-1998-206313, January 1998

[48] J. A. Carlile, R. J. Quentmayer:
An Experimental Investigation of High-Aspect-Ratio Cooling Passages,
AIAA-92-3154, 28th AIAA/ASME/SAE/ASEE Joint Propulsion Conference and Exhibit, Nashville, TN, USA, 6th-8th July 1992

[49] A. Woschnak, M. Oschwald:
Thermo- and Fluidmechanical Analysis of High Aspect Ratio Cooling Channels,
AIAA-2001-3404, 37th AIAA/ASME/SAE/ASEE Joint Propulsion Conference and Exhibit, Salt Lake City, UT, USA, 8th-11th July 2011

[50] J. P. Hartnett, R. C. Birekbak, E. R. G. Eckert:
Velocity Distributions, Temperature Distributions, Effectiveness and Heat Transfer for Air Injected Through a Tangential Slot into a Turbulent Boundary Layer,
Journal on Heat Transfer, Vol. 83, p. 293, 1961

[51] R. Arnold:
Experimentelle Untersuchungen zur Filmkühlung in Raketenbrennkammern,
PhD Thesis [in German], ISBN 978-3-86727-842-3, Cuvillier Verlag, Göttingen, Germany, 2008

[52] R. C. Parkinson, H. Ziebland:
Heat Transfer in Rocket Engines,
AGARDograph No. 148, 1971

[53] J. E. Hatch, S. S. Papell:
Use of Theoretical Flow Model to Correlate Data for Film Cooling or Heating an Adiabatic Wall by Tangential Injection of Gases of Different Fluid Properties.,
NASA TN D-130, 1959

[54] A. H. Lefebvre:
Gas Turbine Combustion,
Taylor & Francis, 1983

[55] C. A. Cruz, A. W. Marshall:
Surface and Gas-Phase Temperatures Near Film Cooled Wall,
AIAA-2004-3654, 40th AIAA/ASME/SAE/ASEE Joint Propulsion Conference and Exhibit, Ft. Lauderdale, FL, USA, 11th-14th July 2004

[56] J. L. Stollery, A. A. M. El-Ehwany:
A Note on the Use of a Boundary-Layer Model for Correlating Film-Cooling Data.,
International Journal on Heat Transfer, Vol. 8, p. 55, 1965

[57] R. C. Stechman:
Film Cooling of Small Rocket Engines,
MIR #264, 1968

[58] R. C. Stechman, J. Oberstone, J. C. Howell:
Film Cooling of Small Rocket Engines,
Journal of Spacecraft and Rockets, Vol. 6 issue 2, February 1969

[59] NASA Space Vehicle Design Criteria (Chemical Propulsion):
Liquid Rocket Engine Self-Cooled Combustion Chambers,
NASA SP-8124, 1977

[60] W. M. Grissom:
Liquid Film Cooling in Rocket Engines,
AEDC-TR-91-1, Final Report, Physics Department, Morehouse College, Atlanta, GA, USA, March 1991

[61] S. S. Kutateladze et al.:
High Temperature.,
High Temperature (Soviet), Vol. 1, September-October 1963

[62] C. J. Marek, R. R. Tacina:
Effect of Free-stream Turbulence on Film Cooling,
NASA TN D-7958, June 1975

[63] L. W. Carlson, E. Talmor:
Gaseous Film Coooling at Various Degrees of Hot Gas Acceleration and Turbulence Levels,
International Journal on Heat and Mass Transfer, Vol. 11 issue 11, p. 1695, 1968

[64] R. J. Goldstein, R. B. Rask, E. R. G. Eckert:
Film Cooling with Helium Injection into an Incompressible Air Flow,
International Journal on Heat and Mass Transfer, Vol. 9 issue 12, p. 1341, 1966

[65] J. A. Landis, W. J. Bowman:
Numerical Study of a Transpiration Cooled Rocket Nozzle,
AIAA-96-2580, 32nd AIAA/ASME/SAE/ASEE Joint Propulsion Conference & Exhibit, Hartford, CT, USA, 1st-3rd July 2008

[66] D. S. Hacker:
Empirical Prediction of Turbulent Boundary Layer Instability along a Flat Plate with Constant Mass Addiction at the Wall.,
Jet Propulsion, Vol. 26, p. 786, 1956

[67] S. S. Kutateladze, A. I. Leontev:
Turbulent Boundary Layers in Compressible Gases.,
translated by D. B. Spalding, Edward Arnold, London, 1964

[68] W. M. Kays, M. E. Crawford, B. Weigand:
Convective Heat and Mass Transfer.,
ISBN 007-123829-8, 4th Ed., McGraw-Hill International Edition, 2005

[69] C. Kirchberger, G. Schlieben, R. Wagner, H.-P. Kau, C. Mäding, S. Soller, P. Martin:
Design and Commissioning of a Combustion Chamber for Cooling and Material Investigations.,
AIAA-2008-5239, 44th AIAA/ASME/SAE/ASEE Joint Propulsion Conference & Exhibit, Hartford, CT, USA, 20th-23rd July 2008

[70] C. Kirchberger, G. Schlieben, A. Hupfer, H.-P. Kau, S. Soller:
Investigation on Film Cooling in a Kerosene/ GOX Combustion Chamber,
AIAA-2009-5406, 45th AIAA/ASME/SAE/ASEE Joint Propulsion Conference & Exhibit, Denver, CO, USA, 2nd-5th August 2009

[71] S. Soller, R. Wagner, H.-P. Kau, P. Martin and C. Mäding:
Characterisation of Main Chamber Injectors for GOX/Kerosene in a Single Element Rocket Combustor,
AIAA-2005-3750, 41st AIAA/ASME/SAE/ ASEE Joint Propulsion Conference and Exhibit, Tucson, AZ, USA, 10th-13th July 2005

[72] S. Soller, R. Wagner, C. Kirchberger, H.-P. Kau, P. Martin and C. Mäding:
Characterisation of Combustion and Heat Transfer using GOX/Kerosene in a Single-Element Rocket Combustor,
AIAA-2005-4529, 41st AIAA/ASME/SAE/ASEE Joint Propulsion Conference and Exhibit, Tucson, AZ, USA, 10th-13th July 2005

[73] S. Soller, R. Wagner, H.-P. Kau, P. Martin and C. Mäding:
Influence of Coaxial Injector Element Design on Heat Transfer in Oxidizer Rich Staged Combustion Cycle Engines,
IAC-06- C4.3.05, International Astronautical Congress, Valencia, Spain, 2nd-6th October 2006

[74] R. Wagner, S. Soller, H.-P. Kau, P. Martin and C. Mäding:
Influence of Injector Element Design on Wall Heat Transfer,
AIAA-2006-4724, 42nd AIAA/ASME/SAE/ ASEE Joint Propulsion Conference and Exhibit, Sacramento, CA, USA, 9th-12th July 2006

[75] R. Wagner, S. Soller, H.-P. Kau, P. Martin, C. Mäding:
Combustion Stability Characteristics of Coax-Swirl-Injectors for Oxygen/Kerosene,
AIAA-2007-5563, 43rd AIAA/ASME/SAE/ASEE Joint Propulsion Conference & Exhibit, Cincinnati, OH, USA, 8th-11th July 2007

[76] R. Wagner, S. Soller, H.-P. Kau, P. Martin, C. Mäding:
Experimental Investigations of Coax Swirl Injectors for Hydrocarbons,

IAC-07- C4.3.06, International Astronautical Congress, Hyderabad, India, 24th-28th September 2007

[77] T. Inamura, H. Tamura, H. Sakamoto:
Characteristics of Liquid Film and Spray Injected from Swirl Coaxial Injector,
Journal of Propulsion and Power, Vol. 19, No. 4, 2003, pp. 632-639

[78] P. A. Starkey, D. G. Talley, J. J. Hutt:
Mixing Characteristics of Coaxial Injectors at High Gas/liquid Momentum Ratios,
Journal of Propulsion and Power, Vol. 17, No. 2, 2001, pp. 402-410

[79] M. R. Long, V. G. Bazarov, W. E. Anderson:
Main Chamber Injectors for Advanced Hydrocarbon Booster Engines,
AIAA-2003-4599, 39th AIAA/ASME/SAE/ASEE Joint Propulsion Conference and Exhibit, Huntsville, AL, USA, 20th-23rd July 2003

[80] M. Bouchez, S. Beyer, S. Schmidt:
PTAH-SOCAR Fuel-Cooled Composite Materials Structure: 2011 Status,
AIAA-2011-2208, 17th AIAA International Space Planes and Hypersonic Systems and Technology Conference, San Francisco, CA, USA, 11th-14th April 2011

[81] NI LabVIEW - Die grafische Programmierumgebung für Ingenieure und Wissenschaftler:
http://www.ni.com/labview/d/,
Internet Source, retrieved on 28th February 2011

[82] B. S. Stratford, G. S. Beavers:
The Calculation of the Compressible Turbulent Boundary Layer in an Arbitrary Pressure Gradient; A Correlation of Certain Previous Methods,
A.R.C., R3207 (ARG,R8), 1964,
in J. Stoll: “Wärmeübergang und Filmkühlung in kompressibler Düsenströmung”, Dissertation [in German], Technische Universität München, Munich, Germany, 1987

[83] S. A. Evans:
JANNAF Rocket Engine Performance Prediction and Evaluation Manual,
ADA127654, 1975

[84] C. Kirchberger:
Conclusion of Run-In Tests and Characterization of New Systems,
Deliverable D.4.1.4 issue 1 revision 1, SPECIFIC TARGETED RESEARCH PROJECT ATLLAS (Aerodynamic and Thermal Load Interactions with Lightweight Advanced Materials for High Speed Flight), Institute of Flight Propulsion, Technische Universität München, Munich, Germany, 2009/2010

[85] *fft :: Functions (MATLAB Function Reference)*,
Documentation, Matlab Version 7.6.0.324 (R2008a), The Mathworks Inc., 2008

[86] P. Duhamel, M. Vetterli:
Fast Fourier Transforms: A Tutorial Review and a State of the Art,
Signal Processing, Vol. 19, pp. 259-299, April 1990

[87] *FFTW*,
(http://www.fftw.org)

[88] R. Arnold, D. Suslov, O. J. Haidn:
Influence Parameters on Film Cooling Effectiveness in a High Pressure Subscale Combustion Chamber,
AIAA-2009-0453, 47th AIAA Aerospace Sciences Meeting Including the New Horizons Forum and Aerospace Exposition, Orlando, FL, USA, 5th-8th January 2009

[89] C. Kirchberger:
Hot Fire Tests and First Evaluation of Test Results with Regenerative and Film Cooling,
Deliverable D.4.1.6, SPECIFIC TARGETED RESEARCH PROJECT ATLLAS (Aerodynamic and Thermal Load Interactions with Lightweight Advanced Materials for High Speed Flight), Institute of Flight Propulsion, Technische Universität München, Munich, Germany, 2010

[90] C. Kirchberger:
Hot Fire Tests and First Evaluation of Test Results for C/C and Oxide-Based Ceramic Modules at High Temperatures,
Deliverable D.4.1.7, SPECIFIC TARGETED RESEARCH PROJECT ATLLAS (Aerodynamic and Thermal Load Interactions with Lightweight Advanced Materials for High Speed Flight), Institute of Flight Propulsion, Technische Universität München, Munich, Germany, 2010

[91] C. Kirchberger:
Hot Fire Tests and First Evaluation of Test Results: Parts A & B,
Deliverable D.4.3.4/ D.4.3.7, SPECIFIC TARGETED RESEARCH PROJECT ATLLAS (Aerodynamic and Thermal Load Interactions with Lightweight Advanced Materials for High Speed Flight), Institute of Flight Propulsion, Technische Universität München, Munich, Germany, 2009

[92] M. Bouchez, E. Dufour, F. Cheuret, J. Steelant, P. Grenard, J. Redford, N. Sandham, A. Passaro, D. Baccarella, M. Dalenbring, J. Smith:
"Material-Aero-Thermal Interaction Computations in the ATLLAS European Programme,
AIAA-2008-4670, 44th AIAA/ASME/SAE/ASEE Joint Propulsion Conference & Exhibit, Hartford, CT, 21st-23rd July 2008

[93] G. Schlieben, C. Kirchberger, A. Hupfer, H.-P. Kau, S. Soller, C. Mäding:
Dynamic Characterization of Double Swirl Injectors for GOX/Kerosene,
AIAA-2011-5924, 47th AIAA/ASME/SAE/ASEE Joint Propulsion Conference & Exhibit, San Diego, CA, USA, 31st July-3rd August 2011

[94] C. Kirchberger, G. Schlieben, A. Hupfer, H.-P. Kau, S. Soller:
Film Cooling Investigations in a Kerosene/ GOX Combustion Chamber,
AIAA-2011-5777, 47th AIAA/ASME/SAE/ASEE Joint Propulsion Conference & Exhibit, San Diego, CA, USA, 31st July-3rd August 2011

[95] C. Kirchberger:
Final Report: Heat Transfer Characterization with Video Data Analysis,
Deliverable D.4.1.10, SPECIFIC TARGETED RESEARCH PROJECT ATLLAS (Aerodynamic and Thermal Load Interactions with Lightweight Advanced Materials for High Speed Flight), Institute of Flight Propulsion, Technische Universität München, Munich, Germany, 2010

[96] C. Kirchberger:
Filmkühlung in THERMTEST (Softwaredokumentation),
Institute for Flight Propulsion (LFA), Technische Universität München, Munich, Germany, 2005

[97] M. Bouchez, E. Dufour, E. Daniau:
Semi-Empirical and CFD Analysis of Actively Cooled Dual-Mode Ramjets: 2006 Status,
AIAA-2006-8073, 14th AIAA/AHI Space Planes and Hypersonic Systems and Technologies Conference, Canberra, Australia, November 6th-9th 2006

[98] M. Kuhn:
Test Prediction for Transpiration Cooled CMCs (TUM) - Structural Test Report on Transpiration Cooled CMCs (TUM),
merged deliverables D.4.2.4/ D.4.2.5 Part B issue 1 revision 4, 19.03.2010, SPECIFIC TARGETED RESEARCH PROJECT ATLLAS (Aerodynamic and Thermal Load Interactions with Lightweight Advanced Materials for High Speed Flight), DLR, Stuttgart, Germany, 2010

[99] A. Woschnak:
Untersuchung des Wärmeübergangs in regenerativ gekühlten Schubkammern kryogener Raketentriebwerke,
PhD Thesis [in German], ISBN 978-3-83228-558-6, Shaker Verlag, Aachen, Germany, 2009

[100] A. Ponomarenko:
Thermal Analysis of Thrust Chambers,
Software Manual, RPA: Tool for Rocket Propulsion Analysis, 2012

[101] V. M. Kudryavtsev:
Fundamentals of Theory and Calculation of Liquid Rocket Engines,
two-volume, Vol. 2, 4th revised and enlarged Edition, Moscow, 1993

[102] M. P. Celano, S. Silvestri, G. Schlieben, C. Kirchberger, O.J. Haidn:
Injector Characterization for a GOX-GCH4 Single Element Combustion Chamber,
5th European Conference for Aeronautics and Space Sciences (EUCASS), Munich, Germany, 1-5 July 2013

[103] C. Kirchberger, G. Schlieben, A. Hupfer and H.-P. Kau:
Experimental Investigation on Film Cooling in a Hydrocarbon/ GOX Rocket Combustion Chamber,
AIAA-2012-0526, 50th AIAA Aerospace Sciences Meeting and Exhibit, Nashville, TN, USA, 9th-12th January 2012

[104] G. Schlieben, C. Kirchberger , O. J. Haidn:
Using Intra Cooling Channel Measurements for Film Cooling Investigations in a GOX/ Kerosene Rocket Combustion Chamber,
AIAA-2012-3910, 48th AIAA/ASME/SAE/ASEE Joint Propulsion Conference and Exhibit, Atlanta, GA, USA, 29th July-1st August 2012

[105] C. Kirchberger, G. Schlieben, O. J. Haidn:
Investigation on Film Cooling in a GOX/ Kerosene Rocket Combustion Chamber,
29th International Symposium on Space Technology and Science, Nagoya-Aichi, Japan, 2nd-9th June 2013

[106] C. Kirchberger, G. Schlieben, O. J. Haidn:
Assessment of Film Cooling Characteristics in a GOX/ Kerosene Rocket Combustion Chamber,
49th AIAA/ASME/SAE/ASEE Joint Propulsion Conference and Exhibit, San Jose, CA, USA, 15th-17th July 2013

[107] S. Schmidt:
Properties of the CarbotexSI-PSR Duct,
Personal Communication Within ATLLAS (Aerodynamic and Thermal Load Interactions with Lightweight Advanced Materials for High Speed Flight), Work Package 4.3, 20th July 2009

List of Student Research Projects

This work benefited from hardware components, tools and procedures developed by students within research projects performed at the Space Propulsion Group, Institute for Flight Propulsion, Technische Universität München. These projects have been attended by the members of research staff, namely P. Martin, S. Soller, R. Wagner, C. Kirchberger, G. Schlieben, M. Celano, S. Silvestri and C. Bauer, and supervised by Prof. Dr.-Ing. Hans-Peter Kau and Prof. Dr.-Ing. Oskar J. Haidn. The subsequent list specifies the student research projects involved.

M. Schulz:
Auslegung und Konstruktion des Kühlsystems für ein Subscale-Raketentriebwerk,
Semester Assignment [in German], 2002

G. Hofer:
Konstruktion von Einspritzelementen für ein Subscale-Raketentriebwerk,
Semester Assignment [in German], 2003

A. Stumvoll:
Auslegung und Konstruktion des Kühlsystems für Raketendüsen,
Semester Assignment [in German], 2003

S. Smollich:
Vergleich verschiedener Verfahren zur Modellierung des kühlkanalseitigen Wärmeübergang-es in regenerativ gekühlten Raketenbrennkammern,
Semester Assignment [in German], 2003

V. Laubach:
Konstruktion von Einspritzelementen für ein Subscale-Raketentriebwerk,
Semester Assignment [in German], 2003

R. O. Kuchar:
Programm zur automatischen Datenauswertung mit Matlab,
Semester Assignment [in German], 2003

C. Kirchberger:
Gestaltung einer Raketenbrennkammer aus faserverstärktem Siliziumcarbid,
Diploma Thesis [in German], 2004

M. Hällfritzsch:
Charakterisierung des Kühlsystems für einen Raketenbrennkammerprüfstand,
Semester Assignment [in German], 2005

S. Rapp:
Auslegung und Konstruktion eines Brennkammersegments mit variabler Kühlkanalgeometrie für ein Prüfstandsraketentriebwerk,
Semester Assignment [in German], 2005

A. Winkler:
Analyse und Konstruktion von Einspritzelementen für Hauptstromtriebwerke,
Semester Assignment [in German], 2005

K. Jerin:
Charakterisierung von Coax-Swirl Injektoren für Hauptstromtriebwerke mit oxidatorreicher Vorverbrennung,
Semester Assignment [in German], 2005

H. Güntner:
Konstruktion eines Spraytestprüfstandes für Injektoren von Hauptstromtriebwerken für die Treibstoffkombination GOX/Kerosin,
Semester Assignment [in German], 2006

A. Steinbeck:
Simulation der Verbrennung in einer Subscale-Raketenbrennkammer für Sauerstoff und Kerosin,
Semester Assignment [in German], 2007

A. Naubert:
Bewertung von Modellen zur Spraysimulation mit ANSYS CFX 10,
Semester Assignment [in German], 2007

A. Steinbeck:
Numerische Untersuchung des Wärmeübergangs in Rakentenbrennkammern für Kohlenwasserstoffe,
Diploma Thesis [in German], 2007

G. Schlieben:
Auslegung und Konstruktion einer Subscale-Raketenbrennkammer,
Semester Assignment [in German], 2007

S. Zawadzki:
Untersuchung der Kerosin-Filmkühlung in einer Subscale-Raketen-Brennkammer,
Semester Assignment [in German], 2007

G. Schlieben:
Auslegung und Konstruktion eines Kühlfilmexperiments für eine Subscale-Raketenbrennkammer,
Diploma Thesis [in German], 2007

H. Kneistler:
Simulation des Wärmeübergangs in einem Subscale-Raketentriebwerk,
Semester Assignment [in German], 2007

S. Fischl:
Brennkammersimulationen zur Eigenfrequenzbestimmung und Vergleich mit Tehora-Versuchsdaten,
Semester Assignment [in German], 2007

D. Bruno:
Numerical Simulation of Fluid Flows within a Regeneratively Cooled Oxidizer-rich Combustion Chamber,
Diploma Thesis, 2007

A. Galbiati:
Predictions and Analysis of Film Cooling Experiments at a Subscale Rocket Combustion Chamber,
Diploma Thesis, 2008

H. Enke:
Transiente Kalibrierung von Thermosensoren am Raketenbrennkammerprüfstand,
Semester Assignment [in German], 2009

S. Bickelmaier:
Prediction and Analysis of Transpiration Cooling Experiments on a Subscale Rocket Combustion Chamber,
Semester Assignment, 2009

M. Kollmar:
Konstruktion eines Wärmetauschers für ein Raketenbrennkammerexperiment,
Semester Assignment [in German], 2009

T. M. Häberlein:
Nutzung von Greenpropellants in Raumfahrtantrieben,
Semester Assignment [in German], 2009

S. Blank:
Auswertung und Modellierung von Experimenten zur Charakterisierung des Wärmeübergangs in einer Raketenbrennkammer,
Diploma Thesis [in German], 2009

S. Huberth:
Machbarkeitsstudie zur Umrüstung des Raketenbrennkammer-Prüfstandes auf Flüssigsauerstoff,
Semester Assignment [in German], 2010

B. Bulat:
Bewertung von Kühlfilmexperimenten in einer Subscale-Raketenbrennkammer anhand des Verbrennungswirkungsgrades,
Semester Assignment [in German], 2010

D. Fueyo Garcia:
Design of a Water-Cooled Torch Igniter for a Subscale Rocket Combustion Chamber,
Diploma Thesis, 2010

M. Karanikolov:
Regelung des Kühlmittelkreislaufs am Raketenprüfstand des LFA,
Semester Assignment [in German], 2010

H. Gomez Martinez:
Design of a Nozzle for a Subscale GOX/Kerosene Rocket Combustion Chamber,
Semester Assignment [in German], 2010

S. Kunze:
Planung und Auslegung eines Regelventils für die Stickstoffkühlmittelversorgung eines Raketenbrennkammerprüfstands,
Semester Assignment [in German], 2010

D. Guy:
Konstruktion eines kalorischen Messsegments für die Subscale-Raketenbrennkammer des LFA,
Semester Assignment [in German], 2010

A. Dahlhaus:
Konstruktion eines Einspritzelementes für eine Subscale-Raketenbrennkammer unter besonderer Berücksichtigung alternativer Treibstoffe,
Semester Assignment [in German], 2010

C. Bauer:
CFD Analysis of a Rocket Combustion Chamber,
Semester Assignment, 2010

S. Hennecke:
Anpassung eines keramischen Injektors zur Verwendung am LFA-Raketenbrennkammerprüfstand,
Semester Assignment [in German], 2011

M. Triebig:
Thermalanalyse eines Thermoelements in einer Brennkammerwand mittels FEM-Simulation,
Semester Assignment [in German], 2011

M. Langer:
Konstruktion eines wassergekühlten Filmlegers,
Semester Assignment [in German], 2011

M. Mindt:
Untersuchung analytischer Filmkühlungsmodelle für eine GOX/Kerosin-Raketenbrennkammer,
Bachelor Thesis [in German], 2011

L. Veggi:
Konstruktion eines kapazitiv gekühlten Messsegments zur Bestimmung von Wandtemperatur und Wärmestrom für einen Raketenbrennkammerprüfstand,
Bachelor Thesis [in German], 2011

C. Bühler:
Untersuchung geeigneter Treibstoffkombinationen für einen studentischen Raketenbrennkammerprüfstand,
Semester Assignment [in German], 2011

R. Hink:
Numerische Untersuchung eines Einspritzelementes für einen Single-Element Subscale-Raketenprüfstand,
Diploma Thesis [in German], 2012

M. Trotti:
Modelling of liquid film cooling in a GOX/Kerosene rocket combustion chamber,
Master Thesis, 2012

S. Licht:
Basis eines Expertensystems zur Überprüfung der Sensorplausibilität an Raketenprüfständen,
Diploma Thesis [in German], 2012

S. Hinrichs:
Design eines axialen Filmlegers für eine Subscale-Raketenbrennkammer,
Semester Assignment [in German], 2012

M. Grohmann:
CFD-Simulation von Raketenbrennkammern unter Berücksichtigung von Gasstrahlung und Ruß,
Diploma Thesis [in German], 2012

C. Franzmann:
Characterization of an Injector Element for a GCH4/GOX Subscale Rocket Combustion Chamber,
Semester Assignment, 2013

B. Ams:
Numerical Investigation of Swirl Effects in Rocket Engine Combustion,
Diploma Thesis, 2013

F. Schily:
Analyse des Einflusses von Rußbildung und Rußablagerung auf den Wärmeübergang in einer Raketenbrennkammer,
Semester Assignment [in German], 2014

Appendix

A. Details of Test Facility and Hardware

A.1 Test Facility

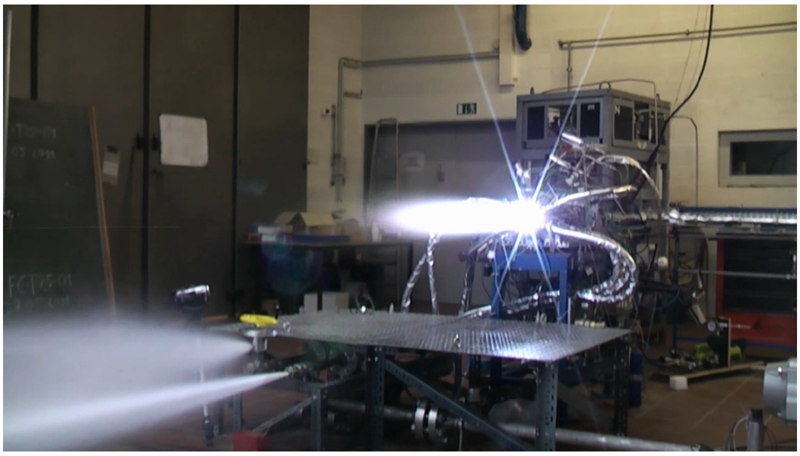

Fig. A.1: Photo of Test Facility During Hot Fire Test

A.2 Test Hardware

A.2.1 Combustion Chamber

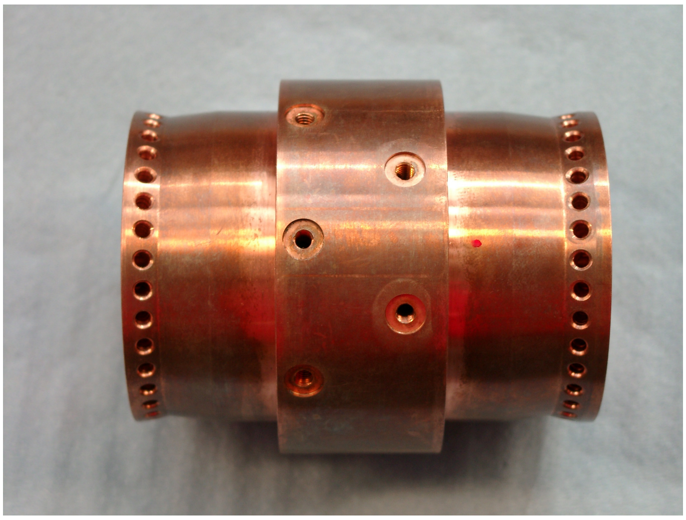

Fig. A.2: Water-Cooled Segment for 37 mm Combustion Chamber (with holes for hot wall temperature measurements)

Fig. A.3: Water-Cooled Nozzle Segment (37 mm CC, $\varepsilon_c = 5.0$)

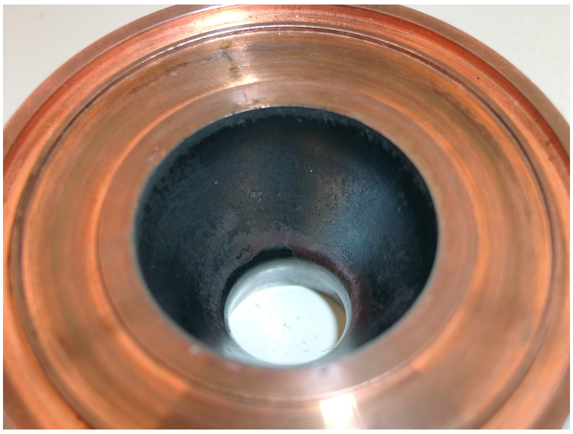

Fig. A.4: Detail of Nozzle Segment After Test (37 mm CC, $\varepsilon_c = 5.0$)

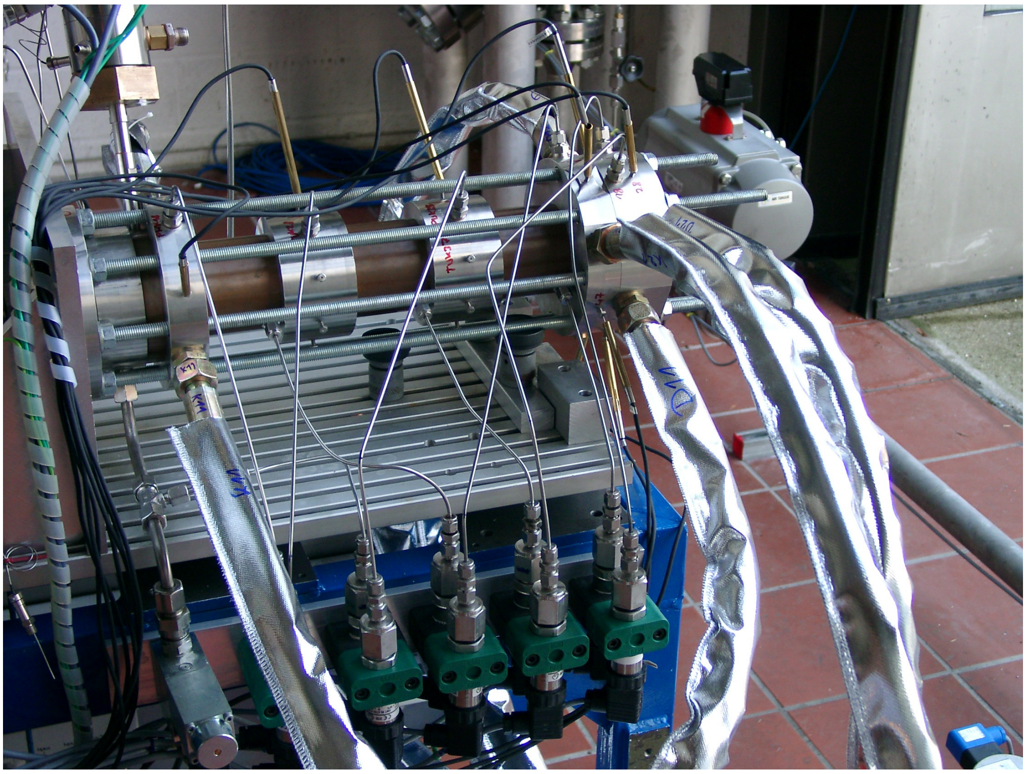

Fig. A.5: Photo of 20 mm Combustion Chamber

A.2.2 Injector

Fig. A.6: Comparison of Injectors for 20 mm and 37 mm Combustion Chamber

A.2.3 Film Cooling Experiments

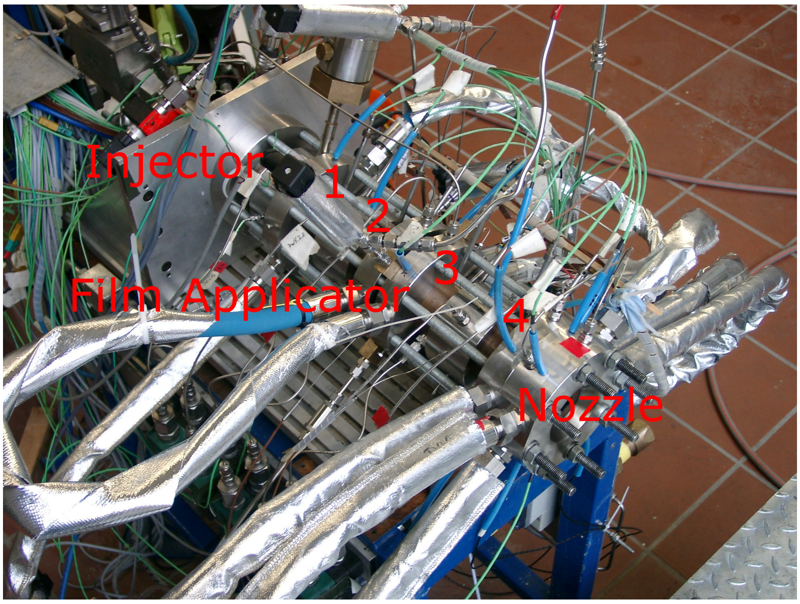

Fig. A.7: Photo of Film Applicator Installed after 2nd Segment

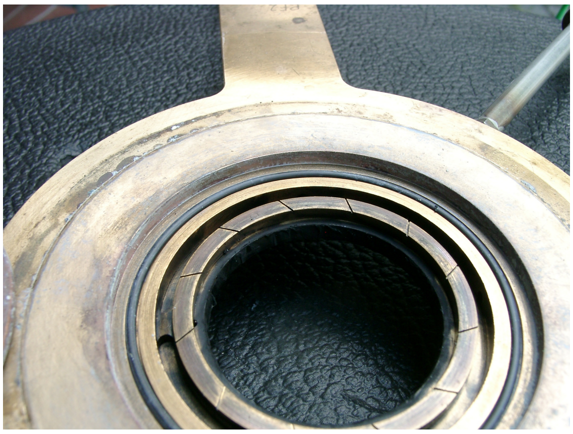

Fig. A.8: Detail of Film Applicator (base plate with lip ring removed, spacer ring with swirl channels visible)

A.2.4 Transpiration Cooled CMC

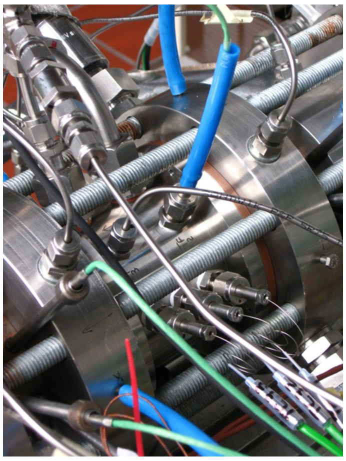

Fig. A.9: Photo of Transpiration-Cooled CMC Installed Between Water-Cooled Segments (Courtesy of German Aerospace Center (DLR) – Institute of Structures and Design)

(a) C/C (b) OXIPOL (c) WHIPOX

Fig. A.10: Transpiration-Cooled CMC – Material Samples (Courtesy of German Aerospace Center (DLR) – Institute of Structures and Design)

A.2.5 Convectively Cooled CMC

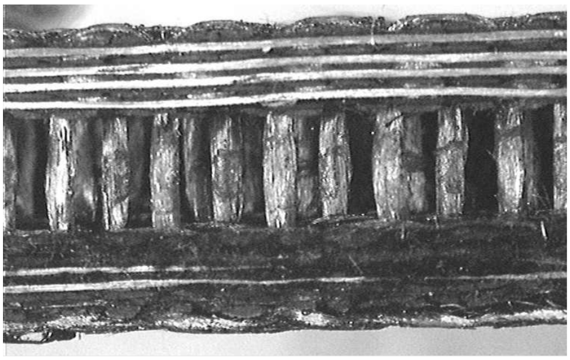

Fig. A.11: Detail of PTAH-SOCAR Duct with Fin Structure (Courtesy of MBDA France)

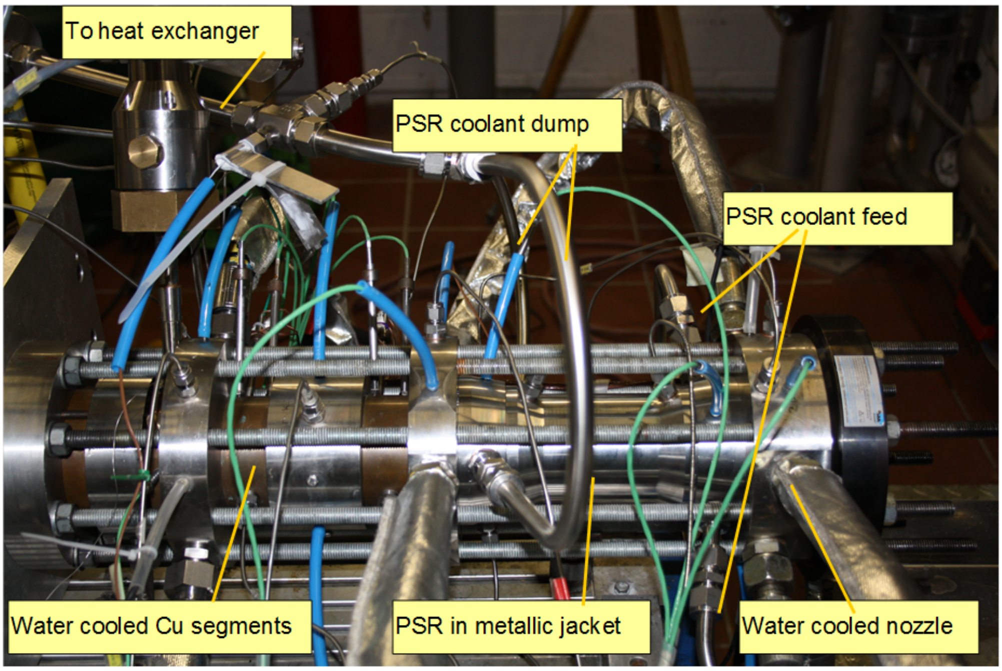

Fig. A.12: Hardware Setup for Convectively-Cooled CMC (Courtesy of Astrium Space Transportation)

A.3 Data Acquisition

A.3.1 Overview of DAQ Channels

Sensor	Unit	Range	Location, Comment
VK	cm^3/s	0-460	Kerosene volume flow rate to injector and film
PN4	bar	0-400	Kerosene pressure regulator pilot pressure
PK2	bar	0-400	Kerosene pressure after pressure regulator
PK3	bar	0-400	Kerosene pressure at tap off to injector / before RVK
TK3	K	173-273	Kerosene temperature at tap off to injector, PT-100, 2 mm
PK5	bar	0-250	Kerosene pressure in injector manifold
PKDYN	bar	±100	Dynamic pressure in kerosene manifold
MO	kg/s	0-0.8	Oxygen mass flow rate to injector
PN3	bar	0-400	Oxygen pressure regulator pilot pressure
TO4	K	173-1623	Oxygen temperature before flow control valve
PO4	bar	0-160	Oxygen pressure before flow control valve
TO5	K	173-1623	Oxygen temperature after flow control valve
PO5	bar	0-160	Oxygen pressure after flow control valve
PODYN	bar	±100	Dynamic pressure after flow control valve
PN2	bar	0-400	Supply pressure purge
PFZ2	bar	0-160	Igniter fuel feed line pressure upstream orifice
POZ2	bar	0-160	Igniter oxidizer feed line pressure upstream orifice
PCZ	bar	0-160	Igniter chamber pressure
PC0	bar	0-160	Chamber pressure, 7 mm from face plate
PCDYN	bar	±100	Dynamic chamber pressure, 7 mm from face plate
PC1	bar	0-160	Chamber pressure 55 mm from face plate
PC2	bar	0-160	Chamber pressure 150 mm from face plate
PC3	bar	0-160	Chamber pressure 245 mm from face plate
PC4	bar	0-160	Chamber pressure 340 mm from face plate
THW11c	K	173-673	Chamber wall temperature 50.5 mm from face plate, Type T
THW21c	K	173-673	Chamber wall temperature 145.5 mm from face plate, Type T
THW31c	K	173-673	Chamber wall temperature 240.5 mm from face plate, Type T
THW41c	K	173-673	Chamber wall temperature 335.5 mm from face plate, Type T
THW11a	K	173-1623	Chamber wall temperature 50.5 mm from face plate, Type K
THW21a	K	173-1623	Chamber wall temperature 145.5 mm from face plate, Type K
THW31a	K	173-1623	Chamber wall temperature 240.5 mm from face plate, Type K
THW41a	K	173-1623	Chamber wall temperature 335.5 mm from face plate, Type K
THW12b	K	173-1623	Chamber wall temperature 70.0 mm from face plate, Type K

Sensor	Unit	Range	Location, Comment
THW22b	K	273-873	Chamber wall temperature 165.0 mm from face plate, Type K
THW32b	K	173-1623	Chamber wall temperature 260.0 mm from face plate, Type K
THW42b	K	273-873	Chamber wall temperature 355.0 mm from face plate, Type K
PN5	bar	0-400	High pressure air pressure regulator pilot pressure
DPWG	bar	0-6	Cooling water differential pressure over measuring orifice, total
DPWK	bar	0-6	Cooling water differential pressure over measuring orifice, chamber
DPWD	bar	0-6	Cooling water differential pressure over measuring orifice, nozzle
PWK1	bar	0-400	Cooling water pressure inlet manifold
PWK2	bar	0-400	Cooling water pressure segment 1 → 2
PWK3	bar	0-250	Cooling water pressure segment 2 → 3
PWK4	bar	0-250	Cooling water pressure segment 3 → 4
PWK5	bar	0-250	Cooling water pressure outlet manifold after 4th segment
PWD1	bar	0-400	Cooling water pressure nozzle inlet
PWD2	bar	0-400	Cooling water pressure nozzle outlet
TWK17	K	173-373	Cooling water temperature inlet, PT-100, 1mm
TWK23	K	173-373	Cooling water temperature segment 1 → 2, PT-100, 1 mm
TWK33	K	173-373	Cooling water temperature segment 2 → 3, PT-100, 1 mm
TWK43	K	173-373	Cooling water temperature segment 3 → 4, PT-100, 1 mm
TWK58	K	173-373	Cooling water temperature outlet manifold after 4th segment, PT-100, 1 mm
TWD11	K	173-373	Cooling water temperature nozzle inlet, PT-100, 1 mm
TWD24	K	173-373	Cooling water temperature nozzle outlet, PT-100, 1 mm
TWK11	K	273-873	Cooling water temperature inlet, Type K
TWK21	K	273-873	Cooling water temperature segment 1 → 2, Type K
TWK31	K	273-873	Cooling water temperature outlet manifold, Type K
TWK41	K	273-873	Cooling water temperature segment 3 → 4, Type K
TWK52	K	273-873	Cooling water temperature outlet manifold after 4th segment, Type K
TWD15	K	273-873	Cooling water temperature nozzle inlet, Type K
TWD28	K	273-873	Cooling water temperature nozzle outlet, Type K

Tab. A.1: Instrumentation of Combustion Chamber Test Facility

Sensor	Type	Accuracy	Location, Comment
MKV (VK)	VSE VSI 0.4/16	±0.3% of measured value	Total kerosene mass flow rate
MK	Rheonik RHM06	Better ±0.2% of measured value within calibrated rage (accuracy is mass flow rate dependant)	Injector kerosene mass flow rate
MO	Rheonik RHM12	At least ±0.5% of measured value (accuracy is mass flow rate dependant)	Oxygen mass flow rate to injector
PK6, PO5, PFZ, POZ, PCZ, PC[0-4], PWK[1-5], PWD[1-2]	WIKA IS-10	±0.5% of range	Standard pressure transducers
PCDYN, PODYN, PKDYN	Kistler 6053C60	$\leq \pm 1$ bar at 1500 Hz, $\leq \pm 2\%$ of mean pressure	Dynamic pressure transducers
TK3	Electronic Sensor PT-100, 1mm	$\pm(0.15\,^{\circ}\mathrm{C} + 0.002 \cdot T[^{\circ}\mathrm{C}])$	Kerosene temperature at tap off to injector
TO5	Thermocoax Type K, 1mm	±1.5 K up to 648 K	Oxygen temperature after flow control valve
THW11c, THW21c, THW31c, THW41c	Type T, 0.38 mm	±1.5 K up to 623 K	Chamber wall temperature
THW11a, THW21a, THW31a, THW41a, THW12b, THW22b, THW32b, THW42b	Type K, 0.35 mm or 0.5 mm	±1.5 K up to 648 K	Chamber wall temperature
TWK17, TWK23, TWK33, TWK43, TWK58, TWD11, TWD24	Electronic Sensor PT-100, 1 mm	$\pm(0.15\,^{\circ}\mathrm{C} + 0.002 \cdot T[^{\circ}\mathrm{C}])$	Cooling water temperature

Sensor	Type	Accuracy	Location, Comment
TWK11, TWK21, TWK31, TWK41, TWK52, TWD15, TWD28	Thermocoax Type K, 1 mm	±1.5 K up to 648 K	Cooling water temperature

Tab. A.2: Accuracy of Measurement for Selected Sensors (General)

A.3.2 Overview of Calculated Data

Data	Unit	Location, Comment
CDK	–	Discharge coefficient injector, kerosene
CDO	–	Discharge coefficient injector, oxygen
Cstar	m/s	Experimental characteristic velocity, injector mass flow only, using PTT
Cstar2	m/s	Experimental characteristic velocity, injector mass flow only, using PTT2
CstarT	m/s	Experimental characteristic velocity, film mass flow considered (throat based), using PTTT
CstarT2	m/s	Experimental characteristic velocity, film mass flow considered (throat based), using PTTT2
CstarTheo	m/s	Theoretic characteristic velocity (injector based)
CstarTheoT	m/s	Theoretic characteristic velocity considering film mass flow rate (throat based)
DPF	bar	Calculated pressure drop over film applicator, =PF1-PF3
DPK	bar	Pressure drop over injector, kerosene
DPO	bar	Pressure drop over injector, oxygen
EtaCstar	–	Combustion efficiency (injector based, LFA-Legacy), calculated from Cstar and CstarTheo
EtaCstar2	–	Combustion efficiency (injector based, JANNAF), calculated from Cstar2 and CstarTheo
EtaCstarT	–	Combustion efficiency (throat based, LFA-Legacy), calculated from CstarT and CstarTheoT
EtaCstarT2	–	Combustion efficiency (throat based, JANNAF), calculated from CstarT2 and CstarTheoT
meanTWK1 ... meanTWK5	K	Cooling water temperature in chamber segments, mean value of positions TWK1x, TWK2x, TWK3x, TWK4x and TWK5x
meanTWD1 ... meanTWD2	K	Cooling water temperature in nozzle segment, mean value of positions TWD1x and TWD2x

Data	Unit	Location, Comment
MK, MKV	kg/s	Calculated kerosene mass flow rate to injector, from VK
MKInjCalc	g/s	Injector kerosene mass flow, calculated from characteristic map of control valve RVK1 or RVK2
MOCalc	g/s	Injector oxygen mass flow, calculated from characteristic map of control valve RVO
MWG	kg/s	Cooling water, total mass flow rate, from DPWG
MWK	kg/s	Cooling water, mass flow rate chamber, from DPWK
MWD	kg/s	Cooling water, mass flow rate nozzle, from DPWD
OF, OZFinj	–	Calculated mixture ratio (injector), = MO/MK
OFT, OZFthr	–	Calculated mixture ratio (throat), = MO/(MK + MF1)
OZFInjCalc	–	Calculated mixture ratio (injector), determined from calculated mass flow rates, = MOCalc/MKInjCalc
OZFThrCalc	–	Calculated mixture ratio (throat), determined from calculated mass flow rates, = MOCalc/(MKInjCalc + MF1Calc)
PCC	bar	Calculated mean pressure in combustion chamber
PCDYNMAX1 ... PCDYNMAX8	bar	Amplitude of HF pressure peaks in descending order, chamber, 7 mm from face plate
PCDYNFREQ1 ... PCDYNFREQ8	Hz	Frequency of HF pressure peaks in descending order, chamber, 7 mm from face plate
PKDYNMAX1 ... PKDYNMAX8	bar	Amplitude of HF pressure peaks in descending order, kerosene feed line
PKDYNFREQ1 ... PKDYNFREQ8	Hz	Frequency of HF pressure peaks in descending order, kerosene feed line
PODYNMAX1 ... PODYNMAX8	bar	Amplitude of HF pressure peaks in descending order, oxygen feed line
PODYNFREQ1 ... PODYNFREQ8	Hz	Frequency of HF pressure peaks in descending order, oxygen feed line
PCDYNMAX1 ... PCDYNMAX8	bar	Amplitude of LF pressure peaks in descending order, chamber, 7 mm from face plate
PCDYNFREQLF1 ... PCDYNFREQLF8	Hz	Frequency of LF pressure peaks in descending order, chamber, 7 mm from face plate
PKDYNMAXLF1 ... PKDYNMAXLF8	bar	Amplitude of LF pressure peaks in descending order, kerosene feed line
PKDYNFREQLF1 ... PKDYNFREQLF8	Hz	Frequency of LF pressure peaks in descending order, kerosene feed line
PODYNMAXLF1 ... PODYNMAXLF8	bar	Amplitude of LF pressure peaks in descending order, oxygen feed line
PODYNFREQLF1 ... PODYNFREQLF8	Hz	Frequency of LF pressure peaks in descending order, oxygen feed line
PTT	bar	Calculated total pressure in throat, injector mass flow only, “LFA-Legacy” method

Data	Unit	Location, Comment
PTT2	bar	Calculated total pressure in throat, injector mass flow only, JANNAF method
PTTT	bar	Calculated total pressure in throat, film mass flow considered (throat based), "LFA-Legacy" method
PTTT2	bar	Calculated total pressure in throat, film mass flow considered (throat based), JANNAF method
QK1...QK4	W	Calculated heat pick up in chamber segment 1 ... 4, rely on MWG or MWK and TWKxx
QD	W	Calculated heat pick up in nozzle segment, relies on MWG or MWD and TWDxx
Q	W	Total heat pick-up in rocket engine
QAK1...QAK4	W/m^2	Calculated heat flux density in chamber segment 1...4
QAD	W/m^2	Calculated heat flux density in nozzle segment
THG	K	Hot gas temperature, calculated with CEA2 (injector based)
THGT	K	Hot gas temperature, calculated with CEA2 (throat based)

Tab. A.3: Data Calculated for Analysis by Test Bench

A.3.3 Film Cooling Specific DAQ

Data Field	Unit	Range	Location, Comment
MF1	kg/s	0.003-0.3	Film coolant mass flow, custom calibration
MF1Calc	g/s	N/A	Film coolant mass flow, calculated from characteristic map of control valve RVK1 or RVK2 (kerosene only)
Mu	–	N/A	Film coolant mass flow ratio, see μ
PN8	bar	0-250	Nitrogen coolant supply pressure upstream sonic orifice BF1/BN4
PK6	bar	0-250	Kerosene feed line pressure after flow control valve
PF1	bar	0-250	Film coolant feed line pressure after flow meter
TF1	K	173-373	Film coolant feed line temperature after flow meter, PT-100, 1.5 mm
PF2	bar	0-250	Film coolant pressure in film applicator manifold
TF2	K	173-1623	Film coolant temperature in film applicator manifold, Type K, 0.25 mm
PF3	bar	0-250	Film coolant pressure at film inlet
TF3	K	173-1623	Film coolant temperature at film inlet, Type K, 0.25 mm
DPF	bar	N/A	Calculated pressure drop over film applicator, =PF1-PF3
CDF	-	N/A	Calculated discharge coefficient for film applicator

Tab. A.4: Special Instrumentation of Film Cooling Setup

Sensor	Type	Accuracy	Location, Comment
MF1	Rheonik Coriolis RHM06	At least ±0.2% of measured value within calibrated rage	Coolant mass flow in
PN8, PK6, PF2, PF3	WIKA IS-10	±0.5% of range	Pressure coolant system
TF1	Electronic Sensor PT-100, 1.5 mm	$\pm(0.15\,^\circ\mathrm{C} + 0.002 \cdot T[^\circ\mathrm{C}])$	Coolant supply temperature
TF2, TF3	Thermocoax Type K	±1.5 K up to 648 K	Coolant temperature

Tab. A.5: Accuracy of Measurements for Selected Sensors (Film Cooling)

A.3.4 Transpiration Cooled CMC Specific DAQ

Data Field	Unit	Range	Location, Comment
MF1	kg/s	0.003-0.3	CMC coolant mass flow in, custom calibration
MF1Calc	g/s	N/A	Film coolant mass flow, calculated from characteristic map of control valve RVK1 or RVK2 (kerosene only)
Mu	-	N/A	Transpiration coolant mass flow ratio, see μ
PN8	bar	0-250	Nitrogen coolant supply pressure upstream sonic orifice BF1/BN4
PK6	bar	0-250	Kerosene feed line pressure after flow control valve
PF1	bar	0-250	Film coolant feed line pressure after flow meter
TF1	K	173-373	Film coolant feed line temperature after flow meter, PT-100, 1.5 mm
PF2	bar	0-40	CMC coolant pressure in reservoir, upstream
TF2	K	173-1623	CMC coolant temperature, Type K, upstream
PF3	bar	0-40	CMC coolant pressure in reservoir, downstream
TF3	K	173-1623	CMC coolant temperature, Type K, downstream
PC2b	bar	0-40	Combustion chamber pressure in 2nd segment
TC31	K	173-1623	CMC solid temperature, Type K, upstream
TC32	K	173-1623	CMC solid temperature, Type K, middle
TC33	K	173-1623	CMC solid temperature, Type K, downstream
DPF	bar	N/A	Calculated pressure difference over CMC wall, =PF2b-PC2b or =PF2-PC2b

Tab. A.6: Special Instrumentation of Transpiration Cooled CMC Test Specimen

Sensor	Type	Accuracy	Location, Comment
MF1	Rheonik Coriolis RHM06	At least ±0.2% of measured value within calibrated rage	Coolant mass flow in
PN8, PK6, PF1	WIKA IS-10	±0.5% of range	Pressure coolant system
PC2b, PF2, PF2b, PF3	Omega	±0.15% of range	Pressure coolant system
TF1	Electronic Sensor PT-100, 1.5 mm	$\pm(0.15\,^\circ\mathrm{C} + 0.002 \cdot T[^\circ\mathrm{C}])$	Coolant supply temperature
TF2, TF3	Thermocoax Type K	±1.5 K up to 648 K	Coolant temperature

Tab. A.7: Accuracy of Measurements for Selected Sensors (Transpiration Cooling)

A.3.5 Convectively Cooled CMC Specific DAQ

Data Field	Unit	Range	Location, Comment
MF1	kg/s	0.006-0.6	PSR coolant mass flow in
MF2	kg/s	0.003-0.3	PSR coolant mass flow out by Coriolis mass flow meter (kerosene)
	kg/s	N/A	PSR coolant mass flow out, calculated from sonic orifice BF2 (nitrogen only)
PN8	bar	0-250	Nitrogen coolant supply pressure upstream sonic orifice BF1
PK6	bar	0-250	Kerosene feed line pressure after flow control valve
PF1	bar	0-250	PSR coolant feed line pressure after flow meter
TF1	K	173-373	Coolant supply temperature after flow meter
PF2a	bar	0-160	PSR coolant pressure PSR inlet manifold (nitrogen only)
	bar	0-40	PSR coolant pressure PSR inlet manifold (kerosene only)
TF2a	K	173-1623	PSR coolant temperature PSR inlet manifold
PF2b	bar	0-400	PSR coolant pressure PSR gap between PSR and jacket (nitrogen only)
	bar	0-160	PSR coolant pressure PSR gap between PSR and jacket (kerosene only)
PF2c	bar	0-160	PSR coolant pressure PSR outlet manifold (nitrogen only)
	bar	0-40	PSR coolant pressure PSR outlet manifold (kerosene only)
TF2c	K	173-1623	PSR coolant temperature PSR outlet manifold
PF3	bar	0-250	PSR coolant pressure PSR dump line after outlet manifold
TF3	K	173-1623	PSR coolant temperature PSR dump line after outlet manifold

Data Field	Unit	Range	Location, Comment
PF4	bar	0-40	PSR coolant pressure PSR dump line after heat exchanger (nitrogen only)
	bar	0-400	PSR coolant pressure PSR dump line after heat exchanger (kerosene only)
TF4	K	173-1623	PSR coolant temperature PSR dump line after heat exchanger
TPW1	K	173-1623	PSR outer diameter temperature at 62 mm from segment start
TPW2	K	273-873	PSR outer diameter temperature at 95 mm from segment start
TPW3	K	273-873	PSR outer diameter temperature at 129 mm from segment start
TF2d3	K	273-873	Surface temperature of PSR outlet line at 112.5°
TF2d7	K	273-873	Surface temperature of PSR outlet line at 292.5°
DPCMC	bar	N/A	Calculated pressure loss over cooling duct, =PF2a-PF2c
DPF	bar	N/A	Calculated pressure difference over CMC wall, =PF2c-PC2
DM	g/s	N/A	Calculated transpiration mass flow rate, =MF1-MF2
QCMC	W	N/A	Calculated heat pick up in CMC segment
QACMC	W/m^2	N/A	Heat flux in CMC segment

Tab. A.8: Special Instrumentation of Convectively Cooled CMC Test Specimen

Sensor	Type	Accuracy	Location, Comment
MF1	Rheonik Coriolis RHM06	At least ±0.2% of measured value within calibrated rage	Coolant mass flow in
PN8, PK6, PF1	WIKA IS-10	±0.5% of range	Pressure coolant system
PC2b, PF2, PF2b, PF3	Omega	±0.15% of range	Pressure coolant system
TF1	Electronic Sensor PT-100, 1.5 mm	$\pm(0.15\,°\mathrm{C} + 0.002 \cdot T[°\mathrm{C}])$	Coolant supply temperature
TF2, TF3	Thermocoax Type K	±1.5 K up to 648 K	Coolant temperature

Tab. A.9: Accuracy of Measurements for Selected Sensors (Convect. Cooled CMC)

B. Experimental Data

B.1 Reference Tests

In this section averaged experimental data for groups of specific combustion pressures p_c and mixture ratios O/F is summarized. Load points and heat fluxes of the reference tests are given in Tab. B.1 for the 37 mm combustion chamber and in Tab. B.2 for the 20 mm combustion chamber.

$p_{c,nom}$ $[MPa]$	$(O/F)_{nom}$ $[-]$	p_c $[MPa]$	O/F $[-]$	Segment 1 [MW/m^2]	Segment 2 [MW/m^2]	Segment 3 [MW/m^2]	Segment 4 [MW/m^2]	Nozzle [MW/m^2]
2.0	1.8	1.94 ± 0.05	1.77 ± 0.14	1.40 ± 0.40	2.03 ± 0.97	2.90 ± 0.93	3.39 ± 0.49	4.78 ± 0.93
2.0	2.4	1.96 ± 0.07	2.43 ± 0.05	4.14 ± 0.32	4.72 ± 0.47	4.92 ± 0.38	5.06 ± 0.40	7.08 ± 1.69
2.0	2.9	1.92 ± 0.06	2.96 ± 0.17	6.22 ± 1.00	6.05 ± 0.50	5.74 ± 0.34	6.04 ± 0.22	6.28 ± 1.58
4.0	1.8	3.84 ± 0.09	1.89 ± 0.12	1.56 ± 0.39	3.48 ± 1.07	5.62 ± 0.81	6.01 ± 0.77	9.69 ± 0.86
4.0	2.4	4.06 ± 0.18	2.39 ± 0.06	4.92 ± 0.51	6.97 ± 0.69	8.50 ± 0.60	9.11 ± 0.75	13.05 ± 0.97
4.0	2.9	4.07 ± 0.29	2.92 ± 0.15	8.58 ± 0.97	9.88 ± 0.90	10.65 ± 0.93	11.64 ± 1.04	17.38 ± 2.12
4.0	3.2	4.08 ± 0.21	3.11 ± 0.13	9.45 ± 0.76	10.62 ± 0.81	11.29 ± 0.81	12.23 ± 1.07	18.00 ± 1.79
6.0	2.4	6.14 ± 0.19	2.40 ± 0.04	5.43 ± 0.46	10.49 ± 0.54	12.33 ± 1.02	15.23 ± 2.06	24.18 ± 1.76
6.0	2.9	5.87 ± 0.20	2.90 ± 0.10	10.17 ± 0.87	12.45 ± 0.99	14.07 ± 1.07	15.79 ± 1.28	28.79 ± 1.65
6.0	3.2	5.88 ± 0.15	2.99 ± 0.04	10.69 ± 0.76	12.84 ± 0.90	14.47 ± 0.98	16.21 ± 1.06	29.21 ± 1.92
8.0	2.4	7.94 ± 0.27	2.27 ± 0.11	6.25 ± 0.76	14.35 ± 0.87	16.00 ± 1.27	14.93 ± 1.77	32.85 ± 1.87
8.0	2.9	7.63 ± 0.19	2.87 ± 0.15	11.22 ± 1.24	15.83 ± 0.64	18.20 ± 0.78	19.33 ± 1.07	37.23 ± 1.46
8.0	3.2	7.67 ± 0.19	3.09 ± 0.12	12.65 ± 0.49	16.70 ± 0.71	19.10 ± 0.71	20.35 ± 0.64	38.20 ± 0.85

Tab. B.1: Mean Experimental Heat Flux of Reference Tests with 37 mm Combustion Chamber (Average±RMS)

$p_{c,nom}$ $[MPa]$	$(O/F)_{nom}$ $[-]$	p_c $[MPa]$	O/F $[-]$	Segment 1 [MW/m^2]	Segment 2 [MW/m^2]	Segment 3 [MW/m^2]	Nozzle [MW/m^2]
4.0	2.9	3.78 ± 0.04	2.98 ± 0.10	12.84 ± 0.70	16.51 ± 0.72	17.32 ± 0.65	18.51 ± 3.02
4.0	3.2	3.80 ± 0.04	3.08 ± 0.10	13.53 ± 0.68	17.21 ± 0.63	17.80 ± 0.60	19.69 ± 3.40
6.0	2.4	5.96 ± 0.09	2.40 ± 0.05	10.51 ± 0.92	17.20 ± 0.96	20.36 ± 0.78	25.20 ± 3.38
6.0	2.9	5.97 ± 0.07	2.97 ± 0.04	18.08 ± 0.44	23.74 ± 0.83	25.76 ± 0.26	35.24 ± 2.85
6.0	3.2	5.94 ± 0.08	3.22 ± 0.14	19.82 ± 0.91	25.33 ± 0.96	26.83 ± 0.59	34.98 ± 2.74
8.0	2.4	7.84 ± 0.11	2.48 ± 0.09	13.53 ± 1.37	22.90 ± 0.96	27.98 ± 0.49	39.95 ± 3.26
8.0	2.9	7.79 ± 0.21	2.96 ± 0.10	21.97 ± 1.44	29.28 ± 1.65	32.13 ± 1.18	46.43 ± 3.28
8.0	3.2	7.84 ± 0.14	3.17 ± 0.15	24.07 ± 1.51	31.56 ± 1.33	33.70 ± 1.08	47.50 ± 3.10

Tab. B.2: Mean Experimental Heat Flux of Reference Tests with 20 mm Combustion Chamber (Average±RMS)

B.2 Film Cooling

In this section averaged experimental data of film cooling tests is summarized for groups of combustion pressure p_c, mixture ratio O/F and film mass flow ratio μ. Heat fluxes are given in Tab. B.3 for coolant kerosene and in Tab. B.5 for nitrogen. Furthermore hot wall temperature measurements are presented in Tab. B.4 and Tab. B.6 for kerosene and nitrogen, respectively.

$p_{c,nom}$ $[MPa]$	$(O/F)_{nom}$ $[-]$	μ_{nom} $[-]$	p_c $[MPa]$	O/F $[-]$	μ $[-]$	Segment 1 $[\mathrm{MW/m^2}]$	Segment 2 $[\mathrm{MW/m^2}]$	Segment 3 $[\mathrm{MW/m^2}]$	Segment 4 $[\mathrm{MW/m^2}]$	Nozzle $[\mathrm{MW/m^2}]$
2.0	3.05	15.0	1.8 ± 0.0	2.98 ± 0.01	15.2 ± 0.5	7.1 ± 0.1	6.7 ± 0.2	2.9 ± 0.1	5.9 ± 0.2	8.0 ± 0.3
2.0	3.21	22.5	1.8 ± 0.0	3.27 ± 0.03	22.8 ± 0.2	7.3 ± 0.1	6.0 ± 0.1	1.9 ± 0.0	5.4 ± 0.1	7.8 ± 0.1
4.0	2.90	10.0	3.9 ± 0.1	2.94 ± 0.10	9.7 ± 1.7	10.0 ± 1.2	12.6 ± 0.4	5.6 ± 1.0	10.4 ± 0.6	20.3 ± 1.1
4.0	3.05	15.0	4.0 ± 0.0	3.07 ± 0.05	14.6 ± 1.9	10.3 ± 0.9	12.9 ± 0.3	4.1 ± 0.7	9.0 ± 0.9	19.3 ± 1.2
4.0	3.21	20.0	3.9 ± 0.0	3.19 ± 0.04	18.0 ± 0.6	11.0 ± 0.8	13.0 ± 0.3	3.5 ± 0.4	8.8 ± 0.7	19.6 ± 0.8
6.0	2.90	5.0	6.2 ± 0.0	2.96 ± 0.02	7.2 ± 0.0	13.2 ± 0.0	18.1 ± 0.4	9.6 ± 0.5	16.9 ± 1.0	32.7 ± 0.8
6.0	3.05	10.0	6.1 ± 0.1	3.14 ± 0.04	10.5 ± 1.5	14.6 ± 1.5	18.3 ± 0.5	8.5 ± 1.9	15.6 ± 1.4	31.5 ± 1.0
6.0	3.21	15.0	6.2 ± 0.1	3.23 ± 0.08	14.9 ± 0.4	16.2 ± 2.4	19.1 ± 0.7	5.8 ± 0.9	14.1 ± 1.7	32.7 ± 0.9

Tab. B.3: Mean Experimental Heat Flux for Kerosene Films (Average±RMS)

Nominal Load Point			Position from Face Plate [mm]								
$p_{c,nom}$ $[MPa]$	$(O/F)_{inj,nom}$ $[-]$	μ_{nom} [%]	51.5 $[K]$	71.0 $[K]$	146.5 $[K]$	166.0 $[K]$	211.0 $[K]$	250.5 $[K]$	270.0 $[K]$	345.5 $[K]$	365.0 $[K]$
2.0	3.05	15.0	441 ± 2	421 ± 1	N/A	422 ± 1	335 ± 1	353 ± 4	369 ± 3	444 ± 1	484 ± 13
2.0	3.21	22.5	444 ± 4	423 ± 1	N/A	413 ± 0	326 ± 0	344 ± 0	336 ± 7	425 ± 1	460 ± 1
4.0	2.90	10.0	462 ± 58	464 ± 58	N/A	550 ± 67	364 ± 4	420 ± 43	395 ± 18	546 ± 52	676 ± 62
4.0	3.05	15.0	458 ± 57	459 ± 58	N/A	534 ± 68	355 ± 5	358 ± 28	363 ± 25	496 ± 37	621 ± 60
4.0	3.21	20.0	494 ± 39	494 ± 38	N/A	553 ± 61	350 ± 3	361 ± 27	354 ± 22	493 ± 30	649 ± 16
6.0	2.90	5.0	448 ± 9	518 ± 3	N/A	700 ± 4	384 ± 1	493 ± 41	421 ± 10	638 ± 52	N/A
6.0	3.05	10.0	521 ± 63	570 ± 54	N/A	727 ± 53	374 ± 7	461 ± 81	409 ± 38	600 ± 37	776 ± 36
6.0	3.21	15.0	579 ± 92	621 ± 79	N/A	770 ± 50	362 ± 1	381 ± 23	381 ± 32	643 ± 131	722 ± 0

Tab. B.4: Experimental Hot Wall Temperatures for Kerosene Films (Average±RMS)

$p_{c,nom}$ $[MPa]$	$(O/F)_{nom}$ $[-]$	μ_{nom} $[-]$	p_c $[MPa]$	O/F $[-]$	μ $[-]$	Segment 1 [MW/m^2]	Segment 2 [MW/m^2]	Segment 3 [MW/m^2]	Segment 4 [MW/m^2]	Nozzle [MW/m^2]
2.0	2.90	5.0	1.8 ± 0.0	2.90 ± 0.04	6.1 ± 0.3	7.2 ± 0.1	6.4 ± 0.1	5.3 ± 0.1	6.4 ± 0.0	8.9 ± 0.1
2.0	2.90	15.0	1.9 ± 0.0	2.91 ± 0.11	15.0 ± 0.7	6.9 ± 0.3	6.5 ± 0.2	4.7 ± 0.1	5.8 ± 0.3	8.1 ± 0.4
2.0	3.20	5.0	1.8 ± 0.0	3.17 ± 0.04	6.8 ± 0.3	7.0 ± 0.1	6.2 ± 0.2	5.1 ± 0.1	6.0 ± 0.0	8.6 ± 0.1
2.0	3.20	15.0	1.8 ± 0.0	3.11 ± 0.04	16.1 ± 0.2	7.0 ± 0.1	6.3 ± 0.3	4.4 ± 0.1	5.6 ± 0.2	7.8 ± 0.4
6.0	2.90	5.0	6.2 ± 0.0	2.96 ± 0.00	5.6 ± 0.1	12.2 ± 0.0	17.9 ± 0.3	15.4 ± 0.1	18.6 ± 0.1	38.0 ± 0.0
6.0	2.90	15.0	6.3 ± 0.0	2.93 ± 0.04	13.2 ± 0.1	11.9 ± 0.4	18.1 ± 0.8	13.2 ± 0.2	16.8 ± 0.5	33.6 ± 1.2
6.0	3.20	5.0	5.9 ± 0.0	3.24 ± 0.00	5.8 ± 0.0	15.6 ± 0.4	18.6 ± 0.2	15.8 ± 0.2	18.6 ± 0.1	34.9 ± 0.2
6.0	3.20	15.0	6.1 ± 0.0	3.22 ± 0.04	14.5 ± 0.0	14.1 ± 1.1	18.8 ± 0.6	13.4 ± 0.3	16.8 ± 0.5	32.0 ± 0.7

Tab. B.5: Mean Experimental Heat Flux for Nitrogen Films (Average±RMS)

Nominal Load Point			Position from Face Plate [mm]								
$p_{c,nom}$ $[MPa]$	$(O/F)_{inj,nom}$ $[-]$	μ_{nom} [%]	51.5 $[K]$	71.0 $[K]$	146.5 $[K]$	166.0 $[K]$	211.0 $[K]$	250.5 $[K]$	270.0 $[K]$	345.5 $[K]$	365.0 $[K]$
2.0	2.90	5.0	559 ± 18	420 ± 3	466 ± 2	424 ± 6	388 ± 1	456 ± 7	411 ± 3	457 ± 2	490 ± 10
2.0	2.90	15.0	523 ± 72	412 ± 5	461 ± 4	408 ± 4	353 ± 2	429 ± 5	399 ± 4	444 ± 6	479 ± 15
2.0	3.20	5.0	327 ± 33	414 ± 1	465 ± 1	410 ± 2	383 ± 1	442 ± 4	401 ± 1	451 ± 0	468 ± 2
2.0	3.20	15.0	489 ± 73	413 ± 1	459 ± 3	405 ± 3	350 ± 1	424 ± 0	394 ± 1	437 ± 5	470 ± 1
6.0	2.90	5.0	403 ± 1	500 ± 4	N/A	658 ± 8	446 ± 0	596 ± 5	572 ± 11	863 ± 47	N/A
6.0	2.90	15.0	399 ± 13	474 ± 2	N/A	641 ± 5	385 ± 2	584 ± 1	547 ± 4	624 ± 14	813 ± 22
6.0	3.20	5.0	553 ± 10	592 ± 5	N/A	703 ± 8	450 ± 0	597 ± 3	563 ± 8	918 ± 11	N/A
6.0	3.20	15.0	492 ± 38	545 ± 28	N/A	665 ± 1	386 ± 3	559 ± 7	555 ± 7	638 ± 1	871 ± 1

Tab. B.6: Experimental Hot Wall Temperatures for Nitrogen Films (Average±RMS)

C. Modeling Data

In this section the deviations of experimental data from predicted heat fluxes are summarized for different modeling approaches. The data presented here are the base for the graphic representations of the model deviations in section 5.2.

C.1 Hot Gas Heat Transfer Model

p_c [MPa]	O/F [$-$]	Segment 1 [%]	Segment 2 [%]	Segment 3 [%]	Segment 4 [%]	Nozzle [%]
2.0	1.8	$+212 \pm 76.2$	$+158 \pm 89.4$	$+115 \pm 61.9$	$+117 \pm 52.4$	$+13 \pm 43.7$
2.0	2.4	$+41.8 \pm 8.1$	$+21.7 \pm 9.7$	$+17.8 \pm 7.2$	$+21.3 \pm 7.9$	$+60.0 \pm 29.9$
2.0	2.9	-1.7 ± 13.0	-6.8 ± 8.8	-5.7 ± 4.8	-5.4 ± 3.9	$+60.7 \pm 6.5$
4.0	1.8	$+226 \pm 55.3$	$+143 \pm 44.8$	$+110 \pm 29.9$	$+112 \pm 30.2$	$+100 \pm 4.3$
4.0	2.4	$+80.6 \pm 14.1$	$+41.8 \pm 8.1$	$+31.8 \pm 5.9$	$+34.7 \pm 7.0$	$+57.9 \pm 16.8$
4.0	2.9	$+16.1 \pm 11.4$	$+1.4 \pm 8.2$	-3.0 ± 7.7	-2.9 ± 7.9	$+25.4 \pm 17.0$
4.0	3.2	$+5.8 \pm 6.1$	-6.2 ± 4.5	-9.9 ± 4.1	-9.9 ± 4.3	$+17.0 \pm 11.8$
6.0	2.4	$+74.7 \pm 8.4$	$+31.0 \pm 3.9$	$+23.2 \pm 4.9$	$+25.9 \pm 5.7$	$+25.1 \pm 9.5$
6.0	2.9	$+25.3 \pm 8.5$	$+6.9 \pm 6.8$	$+1.2 \pm 6.3$	$+1.4 \pm 6.6$	$+0.2 \pm 12.6$
6.0	3.2	$+20.5 \pm 8.2$	$+3.3 \pm 6.6$	-2.1 ± 6.1	-1.8 ± 6.4	-1.9 ± 14.0
8.0	2.4	$+78.0 \pm 4.3$	$+37.0 \pm 2.2$	$+36.3 \pm 3.6$	$+42.4 \pm 4.4$	$+17.6 \pm 14.0$
8.0	2.9	$+27.8 \pm 8.1$	$+6.8 \pm 5.4$	$+2.4 \pm 5.6$	$+3.5 \pm 6.0$	-2.3 ± 10.8
8.0	3.2	$+18.1 \pm 2.3$	$+0.3 \pm 1.4$	-4.2 ± 1.2	-3.3 ± 1.3	-2.6 ± 12.6

Tab. C.1: Deviation of Heat Flux Prediction from Measurements for 37 mm Combustion Chamber Using Bartz Model ("-" underprediction, "+" overprediction)

p_c [MPa]	O/F [$-$]	Segment 1 [%]	Segment 2 [%]	Segment 3 [%]	Nozzle [%]
4.0	2.9	$+45.9 \pm 8.8$	$+13.2 \pm 5.1$	$+7.6 \pm 4.7$	$+60.5 \pm 28.8$
4.0	3.2	$+38.0 \pm 7.6$	$+8.3 \pm 3.8$	$+4.5 \pm 4.4$	$+50.8 \pm 27.6$
6.0	2.4	$+166 \pm 22.5$	$+62.3 \pm 7.4$	$+36.6 \pm 4.6$	$+71.5 \pm 23.2$
6.0	2.9	$+50.9 \pm 3.6$	$+15.1 \pm 3.2$	$+5.8 \pm 1.2$	$+20.2 \pm 10.5$
6.0	3.2	$+36.7 \pm 7.5$	$+6.9 \pm 4.1$	$+0.7 \pm 3.3$	$+20.0 \pm 10.2$
8.0	2.4	$+157 \pm 27.4$	$+51.5 \pm 6.5$	$+23.7 \pm 3.0$	$+33.0 \pm 12.2$
8.0	2.9	$+57.6 \pm 13.0$	$+18.4 \pm 7.7$	$+7.6 \pm 7.4$	$+15.1 \pm 13.4$
8.0	3.2	$+43.7 \pm 15.4$	$+9.5 \pm 8.5$	$+2.3 \pm 7.9$	$+12.1 \pm 11.9$

Tab. C.2: Deviation of Heat Flux Prediction from Measurements for 20 mm Combustion Chamber Using Bartz Model ("-" underprediction, "+" overprediction)

p_c $[MPa]$	O/F $[-]$	Segment 1 [%]	Segment 2 [%]	Segment 3 [%]	Segment 4 [%]	Nozzle [%]
2.0	1.8	-37.2 ± 15.9	-14.0 ± 30.2	-4.7 ± 27.7	$+17.6 \pm 28.6$	$+25.2 \pm 23.9$
2.0	2.4	-71.0 ± 1.6	-58.4 ± 3.2	-46.3 ± 3.3	-32.2 ± 4.7	-13.3 ± 16.5
2.0	2.9	-79.5 ± 2.5	-67.4 ± 2.8	-56.0 ± 1.9	-45.9 ± 1.8	-11.1 ± 4.2
4.0	1.8	-33.8 ± 11.1	-18.3 ± 14.7	-6.3 ± 12.9	$+16.4 \pm 15.8$	$+10.6 \pm 2.1$
4.0	2.4	-62.9 ± 2.8	-51.3 ± 2.7	-39.6 ± 2.6	-24.2 ± 3.7	-12.1 ± 9.3
4.0	2.9	-75.7 ± 2.3	-64.5 ± 2.8	-54.7 ± 3.5	-44.2 ± 4.4	-29.0 ± 9.7
4.0	3.2	-77.9 ± 1.3	-67.1 ± 1.5	-57.8 ± 1.9	-48.0 ± 2.4	-33.6 ± 6.8
6.0	2.4	-63.8 ± 1.7	-54.7 ± 1.3	-42.9 ± 2.1	-28.3 ± 3.1	-28.3 ± 5.2
6.0	2.9	-73.8 ± 1.7	-62.5 ± 2.2	-52.5 ± 2.7	-41.4 ± 3.5	-42.4 ± 7.3
6.0	3.2	-74.8 ± 1.6	-63.7 ± 2.2	-53.9 ± 2.7	-43.1 ± 3.5	-43.4 ± 8.1
8.0	2.4	-62.8 ± 0.9	-52.1 ± 1.0	-36.2 ± 1.0	-18.0 ± 1.4	-31.3 ± 8.7
8.0	2.9	-73.2 ± 1.6	-62.4 ± 1.8	-51.6 ± 2.4	-39.8 ± 3.2	-42.9 ± 6.4
8.0	3.2	-75.1 ± 0.4	-64.5 ± 0.4	-54.5 ± 0.4	-43.4 ± 0.5	-42.8 ± 7.6

Tab. C.3: Deviation of Heat Flux Prediction from Measurements for 37 mm Combustion Chamber Using Gnielinski Model ("-" underprediction, "+" overprediction)

p_c $[MPa]$	O/F $[-]$	Segment 1 [%]	Segment 2 [%]	Segment 3 [%]	Nozzle [%]
4.0	2.9	-71.4 ± 1.7	-59.2 ± 1.7	-47.0 ± 2.2	-16.3 ± 15.0
4.0	3.2	-72.9 ± 1.4	-60.9 ± 1.3	-48.4 ± 2.1	-21.1 ± 14.4
6.0	2.4	-47.5 ± 4.4	-41.3 ± 2.5	-32.5 ± 2.2	-9.3 ± 12.3
6.0	2.9	-69.8 ± 0.7	-57.6 ± 1.1	-46.6 ± 0.6	-35.4 ± 5.8
6.0	3.2	-72.6 ± 1.5	-60.5 ± 1.5	-49.0 ± 1.6	-35.3 ± 5.5
8.0	2.4	-48.1 ± 5.4	-43.9 ± 2.2	-37.5 ± 1.4	-27.6 ± 6.7
8.0	2.9	-67.7 ± 3.0	-55.3 ± 3.3	-44.4 ± 4.6	-36.3 ± 8.3
8.0	3.2	-70.6 ± 3.6	-58.6 ± 3.7	-47.1 ± 4.7	-37.9 ± 7.4

Tab. C.4: Deviation of Heat Flux Prediction from Measurements for 20 mm Combustion Chamber Using Gnielinski Model ("-" underprediction, "+" overprediction)

p_c [MPa]	O/F [$-$]	Segment 1 [%]	Segment 2 [%]	Segment 3 [%]	Segment 4 [%]	Nozzle [%]
2.0	1.8	$+173 \pm 62.1$	$+126 \pm 74.6$	$+88.4 \pm 51.1$	$+89.5 \pm 42.3$	$+105 \pm 35.4$
2.0	2.4	$+35.7 \pm 7.6$	$+16.4 \pm 9.4$	$+12.4 \pm 6.5$	$+15.3 \pm 6.4$	$+49.1 \pm 26.3$
2.0	2.9	-3.7 ± 13.0	-8.7 ± 8.9	-8.0 ± 5.0	-8.1 ± 4.2	$+52.5 \pm 4.6$
4.0	1.8	$+190 \pm 43.7$	$+116 \pm 35.7$	$+85.4 \pm 23.0$	$+87.2 \pm 23.2$	$+75.6 \pm 4.3$
4.0	2.4	$+71.2 \pm 12.6$	$+34.5 \pm 7.0$	$+24.7 \pm 4.9$	$+27.1 \pm 6.1$	$+45.1 \pm 14.8$
4.0	2.9	$+13.3 \pm 10.1$	-1.0 ± 7.1	-5.6 ± 6.7	-5.6 ± 6.8	$+18.0 \pm 14.9$
4.0	3.2	$+4.1 \pm 5.3$	-7.6 ± 3.9	-11.5 ± 3.6	-11.7 ± 3.7	$+11.0 \pm 10.4$
6.0	2.4	$+64.2 \pm 7.7$	$+23.3 \pm 3.4$	$+15.8 \pm 4.4$	$+18.0 \pm 5.2$	$+13.8 \pm 8.6$
6.0	2.9	$+22.0 \pm 8.6$	$+4.2 \pm 6.9$	-1.5 ± 6.3	-1.5 ± 6.7	-6.2 ± 11.6
6.0	3.2	$+17.6 \pm 8.6$	$+1.0 \pm 7.0$	-4.5 ± 6.4	-4.3 ± 6.7	-8.0 ± 13.0
8.0	2.4	$+66.3 \pm 3.6$	$+28.2 \pm 1.9$	$+27.4 \pm 2.2$	$+32.9 \pm 2.8$	$+6.3 \pm 12.9$
8.0	2.9	$+23.4 \pm 7.0$	$+3.4 \pm 4.6$	-1.0 ± 4.8	-0.1 ± 5.2	-9.3 ± 9.9
8.0	3.2	$+14.9 \pm 2.0$	-2.2 ± 1.2	-6.7 ± 1.0	-6.0 ± 1.0	-9.0 ± 11.9

Tab. C.5: Deviation of Heat Flux Prediction from Measurements for 37 mm Combustion Chamber Using Modified Sinyarev Model ("-" underprediction, "+" overprediction)

p_c [MPa]	O/F [$-$]	Segment 1 [%]	Segment 2 [%]	Segment 3 [%]	Nozzle [%]
4.0	2.9	$+34.7 \pm 7.6$	$+4.5 \pm 4.4$	-0.9 ± 4.0	$+50.0 \pm 26.8$
4.0	3.2	$+27.8 \pm 6.8$	$+0.2 \pm 3.3$	-3.5 ± 3.9	$+41.3 \pm 25.8$
6.0	2.4	$+135 \pm 19.6$	$+43.3 \pm 6.1$	$+20.6 \pm 3.9$	$+54.5 \pm 20.8$
6.0	2.9	$+37.3 \pm 3.2$	$+4.7 \pm 2.8$	-3.9 ± 1.1	$+10.5 \pm 9.8$
6.0	3.2	$+24.8 \pm 6.5$	-2.4 ± 3.5	-8.2 ± 2.7	$+10.8 \pm 9.3$
8.0	2.4	$+127 \pm 23.0$	$+33.5 \pm 5.0$	$+8.8 \pm 2.2$	$+19.2 \pm 10.9$
8.0	2.9	$+41.8 \pm 11.6$	$+6.6 \pm 6.9$	-3.2 ± 6.7	$+4.8 \pm 12.2$
8.0	3.2	$+29.7 \pm 13.7$	-1.0 ± 7.6	-7.6 ± 7.0	$+2.4 \pm 10.8$

Tab. C.6: Deviation of Heat Flux Prediction from Measurements for 20 mm Combustion Chamber Using Modified Sinyarev Model ("-" underprediction, "+" overprediction)

C.2 Hot Gas Radiation

p_c [MPa]	O/F [−]	Segment 1 [%]	Segment 2 [%]	Segment 3 [%]	Segment 4 [%]	Nozzle [%]
2.0	1.8	+191 ± 61.9	+141 ± 76.0	+101 ± 51.4	+103 ± 41.9	+110 ± 36.0
2.0	2.4	+52.6 ± 8.5	+30.9 ± 10.4	+26.4 ± 7.3	+29.8 ± 7.4	+55.7 ± 27.6
2.0	2.9	+9.7 ± 14.4	+4.1 ± 9.7	+4.9 ± 5.3	+5.0 ± 4.4	+60.2 ± 5.3
4.0	1.8	+208 ± 43.5	+129.4 ± 35.7	+97.5 ± 22.5	+99.4 ± 22.7	+79.6 ± 4.7
4.0	2.4	+87.2 ± 13.6	+47.2 ± 7.5	+36.5 ± 5.3	+39.2 ± 6.5	+49.9 ± 15.3
4.0	2.9	+25.3 ± 10.9	+9.5 ± 7.6	+4.5 ± 7.2	+4.4 ± 7.3	+22.6 ± 15.5
4.0	3.2	+15.3 ± 6.0	+2.3 ± 4.4	−2.0 ± 4.0	−2.1 ± 4.2	+15.3 ± 10.9
6.0	2.4	+77.5 ± 8.2	+33.3 ± 3.6	+25.3 ± 4.7	+27.7 ± 5.6	+17.1 ± 8.8
6.0	2.9	+33.2 ± 9.3	+13.8 ± 7.4	+7.6 ± 6.8	+7.7 ± 7.2	−3.0 ± 12.0
6.0	3.2	+28.6 ± 9.3	+10.4 ± 7.6	+4.5 ± 6.9	+4.7 ± 7.3	−4.8 ± 13.4
8.0	2.4	+78.8 ± 4.3	+37.9 ± 2.9	+37.1 ± 2.2	+43.0 ± 2.3	+9.2 ± 13.4
8.0	2.9	+33.8 ± 7.4	+12.0 ± 4.8	+7.3 ± 5.0	+8.3 ± 5.5	−6.5 ± 10.2
8.0	3.2	+24.7 ± 2.1	+6.1 ± 1.3	+1.3 ± 1.1	+2.1 ± 1.1	−6.2 ± 12.3

Tab. C.7: Deviation of Heat Flux Prediction from Measurements for 37 mm Combustion Chamber Using Modified Sinyarev Model Considering Heat Transfer by Radiation ("-" underprediction, "+" overprediction)

p_c [MPa]	O/F [−]	Segment 1 [%]	Segment 2 [%]	Segment 3 [%]	Nozzle [%]
4.0	2.9	+40.3 ± 7.9	+8.9 ± 4.5	+3.3 ± 4.1	+53.7 ± 27.5
4.0	3.2	+33.2 ± 7.0	+4.4 ± 3.4	+0.6 ± 4.0	+44.8 ± 26.4
6.0	2.4	+143 ± 20.2	+48.0 ± 6.2	+24.5 ± 4.0	+57.3 ± 21.2
6.0	2.9	+42.3 ± 3.3	+8.6 ± 2.9	−0.3 ± 1.1	+12.9 ± 10.0
6.0	3.2	+29.5 ± 6.7	+1.3 ± 3.6	−4.7 ± 2.8	+13.2 ± 9.5
8.0	2.4	+134 ± 23.5	+37.6 ± 5.0	+12.2 ± 2.2	+21.3 ± 11.0
8.0	2.9	+46.9 ± 12.4	+10.5 ± 7.3	+0.3 ± 7.3	+7.0 ± 12.7
8.0	3.2	+34.4 ± 14.6	+2.6 ± 8.1	−4.2 ± 7.6	+4.6 ± 11.2

Tab. C.8: Deviation of Heat Flux Prediction from Measurements for 20 mm Combustion Chamber Using Modified Sinyarev Model Considering Heat Transfer by Radiation ("-" underprediction, "+" overprediction)

C.3 Coolant Heat Transfer Model

p_c [MPa]	O/F [$-$]	Segment 1 [%]	Segment 2 [%]	Segment 3 [%]	Segment 4 [%]	Nozzle [%]
2.0	1.8	$+173 \pm 62.1$	$+126 \pm 74.6$	$+88.4 \pm 51.1$	$+89.5 \pm 42.3$	$+105 \pm 35.4$
2.0	2.4	$+35.7 \pm 7.6$	$+16.4 \pm 9.4$	$+12.4 \pm 6.5$	$+15.3 \pm 6.4$	$+49.1 \pm 26.3$
2.0	2.9	-3.7 ± 13.0	-8.7 ± 8.9	-8.0 ± 5.0	-8.1 ± 4.2	$+52.5 \pm 4.6$
4.0	1.8	$+190 \pm 43.7$	$+116 \pm 35.7$	$+85.4 \pm 23.0$	$+87.2 \pm 23.2$	$+75.6 \pm 4.3$
4.0	2.4	$+71.2 \pm 12.6$	$+34.5 \pm 7.0$	$+24.7 \pm 4.9$	$+27.1 \pm 6.1$	$+45.1 \pm 14.8$
4.0	2.9	$+13.3 \pm 10.1$	-1.0 ± 7.1	-5.6 ± 6.7	-5.6 ± 6.8	$+18.0 \pm 14.9$
4.0	3.2	$+4.1 \pm 5.3$	-7.6 ± 3.9	-11.5 ± 3.6	-11.7 ± 3.7	$+11.0 \pm 10.4$
6.0	2.4	$+64.2 \pm 7.7$	$+23.3 \pm 3.4$	$+15.8 \pm 4.4$	$+18.0 \pm 5.2$	$+13.8 \pm 8.6$
6.0	2.9	$+22.0 \pm 8.6$	$+4.2 \pm 6.9$	-1.5 ± 6.3	-1.5 ± 6.7	-6.2 ± 11.6
6.0	3.2	$+17.6 \pm 8.6$	$+1.0 \pm 7.0$	-4.5 ± 6.4	-4.3 ± 6.7	-8.0 ± 13.0
8.0	2.4	$+66.3 \pm 3.6$	$+28.2 \pm 1.9$	$+27.4 \pm 2.2$	$+32.9 \pm 2.8$	$+6.3 \pm 12.9$
8.0	2.9	$+23.4 \pm 7.0$	$+3.4 \pm 4.6$	-1.0 ± 4.8	-0.1 ± 5.2	-9.3 ± 9.9
8.0	3.2	$+14.9 \pm 2.0$	-2.2 ± 1.2	-6.7 ± 1.0	-6.0 ± 1.0	-9.0 ± 11.9

Tab. C.9: Deviation of Heat Flux Prediction from Measurements for 37 mm Combustion Chamber Using Kraussold Model ("-" underprediction, "+" overprediction)

p_c [MPa]	O/F [$-$]	Segment 1 [%]	Segment 2 [%]	Segment 3 [%]	Nozzle [%]
4.0	2.9	$+34.7 \pm 7.6$	$+4.5 \pm 4.4$	-0.9 ± 4.0	$+50.0 \pm 26.8$
4.0	3.2	$+27.8 \pm 6.8$	$+0.2 \pm 3.3$	-3.5 ± 3.9	$+41.3 \pm 25.8$
6.0	2.4	$+135 \pm 19.6$	$+43.3 \pm 6.1$	$+20.6 \pm 3.9$	$+54.5 \pm 20.8$
6.0	2.9	$+37.3 \pm 3.2$	$+4.7 \pm 2.8$	-3.9 ± 1.1	$+10.5 \pm 9.8$
6.0	3.2	$+24.8 \pm 6.5$	-2.4 ± 3.5	-8.2 ± 2.7	$+10.8 \pm 9.3$
8.0	2.4	$+127 \pm 23.0$	$+33.5 \pm 5.0$	$+8.8 \pm 2.2$	$+19.2 \pm 10.9$
8.0	2.9	$+41.8 \pm 11.6$	$+6.6 \pm 6.9$	-3.2 ± 6.7	$+4.8 \pm 12.2$
8.0	3.2	$+29.7 \pm 13.7$	-1.0 ± 7.6	-7.6 ± 7.0	$+2.4 \pm 10.8$

Tab. C.10: Deviation of Heat Flux Prediction from Measurements for 20 mm Combustion Chamber Using Kraussold Model ("-" underprediction, "+" overprediction)

p_c [MPa]	O/F [$-$]	Segment 1 [%]	Segment 2 [%]	Segment 3 [%]	Segment 4 [%]	Nozzle [%]
2.0	1.8	+175 ± 62.7	+127 ± 75.1	+89.3 ± 51.4	+90.4 ± 42.7	+111 ± 36.6
2.0	2.4	+36.5 ± 7.6	+16.9 ± 9.4	+12.9 ± 6.5	+15.8 ± 6.4	+53.1 ± 27.2
2.0	2.9	−3.1 ± 13.0	−8.2 ± 8.9	−7.6 ± 5.0	−7.7 ± 4.2	+56.4 ± 4.4
4.0	1.8	+192 ± 44.1	+117 ± 35.9	+86.5 ± 23.2	+88.3 ± 23.4	+82.5 ± 4.3
4.0	2.4	+72.4 ± 12.7	+35.3 ± 7.1	+25.3 ± 5.0	+27.8 ± 6.2	+50.0 ± 15.5
4.0	2.9	+14.1 ± 10.2	−0.4 ± 7.2	−5.1 ± 6.8	−5.2 ± 6.9	+22.0 ± 15.8
4.0	3.2	+4.8 ± 5.4	−7.1 ± 3.9	−11.1 ± 3.6	−11.3 ± 3.8	+14.5 ± 11.1
6.0	2.4	+65.5 ± 7.8	+24.1 ± 3.4	+16.5 ± 4.4	+18.6 ± 5.2	+18.0 ± 8.9
6.0	2.9	+22.8 ± 8.6	+4.8 ± 6.9	−1.0 ± 6.3	−1.0 ± 6.7	−3.1 ± 12.0
6.0	3.2	+18.5 ± 8.6	+1.6 ± 7.0	−4.0 ± 6.4	−3.8 ± 6.8	−5.0 ± 13.5
8.0	2.4	+67.6 ± 3.6	+29.1 ± 1.9	+28.1 ± 2.3	+33.6 ± 2.8	+10.0 ± 13.3
8.0	2.9	+24.4 ± 7.1	+4.0 ± 4.6	−0.5 ± 4.8	+0.4 ± 5.2	−6.3 ± 10.3
8.0	3.2	+15.8 ± 2.0	−1.6 ± 1.2	−6.2 ± 1.0	−5.5 ± 1.0	−6.0 ± 12.3
8.0	3.2	+14.9 ± 2.0	−2.2 ± 1.2	−6.7 ± 1.0	−6.0 ± 1.0	−9.0 ± 11.9

Tab. C.11: Deviation of Heat Flux Prediction from Measurements for 37 mm Combustion Chamber Using Kraussold Model with Corrections ("-" underprediction, "+" overprediction)

p_c [MPa]	O/F [$-$]	Segment 1 [%]	Segment 2 [%]	Segment 3 [%]	Nozzle [%]
4.0	2.9	+35.3 ± 7.7	+4.9 ± 4.4	−0.5 ± 4.0	+52.5 ± 27.3
4.0	3.2	+28.4 ± 6.8	+0.6 ± 3.3	−3.2 ± 3.9	+43.6 ± 26.3
6.0	2.4	+137 ± 19.7	+44.0 ± 6.1	+21.1 ± 3.9	+57.8 ± 21.3
6.0	2.9	+38.0 ± 3.2	+5.2 ± 2.8	−3.5 ± 1.1	+12.6 ± 9.9
6.0	3.2	+25.5 ± 6.6	−1.9 ± 3.6	−7.8 ± 2.7	+12.8 ± 9.5
8.0	2.4	+128 ± 23.1	+34.2 ± 5.0	+9.3 ± 2.2	+21.9 ± 11.1
8.0	2.9	+42.6 ± 11.7	+7.2 ± 6.9	−2.8 ± 6.7	+6.9 ± 12.5
8.0	3.2	+30.5 ± 13.8	−0.5 ± 7.6	−7.2 ± 7.1	+4.4 ± 11.1

Tab. C.12: Deviation of Heat Flux Prediction from Measurements for 20 mm Combustion Chamber Using Kraussold Model with Corrections ("-" underprediction, "+" overprediction)

p_c [MPa]	O/F [−]	Segment 1 [%]	Segment 2 [%]	Segment 3 [%]	Segment 4 [%]	Nozzle [%]
2.0	1.8	+171 ± 61.5	+124 ± 74.0	+87.3 ± 50.6	+88.6 ± 42.0	+103 ± 35.2
2.0	2.4	+34.8 ± 7.6	+15.8 ± 9.3	+11.9 ± 6.4	+14.8 ± 6.4	+48.1 ± 26.2
2.0	2.9	−4.3 ± 12.9	−9.2 ± 8.9	−8.4 ± 5.0	−8.4 ± 4.2	+51.5 ± 4.9
4.0	1.8	+187 ± 43.3	+114 ± 35.5	+84.4 ± 22.9	+86.4 ± 23.1	+73.8 ± 4.3
4.0	2.4	+69.8 ± 12.5	+33.6 ± 7.0	+24.0 ± 4.9	+26.5 ± 6.1	+43.7 ± 14.6
4.0	2.9	+12.4 ± 10.0	−1.6 ± 7.0	−6.1 ± 6.7	−6.1 ± 6.8	+17.0 ± 14.7
4.0	3.2	+3.3 ± 5.3	−8.2 ± 3.8	−12.0 ± 3.6	−12.1 ± 3.7	+10.0 ± 10.3
6.0	2.4	+62.7 ± 7.6	+22.3 ± 3.4	+15.1 ± 4.4	+17.4 ± 5.2	+12.6 ± 8.5
6.0	2.9	+20.9 ± 8.5	+3.5 ± 6.8	−2.1 ± 6.3	−2.0 ± 6.6	−7.1 ± 11.5
6.0	3.2	+16.6 ± 8.5	+0.3 ± 6.9	−5.0 ± 6.3	−4.8 ± 6.7	−8.8 ± 12.8
8.0	2.4	+64.6 ± 3.5	+27.3 ± 1.9	+26.6 ± 2.2	+32.2 ± 2.8	+5.3 ± 12.7
8.0	2.9	+22.3 ± 7.0	+2.6 ± 4.6	−1.7 ± 4.8	−0.7 ± 5.2	−10.2 ± 9.8
8.0	3.2	+13.8 ± 2.0	−3.0 ± 1.2	−7.3 ± 1.0	−6.5 ± 1.0	−9.9 ± 11.8

Tab. C.13: Deviation of Heat Flux Prediction from Measurements for 37 mm Combustion Chamber Using McAdams Model ("-" underprediction, "+" overprediction)

p_c [MPa]	O/F [−]	Segment 1 [%]	Segment 2 [%]	Segment 3 [%]	Nozzle [%]
4.0	2.9	+33.6 ± 7.6	+3.8 ± 4.3	−1.4 ± 4.0	+49.4 ± 26.7
4.0	3.2	+26.9 ± 6.7	−0.4 ± 3.3	−4.0 ± 3.9	+40.8 ± 25.7
6.0	2.4	+133 ± 19.4	+42.3 ± 6.0	+19.9 ± 3.9	+53.7 ± 20.7
6.0	2.9	+36.0 ± 3.1	+3.9 ± 2.8	−4.4 ± 1.1	+10.0 ± 9.7
6.0	3.2	+23.7 ± 6.5	−3.0 ± 3.5	−8.7 ± 2.7	+10.3 ± 9.3
8.0	2.4	+124 ± 22.7	+32.4 ± 4.9	+8.2 ± 2.2	+18.6 ± 10.8
8.0	2.9	+40.3 ± 11.5	+5.8 ± 6.8	−3.7 ± 6.7	+4.3 ± 12.2
8.0	3.2	+28.5 ± 13.5	−1.7 ± 7.5	−8.1 ± 7.0	+2.0 ± 10.7

Tab. C.14: Deviation of Heat Flux Prediction from Measurements for 20 mm Combustion Chamber Using McAdams Model ("-" underprediction, "+" overprediction)

C.4 Optimized Sinyarev Model Parameters

p_c [MPa]	O/F [−]	Segment 1 [%]	Segment 2 [%]	Segment 3 [%]	Segment 4 [%]	Nozzle [%]
2.0	1.8	+57.1 ± 32.0	+29.3 ± 39.7	+7.7 ± 26.7	+8.0 ± 21.5	+37.1 ± 20.2
2.0	2.4	−9.7 ± 4.9	−22.8 ± 6.3	−25.7 ± 3.9	−24.2 ± 2.5	+8.2 ± 15.6
2.0	2.9	−34.1 ± 9.6	−37.8 ± 6.8	−37.6 ± 4.2	−38.0 ± 3.7	+10.7 ± 3.8
4.0	1.8	+119 ± 27.7	+63.1 ± 22.8	+39.2 ± 13.7	+39.8 ± 13.7	+48.9 ± 4.2
4.0	2.4	+43.9 ± 10.2	+13.0 ± 5.3	+4.1 ± 3.9	+5.6 ± 5.4	+32.3 ± 11.7
4.0	2.9	−1.6 ± 8.4	−14.0 ± 6.0	−18.5 ± 5.8	−19.0 ± 5.9	+10.0 ± 11.3
4.0	3.2	−8.7 ± 3.5	−19.0 ± 2.3	−22.9 ± 2.2	−23.5 ± 2.2	+4.6 ± 7.9
6.0	2.4	+55.5 ± 7.6	+16.8 ± 3.0	+9.3 ± 3.3	+10.7 ± 4.1	+14.5 ± 7.9
6.0	2.9	+18.7 ± 8.6	+1.6 ± 7.0	−4.4 ± 6.4	−4.9 ± 6.8	−3.2 ± 11.6
6.0	3.2	+14.9 ± 9.5	−1.1 ± 7.8	−6.9 ± 7.1	−7.2 ± 7.5	−4.8 ± 13.2
8.0	2.4	+68.9 ± 4.2	+30.9 ± 3.0	+29.7 ± 2.1	+34.8 ± 2.0	+13.6 ± 13.7
8.0	2.9	+28.5 ± 6.6	+8.0 ± 4.3	+3.2 ± 4.5	+3.7 ± 4.8	−1.0 ± 11.2
8.0	3.2	+20.5 ± 1.1	+3.0 ± 0.4	−2.0 ± 0.2	−1.5 ± 0.3	−0.1 ± 13.6

Tab. C.15: Deviation of Heat Flux Prediction from Measurements for 37 mm Combustion Chamber Using Optimized Sinyarev Model Parameters ("-" underprediction, "+" overprediction)

p_c [MPa]	O/F [−]	Segment 1 [%]	Segment 2 [%]	Segment 3 [%]	Nozzle [%]
4.0	2.9	+7.2 ± 5.8	−17.0 ± 3.1	−21.8 ± 3.0	+26.1 ± 22.8
4.0	3.2	+2.2 ± 5.4	−20.1 ± 2.4	−23.6 ± 3.1	+19.1 ± 22.1
6.0	2.4	+107 ± 16.7	+25.8 ± 4.7	+5.4 ± 3.4	+43.3 ± 19.5
6.0	2.9	+23.5 ± 2.7	−5.9 ± 2.2	−13.9 ± 1.2	+4.2 ± 9.5
6.0	3.2	+12.2 ± 6.1	−12.3 ± 3.1	−17.9 ± 2.5	+4.2 ± 9.0
8.0	2.4	+113 ± 20.4	+25.5 ± 4.3	+2.0 ± 2.2	+17.6 ± 11.0
8.0	2.9	+34.5 ± 10.2	+1.4 ± 6.1	−8.2 ± 5.9	+3.8 ± 11.6
8.0	3.2	+23.6 ± 12.2	−5.4 ± 6.6	−12.0 ± 6.1	+1.8 ± 10.3

Tab. C.16: Deviation of Heat Flux Prediction from Measurements for 20 mm Combustion Chamber Using Optimized Sinyarev Model Parameters ("-" underprediction, "+" overprediction)

C.5 Adaption of Local Adiabatic Wall Temperature

p_c [MPa]	O/F [−]	Segment 1 [%]	Segment 2 [%]	Segment 3 [%]	Segment 4 [%]	Nozzle [%]
2.0	1.8	+193 ± 66.0	+141 ± 76.0	+101 ± 51.4	+102 ± 41.9	+109 ± 35.9
2.0	2.4	+53.0 ± 8.4	+30.8 ± 10.4	+26.4 ± 7.3	+29.7 ± 7.4	+55.7 ± 27.6
2.0	2.9	+10.8 ± 14.3	+4.1 ± 9.6	+4.9 ± 5.2	+5.0 ± 4.3	+60.2 ± 5.4
4.0	1.8	+208 ± 43.3	+129 ± 35.7	+97.4 ± 22.5	+99.3 ± 22.7	+79.5 ± 4.7
4.0	2.4	+87.4 ± 13.5	+47.1 ± 7.5	+36.4 ± 5.3	+39.1 ± 6.5	+49.9 ± 15.3
4.0	2.9	+25.6 ± 10.8	+9.5 ± 7.6	+4.5 ± 7.2	+4.4 ± 7.3	+22.5 ± 15.5
4.0	3.2	+15.7 ± 5.9	+2.4 ± 4.2	−1.9 ± 3.9	−2.0 ± 4.1	+15.4 ± 10.8
6.0	2.4	+77.6 ± 8.2	+33.3 ± 3.6	+25.3 ± 4.7	+27.6 ± 5.6	+17.1 ± 8.8
6.0	2.9	+33.4 ± 9.3	+13.8 ± 7.4	+7.6 ± 6.8	+7.6 ± 7.2	−3.1 ± 12.0
6.0	3.2	+28.7 ± 9.3	+10.4 ± 7.5	+4.5 ± 6.9	+4.7 ± 7.3	−4.8 ± 13.4
8.0	2.4	+71.6 ± 7.0	+32.3 ± 4.6	+31.5 ± 6.3	+37.3 ± 7.4	+5.1 ± 11.7
8.0	2.9	+33.8 ± 7.4	+12.0 ± 4.8	+7.3 ± 5.0	+8.3 ± 5.5	−6.6 ± 10.2
8.0	3.2	+24.9 ± 2.0	+6.2 ± 1.2	+1.4 ± 1.0	+2.2 ± 1.0	−6.1 ± 12.4

Tab. C.17: Deviation of Heat Flux Prediction from Measurements for 37 mm Combustion Chamber Using Modified Sinyarev Model with Fuel Rich Boundary Layer ("-" underprediction, "+" overprediction)

C.6 Adaption of Heat Transfer Coefficient

p_c $[MPa]$	O/F $[-]$	Segment 1 [%]	Segment 2 [%]	Segment 3 [%]	Segment 4 [%]	Nozzle [%]
2.0	1.8	$+0.2 \pm 10.5$	$+5.1 \pm 23.9$	-5.1 ± 16.6	-6.5 ± 10.8	-30.2 ± 11.2
2.0	2.4	-6.3 ± 4.7	-7.9 ± 7.1	-7.8 ± 5.1	-6.1 ± 5.1	-25.2 ± 12.1
2.0	2.9	-4.3 ± 3.2	-2.2 ± 1.3	-0.2 ± 2.9	-0.0 ± 3.9	-2.7 ± 7.8
4.0	1.8	$+14.7 \pm 3.3$	$+12.1 \pm 7.1$	$+5.2 \pm 3.3$	$+1.9 \pm 2.8$	-10.0 ± 7.6
4.0	2.4	$+5.2 \pm 4.1$	$+0.8 \pm 2.5$	-0.9 ± 2.3	-1.9 ± 3.2	-2.4 ± 8.0
4.0	2.9	-0.4 ± 1.7	-0.2 ± 1.2	-1.5 ± 1.5	-3.2 ± 1.6	-1.2 ± 9.1
4.0	3.2	$+2.4 \pm 3.8$	$+2.1 \pm 3.2$	$+0.4 \pm 3.7$	-1.0 ± 3.6	-0.4 ± 7.2
6.0	2.4	-2.7 ± 4.4	-8.1 ± 1.9	-7.7 ± 2.3	-9.5 ± 3.0	-6.9 ± 5.2
6.0	2.9	$+1.3 \pm 5.5$	$+2.0 \pm 5.0$	$+1.0 \pm 4.8$	-1.8 ± 5.2	-9.4 ± 11.6
6.0	3.2	$+3.0 \pm 5.8$	$+3.3 \pm 5.7$	$+2.0 \pm 5.5$	-0.5 ± 5.7	-8.2 ± 13.0
8.0	2.4	-12.3 ± 8.1	-11.8 ± 7.3	-5.1 ± 6.1	-5.6 ± 5.7	-6.4 ± 14.3
8.0	2.9	-2.5 ± 3.6	-1.6 ± 3.4	-0.5 ± 2.7	-2.9 ± 2.2	-2.7 ± 12.6
8.0	3.2	$+2.9 \pm 4.7$	$+3.2 \pm 4.3$	$+3.2 \pm 4.0$	$+1.0 \pm 4.0$	$+5.1 \pm 18.6$

Tab. C.18: Deviation of Heat Flux Prediction from Measurements for 37 mm Combustion Chamber Using Modified Sinyarev Model with Empiric Corrections ("-" underprediction, "+" overprediction)

C.7 Simple Injector Correction

p_c $[MPa]$	O/F $[-]$	Segment 1 [%]	Segment 2 [%]	Segment 3 [%]	Segment 4 [%]	Nozzle [%]
2.0	1.8	-4.5 ± 8.5	$+0.6 \pm 17.7$	-14.6 ± 10.7	-13.5 ± 5.3	-5.9 ± 18.1
2.0	2.4	-10.8 ± 4.7	-12.5 ± 6.9	-15.3 ± 5.1	-13.0 ± 5.6	$+6.0 \pm 19.2$
2.0	2.9	-26.8 ± 9.6	-26.0 ± 7.2	-25.3 ± 4.0	-25.3 ± 3.4	$+15.2 \pm 2.7$
4.0	1.8	-2.7 ± 4.5	$+6.1 \pm 10.7$	-5.5 ± 7.0	-4.1 ± 7.3	-10.0 ± 4.8
4.0	2.4	-6.5 ± 3.4	-7.4 ± 2.4	-13.5 ± 2.5	-11.8 ± 3.5	-2.7 ± 8.0
4.0	2.9	-12.0 ± 2.6	-10.2 ± 2.3	-14.2 ± 2.5	-14.2 ± 2.6	$+1.7 \pm 9.7$
4.0	3.2	-14.5 ± 2.9	-12.1 ± 1.7	-15.7 ± 1.9	-15.9 ± 1.9	-0.2 ± 7.8
6.0	2.4	-4.9 ± 4.5	$+0.6 \pm 2.6$	-3.4 ± 2.1	-1.3 ± 3.0	-8.0 ± 5.2
6.0	2.9	-7.0 ± 5.0	$+3.4 \pm 5.0$	-1.3 ± 4.6	-1.2 ± 5.0	-10.5 ± 11.3
6.0	3.2	-7.3 ± 6.1	$+2.9 \pm 6.4$	-1.7 ± 5.9	-1.5 ± 6.2	-10.2 ± 12.7
8.0	2.4	-13.3 ± 2.9	-0.6 ± 2.8	$+2.5 \pm 1.8$	$+7.4 \pm 1.5$	-16.3 ± 10.3
8.0	2.9	-8.9 ± 2.3	$+3.5 \pm 1.5$	$+0.8 \pm 1.6$	$+1.8 \pm 1.5$	-11.7 ± 10.1
8.0	3.2	-8.9 ± 0.2	$+1.9 \pm 1.0$	-1.6 ± 1.1	-0.7 ± 1.1	-8.7 ± 11.9

Tab. C.19: Deviation of Heat Flux Prediction from Measurements for 37 mm Combustion Chamber Using Modified Sinyarev Model with Startup Correction ("-" underprediction, "+" overprediction)

p_c $[MPa]$	O/F $[-]$	Segment 1 [%]	Segment 2 [%]	Segment 3 [%]	Nozzle [%]
4.0	2.9	-0.2 ± 5.4	-5.3 ± 3.0	-9.9 ± 2.8	$+34.1 \pm 24.1$
4.0	3.2	-4.5 ± 4.2	-7.6 ± 1.9	-10.8 ± 3.0	$+28.5 \pm 23.3$
6.0	2.4	-2.7 ± 8.4	$+3.6 \pm 2.7$	-3.2 ± 4.3	$+24.6 \pm 17.0$
6.0	2.9	-4.7 ± 1.8	$+8.5 \pm 1.7$	$+3.4 \pm 1.4$	$+17.2 \pm 11.1$
6.0	3.2	-3.6 ± 2.5	$+2.9 \pm 3.2$	-1.6 ± 3.2	$+16.7 \pm 10.0$
8.0	2.4	-0.5 ± 5.8	$+8.6 \pm 3.5$	$+5.8 \pm 4.1$	$+19.2 \pm 12.5$
8.0	2.9	-9.5 ± 6.0	$+8.9 \pm 5.5$	$+6.6 \pm 7.3$	$+14.4 \pm 13.3$
8.0	3.2	-10.1 ± 5.1	$+5.5 \pm 5.7$	$+3.7 \pm 7.1$	$+13.4 \pm 11.5$

Tab. C.20: Deviation of Heat Flux Prediction from Measurements for 20 mm Combustion Chamber Using Modified Sinyarev Model with Startup Correction ("-" underprediction, "+" overprediction)

Afterword

This work was performed within the 'A*erodynamic and* T*hermal* L*oad Interactions with* L*ightweight* A*dvanced Materials for High* S*peed Flight*' project investigating high-speed transport. ATLLAS, coordinated by ESA-ESTEC, was supported by the EU within the 6th Framework Programme Priority 1.4, Aeronautic and Space, Contract Number: AST5-CT-2006-030729. Further information on the ATLLAS program can be found on `http://www.esa.int/techresources/atllas`.

Financial support was provided by the German Research Foundation (Deutsche Forschungsgemeinschaft – DFG) in the framework of the Sonderforschungsbereich Transregio 40.